The Astrophysical Journal, 740:16 (17pp), 2011 October 10 doi:10.1088/0004-637X/740/1/16

OBSERVATION OF ANISOTROPY IN THE ARRIVAL DIRECTIONS OF GALACTIC COSMIC RAYS AT MULTIPLE ANGULAR SCALES WITH IceCube

R. Abbasi[1], Y. Abdou[2], T. Abu-Zayyad[3], J. Adams[4], J. A. Aguilar[1], M. Ahlers[5], D. Altmann[6], K. Andeen[1], J. Auffenberg[7], X. Bai[8], M. Baker[1], S. W. Barwick[9], R. Bay[10], J. L. Bazo Alba[11], K. Beattie[12], J. J. Beatty[13,14], S. Bechet[15], J. K. Becker[16], K.-H. Becker[7], M. L. Benabderrahmane[11], S. BenZvi[1], J. Berdermann[11], P. Berghaus[8], D. Berley[17], E. Bernardini[11], D. Bertrand[15], D. Z. Besson[18], D. Bindig[7], M. Bissok[6], E. Blaufuss[17], J. Blumenthal[6], D. J. Boersma[6], C. Bohm[19], D. Bose[20], S. Böser[21], O. Botner[22], A. M. Brown[4], S. Buitink[20], K. S. Caballero-Mora[23], M. Carson[2], D. Chirkin[1], B. Christy[17], J. Clem[8], F. Clevermann[24], S. Cohen[25], C. Colnard[26], D. F. Cowen[23,27], M. V. D'Agostino[10], M. Danninger[19], J. Daughhetee[28], J. C. Davis[13], C. De Clercq[20], L. Demirörs[25], T. Denger[21], O. Depaepe[20], F. Descamps[2], P. Desiati[1], G. de Vries-Uiterweerd[2], T. DeYoung[23], J. C. Díaz-Vélez[1], M. Dierckxsens[15], J. Dreyer[16], J. P. Dumm[1], R. Ehrlich[17], J. Eisch[1], R. W. Ellsworth[17], O. Engdegård[22], S. Euler[6], P. A. Evenson[8], O. Fadiran[29], A. R. Fazely[30], A. Fedynitch[16], J. Feintzeig[1], T. Feusels[2], K. Filimonov[10], C. Finley[19], T. Fischer-Wasels[7], M. M. Foerster[23], B. D. Fox[23], A. Franckowiak[21], R. Franke[11], T. K. Gaisser[8], J. Gallagher[31], L. Gerhardt[10,12], L. Gladstone[1], T. Glüsenkamp[6], A. Goldschmidt[12], J. A. Goodman[17], D. Gora[11], D. Grant[32], T. Griesel[33], A. Groß[4,26], S. Grullon[1], M. Gurtner[7], C. Ha[23], A. Hajismail[2], A. Hallgren[22], F. Halzen[1], K. Han[11], K. Hanson[1,15], D. Heinen[6], K. Helbing[7], P. Herquet[34], S. Hickford[4], G. C. Hill[1], K. D. Hoffman[17], A. Homeier[21], K. Hoshina[1], D. Hubert[20], W. Huelsnitz[17], J.-P. Hülß[6], P. O. Hulth[19], K. Hultqvist[19], S. Hussain[8], A. Ishihara[35], J. Jacobsen[1], G. S. Japaridze[29], H. Johansson[19], J. M. Joseph[12], K.-H. Kampert[7], A. Kappes[36], T. Karg[7], A. Karle[1], P. Kenny[18], J. Kiryluk[10,12], F. Kislat[11], S. R. Klein[10,12], J.-H. Köhne[24], G. Kohnen[34], H. Kolanoski[36], L. Köpke[33], S. Kopper[7], D. J. Koskinen[23], M. Kowalski[21], T. Kowarik[33], M. Krasberg[1], T. Krings[6], G. Kroll[33], N. Kurahashi[1], T. Kuwabara[8], M. Labare[20], S. Lafebre[23], K. Laihem[6], H. Landsman[1], M. J. Larson[23], R. Lauer[11], J. Lünemann[33], B. Madajczyk[1], J. Madsen[3], P. Majumdar[11], A. Marotta[15], R. Maruyama[1], K. Mase[35], H. S. Matis[12], K. Meagher[17], M. Merck[1], P. Mészáros[23,27], T. Meures[15], E. Middell[11], N. Milke[24], J. Miller[22], T. Montaruli[1,37], R. Morse[1], S. M. Movit[27], R. Nahnhauer[11], J. W. Nam[9], U. Naumann[7], P. Nießen[8], D. R. Nygren[12], S. Odrowski[26], A. Olivas[17], M. Olivo[16], A. O'Murchadha[1], M. Ono[35], S. Panknin[21], L. Paul[6], C. Pérez de los Heros[22], J. Petrovic[15], A. Piegsa[33], D. Pieloth[24], R. Porrata[10], J. Posselt[7], C. C. Price[1], P. B. Price[10], G. T. Przybylski[12], K. Rawlins[38], P. Redl[17], E. Resconi[26], W. Rhode[24], M. Ribordy[25], A. Rizzo[20], J. P. Rodrigues[1], P. Roth[17], F. Rothmaier[33], C. Rott[13], T. Ruhe[24], D. Rutledge[23], B. Ruzybayev[8], D. Ryckbosch[2], H.-G. Sander[33], M. Santander[1], S. Sarkar[5], K. Schatto[33], T. Schmidt[17], A. Schönwald[11], A. Schukraft[6], A. Schultes[7], O. Schulz[26], M. Schunck[6], D. Seckel[8], B. Semburg[7], S. H. Seo[19], Y. Sestayo[26], S. Seunarine[39], A. Silvestri[9], A. Slipak[23], G. M. Spiczak[3], C. Spiering[11], M. Stamatikos[13,40], T. Stanev[8], G. Stephens[23], T. Stezelberger[12], R. G. Stokstad[12], A. Stössl[11], S. Stoyanov[8], E. A. Strahler[20], T. Straszheim[17], M. Stür[21], G. W. Sullivan[17], Q. Swillens[15], H. Taavola[22], I. Taboada[28], A. Tamburro[3], A. Tepe[28], S. Ter-Antonyan[30], S. Tilav[8], P. A. Toale[41], S. Toscano[1], D. Tosi[11], D. Turčan[17], N. van Eijndhoven[20], J. Vandenbroucke[10], A. Van Overloop[2], J. van Santen[1], M. Vehring[6], M. Voge[21], C. Walck[19], T. Waldenmaier[36], M. Wallraff[6], M. Walter[11], Ch. Weaver[1], C. Wendt[1], S. Westerhoff[1], N. Whitehorn[1], K. Wiebe[33], C. H. Wiebusch[6], D. R. Williams[41], R. Wischnewski[11], H. Wissing[17], M. Wolf[26], T. R. Wood[32], K. Woschnagg[10], C. Xu[8], X. W. Xu[30], G. Yodh[9], S. Yoshida[35], P. Zarzhitsky[41], and M. Zoll[19]

(IceCube Collaboration)

[1] Department of Physics, University of Wisconsin, Madison, WI 53706, USA
[2] Department of Physics and Astronomy, University of Gent, B-9000 Gent, Belgium
[3] Department of Physics, University of Wisconsin, River Falls, WI 54022, USA
[4] Department of Physics and Astronomy, University of Canterbury, Private Bag 4800, Christchurch, New Zealand
[5] Department of Physics, University of Oxford, 1 Keble Road, Oxford OX1 3NP, UK
[6] III. Physikalisches Institut, RWTH Aachen University, D-52056 Aachen, Germany
[7] Department of Physics, University of Wuppertal, D-42119 Wuppertal, Germany
[8] Bartol Research Institute and Department of Physics and Astronomy, University of Delaware, Newark, DE 19716, USA
[9] Department of Physics and Astronomy, University of California, Irvine, CA 92697, USA
[10] Department of Physics, University of California, Berkeley, CA 94720, USA
[11] DESY, D-15735 Zeuthen, Germany
[12] Lawrence Berkeley National Laboratory, Berkeley, CA 94720, USA
[13] Department of Physics and Center for Cosmology and Astro-Particle Physics, Ohio State University, Columbus, OH 43210, USA
[14] Department of Astronomy, Ohio State University, Columbus, OH 43210, USA
[15] Université Libre de Bruxelles, Science Faculty CP230, B-1050 Brussels, Belgium
[16] Fakultät für Physik & Astronomie, Ruhr-Universität Bochum, D-44780 Bochum, Germany
[17] Department of Physics, University of Maryland, College Park, MD 20742, USA
[18] Department of Physics and Astronomy, University of Kansas, Lawrence, KS 66045, USA
[19] Oskar Klein Centre and Department of Physics, Stockholm University, SE-10691 Stockholm, Sweden
[20] Vrije Universiteit Brussel, Dienst ELEM, B-1050 Brussels, Belgium
[21] Physikalisches Institut, Universität Bonn, Nussallee 12, D-53115 Bonn, Germany
[22] Department of Physics and Astronomy, Uppsala University, Box 516, S-75120 Uppsala, Sweden
[23] Department of Physics, Pennsylvania State University, University Park, PA 16802, USA

[24] Department of Physics, TU Dortmund University, D-44221 Dortmund, Germany
[25] Laboratory for High Energy Physics, École Polytechnique Fédérale, CH-1015 Lausanne, Switzerland
[26] Max-Planck-Institut für Kernphysik, D-69177 Heidelberg, Germany
[27] Department of Astronomy and Astrophysics, Pennsylvania State University, University Park, PA 16802, USA
[28] School of Physics and Center for Relativistic Astrophysics, Georgia Institute of Technology, Atlanta, GA 30332, USA
[29] CTSPS, Clark-Atlanta University, Atlanta, GA 30314, USA
[30] Department of Physics, Southern University, Baton Rouge, LA 70813, USA
[31] Department of Astronomy, University of Wisconsin, Madison, WI 53706, USA
[32] Department of Physics, University of Alberta, Edmonton, Alberta T6G 2G7, Canada
[33] Institute of Physics, University of Mainz, Staudinger Weg 7, D-55099 Mainz, Germany
[34] Université de Mons, 7000 Mons, Belgium
[35] Department of Physics, Chiba University, Chiba 263-8522, Japan
[36] Institut für Physik, Humboldt-Universität zu Berlin, D-12489 Berlin, Germany
[37] Dipartimento di Fisica, I-70126, Università di Bari and Sezione INFN, Bari, Italy
[38] Department of Physics and Astronomy, University of Alaska Anchorage, 3211 Providence Dr., Anchorage, AK 99508, USA
[39] Department of Physics, University of the West Indies, Cave Hill Campus, Bridgetown BB11000, Barbados
[40] NASA Goddard Space Flight Center, Greenbelt, MD 20771, USA
[41] Department of Physics and Astronomy, University of Alabama, Tuscaloosa, AL 35487, USA
Received 2011 May 11; accepted 2011 July 6; published 2011 September 20

ABSTRACT

Between 2009 May and 2010 May, the IceCube neutrino detector at the South Pole recorded 32 billion muons generated in air showers produced by cosmic rays with a median energy of 20 TeV. With a data set of this size, it is possible to probe the southern sky for per-mil anisotropy on all angular scales in the arrival direction distribution of cosmic rays. Applying a power spectrum analysis to the relative intensity map of the cosmic ray flux in the southern hemisphere, we show that the arrival direction distribution is not isotropic, but shows significant structure on several angular scales. In addition to previously reported large-scale structure in the form of a strong dipole and quadrupole, the data show small-scale structure on scales between 15° and 30°. The skymap exhibits several localized regions of significant excess and deficit in cosmic ray intensity. The relative intensity of the smaller-scale structures is about a factor of five weaker than that of the dipole and quadrupole structure. The most significant structure, an excess localized at (right ascension $\alpha = 122.^{\circ}4$ and declination $\delta = -47.^{\circ}4$), extends over at least 20° in right ascension and has a post-trials significance of 5.3σ. The origin of this anisotropy is still unknown.

Key words: astroparticle physics – cosmic rays

Online-only material: color figures

1. INTRODUCTION

The IceCube detector, deployed 1450 m below the surface of the South Polar ice sheet, is designed to detect upward-going neutrinos from astrophysical sources. However, it is also sensitive to downward-going muons produced in cosmic ray air showers. To penetrate the ice and trigger the detector, the muons must possess an energy of at least several hundred GeV, which means they are produced by primary cosmic rays with energies in excess of several TeV. Simulations show that the detected direction of an air shower muon is typically within $0.^{\circ}2$ of the direction of the primary particle, so the arrival direction distribution of muons recorded in the detector is also a map of the cosmic ray arrival directions between about 1 TeV and several 100 TeV. IceCube is currently the only instrument that can produce such a skymap of cosmic ray arrival directions in the southern sky. It records several 10^{10} cosmic ray events per year, which makes it possible to study anisotropy in the arrival direction distribution at the 10^{-4} level and below.

It is believed that charged cosmic rays at TeV energies are accelerated in supernova remnants in the Galaxy. It is also expected that interactions of cosmic rays with Galactic magnetic fields should completely scramble their arrival directions. For example, the Larmor radius of a proton with 10 TeV energy in a μG magnetic field is approximately 0.01 pc, orders of magnitude less than the distance to any potential accelerator. Nevertheless, multiple observations of anisotropy in the arrival direction distribution of cosmic rays have been reported on large and small angular scales, mostly from detectors in the northern hemisphere. These deviations from isotropy in the cosmic ray flux between several TeV and several hundred TeV are at the part-per-mil level, according to data from the Tibet ASγ array (Amenomori et al. 2005, 2006), the Super-Kamiokande Detector (Guillian et al. 2007), the Milagro Gamma Ray Observatory (Abdo et al. 2008, 2009), ARGO-YBJ (Vernetto et al. 2009), and EAS-TOP (Aglietta et al. 2009). Recently, a study of muons observed with the IceCube detector has revealed a large-scale anisotropy in the southern sky that is similar to that detected in the north (Abbasi et al. 2010b).

In this paper, we present the results of a search for cosmic ray anisotropy on all scales in the southern sky with data recorded between 2009 May and 2010 May with the IceCube detector in its 59-string configuration. An angular power spectrum analysis reveals that the cosmic ray skymap as observed by IceCube is dominated by a strong dipole and quadrupole moment, but it also exhibits significant structure on scales down to about 15°. This small-scale structure is about a factor of five weaker in relative intensity than the dipole and quadrupole and becomes visible when these large-scale structures are subtracted from the data. A comprehensive search for deviations of the cosmic ray flux from isotropy on all angular scales reveals several localized regions of cosmic ray excess and deficit, with a relative intensity of the order of 10^{-4}. The most significant structure is located at right ascension $\alpha = 122.^{\circ}4$ and declination $\delta = -47.^{\circ}4$ and has a significance of 5.3σ after correcting for trials. A comparison with data taken with fewer strings in the two years prior to this period confirms that these structures are a persistent feature of the southern sky.

The paper is organized as follows. In this section, we give a short summary of previous observations, almost exclusively in the northern hemisphere, of anisotropy in the cosmic ray arrival skymap at TeV energies. After the description of the IceCube detector and the data set used for this analysis (Section 2), the analysis techniques and results are presented in Section 3. In Section 4, we show the outcome of several systematic checks of the analysis. The results are summarized and compared to Milagro results in the northern hemisphere in Section 5.

1.1. Past Observations of Large- and Small-scale Anisotropy

The presence of a large-scale anisotropy in the distribution of charged cosmic rays can be caused by several effects. For example, configurations of the heliospheric magnetic field and other fields in the neighborhood of the solar system may be responsible. In this case, it is expected that the strength of the anisotropy should weaken with energy due to the increasing magnetic rigidity of the primary particles. The present data cannot unambiguously support or refute this hypothesis. Measurements from the Tibet ASγ experiment indicate that the anisotropy disappears above a few hundred TeV (Amenomori et al. 2006), but a recent analysis of EAS-TOP data appears to show an increase in the amplitude of the anisotropy above 400 TeV (Aglietta et al. 2009).

Existing data sets have also been searched for a time-dependent modulation of the anisotropy, which could be due to solar activity perhaps correlated with the 11 year solar cycle. Results are inconclusive at this point. Whereas the Milagro data exhibit an increase in the mean depth of a large deficit region in the field of view over time (Abdo et al. 2009), no variation of the anisotropy with the solar cycle has been observed in Tibet ASγ data (Amenomori et al. 2010). If these results are confirmed with more data recorded over longer time periods, different structures might show a different long-term behavior.

A large-scale anisotropy can also be caused by any relative motion of the Earth through the rest frame of the cosmic rays. The intensity of the cosmic ray flux should be enhanced in the direction of motion and reduced in the opposite direction, causing a dipole anisotropy in the coordinate frame where the direction of motion is fixed. However, Earth's motion through space is complex and a superposition of several components, and the rest frame of the cosmic ray plasma is not known. If we assume that the cosmic rays are at rest with respect to the Galactic center, then a dipole of amplitude 0.35% should be observed due to the solar orbit about the Galactic center. Such a dipole anisotropy, which would be inclined at about 45° with respect to the celestial equator, was first proposed by Compton & Getting (1935). Although the effect is strong enough to be measured by modern detectors, it has not been observed. This null result likely indicates that galactic cosmic rays corotate with the local Galactic magnetic field (Amenomori et al. 2006).

The motion of the Earth around the Sun also causes a dipole in the arrival directions of cosmic rays. The dipole is aligned with the ecliptic plane, and its strength is expected to be of order 10^{-4}. This solar dipole effect has been observed by the Tibet ASγ experiment (Amenomori et al. 2004) and Milagro (Abdo et al. 2009) and provides a sensitivity test for all methods looking for large-scale anisotropy in equatorial coordinates.

In addition to the large-scale anisotropy, data from several experiments in the northern hemisphere indicate the presence of small-scale structures with scales of order 10°. Using seven years of data, the Milagro Collaboration published the detection of two regions of enhanced flux with amplitude 10^{-4} and a median energy of 1 TeV with significance $>10\sigma$ (Abdo et al. 2008). The same excess regions also appear on skymaps produced by ARGO-YBJ (Vernetto et al. 2009).

Small-scale structures in the arrival direction distribution may indicate nearby sources of cosmic rays, although the small Larmor radius at TeV energies makes it impossible for these particles to point back to their sources unless some unconventional propagation mechanism is assumed (Malkov et al. 2010). Diffusion from nearby supernova remnants, magnetic funneling (Drury & Aharonian 2008), and cosmic ray acceleration from magnetic reconnection in the solar magnetotail (Lazarian & Desiati 2010) have all been suggested as possible causes for the small-scale structure in the northern hemisphere.

1.2. Analysis Techniques

While the presence of large-scale structure in the southern sky has already been established using IceCube data (Abbasi et al. 2010b), there has not been a search of the southern sky for correlations on smaller angular scales. In this paper, we present a comprehensive study of the cosmic ray arrival directions in IceCube which includes, but is not limited to, the search for small-scale structures.

Large- and small-scale structures have traditionally been analyzed with very different methods. The presence of a large-scale anisotropy is usually established by fitting the exposure-corrected arrival direction distribution in right ascension to the first few elements of a harmonic series (Amenomori et al. 2006). While essentially a one-dimensional method, the procedure can be applied to the right ascension distribution in several declination bands to probe the strength of dipole and quadrupole moments as a function of declination (Abdo et al. 2009). To search for small-scale structure, the estimation for an isotropic sky is compared to the actual arrival direction distribution to find significant deviations from isotropy (Abdo et al. 2008; Vernetto et al. 2009).

Since both the large- and small-scale structures in the cosmic ray data are currently unexplained, it is not obvious whether a "clean" separation between large and small scales is the right approach. The anisotropy in the arrival direction distribution might be a superposition of several effects, with the small-scale structure being caused by a different mechanism than the large-scale structure, or it might be the result of a single mechanism producing a complex skymap with structure on all scales.

The analysis presented in this paper makes use of a number of complementary methods to study the arrival direction distribution without prior separation into searches for large- and small-scale structure. The basis of this study is the angular power spectrum of the arrival direction distribution. A power spectrum analysis decomposes the skymap into spherical harmonics and provides information on the angular scale of the anisotropy in the map. The power spectrum indicates which multipole moments $\ell = (0, 1, 2, \ldots)$ in the spherical harmonic expansion contribute significantly to the observed arrival direction distribution. To produce a skymap of the contribution of the $\ell \geqslant 3$ multipoles, the strong contributions from the dipole ($\ell = 1$) and quadrupole ($\ell = 2$) have to be subtracted first. The residual map can then be studied for structure on angular scales corresponding to $\ell \geqslant 3$. This is the first search for structure at these scales in the arrival direction distribution of TeV cosmic rays in the southern sky.

2. THE IceCube DETECTOR

IceCube is a km^3-size neutrino detector frozen into the glacial ice sheet at the geographic South Pole. The ice serves as the detector medium. High-energy neutrinos are detected by observing the Cherenkov radiation from charged particles produced by neutrino interactions in the ice or in the bedrock below the detector.

The Cherenkov light is detected by an array of Digital Optical Modules (DOMs) embedded in the ice. Each DOM is a pressure-resistant glass sphere that contains a 25 cm photomultiplier tube (Abbasi et al. 2010a) and electronics that digitize, timestamp, and transmit signals to the data acquisition system (Abbasi et al. 2009b). The IceCube array contains 5160 DOMs deployed at depths between 1450 m and 2450 m below the surface of the ice sheet. The DOMs are attached to 86 vertical cables, or strings, which are used for deployment and to transmit data to the surface. The horizontal distance between strings in the standard detector geometry is about 125 m, while the typical vertical spacing between consecutive DOMs in each string is about 17 m. Six strings are arranged into a more compact configuration, with smaller spacing between DOMs, at the bottom of the detector, forming DeepCore, designed to extend the energy reach of IceCube to lower neutrino energies. On the ice surface sits IceTop, an array of detectors dedicated to the study of the energy spectrum and composition of cosmic rays with energies between 500 TeV and 1 EeV, several orders of magnitude larger in energy than the cosmic rays studied in this analysis. All data used in this work come from the IceCube in-ice detector only.

Construction of IceCube has recently been completed with all 86 strings deployed. The detector has been operating in various configurations since 2005 (Achterberg et al. 2006). Between 2007 and 2008, it operated with 22 strings deployed (IC22), between 2008 and 2009 with 40 strings (IC40), and between 2009 and 2010 with 59 strings (IC59).

IceCube is sensitive to all neutrino flavors. Muon neutrinos, identified by the "track-like" signature of the muon produced in a charged-current interaction, form the dominant detection channel. Muons produced by astrophysical neutrinos are detected against an overwhelming background of muons produced in cosmic ray air showers in the atmosphere above the detector. IceCube searches are most sensitive to neutrino sources in the northern hemisphere, where the Earth can be used as a filter against atmospheric muons (Abbasi et al. 2009a).

While atmospheric muons are a background for neutrino astrophysics, they are a valuable tool in the analysis of the cosmic rays that produce them. The downgoing muons preserve the direction of the cosmic ray air shower, and thus the cosmic ray primary, and can be used to study the arrival direction distribution of cosmic rays at energies above roughly 10 TeV.

2.1. DST Data Set

The trigger rates of downgoing muons are about 0.5 kHz in IC22, 1.1 kHz in IC40, and 1.7 kHz in IC59. These rates are of order 10^6 times the neutrino rate, and too large to allow for storage of the raw data. Instead, downgoing muon events are stored in a separate Data Storage and Transfer (DST) format suitable for recording high-rate data at the South Pole. The DST format is used to store the results of an online reconstruction performed on all events that trigger the IceCube detector. Most of the data are downward-going muons produced by cosmic ray air showers. Because of the high trigger rate, the DST filter stream is used to save a very limited set of information for every event. Basic event parameters such as energy estimators are stored, while digitized waveforms are only transmitted for a limited subset of events. The data are encoded in a compressed format that allows for the transfer of about 3 GB day^{-1} via the South Pole Archival and Data Exchange satellite communication system.

The main trigger used for physics analysis in IceCube is a simple majority trigger which requires coincidence of eight or more DOMs hit in the deep ice within a 5 μs window. In order to pass the trigger condition, those hits have to be in coincidence with at least one other hit in the nearest or next-to-nearest neighboring DOM within $\pm 1\,\mu$s (local coincidence hits). Triggered events are reconstructed using two fast online algorithms (Ahrens et al. 2004). The first reconstruction is a line-fit algorithm based on an analytic χ^2 minimization. It produces an initial event track from the position and timing of the hits and the total charge, but it does not account for the geometry of the Cherenkov cone and the scattering and absorption of photons in the ice. The second algorithm is a maximum likelihood-based muon track reconstruction, seeded with the line-fit estimate of the arrival direction. The likelihood reconstruction is more accurate, but also more computationally expensive, so it is applied only when at least 10 optical sensors are triggered by the event. The analysis presented in this work uses only events reconstructed with the maximum likelihood algorithm.

In addition to particle arrival directions, the DST data also contain the number of DOMs and hits participating in the event, as well as the total number of triggered strings, and the position of the center of gravity of the event. The number of DOMs in the event can be used as a measure of the energy of the primary cosmic ray. Above 1 TeV, the energy resolution is of order 0.5 in $\Delta(\log(E))$, where E is the energy of the primary cosmic ray. Most of the uncertainty originates in the physics of the air shower. In this energy range, we are dominated by air showers containing muons with energies near the threshold necessary to reach the deep ice. Fluctuations in the generation of these muons are the main contribution to the uncertainty in the determination of the energy of the primary cosmic ray.

2.2. Data Quality Cuts, Median Energy, and Angular Resolution

The analysis presented in this paper uses the DST data collected during IC59 operations between 2009 May 20 and 2010 May 30. The data set contains approximately 3.4×10^{10} muon events detected with an integrated livetime of 334.5 days. A cut in zenith angle to remove misreconstructed tracks near the horizon (see below) reduces the final data set to 3.2×10^{10} events.

Simulated air showers are used to evaluate the median angular resolution of the likelihood reconstruction and the median energy of the downgoing muon DST data set. The simulated data are created using the standard air shower Monte Carlo program CORSIKA[42] (Heck et al. 1998). The cosmic ray spectrum and composition are simulated using the polygonato model of Hörandel (2003), and the air showers are generated with the SIBYLL model of high-energy hadronic interactions (Ahn et al. 2009).

The simulations show that, for zenith angles smaller than 65°, the median angular resolution is 3°. This is not to be confused with the angular resolution of IceCube for neutrino-induced

[42] COsmic Ray SImulations for KAscade: http://www-ik.fzk.de/corsika/.

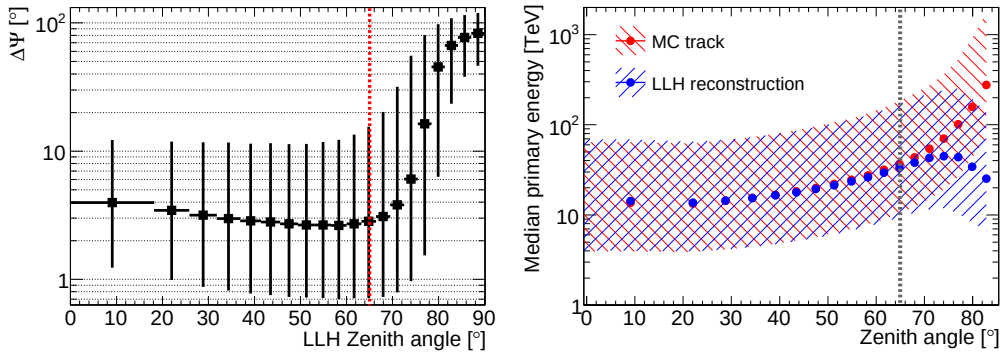

Figure 1. Median angular resolution (left) and median energy (right) as a function of zenith angle for simulated cosmic ray events. The error bars on the left plot and the hatched regions on the right one correspond to a 68% containing interval. The median primary energy is shown both as a function of the true zenith angle (MC track) and the reconstructed zenith angle (LLH reconstruction), while the median angular resolution (left) is shown as a function of the reconstructed zenith angle only. The dotted vertical line at $\theta = 65^\circ$ indicates the cut in zenith angle performed in this work.

(A color version of this figure is available in the online journal.)

tracks (better than 1°), where more sophisticated reconstruction algorithms and more stringent quality cuts are applied. The resolution depends on the zenith angle of the muon. Figure 1 (left) shows the median angular resolution as a function of zenith angle. The resolution improves from 4° at small zenith angles to about 2.°5 near 60°. The larger space angle error at small zenith angles is caused by the detector geometry, which makes it difficult to reconstruct the azimuth angle for near-vertical showers. Consequently, with the azimuth angle being essentially unknown, the angular error can be large. For zenith angles greater than 65°, the angular resolution degrades markedly. The reason is that more and more events with apparent zenith angle greater than 65° are misreconstructed tracks of smaller zenith angle and lower energy. The energy threshold for muon triggers increases rapidly with slant depth in the atmosphere and ice, and the statistics at large zenith angle become quite poor. We restrict our analysis to events with zenith angles smaller than 65°. Within this range, the angular resolution is roughly constant and much smaller than the angular size of arrival direction structure we are trying to study.

Using simulated data, we estimate that the overall median energy of the primary cosmic rays that trigger the IceCube detector is 20 TeV. Simulations show that at this energy the detector is more sensitive to protons than to heavy nuclei like iron. The median energy increases monotonically with the true zenith angle of the primary particle (Figure 1, right) due to the attenuation of low-energy muons with increasing slant depth of the atmosphere and ice. The median energy also increases as a function of reconstructed zenith angle. Near the horizon, the large fraction of misreconstructed events causes the median energy to fall.

3. ANALYSIS

The arrival direction distribution of cosmic rays observed by detectors like IceCube is not isotropic. Nonuniform exposure to different parts of the sky, gaps in the uptime, and other detector-related effects will cause a spurious anisotropy in the measured arrival direction distribution even if the true cosmic ray flux is isotropic. Consequently, in any search for anisotropy in the cosmic ray flux, these detector-related effects need to be accounted for. The first step in this search is therefore the creation of a "reference map" to which the actual data map is compared. The reference map essentially shows what the skymap would look like if the cosmic ray flux was isotropic. It is not in itself isotropic, because it includes the detector effects mentioned above. The reference map must be subtracted from the real skymap in order to find regions where the actual cosmic ray flux deviates from the isotropic expectation.

In this section, we first describe the construction of the reference map for the subsequent analysis. The reference map is then compared to the actual data map, and a map of the relative cosmic ray intensity is produced. We then perform several analyses to search for the presence of significant anisotropy in the relative intensity map.

3.1. Calculation of the Reference Level

For the construction of a reference map that represents the detector response to an isotropic sky, it is necessary to determine the exposure of the detector as a function of time and integrate it over the livetime. We use the method of Alexandreas et al. (1993) to calculate the exposure from real data. This technique is commonly used in γ-ray astronomy to search for an excess of events above the exposure-weighted isotropic reference level.

The method works as follows. The sky is binned into a fine grid in equatorial coordinates (right ascension α, declination δ). Two skymaps are then produced. The data map $N(\alpha, \delta)$ stores the arrival directions of all detected events. For each detected event that is stored in the data map, 20 "fake" events are generated by keeping the local zenith and azimuth angles (θ, ϕ) fixed and calculating new values for right ascension using times randomly selected from within a pre-defined time window Δt bracketing the time of the event being considered. These fake events are stored in the reference map with a weight of $1/20$. Using 20 fake events per real event, the statistical error on the reference level can be kept small.

Created in this way, the events in the reference map have the same local arrival direction distribution as the real events. Furthermore, this "time scrambling" method naturally compensates for variations in the event rate, including the presence of gaps in the detector uptime. The buffer length Δt needs to be chosen such that the detector conditions remain stable within this period. Due to its unique location at the South Pole, the angular acceptance of IceCube is stable over long periods. The longest Δt used in this analysis is one day, and the detector stability over this time period has been verified by χ^2-tests comparing the arrival direction distributions at various times inside the window. The IceCube detector is, in fact, stable over periods longer than 24 hr.

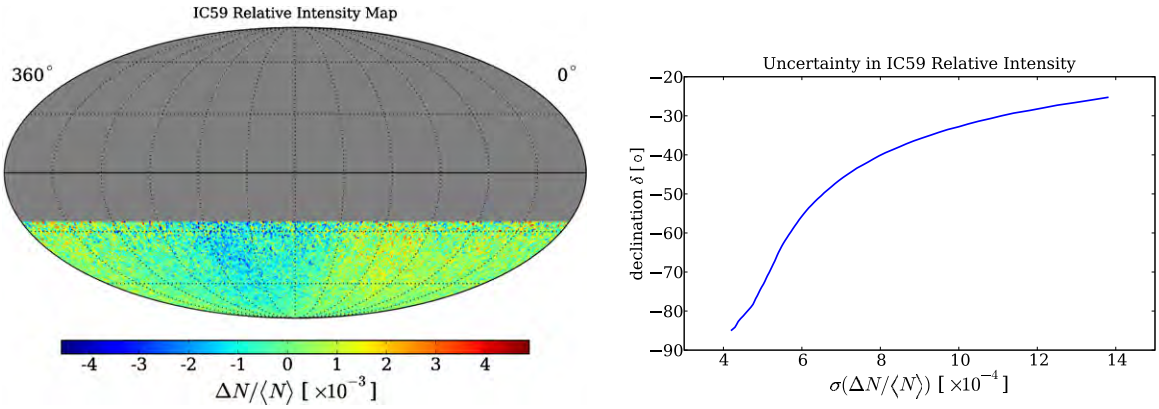

Figure 2. Left: relative intensity $\Delta N/\langle N\rangle$ of the IC59 data in equatorial coordinates, produced with a time window of 24 hr. Right: dependence of the statistical error on the declination.

(A color version of this figure is available in the online journal.)

Deviations from isotropy are known to bias estimates of the reference level produced by this method. In the vicinity of a strong excess, the method can create artificial deficits, as the events from the excess region are included in the estimation of the reference level. Similarly, there can be artificial excesses near strong deficits. In searches for point sources, the effect is usually negligible, but it can become significant in the presence of extended regions of strong excess or deficit flux.

Since the Earth rotates by 15° every hour, the right ascension range of the scrambled data is $15^\circ\ \mathrm{hr}^{-1} \times \Delta t$, so any structure in the data map that is larger than $15^\circ\ \mathrm{hr}^{-1} \times \Delta t$ will also appear in the reference map and therefore be suppressed in the relative intensity map $\Delta N/\langle N\rangle$. For example, $\Delta t = 2$ hr will suppress structures larger than 30° in the relative intensity map. To be sensitive to large-scale structure such as a dipole, a time window of 24 hr (or higher) must be used.

3.2. Relative Intensity and Significance Maps

Once the data and reference maps are calculated, deviations from isotropy can be analyzed by calculating the relative intensity:

$$\frac{\Delta N_i}{\langle N\rangle_i} = \frac{N_i(\alpha,\delta) - \langle N_i(\alpha,\delta)\rangle}{\langle N_i(\alpha,\delta)\rangle}, \quad (1)$$

which gives the amplitude of deviations from the isotropic expectation in each angular bin i. The deviations from isotropy can also be expressed in terms of a statistical significance using the method of Li & Ma (1983). We report both relative intensity maps and significance maps in this paper.

The analyses in this paper use the HEALPix[43] library for the production of skymaps (Gorski et al. 2005). HEALPix produces an equal-area division of the unit sphere with pixels of roughly equal shape. The resolution of the HEALPix grid is defined by a parameter called N_{side}, which is related to the number of pixels in the grid by $N_{\mathrm{pix}} = 12N_{\mathrm{side}}^2$. Here, $N_{\mathrm{side}} = 64$ has been chosen, so that the sky is divided into 49,152 pixels with an average pixel size of about 0.°9. Due to the zenith angle cut of 65° discussed in Section 2.2, the pixels above declination $\delta = -25^\circ$ are masked in the analysis. This leaves 14,196 pixels in the region between $\delta = -25^\circ$ and the celestial South Pole at $\delta = -90^\circ$. The skymaps are plotted in equatorial coordinates using an equal-area homolographic projection.

[43] Hierarchical Equal-Area isoLatitude Pixelization of the sphere: http://healpix.jpl.nasa.gov.

Figure 2 (left) shows the relative intensity when a 24 hr time window is used to estimate the reference level. The map exhibits clear structures. The most obvious features are a broad excess in the relative counts near right ascension 105° and a broad deficit near 225°. The relative intensity in the excess (and deficit) region is of order 10^{-3}. This structure is the large-scale anisotropy first observed in the analysis of the IC22 data set and reported in Abbasi et al. (2010b). Since the IC59 data set is larger than the IC22 data set by an order of magnitude, it is now possible to see the large-scale structure directly in the data without further rebinning or averaging over many pixels.

Figure 2 (right) shows the statistical error on the relative intensity map. Relative intensity skymaps have declination-dependent statistical uncertainties due to the fact that the detector acceptance decreases with larger zenith angle. Since IceCube is located at the South Pole, the relative intensity exhibits large fluctuations near the horizon, corresponding to declinations $\delta > -30^\circ$. Such edge effects are not as severe for skymaps of the significance of the fluctuations, though one must note that the location of structures with large (or small) significance may not coincide with regions of large (or small) relative intensity.

Figure 3 (left) shows the significance map corresponding to the relative intensity map shown in Figure 2. The right panel also shows a distribution of the significance values in each bin. In an isotropic skymap, the distribution of the significance values should be normal (red dashed line). However, the best Gaussian fit to the distribution (black solid line) exhibits large deviations from a normal distribution caused by the large-scale structure.

3.3. Angular Power Spectrum Analysis

To observe correlations between pixels at several angular scales, we calculate the angular power spectrum of the relative intensity map $\delta I = \Delta N/\langle N\rangle$ described in Section 3.2. The relative intensity can be treated as a scalar field which we expand in terms of a spherical harmonic basis,

$$\delta I(\mathbf{u}_i) = \sum_{\ell=1}^{\infty} \sum_{m=-\ell}^{\ell} a_{\ell m} Y_{\ell m}(\mathbf{u}_i) \quad (2)$$

$$a_{\ell m} \sim \Omega_p \sum_{i=0}^{N_{\mathrm{pix}}} \delta I(\mathbf{u}_i) Y^*_{\ell m}(\mathbf{u}_i). \quad (3)$$

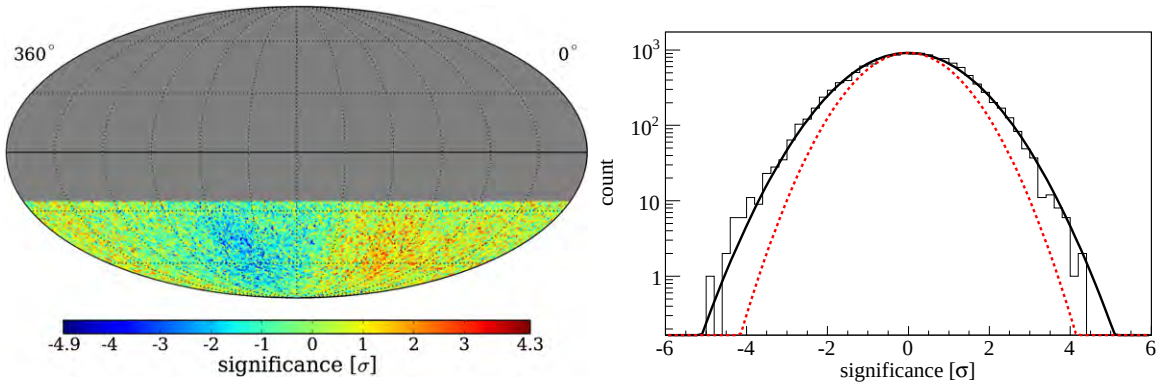

Figure 3. Left: significance skymap of the IC59 data in equatorial coordinates, produced using a time window of 24 hr. Right: one-dimensional distribution of the significance values together with the best-fit (black solid line) performed with a Gaussian function. For comparison, a Gaussian function of mean zero and unit variance (red dashed line), expected from an isotropic sky, has been superimposed.

(A color version of this figure is available in the online journal.)

In Equations (2) and (3), the $Y_{\ell m}$ are the Laplace spherical harmonics, the $a_{\ell m}$ are the multipole coefficients of the expansion, Ω_p is the solid angle observed by each pixel (which is constant across the sphere in HEALPix), $\mathbf{u}_i = (\alpha_i, \delta_i)$ is the pointing vector associated with the ith pixel, and $N_{\rm pix}$ is the total number of pixels in the skymap. The power spectrum for the relative intensity field is defined as the variance of the multipole coefficients $a_{\ell m}$,

$$\mathcal{C}_\ell = \frac{1}{2\ell+1} \sum_{m=-\ell}^{\ell} |a_{\ell m}|^2. \quad (4)$$

The amplitude of the power spectrum at some multipole order ℓ is associated with the presence of structures in the sky at angular scales of about $180^\circ/\ell$. In the case of complete and uniform sky coverage, a straightforward Fourier decomposition of the relative intensity maps would yield an unbiased estimate of the power spectrum. However, due to the limited exposure of the detector, we only have direct access to the so-called pseudo-power spectrum, which is the convolution of the real underlying power spectrum and the power spectrum of the relative exposure map of the detector in equatorial coordinates. In the case of partial sky coverage, the standard $Y_{\ell m}$ spherical harmonics do not form an orthonormal basis that we can use to expand the relative intensity field directly. As a consequence of this, the pseudo-power spectrum displays a systematic correlation between different ℓ modes that needs to be corrected for.

The deconvolution of pseudo-power spectra has been a longstanding problem in the study of the cosmic microwave background (CMB), and there are several computationally efficient tools available from the CMB community. (For a discussion on the bias introduced by partial sky coverage in power spectrum estimation and a description of several bias removal methods, see Ansari & Magneville 2010.) To calculate the power spectrum of the IC59 data, we use the publicly available `PolSpice`[44] software package (Szapudi et al. 2001; Chon et al. 2004).

In `PolSpice`, the correction for partial sky bias is performed not on the power spectrum itself, but on the two-point correlation function of the relative intensity map. The two-point correlation function $\xi(\eta)$ is defined as

$$\xi(\eta) = \langle \delta I(\mathbf{u}_i)\, \delta I(\mathbf{u}_j) \rangle, \quad (5)$$

where $\delta I(\mathbf{u}_k)$ is the observed relative intensity in the direction of the kth pixel. Note that $\xi(\eta)$ depends only on the angle η between any two pixels. The two-point correlation function can be expanded into a Legendre series,

$$\xi(\eta) = \frac{1}{4\pi} \sum_{\ell=0}^{\infty} (2\ell+1)\, \mathcal{C}_\ell\, P_\ell(\cos\eta), \quad (6)$$

where the $\mathcal{C}_\ell$ are the coefficients of the angular power spectrum and the P_ℓ are the Legendre polynomials. The inverse operation

$$\mathcal{C}_\ell = 2\pi \int_{-1}^{1} \xi(\eta) P_\ell(\cos\eta)\, d(\cos\eta) \quad (7)$$

can be used to calculate the angular power spectrum coefficients from a known two-point correlation function.

In order to obtain an unbiased estimator of the true power spectrum, `PolSpice` first calculates the $a_{\ell m}$ coefficients of both the relative intensity map and the relative exposure map doing a spherical harmonics expansion equivalent to that shown in Equation (3). Pseudo-power spectra for both maps are computed from these coefficients using Equation (4), and these spectra are subsequently converted into correlation functions using Equation (6). An unbiased estimator $\tilde{\xi}(\eta)$ of the true correlation function of the data is computed by taking the ratio of the correlation functions of the relative intensity map and the relative exposure map. An estimate $\tilde{\mathcal{C}}_\ell$ of the true power spectrum can then be obtained from the corrected two-point correlation function using the integral expression shown in Equation (7).

This process reduces the correlation between different ℓ modes introduced by the partial sky coverage. Minor ringing artifacts associated with the limited angular range over which the correlation function is evaluated are minimized by applying an apodization function to the correlation function in η-space as described in Chon et al. (2004). The cosine apodization scheme provided by `PolSpice` and used in this work allows the correlation function to fall slowly to zero at large angular scales where statistics are low, minimizing any ringing artifacts that could arise from the calculation of the power spectrum from the corrected correlation function using Equation (7).

Figure 4 (blue points) shows the angular power spectrum for the IC59 relative intensity map from Figure 2. In addition to a strong dipole and quadrupole moment ($\ell = 1, 2$), higher

[44] `PolSpice` website: http://prof.planck.fr/article141.html.

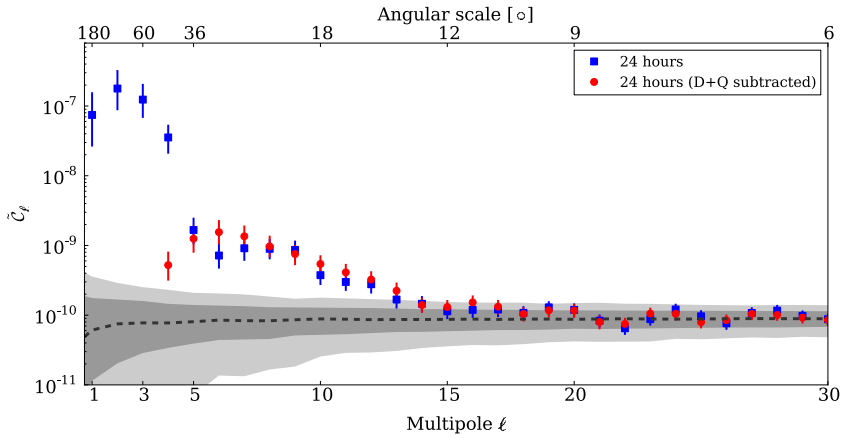

Figure 4. Angular power spectra for the relative intensity map shown in Figure 2. The blue and red points show the power spectrum before and after the subtraction of the dominant dipole and quadrupole terms from the relative intensity map. Error bars are statistical, but a possible systematic error is discussed in the text. The gray bands indicate the distribution of the power spectra in a large sample of isotropic data sets, showing the 68% (dark) and 95% (light) spread in the $\tilde{C}_\ell$.

(A color version of this figure is available in the online journal.)

order terms up to $\ell = 12$ contribute significantly to the skymap. The error bars on the $\tilde{C}_\ell$ are statistical. The gray bands indicate the 68% and 95% spread in the $\tilde{C}_\ell$ for a large number of power spectra for isotropic data sets (generated by introducing Poisson fluctuations in the reference skymap). As the $\tilde{C}_\ell$ are still not entirely independent (even after the correction for partial sky coverage is performed), a strong dipole moment in the data can lead to significant higher order multipoles, and it is important to study whether the structure for $3 \leqslant \ell \leqslant 12$ is a systematic effect caused by the strong lower order moments $\ell = 1, 2$. Figure 4 (red points) shows the angular power spectrum after the strong dipole and quadrupole moments are removed from the relative intensity map by a fit procedure described in the next section. The plot illustrates that after the removal of the lower order multipoles, indicated by the drop in $\tilde{C}_\ell$ for $\ell = 1, 2$ (both are consistent with 0 after the subtraction), most of the higher order terms are still present. Only the strength of $\tilde{C}_3$ and $\tilde{C}_4$ is considerably reduced (the former to a value that is below the range of the plot).

Regarding systematic uncertainties, for $\ell = 3$ and $\ell = 4$ the effects of the strong dipole and quadrupole suggest that there is significant coupling between the low-ℓ modes. Therefore, we cannot rule out that $\tilde{C}_3$ and $\tilde{C}_4$ are entirely caused by systematic effects. For the higher multipoles, the systematic effects of this distortion are much lower. After explicit subtraction of the $\ell = 1$ and $\ell = 2$ terms, the residual power spectrum agrees with the original power spectrum within the statistical uncertainties. Therefore, we conclude that the systematic uncertainties in these data points are, at most, of the same order as the statistical uncertainties.

In summary, the skymap of cosmic ray arrival directions contains significant structures on scales down to $\sim 15^\circ$. In the next sections, we describe analysis techniques to make the smaller-scale structure visible in the presence of the much stronger dipole and quadrupole moments.

3.4. Subtraction of the Dipole and Quadrupole Moments

A straightforward approach to understand the contribution of higher order multipoles and the corresponding structure in the skymap is to remove the strong dipole and quadrupole moments from the relative intensity map and study the residuals. This requires a dipole and quadrupole fit to the IC59 map. Once fit, the dipole and quadrupole can be subtracted from the skymap. We fit the relative intensity map using the function

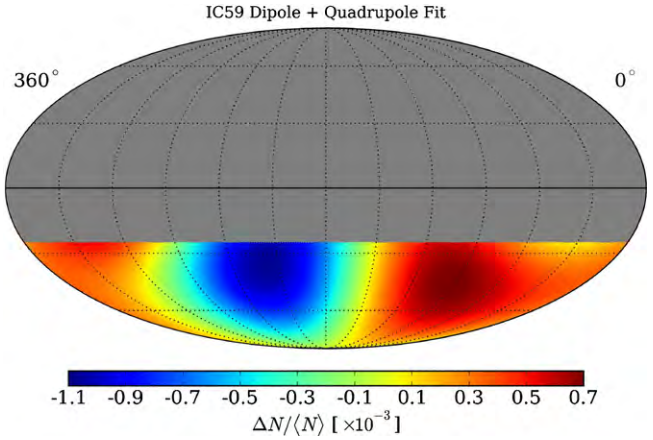

Figure 5. Fit of Equation (8) to the IC59 relative intensity distribution $\Delta N/\langle N\rangle$ shown in Figure 2.

(A color version of this figure is available in the online journal.)

$$\begin{aligned}\delta I(\alpha, \delta) = {} & m_0 + p_x \cos\delta\cos\alpha + p_y \cos\delta \sin\alpha + p_z \sin\delta \\ & + \frac{1}{2} Q_1 (3\cos^2\delta - 1) + Q_2 \sin 2\delta \cos\alpha \\ & + Q_3 \sin 2\delta \sin\alpha + Q_4 \cos^2\delta \cos 2\alpha \\ & + Q_5 \cos^2\delta \sin 2\alpha. \end{aligned} \quad (8)$$

Equation (8) is a multipole expansion of the relative count distribution in terms of real-valued spherical harmonic functions and follows a normalization convention commonly used in CMB physics (Smoot & Lubin 1979). The quantity m_0 is the "monopole" moment of the distribution and corresponds to a constant offset of the data from zero. The values (p_x, p_y, p_z) are the components of the dipole moment, and the quantities $(Q_1, \ldots, Q_5)$ are the five independent components of the quadrupole moment.

The two-dimensional harmonic expansion of Equation (8) was fit to the 14,196 pixels in the IC59 relative intensity map that lie between the celestial South Pole and declination $\delta = -25^\circ$. The best-fit dipole and quadrupole coefficients are provided in Table 1, and the corresponding sky distribution is shown in Figure 5. By themselves, the dipole and quadrupole terms can

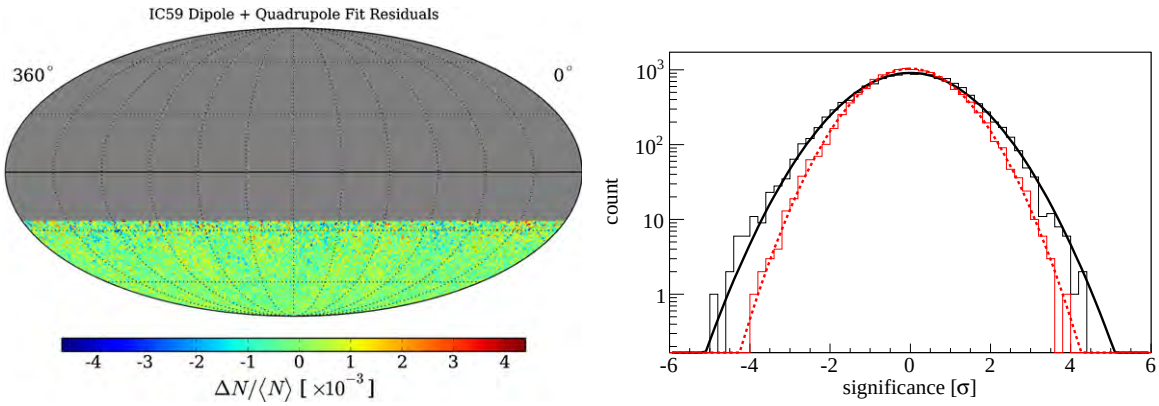

Figure 6. Left: residual of the fit of Equation (8) to the relative intensity distribution shown in Figure 2. Right: distribution of pixel significance values in the skymap before (solid black line) and after (dashed red line) subtraction of the dipole and quadrupole. Gaussian fits to the data yield a mean of $(-0.20 \pm 1.05) \times 10^{-2}$ and a width of 1.23 ± 0.01 before the dipole and quadrupole subtraction, and $(0.28 \pm 0.89) \times 10^{-2}$ and 1.02 ± 0.01 after.

(A color version of this figure is available in the online journal.)

Table 1
Coefficients for the Fit of Equation (8) to the IC59 Relative Intensity Distribution

Coefficient	Value (Stat. + Syst.) ($\times 10^{-4}$)	Correlation Coefficients $\chi^2/\text{ndf} = 14743/14187 : \Pr(\chi^2\|\text{ndf}) = 5.5 \times 10^{-4}$								
m_0	$0.32 \pm 2.26 \pm 0.28$	1.00								
p_x	$2.44 \pm 0.71 \pm 0.30$	0.00	1.00							
p_y	$-3.86 \pm 0.71 \pm 0.94$	0.00	0.00	1.00						
p_z	$0.55 \pm 3.87 \pm 0.45$	1.00	0.00	0.00	1.00					
Q_1	$0.23 \pm 1.70 \pm 0.17$	0.99	0.00	0.00	0.99	1.00				
Q_2	$-2.95 \pm 0.49 \pm 0.74$	0.00	0.98	0.00	0.00	0.00	1.00			
Q_3	$-8.80 \pm 0.49 \pm 0.50$	0.00	0.00	0.98	0.00	0.00	0.00	1.00		
Q_4	$-2.15 \pm 0.20 \pm 0.50$	0.00	0.00	0.00	0.00	0.00	0.00	0.00	1.00	
Q_5	$-5.27 \pm 0.20 \pm 0.06$	0.00	0.00	0.00	0.00	0.00	0.00	0.00	0.00	1.00

Notes. The correlation coefficients indicate that there is some degeneracy between the contributions of p_x and Q_2, p_y and Q_3, and p_z and Q_1 due to the fact that the IceCube detector only has a partial view of the sky. The systematic error on the fit parameters is estimated using the results of a fit using anti-sidereal time as described in Section 4.2.

account for much of the amplitude of the part-per-mil anisotropy observed in the IceCube data. We note that the quadrupole moment is actually the dominant term in the expansion, with a total amplitude that is about 2.5 times larger than the dipole magnitude. However, the $\chi^2/\text{ndf} = 14{,}743/14{,}187$ corresponds to a χ^2-probability of approximately 0.05%, so while the dipole and quadrupole are dominant terms in the arrival direction anisotropy, they do not appear to be sufficient to explain all of the structures observed in the angular distribution of $\Delta N/\langle N\rangle$. This result is consistent with the result of the angular power spectrum analysis in Section 3.3, which also indicates the need for higher order multipole moments to describe the structures in the relative intensity skymap.

Subtraction of the dipole and quadrupole fits from the relative intensity map shown in Figure 2 yields the residual map shown in Figure 6. The fit residuals are relatively featureless at first glance, and the significance values are well-described by a normal distribution, which is expected when no anisotropy is present. However, the bin size in this plot is not optimized for a study of significant anisotropy at angular scales larger than the angular resolution of the detector. To improve the sensitivity to larger features, we apply a smoothing procedure which simply takes the reference level and residual data counts in each bin and adds the counts from pixels within some angular radius of the bin. This procedure results in a map with Poisson uncertainties, though the bins are no longer statistically independent.

The actual size of any possible excess or deficit region (and thus the optimal smoothing scale) is not known a priori. Furthermore, the skymap may contain several significant structures of different size, with the optimal smoothing radius differing for each structure. To make the search as comprehensive as possible, we study the skymap on all smoothing scales from 3° (the angular resolution) to 45° in steps of 1° and search for regions of high significance at any location. Applying this procedure, the two most significant localized excesses on the sky are a region with a peak significance of 7.0σ at a smoothing radius of 22° at ($\alpha = 122.^\circ4, \delta = -47.^\circ4$), and a region of peak significance 6.7σ at a smoothing radius of 13° at ($\alpha = 263.^\circ0, \delta = -44.^\circ1$). These values do not account for statistical trials due to the scan over smoothing radii or the scan for the peak significance in the 14,196 pixels. We have estimated the trial factors by applying the same search strategy to a large number of simulated isotropic data sets. After trial factors are applied, the maximum significance of the "hot spot" with an optimal smoothing radius of 22° is reduced to 5.3σ, and the "hot spot" at 13° is reduced to 4.9σ.

Skymaps of the relative intensity and the significance of the residual data are plotted in Figure 7, where a smoothing radius of 20° has been used. The radius is not optimal for any of the most significant excesses, but with this choice all of the significant features can be seen with reasonable resolution. Compared with the intensity of the dipole and quadrupole shown in Figure 2, the smaller structures are weaker by about a factor of five.

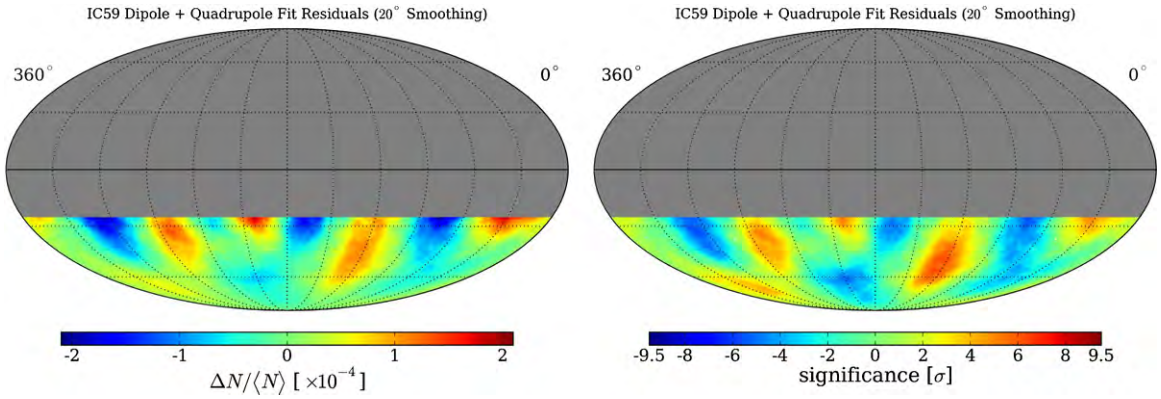

Figure 7. Left: residual intensity map plotted with 20° smoothing. Right: significances of the residual map (pre-trials), plotted with 20° smoothing.
(A color version of this figure is available in the online journal.)

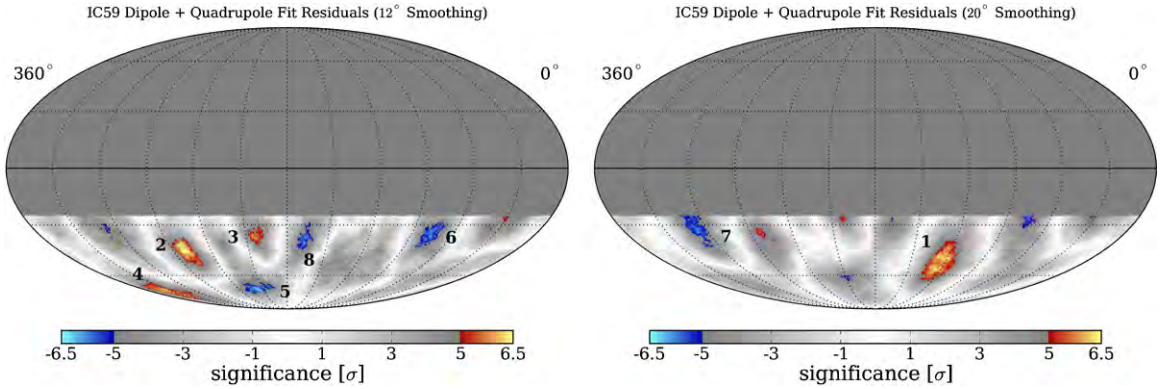

Figure 8. Left: significances of the IC59 residual map plotted with 12° smoothing. Right: significances of the IC59 residual map plotted with 20° smoothing. The regions with a pre-trial significance larger than $\pm 5\sigma$ are indicated according to the numbers used in Table 2.
(A color version of this figure is available in the online journal.)

Table 2
Location and Optimal Smoothing Scale for Regions of the IC59 Skymap with a Pre-trials Significance Larger than $\pm 5\sigma$

Region	Right Ascension	Declination	Optimal Scale	Peak Significance	Post-trials
1	$(122.4^{+4.1}_{-4.7})^\circ$	$(-47.4^{+7.5}_{-3.2})^\circ$	22°	7.0σ	5.3σ
2	$(263.0^{+3.7}_{-3.8})^\circ$	$(-44.1^{+5.3}_{-5.1})^\circ$	13°	6.7σ	4.9σ
3	$(201.6^{+6.0}_{-1.1})^\circ$	$(-37.0^{+2.2}_{-1.9})^\circ$	11°	6.3σ	4.4σ
4	$(332.4^{+9.5}_{-7.1})^\circ$	$(-70.0^{+4.2}_{-7.6})^\circ$	12°	6.2σ	4.2σ
5	$(217.7^{+10.2}_{-7.8})^\circ$	$(-70.0^{+3.6}_{-2.3})^\circ$	12°	-6.4σ	-4.5σ
6	$(77.6^{+3.9}_{-8.4})^\circ$	$(-31.9^{+3.2}_{-8.6})^\circ$	13°	-6.1σ	-4.1σ
7	$(308.2^{+4.8}_{-7.7})^\circ$	$(-34.5^{+9.6}_{-6.9})^\circ$	20°	-6.1σ	-4.1σ
8	$(166.5^{+4.5}_{-5.7})^\circ$	$(-37.2^{+5.0}_{-5.7})^\circ$	12°	-6.0σ	-4.0σ

Note. The errors on the equatorial coordinates indicate the range over which the significance drops by 1σ from the local extremum.

Table 2 contains the location and optimal smoothing scales of all the regions in the IC59 skymap that have a pre-trials significance beyond $\pm 5\sigma$. The data also exhibit additional regions of excess and deficit. It is possible that the deficits are at least in part artifacts of the reference level estimation procedure, which can produce artificial deficits around regions of significant excess counts (or in principle, excesses in the presence of strong physical deficits). While several of the deficit and excess regions are observed at large zenith angles near the edge of the IC59 exposure region, we do not believe these features are statistical fluctuations or edge effects. As we will show in Section 4.3, the features are also present in IC22 and IC40 data and grow in significance as the statistics increase.

Figure 8 shows the significance maps with regions with a pre-trial significance larger than $\pm 5\sigma$ indicated according to the numbers used in Table 2. Since the optimal scales vary from region to region and no single smoothing scale shows all regions, we show the maps with two smoothing scales, 12° (left) and 20° (right).

The angular power spectrum of the residual map is shown in red in Figure 4. As expected, there is no significant dipole or quadrupole moment left in the skymap, and the $\ell = 3$ and $\ell = 4$ moments have also disappeared or have been weakened substantially. However, the moments corresponding to $5 \leqslant \ell \leqslant 12$ are still present at the same strength as before the subtraction and indicate the presence of structure of angular

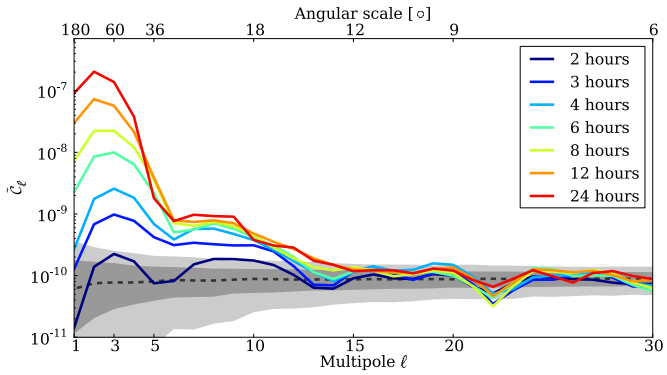

Figure 9. Power spectra for different values of the time scrambling period Δt. The filtering effect of the time scrambling on large-scale structure can be easily seen as a monotonic reduction in the strength of low-ℓ components of the power spectrum. The gray bands show 1σ and 2σ bands for a large set of isotropic skymaps. See Figure 4 and Section 3.3 for statistical uncertainties and a discussion of systematic uncertainties.

(A color version of this figure is available in the online journal.)

size 15°–35° in the data. The excesses and deficits in Figure 7 correspond in size to these moments.

3.5. A Filter for Structure on Small Angular Scales

In previous works (Abdo et al. 2008; Vernetto et al. 2009), a different method is applied to filter the lower ℓ terms and create skymaps showing the small-scale structure. In these analyses, the dipole and quadrupole moments are not fit and subtracted, but suppressed by varying the time window Δt over which the reference level is estimated (i.e., the length of time in which the time scrambling, or any other method for generating an isotropic sky, is performed). We apply this method to the IC59 data to compare the results to the dipole and quadrupole subtraction outlined in Section 3.4.

Different time windows probe the presence of anisotropy at different angular scales. The time scrambling fits structures that are larger than $15^\circ\ \mathrm{hr}^{-1} \times \Delta t$, and the angular size of a multipole of order ℓ in the sky is $\sim 180^\circ/\ell$. This implies that the technique filters out modes with $\ell < 12\,\mathrm{hr}/\Delta t$ and reduces the magnitude of the modes near this threshold.

The efficiency of the method in suppressing larger structures (low-ℓ moments) is demonstrated in Figure 9, where the angular power spectra are plotted for relative intensity maps constructed with seven values of Δt between 2 hr and 24 hr. As expected, the strength of the low-order multipoles decreases monotonically with Δt. However, the power spectrum also reveals that the low-ℓ moments, in particular the quadrupole term, are not completely removed from the data unless Δt is as small as 3 hr. In addition, the choice of $\Delta t \leqslant 3$ hr also appears to weaken the power observed in the modes $3 \leqslant \ell \leqslant 12$. Consequently, the residual map from Section 3.4 and the skymaps produced by choosing a small Δt cannot be expected to agree in all details. Nevertheless, a comparison of the skymaps produced with the two methods provides an important crosscheck.

To best compare this analysis to the results of Section 3.4, the reference level is calculated using a scrambling time window of $\Delta t = 4$ hr. This choice of Δt is motivated by the angular power spectrum in Figure 9. With $\Delta t = 4$ hr, the spectrum shows the strongest suppression of the dipole and quadrupole while still retaining most of power in the higher multipole moments.

Skymaps of the relative intensity and significance for $\Delta t = 4$ hr are shown in Figure 10. The maps have been smoothed by 20° to allow for a direct comparison with Figure 7. The most prominent features of the map are a single broad excess and deficit, with several small excess regions observed near the edge of the exposure region. The broad excess is centered at $\alpha = (121.7^{+4.8}_{-7.1})^\circ$ and $\delta = (-44.2^{+12.1}_{-7.8})^\circ$, at the same position as Region 1 in Table 2. The optimal smoothing scale of the excess is 25°, with a pre-trials significance of 9.6σ. A second significant excess is observed at $\alpha = (341.7^{+1.4}_{-5.6})^\circ$ and $\delta = (-34.9^{+3.6}_{-6.8})^\circ$ with a peak significance of 5.8σ at a smoothing scale of 9°. This feature does not appear to have a direct match in Figure 7, but is roughly aligned in right ascension with the excess identified in Table 2 as Region 4. We also note that the second-largest excess in Table 2, Region 2, is visible near $\alpha = 263.^\circ 0$ in Figure 10, but with a pre-trials peak significance of 4.5σ after smoothing by 13°.

The differences in significance between Figures 7 and 10 can be attributed to the fact that some contributions from the low-ℓ moments are still present in this analysis. The broad excess observed here is co-located with the maximum of the large-scale structure shown in Figure 5, enhancing its significance. By comparison, the excess in Region 2 is close to the minimum of the large-scale structure, weakening its significance. The leakage of large-scale structure into the $\Delta t = 4$ hr skymap also explains the large deficit near $\alpha = 220^\circ$; due to its co-location with the minimum of the dipole and quadrupole, the size of the deficit is enhanced considerably.

This effect is illustrated in Figure 11, which shows the relative intensity for the declination range $-45^\circ < \delta < -30^\circ$, projected onto the right ascension axis. This declination range is chosen because it contains some of the most significant structures of the skymaps. The blue points show the relative intensity

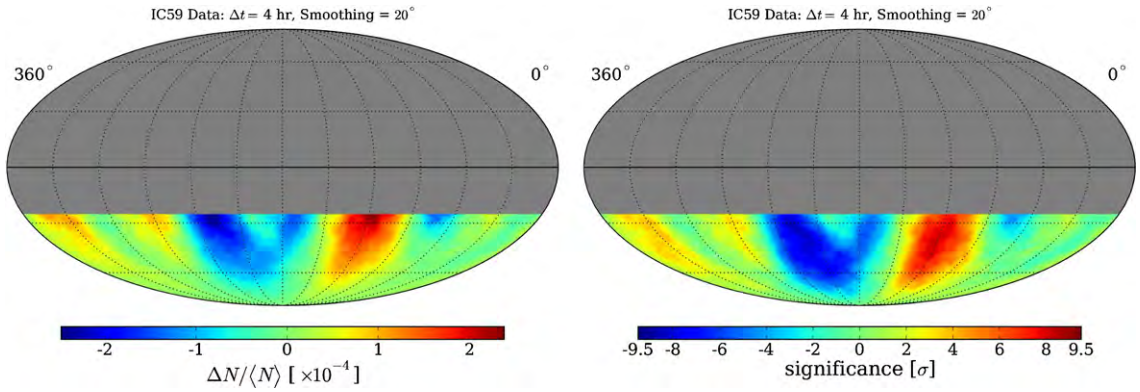

Figure 10. Relative intensity (left) and significance (right) map in equatorial coordinates for $\Delta t = 4$ hr and an integration radius of 20°.

(A color version of this figure is available in the online journal.)

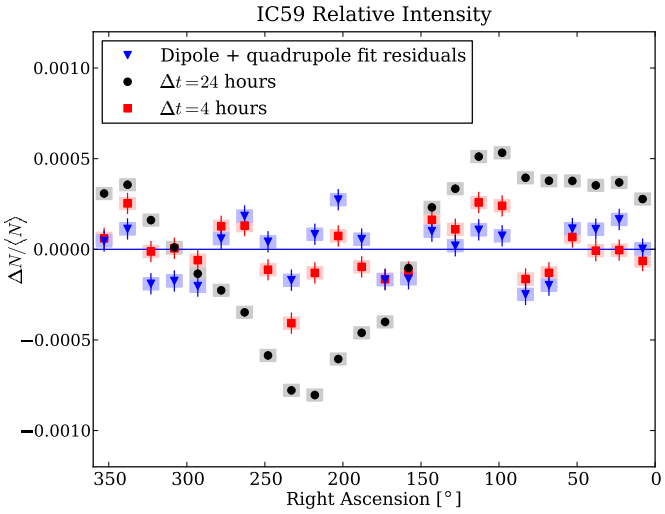

Figure 11. Relative intensity in the declination band $-45^\circ < \delta < -30^\circ$. The blue points show the result after subtracting the dipole and quadrupole moments. The black points correspond to Δt =24 hr and show the large-scale structure, the red points correspond to Δt = 4 hr. The error boxes represent systematic uncertainties.

(A color version of this figure is available in the online journal.)

corresponding to Figure 7, i.e., the skymap after subtraction of dipole and quadrupole moments. The black and red points show the relative intensity for skymaps obtained with the method described in this section; the black points correspond to $\Delta t = 24$ hr, the red points to $\Delta t = 4$ hr. In the case of $\Delta t = 24$ hr, the large-scale structure dominates. For $\Delta t = 4$ hr, the large-scale structure is suppressed, and the smaller features become visible. The blue and red curves show excesses and deficits at the same locations, but with different strengths. As the red curve still contains some remaining large-scale structure, maxima and minima are enhanced or weakened depending on where they are located with respect to the maximum and minimum of the large-scale structure. The systematic error for the relative intensity values in Figure 11 is taken from the analysis of the data in anti-sidereal time as described in the next section.

Finally, we note that the presence of the small-scale structure can be verified by inspection of the raw event counts in the data. Figure 12 shows the observed and expected event counts for declinations $-45^\circ < \delta < -30^\circ$, projected onto the right ascension axis. The seven panels of the figure contain the projected counts for seven time scrambling windows $\Delta t = \{2, 3, 4, 6, 8, 12, 24\,\mathrm{hr}\}$. For small values of Δt, the expected counts agree with the data; for example, when $\Delta t = 2$ hr, the data exhibit no visible deviation from the expected counts. For larger values of Δt, the expected count distribution flattens out as the technique to estimate the reference level no longer overfits the large structures. When $\Delta t = 24$ hr, the reference level is nearly flat, and the shape of the large-scale anisotropy is clearly visible from the raw data.

4. SYSTEMATIC CHECKS

Several tests have been performed on the data to ensure the stability of the observed anisotropy and to rule out possible sources of systematic bias. Among the influences that might cause spurious anisotropy are the detector geometry, the detector livetime, nonuniform exposure of the detector to different regions of the sky, and diurnal and seasonal variations in atmospheric conditions. Due to the unique location of the IceCube detector at the South Pole, many of these effects play a lesser role for IceCube than for detectors located in the middle latitudes. The southern celestial sky is fully visible to IceCube at any time and changes in the event rate tend to affect the entire visible sky. Seasonal variations are of order $\pm 10\%$ (Tilav et al. 2009), but the changes are slow and the reference level estimation technique is designed to take these changes into account. This is also true for any effects caused by the asymmetric detector response due to the geometrical configuration of the detector. In this section, we test the accuracy of these assumptions.

4.1. Solar Dipole Analysis

As mentioned in Section 1.1, any observer moving through a plasma of isotropic cosmic rays should observe a difference in intensity between the direction of the velocity vector and the opposite direction. Therefore, cosmic rays received on Earth should exhibit a dipole modulation in solar time caused by Earth's orbital velocity around the Sun. The expected change in the relative intensity is given by

$$\frac{\Delta I}{\langle I \rangle} = (\gamma + 2)\,\frac{v}{c}\cos\rho, \tag{9}$$

where I is the cosmic ray intensity, $\gamma = 2.7$ the power-law index of the cosmic ray energy spectrum, v/c the ratio of Earth's velocity with respect to the speed of light, and ρ the angle between the cosmic ray arrival direction and the direction of motion (Gleeson & Axford 1968). With a velocity of $v = 30\,\mathrm{km\,s^{-1}}$, the expected amplitude is 4.7×10^{-4}. Note that the power-law spectral index has a systematic uncertainty (see, for example, Biermann et al. 2010 for a discussion) and Earth's velocity is not precisely constant, but both of these uncertainties are too small to be relevant in our comparison of the predicted dipole strength to the measured strength. The solar dipole effect has been measured with several experiments (Amenomori et al. 2004, 2008; Abdo et al. 2009) and provides an important check of the reliability of the analysis techniques presented earlier, as it verifies that the techniques are sensitive to a known dipole with an amplitude of roughly the same size as the structures in the equatorial skymap.

In principle, the solar dipole is not a cause of systematic uncertainties in the analysis of cosmic ray anisotropy in sidereal time (equatorial coordinates). The solar dipole is visible only when the arrival directions are plotted in a frame where the Sun's position is fixed in the sky. A signal in this coordinate system averages to zero in sidereal time over the course of one year. However, any seasonal variation of the solar dipole can cause a spurious anisotropy in equatorial coordinates. The effect works both ways: a seasonal variation in the sidereal anisotropy will affect the solar dipole. A standard way to study the extent of these contaminations is by use of two artificial timescales, anti-sidereal and extended-sidereal time. Anti-sidereal time is calculated by reversing the sign of the transformation between universal time and sidereal time. Each sidereal day is slightly shorter than the solar day (universal time) by about 4 minutes, while each anti-sidereal day is longer than a solar day by the same. Anti-sidereal time therefore has 364.25 days (i.e., complete revolutions in the coordinate frame) per year, one day less than the solar year (365.25 days) and two days less than the sidereal year (366.25 days). Similarly, each extended sidereal day is shorter than a sidereal day by about 4 minutes (8 minutes shorter than the solar day). Extended sidereal time has therefore 367.25 days yr^{-1}. No physical phenomena are expected to occur

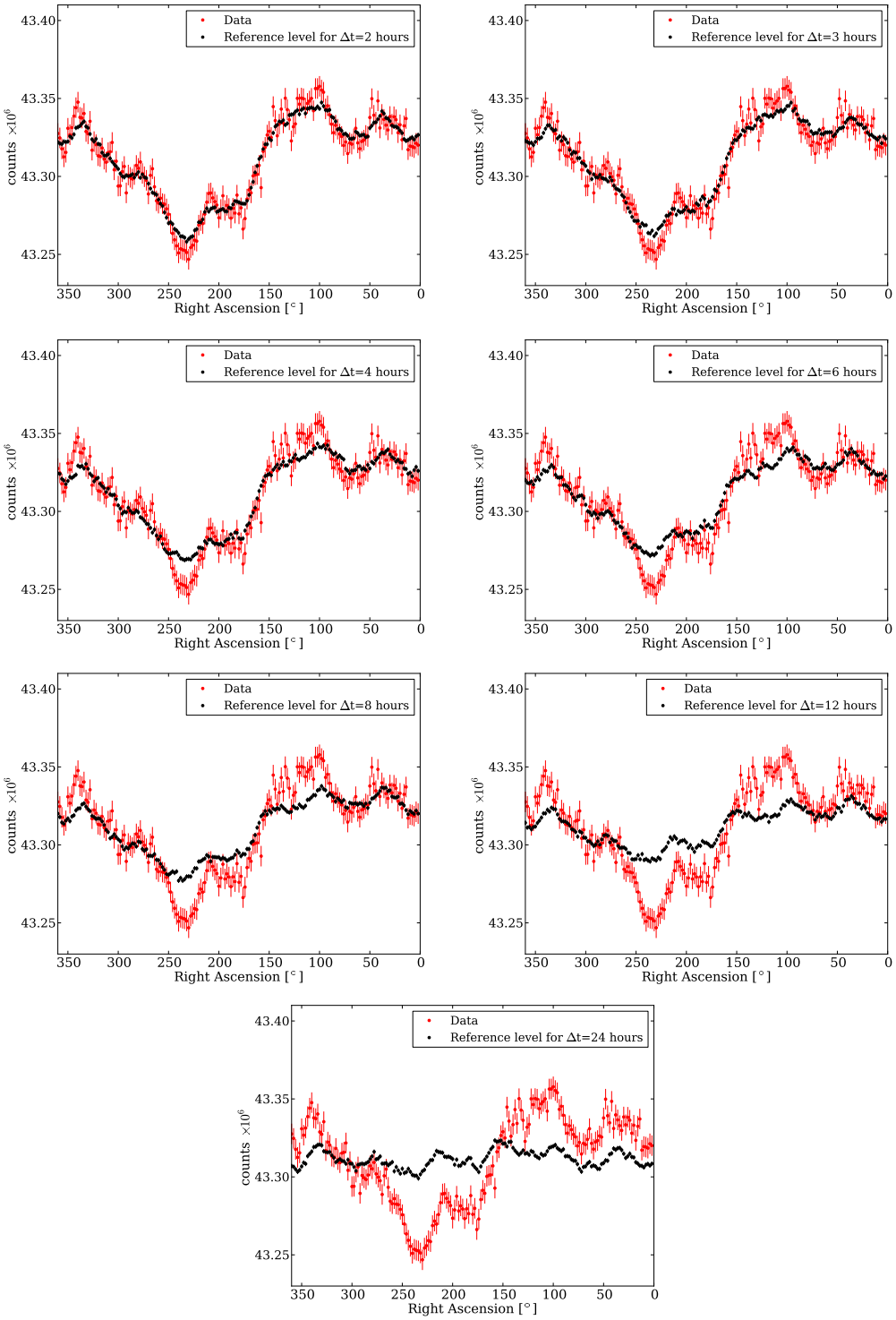

Figure 12. Number of events (red) and reference level (black), with statistical uncertainties, as a function of right ascension for the declination range $-45^\circ < \delta < -30^\circ$. The reference level is estimated in different time windows, from 2 hr (top left) to 24 hr (bottom). Each plot has been created using independent $15^\circ \delta \times 2^\circ$ bins in right ascension.

(A color version of this figure is available in the online journal.)

in the anti-sidereal or in the extended-sidereal frame. However, systematic distortions in the sidereal anisotropy due to seasonal variations of the solar dipole will produce a "signal" in anti-sidereal time. Similarly, distortions in the solar dipole due to seasonal variations of the sidereal anisotropy will produce a "signal" in extended-sidereal time. We follow the example of Amenomori et al. (2008) and Abdo et al. (2009) and use anti-sidereal time for an estimate of the error from seasonal variations on the amplitude of the sidereal anisotropy, and extended-sidereal time to estimate the systematic error on the solar dipole amplitude.

To measure the solar dipole anisotropy, we estimate the reference level using a time window $\Delta t = 24$ hr, which maximizes the sensitivity to large-scale features. The data and

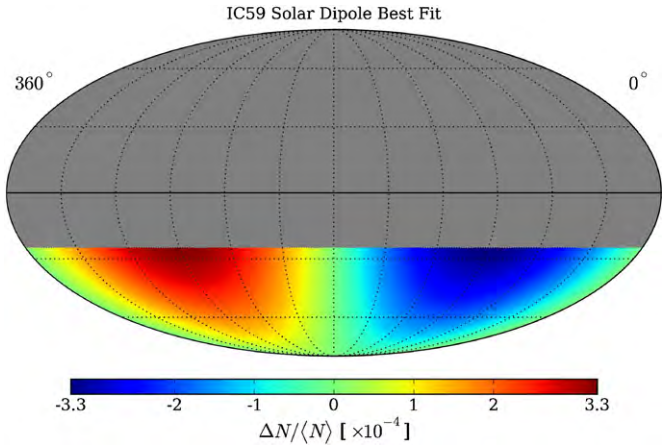

Figure 13. Best-fit results to the IC59 data expressed in solar coordinates. In this coordinate system, the velocity vector of the motion of the Earth about the Sun is oriented at a longitude of 270°.

(A color version of this figure is available in the online journal.)

reference maps are produced in a coordinate system where the latitude coordinate is declination and the longitude coordinate represents the angular distance from the Sun in right ascension, defined as the difference between the right ascension of each event and the right ascension of the Sun. In this coordinate system the Sun's longitude is fixed at 0° and we expect, over a full year, an excess in the direction of motion of Earth's velocity vector (at 270°) and a minimum in the opposite direction.

The data are fit using the dipole and quadrupole expansion given in Equation (8). The quadrupole coefficients are found to be equivalent to zero within the fit uncertainties, so the fit is repeated with only a dipole term and a constant offset. The dipole describes the data well; the fit $\chi^2/\mathrm{ndf} = 14207/14192$ corresponds to a χ^2-probability of 41.6%. The results of the fit are shown in Figure 13 and the best-fit coefficients are listed in Table 3. Only one free parameter, the p_y component of the dipole fit, differs significantly from zero. Hence, the dipole is aligned at a longitude of 270° within the equatorial plane of this coordinate system, following the expectation for a dipole in the cosmic ray skymap caused by relative motion about the Sun.

The amplitude of the dipole is $(3.66 \pm 0.14_{\mathrm{stat}} \pm 0.99_{\mathrm{sys}}) \times 10^{-4}$. The systematic uncertainty is evaluated by fitting a dipole to the data in a coordinate system using extended-sidereal time. We have conservatively estimated this systematic uncertainty by taking the amplitude of the dipole in extended-sidereal coordinates. Within the large systematic error, the amplitude of the solar dipole agrees with the prediction. A more detailed study of the solar dipole anisotropy in IceCube data will follow in a separate publication.

4.2. Anti-sidereal Time Analysis

As described in the previous section, we use the analysis of the data in the anti-sidereal time frame to study systematic effects caused by seasonal variations. For this test, we produce skymaps where anti-sidereal time is used instead of sidereal time in the coordinate transformation from local detector coordinates to "equatorial" coordinates. Skymaps produced in this way are subjected to the same analyses as the true equatorial maps. Neither the angular power spectrum nor the skymaps show any significant deviation from isotropy. In particular, no regions of significant excess or deficit are observed in the anti-sidereal skymaps for any smoothing scale. The systematic error bars shown in Figure 11 are estimated by using the variation in anti-sidereal time as a measure of this error.

Table 3
Coefficients of a Dipole and Constant Offset Fit to the IC59 Solar Coordinate Data

Coefficient	Value (Stat. + Syst.) ($\times 10^{-4}$)
m_0	$-0.03 \pm 0.06 \pm 0.02$
p_x	$0.02 \pm 0.14 \pm 0.97$
p_y	$-3.66 \pm 0.14 \pm 0.17$
p_z	$-0.03 \pm 0.07 \pm 0.01$

Notes. The systematic error on the fit parameters is estimated using the results of a fit using extended-sidereal time as described in the text.

4.3. Comparison with IC22 and IC40

An important crosscheck of the structure seen in the IC59 data set can be made by applying the IC59 analysis to data recorded in the two data periods prior to IC59. The IC22 data set contains 5 billion events recorded between 2007 July and 2008 April, and the IC40 data set contains 19 billion events recorded between 2008 April and 2009 May. While these data sets are smaller than the IC59 data set due to the smaller detector size, we nevertheless expect to observe the most prominent structures in these data, albeit with reduced significance.

The IC22 and IC40 data can be used to verify that the structures observed in the arrival direction distribution do not depend on the geometry of the detector or the data taking period. The shapes of both detector configurations are highly asymmetric, with a long axis and a short axis. The asymmetry introduces a trigger bias into the data, because muon tracks aligned with the long axis are much more likely to satisfy the simple majority trigger conditions than events arriving along the short axis. As a result, the local arrival direction distribution of the IC22 and IC40 data is highly nonuniform in azimuth.

We repeat the main analysis steps described in Section 3. Figure 14 shows the angular power spectrum for IC22, IC40, and IC59. Both small- and large-scale structures are present in all three data sets.

Figure 15 shows the result of the dipole and quadrupole fits (left) and the residual map after subtraction of dipole and quadrupole (right) for IC22 (top) and IC40 (bottom). The residual maps are smoothed with a 20° radius so they can be directly compared to Figure 7. While none of the features in IC22 and IC40 have a pre-trials significance above 5σ, they align with the regions of deficit and excess observed with IC59 data (cf. Figure 7). The main features on both small and large scales appear to be persistent in all data sets.

Figure 16 compares the results of the analysis described in Section 3.5 for the IC22 and IC40 data. The figure shows the relative intensity as a function of right ascension for the declination band between −45° and −30°, where the most significant deviations from isotropy are found. The systematic error band is estimated from the relative intensity distribution in anti-sidereal time as described in Section 4.2. The results for IC22 (left) and IC40 (right) show that similar deviations are present in the IC22, IC40, and IC59 data, again with increasing significance due to the increasing size of the data sets.

The stability of the results over several years of data taking and three different detector configurations indicates that the

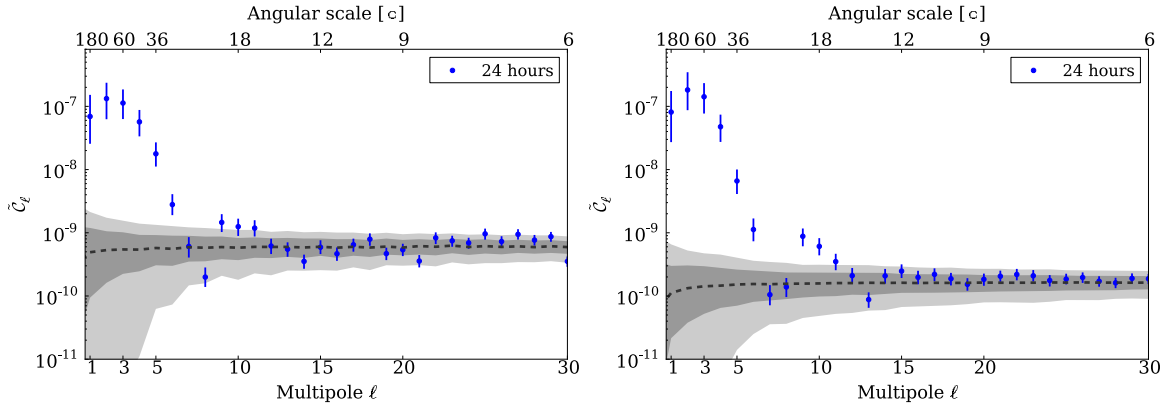

Figure 14. Angular power spectra for the relative intensity maps from IC22 (left) and IC40 data (right). Error bars are statistical. The gray bands indicate the distribution of the power spectra in a large sample of isotropic data sets, showing the 68% (dark) and 95% (light) spread in the $\tilde{C}_\ell$.
(A color version of this figure is available in the online journal.)

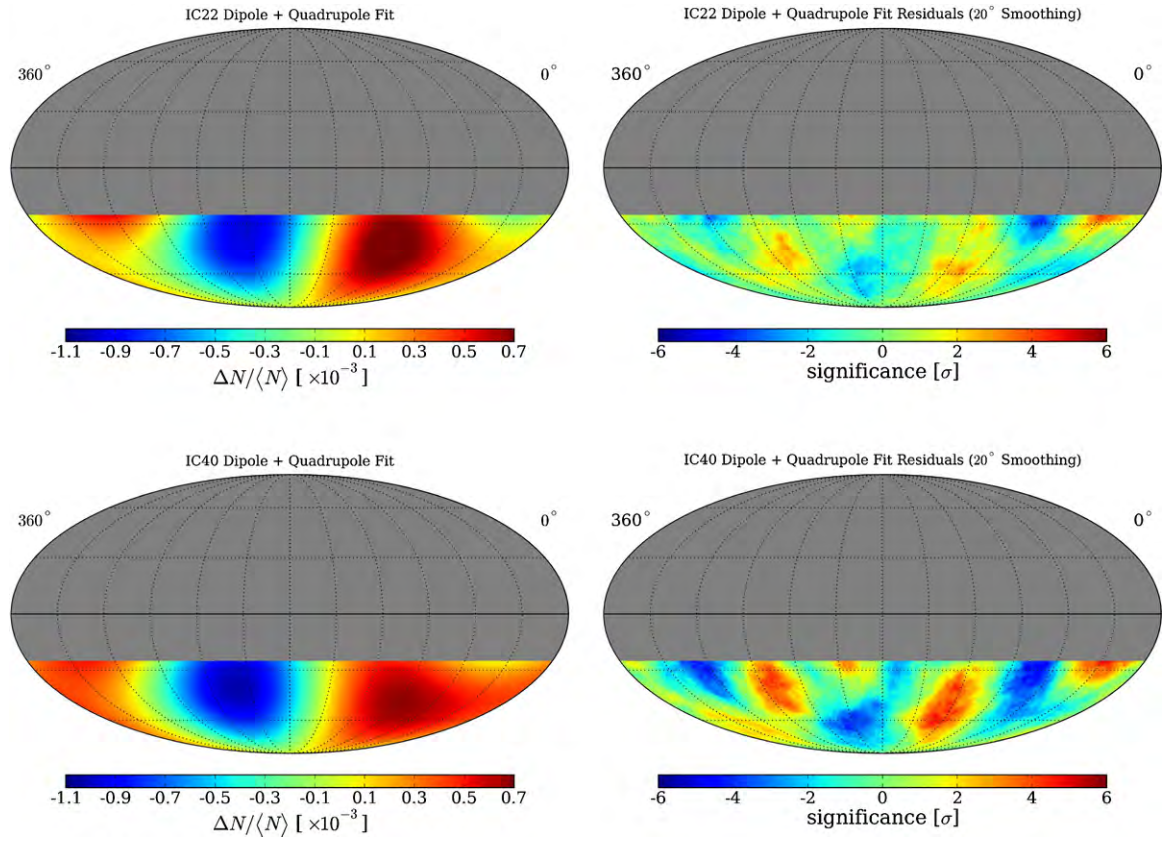

Figure 15. Top: combined dipole and quadrupole fit of Equation (8) to data from IC22 (left) and fit residuals after 20° smoothing (right). Bottom: dipole and quadrupole fit to data from IC40 (left) and fit residuals (right).
(A color version of this figure is available in the online journal.)

anisotropy is not produced by the geometry of the detector. Since the temporal distribution of detector livetime is also different for all three data sets, the stability of the results indicates that the anisotropy is not affected by nonuniformities in the detector livetime. As expected, the time scrambling method accounts for this effect.

5. CONCLUSIONS

Using 32 billion events recorded with the partially deployed IceCube detector between 2009 May and 2010 May, we have shown that the arrival direction distribution of cosmic rays with a median energy of 20 TeV exhibits significant anisotropy on all scales up to $\ell = 12$ in the angular power spectrum. The power spectrum is dominated by a dipole and quadrupole moment, but also indicates the presence of significant structure on angular scales down to about 15°. These structures become visible in the skymap when the dominant dipole and quadrupole moments are either subtracted or suppressed. The residual skymap shows both significant excesses and deficits, with the most important excess reaching a post-trial significance of 5.3σ in IC59. The relative intensity of the smaller-scale structures is about a factor of five weaker than the dipole and quadrupole structure. A study of data taken with the smaller IC22 and IC40 detectors in previous

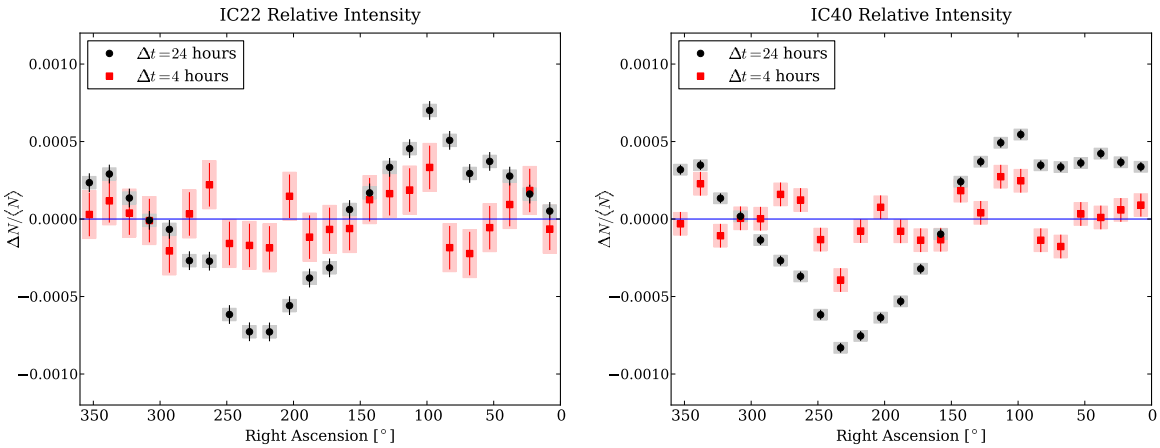

Figure 16. Relative intensity in the declination band between −45° and −30° for $\Delta t = 4$ hr for data from IC22 (left) and IC40 (right). Statistical and systematic uncertainties are shown, with systematics calculated from the relative intensity distribution in anti-sidereal coordinates.

(A color version of this figure is available in the online journal.)

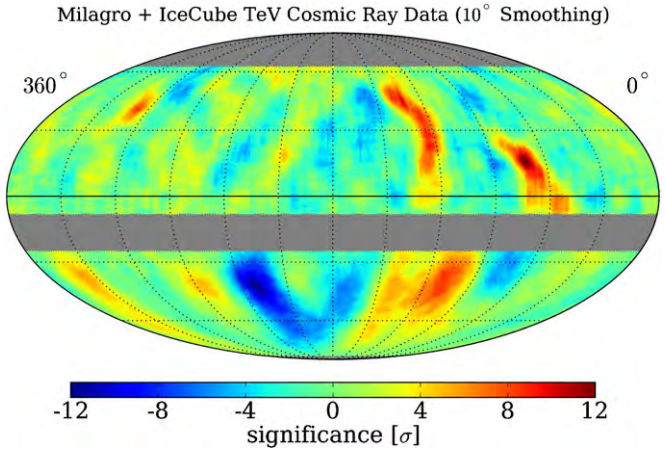

Figure 17. Combined map of significances in the cosmic ray arrival direction distribution observed by Milagro in the northern hemisphere (Abdo et al. 2008) and IceCube in the southern hemisphere (this analysis). Both maps have been smoothed with a 10° radius.

(A color version of this figure is available in the online journal.)

years confirms that these deviations from an isotropic flux are consistently present in all data sets.

Together with data from the γ-ray experiments in the northern hemisphere, we now have an almost complete cosmic ray map of the entire sky at TeV energies. Figure 17 shows the combined IceCube and Milagro skymaps of small-scale anisotropy. For this map, all available IceCube data (IC22, IC40, and IC59) have been used, with a total of 5.6×10^{10} events, and the analysis is performed using the method described in Section 3.5 with a smoothing radius of 10° to match the Milagro analysis. The combined skymap shows significant excess regions in both hemispheres. It is possible that the structure around right ascension 120° spans both hemispheres, as the drop in significances around declination $\delta = 0°$ could be an artifact of the smaller exposure of both detectors near $\delta = 0°$, which corresponds to a region close to the horizon for both detectors.

There is currently no explanation for these local enhancements in the cosmic ray flux. We note that the two most significant excess regions in the southern sky (Regions 1 and 2 in Table 2) are both located near the Galactic plane. In addition, the position of one of the excess regions (Region 1) coincides with the location of the Vela pulsar at ($\alpha = 128.^{\circ}8, \delta = -45.^{\circ}2$). At a distance of about 300 pc (Caraveo et al. 2001), Vela is one of the closest known supernova remnants and has long been considered a candidate source for Galactic cosmic ray acceleration. However, the Larmor radius of 10 TeV protons in a μG magnetic field is approximately 0.01 pc, many orders of magnitude smaller than the distance to Vela, and unless unconventional propagation mechanisms are assumed, charged particles from Vela will have lost all directional information upon their arrival at Earth.

Recently, several authors have investigated the extent to which the stochastic nature of nearby supernova remnants can lead to spatial and temporal variations in the cosmic ray flux (Ptuskin et al. 2006; Blasi & Amato 2011). The random nature of the sources makes quantitative predictions difficult and can lead to bumps and dips in the amplitude of the anisotropy as a function of energy that depend on the specific source distribution used in the simulation of the cosmic ray flux. Qualitatively, the models make specific predictions for the energy dependence of the amplitude of the cosmic ray anisotropy.

In the TeV–PeV range, the energy resolution of IceCube is poor for cosmic ray events (see Section 2.1). However, given the large rate of cosmic ray triggers, it is possible to isolate a sufficiently large subset of showers with a median energy of several hundred TeV which is not significantly contaminated by low-energy events. A paper focusing on this study is currently in preparation.

The study of cosmic ray arrival directions at TeV energies will continue to be a major ongoing research effort in IceCube. IceCube and the future High Altitude Water Cherenkov γ-ray observatory (Sinnis et al. 2004) under construction in Mexico can be used to monitor the southern and northern hemisphere, respectively, with high sensitivity. The combined data sets will soon allow for all-sky power spectra and the analysis of the entire sky at all angular scales.

Over the next few years, with the IceCube detector now operating in its complete 86-string configuration, our data set will increase at a rate of about 45×10^9 muon events per year. With this level of statistics we will also be able to study possible time dependencies of the anisotropy in the southern hemisphere and compare to similar studies performed with data from instruments in the northern hemisphere (Abdo et al. 2009; Amenomori et al. 2010).

We thank Eric Hivon for helpful comments and suggestions about the angular power spectrum analysis, and the Milagro Collaboration for providing us with their data to produce the combined skymap in Figure 17.

Some of the results in this paper have been derived using the HEALPix (Gorski et al. 2005) and the PolSpice (Szapudi et al. 2001; Chon et al. 2004) software libraries.

We acknowledge the support from the following agencies: U. S. National Science Foundation-Office of Polar Programs, U. S. National Science Foundation-Physics Division, University of Wisconsin Alumni Research Foundation, the Grid Laboratory Of Wisconsin (GLOW) grid infrastructure at the University of Wisconsin-Madison, the Open Science Grid (OSG) grid infrastructure; U. S. Department of Energy, and National Energy Research Scientific Computing Center, the Louisiana Optical Network Initiative (LONI) grid computing resources; National Science and Engineering Research Council of Canada; Swedish Research Council, Swedish Polar Research Secretariat, Swedish National Infrastructure for Computing (SNIC), and Knut and Alice Wallenberg Foundation, Sweden; German Ministry for Education and Research (BMBF), Deutsche Forschungsgemeinschaft (DFG), Research Department of Plasmas with Complex Interactions (Bochum), Germany; Fund for Scientific Research (FNRS-FWO), FWO Odysseus programme, Flanders Institute to encourage scientific and technological research in industry (IWT), Belgian Federal Science Policy Office (Belspo); University of Oxford, United Kingdom; Marsden Fund, New Zealand; Japan Society for Promotion of Science (JSPS); the Swiss National Science Foundation (SNSF), Switzerland; A. Groß acknowledges support by the EU Marie Curie OIF Program; J. P. Rodrigues acknowledges support by the Capes Foundation, Ministry of Education of Brazil.

REFERENCES

Abbasi, R., Abdou, Y., Abu-Zayyad, T., et al. 2010a, Nucl. Instrum. Methods Phys. Res. A, 618, 139
Abbasi, R., Abdou, Y., Abu-Zayyad, T., et al. 2010b, ApJ, 718, L194
Abbasi, R., Abdou, Y., Ackermann, M., et al. 2009a, ApJ, 701, L47
Abbasi, R., Ackermann, M., Adams, J., et al. 2009b, Nucl. Instrum. Methods Phys. Res. A, 601, 294
Abdo, A. A., Allen, B., Aune, T., et al. 2008, Phys. Rev. Lett., 101, 221101
Abdo, A. A., Allen, B. T., Aune, T., et al. 2009, ApJ, 698, 2121
Achterberg, A., Ackermann, M., Adams, J., et al. 2006, Astropart. Phys., 26, 155
Aglietta, M., Alekseenko, V. V., Alessandro, B., et al. 2009, ApJ, 692, L130
Ahn, E.-J., Engel, R., Gaisser, T. K., Lipari, P., & Stanev, T. 2009, Phys. Rev. D, 80, 094003
Ahrens, J., Bai, X., Bay, R., et al. 2004, Nucl. Instrum. Methods Phys. Res. A, 524, 169
Alexandreas, D. E., Berley, D., Biller, S., et al. 1993, Nucl. Instrum. Methods Phys. Res. A, 328, 570
Amenomori, M., Ayabe, S., Bi, X. J., et al. 2006, Science, 314, 439
Amenomori, M., Ayabe, S., Cui, S. W., et al. 2004, Phys. Rev. Lett., 93, 061101
Amenomori, M., Ayabe, S., Cui, S. W., et al. 2005, ApJ, 626, L29
Amenomori, M., Bi, X. J., Chen, D., et al. 2008, ApJ, 672, L53
Amenomori, M., Bi, X. J., Chen, D., et al. 2010, ApJ, 711, 119
Ansari, R., & Magneville, C. 2010, MNRAS, 405, 1421
Biermann, P. L., Becker, J. K., Dreyer, J., et al. 2010, ApJ, 725, 184
Blasi, P., & Amato, E. 2011, JCAP, submitted (arXiv:1105.4529v1)
Caraveo, P., De Luca, A., Mignani, R. P., & Bignami, G. F. 2001, ApJ, 561, 930
Chon, G., Challinor, A., Prunet, S., Hivon, E., & Szapudi, I. 2004, MNRAS, 350, 914
Compton, A. H., & Getting, I. A. 1935, Phys. Rev., 47, 817
Drury, L., & Aharonian, F. 2008, Astropart. Phys., 29, 420
Gleeson, L., & Axford, W. 1968, Astrophys. Space Sci., 2, 431
Gorski, K. M., Hivon, E., Banday, A. J., et al. 2005, ApJ, 622, 759
Guillian, G., Hosaka, J., Ishihara, K., et al. 2007, Phys. Rev. D, 75, 062003
Heck, D., Knapp, J., Capdevielle, J. N., Schatz, G., & Thouw, T. 1998, CORSIKA: A Monte Carlo Code to Simulate Extensive Air Showers, Forschungszentrum Karlsruhe Report FZKA 6019 (http://www.ik.fzk.de/corsika/physics_description/corsika_phys.html)
Hörandel, J. R. 2003, Astropart. Phys., 19, 193
Lazarian, A., & Desiati, P. 2010, ApJ, 722, 188
Li, T.-P., & Ma, Y.-Q. 1983, ApJ, 272, 317
Malkov, M. A., Diamond, P. H., O'C. Drury, L., & Sagdeev, R. Z. 2010, ApJ, 721, 750
Ptuskin, V., Jones, F., Seo, E., & Sina, R. 2006, Adv. Space Res., 37, 1909
Sinnis, G., Smith, A., & McEnery, J. E. 2004, in Tenth Marcel Grossman Meeting on General Relativity-Part Co, ed. M. Novello & S. Perez Bergliaffa (Singapore: World Scientific), 1068
Smoot, G. F., & Lubin, P. M. 1979, ApJ, 234, L83
Szapudi, I., Prunet, S., Pogosyan, D., Szalay, A. S., & Bond, J. R. 2001, ApJ, 548, L115
Tilav, S., Desiati, P., Kuwabara, T., et al. 2009, Proc. 31st ICRC (Łódź), arXiv:1001.0776
Vernetto, S., Guglielmotto, Z., Zhang, J. L., et al. 2009, Proc. 31st ICRC (Łódź), arXiv:0907.4615

The Astrophysical Journal, 732:18 (16pp), 2011 May 1 doi:10.1088/0004-637X/732/1/18

TIME-INTEGRATED SEARCHES FOR POINT-LIKE SOURCES OF NEUTRINOS WITH THE 40-STRING IceCube DETECTOR

R. Abbasi[1], Y. Abdou[2], T. Abu-Zayyad[3], J. Adams[4], J. A. Aguilar[1], M. Ahlers[5], K. Andeen[1], J. Auffenberg[6], X. Bai[7], M. Baker[1], S. W. Barwick[8], R. Bay[9], J. L. Bazo Alba[10], K. Beattie[11], J. J. Beatty[12,13], S. Bechet[14], J. K. Becker[15], K.-H. Becker[6], M. L. Benabderrahmane[10], S. BenZvi[1], J. Berdermann[10], P. Berghaus[1], D. Berley[16], E. Bernardini[10], D. Bertrand[14], D. Z. Besson[17], M. Bissok[18], E. Blaufuss[16], J. Blumenthal[18], D. J. Boersma[18], C. Bohm[19], D. Bose[20], S. Böser[21], O. Botner[22], J. Braun[1], A. M. Brown[4], S. Buitink[11], M. Carson[2], D. Chirkin[1], B. Christy[16], J. Clem[7], F. Clevermann[23], S. Cohen[24], C. Colnard[25], D. F. Cowen[26,27], M. V. D'Agostino[9], M. Danninger[19], J. Daughhetee[28], J. C. Davis[12], C. De Clercq[20], L. Demirörs[24], O. Depaepe[20], F. Descamps[2], P. Desiati[1], G. de Vries-Uiterweerd[2], T. DeYoung[26], J. C. Díaz-Vélez[1], M. Dierckxsens[14], J. Dreyer[15], J. P. Dumm[1], R. Ehrlich[16], J. Eisch[1], R. W. Ellsworth[16], O. Engdegård[22], S. Euler[18], P. A. Evenson[7], O. Fadiran[29], A. R. Fazely[30], A. Fedynitch[15], T. Feusels[2], K. Filimonov[9], C. Finley[19], M. M. Foerster[26], B. D. Fox[26], A. Franckowiak[21], R. Franke[10], T. K. Gaisser[7], J. Gallagher[31], M. Geisler[18], L. Gerhardt[9,11], L. Gladstone[1], T. Glüsenkamp[18], A. Goldschmidt[11], J. A. Goodman[16], D. Grant[32], T. Griesel[33], A. Groß[4,25], S. Grullon[1], M. Gurtner[6], C. Ha[26], A. Hallgren[22], F. Halzen[1], K. Han[4], K. Hanson[1,14], K. Helbing[6], P. Herquet[34], S. Hickford[4], G. C. Hill[1], K. D. Hoffman[16], A. Homeier[21], K. Hoshina[1], D. Hubert[20], W. Huelsnitz[16], J.-P. Hülß[18], P. O. Hulth[19], K. Hultqvist[19], S. Hussain[7], A. Ishihara[35], J. Jacobsen[1], G. S. Japaridze[29], H. Johansson[19], J. M. Joseph[11], K.-H. Kampert[6], A. Kappes[36], T. Karg[6], A. Karle[1], J. L. Kelley[1], N. Kemming[36], P. Kenny[17], J. Kiryluk[9,11], F. Kislat[10], S. R. Klein[9,11], J.-H. Köhne[23], G. Kohnen[34], H. Kolanoski[36], L. Köpke[33], D. J. Koskinen[26], M. Kowalski[21], T. Kowarik[33], M. Krasberg[1], T. Krings[18], G. Kroll[33], K. Kuehn[12], T. Kuwabara[7], M. Labare[20], S. Lafebre[26], K. Laihem[18], H. Landsman[1], M. J. Larson[26], R. Lauer[10], R. Lehmann[36], J. Lünemann[33], J. Madsen[3], P. Majumdar[10], A. Marotta[14], R. Maruyama[1], K. Mase[35], H. S. Matis[11], M. Matusik[6], K. Meagher[16], M. Merck[1], P. Mészáros[26,27], T. Meures[18], E. Middell[10], N. Milke[23], J. Miller[22], T. Montaruli[1], R. Morse[1], S. M. Movit[27], R. Nahnhauer[10], J. W. Nam[8], U. Naumann[6], P. Nießen[7], D. R. Nygren[11], S. Odrowski[25], A. Olivas[16], M. Olivo[15,22], A. O'Murchadha[1], M. Ono[35], S. Panknin[21], L. Paul[18], C. Pérez de los Heros[22], J. Petrovic[14], A. Piegsa[33], D. Pieloth[23], R. Porrata[9], J. Posselt[6], P. B. Price[9], M. Prikockis[26], G. T. Przybylski[11], K. Rawlins[37], P. Redl[16], E. Resconi[25], W. Rhode[23], M. Ribordy[24], A. Rizzo[20], J. P. Rodrigues[1], P. Roth[16], F. Rothmaier[33], C. Rott[12], T. Ruhe[23], D. Rutledge[26], B. Ruzybayev[7], D. Ryckbosch[2], H.-G. Sander[33], M. Santander[1], S. Sarkar[5], K. Schatto[33], S. Schlenstedt[10], T. Schmidt[16], A. Schukraft[18], A. Schultes[6], O. Schulz[25], M. Schunck[18], D. Seckel[7], B. Semburg[6], S. H. Seo[19], Y. Sestayo[25], S. Seunarine[38], A. Silvestri[8], K. Singh[20], A. Slipak[26], G. M. Spiczak[3], C. Spiering[10], M. Stamatikos[12,39], T. Stanev[7], G. Stephens[26], T. Stezelberger[11], R. G. Stokstad[11], S. Stoyanov[7], E. A. Strahler[20], T. Straszheim[16], G. W. Sullivan[16], Q. Swillens[14], H. Taavola[22], I. Taboada[28], A. Tamburro[3], O. Tarasova[10], A. Tepe[28], S. Ter-Antonyan[30], S. Tilav[7], P. A. Toale[26], S. Toscano[1], D. Tosi[10], D. Turčan[16], N. van Eijndhoven[20], J. Vandenbroucke[9], A. Van Overloop[2], J. van Santen[1], M. Vehring[18], M. Voge[25], B. Voigt[10], C. Walck[19], T. Waldenmaier[36], M. Wallraff[18], M. Walter[10], Ch. Weaver[1], C. Wendt[1], S. Westerhoff[1], N. Whitehorn[1], K. Wiebe[33], C. H. Wiebusch[18], D. R. Williams[40], R. Wischnewski[10], H. Wissing[16], M. Wolf[25], K. Woschnagg[9], C. Xu[7], X. W. Xu[30], G. Yodh[8], S. Yoshida[35], and P. Zarzhitsky[40]

(IceCube Collaboration)

[1] Department of Physics, University of Wisconsin, Madison, WI 53706, USA
[2] Department of Subatomic and Radiation Physics, University of Gent, B-9000 Gent, Belgium
[3] Department of Physics, University of Wisconsin, River Falls, WI 54022, USA
[4] Department of Physics and Astronomy, University of Canterbury, Private Bag 4800, Christchurch, New Zealand
[5] Department of Physics, University of Oxford, 1 Keble Road, Oxford OX1 3NP, UK
[6] Department of Physics, University of Wuppertal, D-42119 Wuppertal, Germany
[7] Bartol Research Institute and Department of Physics and Astronomy, University of Delaware, Newark, DE 19716, USA
[8] Department of Physics and Astronomy, University of California, Irvine, CA 92697, USA
[9] Department of Physics, University of California, Berkeley, CA 94720, USA
[10] DESY, D-15735 Zeuthen, Germany
[11] Lawrence Berkeley National Laboratory, Berkeley, CA 94720, USA
[12] Department of Physics and Center for Cosmology and Astro-Particle Physics, Ohio State University, Columbus, OH 43210, USA
[13] Department of Astronomy, Ohio State University, Columbus, OH 43210, USA
[14] Université Libre de Bruxelles, Science Faculty CP230, B-1050 Brussels, Belgium
[15] Fakultät für Physik & Astronomie, Ruhr-Universität Bochum, D-44780 Bochum, Germany
[16] Department of Physics, University of Maryland, College Park, MD 20742, USA
[17] Department of Physics and Astronomy, University of Kansas, Lawrence, KS 66045, USA
[18] III. Physikalisches Institut, RWTH Aachen University, D-52056 Aachen, Germany
[19] Oskar Klein Centre and Deptartment of Physics, Stockholm University, SE-10691 Stockholm, Sweden
[20] Vrije Universiteit Brussel, Dienst ELEM, B-1050 Brussels, Belgium
[21] Physikalisches Institut, Universität Bonn, Nussallee 12, D-53115 Bonn, Germany
[22] Department of Physics and Astronomy, Uppsala University, Box 516, S-75120 Uppsala, Sweden
[23] Department of Physics, TU Dortmund University, D-44221 Dortmund, Germany
[24] Laboratory for High Energy Physics, École Polytechnique Fédérale, CH-1015 Lausanne, Switzerland

[25] Max-Planck-Institut für Kernphysik, D-69177 Heidelberg, Germany
[26] Department of Physics, Pennsylvania State University, University Park, PA 16802, USA
[27] Department of Astronomy and Astrophysics, Pennsylvania State University, University Park, PA 16802, USA
[28] School of Physics and Center for Relativistic Astrophysics, Georgia Institute of Technology, Atlanta, GA 30332, USA
[29] CTSPS, Clark-Atlanta University, Atlanta, GA 30314, USA
[30] Department of Physics, Southern University, Baton Rouge, LA 70813, USA
[31] Department of Astronomy, University of Wisconsin, Madison, WI 53706, USA
[32] Department of Physics, University of Alberta, Edmonton, Alberta, T6G 2G7, Canada
[33] Institute of Physics, University of Mainz, Staudinger Weg 7, D-55099 Mainz, Germany
[34] Université de Mons, 7000 Mons, Belgium
[35] Department of Physics, Chiba University, Chiba 263-8522, Japan
[36] Institut für Physik, Humboldt-Universität zu Berlin, D-12489 Berlin, Germany
[37] Department of Physics and Astronomy, University of Alaska Anchorage, 3211 Providence Dr., Anchorage, AK 99508, USA
[38] Department of Physics, University of the West Indies, Cave Hill Campus, Bridgetown BB11000, Barbados
[39] NASA Goddard Space Flight Center, Greenbelt, MD 20771, USA
[40] Department of Physics and Astronomy, University of Alabama, Tuscaloosa, AL 35487, USA
Received 2010 November 30; accepted 2011 February 27; published 2011 April 8

ABSTRACT

We present the results of time-integrated searches for astrophysical neutrino sources in both the northern and southern skies. Data were collected using the partially completed IceCube detector in the 40-string configuration recorded between 2008 April 5 and 2009 May 20, totaling 375.5 days livetime. An unbinned maximum likelihood ratio method is used to search for astrophysical signals. The data sample contains 36,900 events: 14,121 from the northern sky, mostly muons induced by atmospheric neutrinos, and 22,779 from the southern sky, mostly high-energy atmospheric muons. The analysis includes searches for individual point sources and stacked searches for sources in a common class, sometimes including a spatial extent. While this analysis is sensitive to TeV–PeV energy neutrinos in the northern sky, it is primarily sensitive to neutrinos with energy greater than about 1 PeV in the southern sky. No evidence for a signal is found in any of the searches. Limits are set for neutrino fluxes from astrophysical sources over the entire sky and compared to predictions. The sensitivity is at least a factor of two better than previous searches (depending on declination), with 90% confidence level muon neutrino flux upper limits being between $E^2 d\Phi/dE \sim 2\text{–}200 \times 10^{-12}$ TeV cm^{-2} s^{-1} in the northern sky and between $3\text{–}700 \times 10^{-12}$ TeV cm^{-2} s^{-1} in the southern sky. The stacked source searches provide the best limits to specific source classes. The full IceCube detector is expected to improve the sensitivity to $d\Phi/dE \propto E^{-2}$ sources by another factor of two in the first year of operation.

Key words: astroparticle physics – cosmic rays – neutrinos

Online-only material: color figures

1. INTRODUCTION

Neutrino astronomy is tightly connected to cosmic ray (CR) and gamma-ray astronomy, since neutrinos likely share their origins with these other messengers. With a possible exception at the highest observed energies, CRs propagate diffusively losing directional information due to magnetic fields, and both CRs and gamma rays at high energies are absorbed due to interactions on photon backgrounds. Neutrinos, on the other hand, are practically unabsorbed en route and travel directly from cosmological sources to the Earth. Neutrinos are therefore fundamental to understanding CR acceleration processes up to the highest energies, and the detection of astrophysical neutrino sources could unveil the origins of hadronic CR acceleration. Whether or not gamma-ray energy spectra above about 10 TeV can be accounted for by only inverse Compton processes is still an open question. Some observations suggest contributions from hadronic acceleration processes (Morlino et al. 2009; Boettcher et al. 2009). Acceleration of CRs is thought to take place in shocks in supernova remnants (SNRs) or in jets produced in the vicinity of accretion disks by processes which are not fully understood. Black holes in active galactic nuclei (AGNs), galactic micro-quasars and magnetars, or disruptive phenomena such as collapsing stars or binary mergers leading to gamma-ray bursts (GRBs), all characterized by relativistic outflows, could also be powerful accelerators. The canonical model for acceleration of CRs is the Fermi model (Fermi 1949), called first-order Fermi acceleration when applied to non-relativistic shock fronts. This model naturally gives a CR energy spectrum similar to $d\Phi/dE \propto E^{-2}$ at the source. The neutrinos, originating in CR interactions near the source, are expected to follow a similar energy spectrum. More recently, models such as those in Caprioli et al. (2010) can yield significantly harder source spectra. In the framework of these models, it is possible to account for galactic CR acceleration to energies up to the knee, at about $Z \times 4 \times 10^{15}$ eV, where Z is the atomic number of the CR. Extragalactic sources, on the other hand, are believed to be responsible for ultra-high-energy CRs observed up to about 10^{20} eV.

The concept of a neutrino telescope as a three-dimensional matrix of photomultiplier tubes (PMTs) was originally proposed by Markov & Zheleznykh (1961). These sensors detect the Cerenkov light induced by relativistic charged particles passing through a transparent and dark medium such as deep water or the Antarctic ice sheet. The depth of these detectors helps to filter out the large number of atmospheric muons, making it possible to detect the rarer neutrino events. The direction and energy of particles are reconstructed using the arrival time and number of the Cerenkov photons. High-energy muon–neutrino interactions produce muons that can travel many kilometers. On average, the muons scatter $<0.^\circ 1$ with respect to the original neutrino direction for $E_\nu > 10$ TeV. The first cubic-kilometer

neutrino telescope, IceCube, is being completed at the South Pole. IceCube has a large target mass. This gives it excellent sensitivity to astrophysical neutrinos, enabling it to test many theoretical predictions.

Reviews on neutrino sources and telescopes can be found in Anchordoqui & Montaruli (2010), Chiarusi & Spurio (2010), Becker (2008), Lipari (2006), Bednarek et al. (2005), Halzen & Hooper (2002), Learned & Mannheim (2000), and Gaisser et al. (1995). Recent results on searches for neutrino sources have been published by IceCube in the 22-string configuration (Abbasi et al. 2009a, 2009b), AMANDA-II (Abbasi et al. 2009c), Super-Kamiokande (Thrane et al. 2009), and MACRO (Ambrosio et al. 2001).

This paper is structured as follows: Section 2 describes the detector. The data sample and cut parameters are discussed in Section 3, along with the simulation. In Section 4, the detector performance is characterized for searches. Section 5 describes the unbinned maximum likelihood search method, and in Section 6 the point-source and stacking searches are discussed. After discussing the systematic errors in Section 7, the results are presented in Section 8. Section 9 discusses the impact of our results on various possible neutrino emission models, and Section 10 offers some conclusions.

2. DETECTOR AND DATA SAMPLE

The IceCube Neutrino Observatory is composed of a deep array of 86 strings holding 5160 digital optical modules (DOMs) deployed between 1.45 and 2.45 km below the surface of the South Pole ice. The strings are typically separated by about 125 m with DOMs separated vertically by about 17 m along each string. IceCube construction started with the first string installed in the 2005–2006 austral summer (Achterberg et al. 2006a) and was completed in 2010 December. Six of the strings in the final detector use high quantum efficiency DOMs and a spacing of about 70 m horizontally and 7 m vertically. Two more strings have standard IceCube DOMs and 7 m vertical spacing but an even smaller horizontal spacing of 42 m. These eight strings along with seven neighboring standard strings make up DeepCore, designed to enhance the physics performance of IceCube below 1 TeV. The observatory also includes a surface array, IceTop, for extensive air shower measurements on the composition and spectrum of CRs.

Each DOM consists of a 25 cm diameter Hamamatsu PMT (Abbasi et al. 2010a), electronics for waveform digitization (Abbasi et al. 2009d), and a spherical, pressure-resistant glass housing. A single Cerenkov photon arriving at a DOM can produce a photoelectron, which is called a hit if the analog output of the PMT exceeds a threshold equivalent to 0.25 of the average single photoelectron (SPE) charge. The waveform of the PMT total charge is digitized and sent to the surface if hits are in coincidence with at least one other hit in the nearest or next-to-nearest neighboring DOMs within ±1000 ns. Hits that satisfy this condition are called local coincidence hits. The waveforms can contain multiple hits. The total number of photoelectrons and their arrival times are extracted with an iterative Bayesian-based unfolding algorithm. This algorithm uses the template shape representing an average hit.

Forty strings of IceCube were in operation from 2008 April 5 to 2009 May 20. The layout of these strings in relation to the final 86-string IceCube configuration is shown in Figure 1. Over the entire period the detector ran with an uptime of 92%, yielding 375.5 days of total exposure. Dead time is mainly due to test runs during and after the construction season dedicated to calibrating the additional strings and upgrading data acquisition systems.

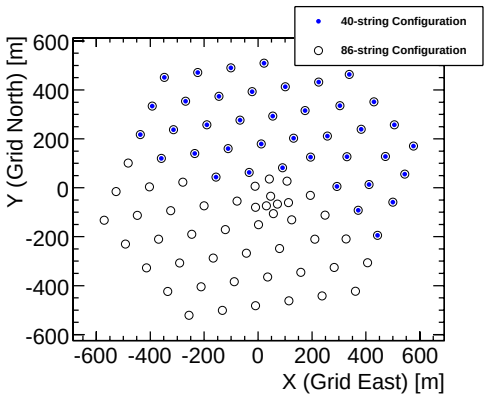

Figure 1. Overhead view of the 40-string configuration, along with additional strings that will make up the complete IceCube detector.
(A color version of this figure is available in the online journal.)

IceCube uses a simple multiplicity trigger, requiring local coincidence hits in eight DOMs within 5 μs. Once the trigger condition is met, local coincidence hits within a readout window ±10 μs are recorded, and overlapping readout windows are merged together. IceCube triggers primarily on down-going muons at a rate of about 950 Hz in this (40-string) configuration. Variations in the trigger rate by about ±10% are due to seasonal changes affecting development of CR showers and muon production in the atmosphere, with higher rates during the austral summer (Tilav et al. 2010).

3. DATA AND SIMULATION

3.1. Data Sample

Traditional astrophysical neutrino point-source searches have used the Earth to block all upward traveling (up-going) particles except muons induced by neutrinos, as in Abbasi et al. (2009b). There remains a background of up-going muons from neutrinos, which are created in CR air showers and can penetrate the entire Earth. These atmospheric neutrinos have a softer energy spectrum than many expectations for astrophysical neutrinos. The measurement of the atmospheric neutrino spectrum for the 40-string detector is discussed in Abbasi et al. (2010b). A large number of muons produced in CR showers in the atmosphere and moving downward through the detector (down-going) are initially misreconstructed as up-going. These mask the neutrino events until quality selections are made, leaving only a small residual of misreconstructed events.

The down-going region is dominated by atmospheric muons that also have a softer spectrum compared to muons induced by astrophysical neutrinos. At present, this large background reduces the IceCube sensitivity to neutrino sources in the southern sky in the sub-PeV energy region. While veto techniques are in development which will enable larger detector configurations to isolate neutrino-induced events starting within the detector, point-source searches can meanwhile be extended to the down-going region if the softer-spectrum atmospheric muon background is reduced by an energy selection. This was done for the first time using the previous 22-string configuration of IceCube (Abbasi et al. 2009a), extending IceCube's field of view to −50° declination. In this paper, we extend the field of view to −85° declination (the exclusion between −85° and −90° is due to the use of scrambled data for background estimation in the analysis,

Table 1
Number of Events at Each Processing Level for the 375.5 days of Livetime

Triggered events	3.3×10^{10}
L1 filtered events	8.0×10^{8}
Events in final sample	36,900

described in Section 5). Downgoing muons can also be created in showers caused by gamma rays, which point back to their source like neutrinos. The possibility for IceCube to detect PeV gamma-ray sources in the southern sky is discussed in Halzen et al. (2009), which concludes that a realistic source could be detected using muons in the ice only after 10 years of observing. Gamma-ray sources will not be considered further here.

Two processing levels are used to reduce the approximately 3.3×10^{10} triggered events down to a suitable sample for analysis (see Table 1). Random noise at the level of about 500 Hz per DOM is mainly due to radioactive decays in the materials in the DOMs. The contribution to triggered events by this random noise is highly suppressed by the local coincident hit requirement. To further reduce the contribution from noise, only hits within a 6 μs time window are used for the reconstructions. This time window is defined as the window that contains the most hits during the event. About 5% of down-going muons which trigger the detector are initially misreconstructed as up-going by the first stages of event processing. A persistent background that grows with the size of the detector is CR muons (or bundles of muons) from different showers which arrive in coincidence. At trigger level, they make up about 13% of the events. These coincident muon bundles can mimic the hit pattern of good up-going events, confusing a single-muon fit.

A likelihood-based muon track reconstruction is first performed at the South Pole (L1 filter). The likelihood function (Ahrens et al. 2004) parameterizes the probability of observing the geometry and timing of the hits in terms of a muon track's position, zenith angle, and azimuth angle. This likelihood is maximized, yielding the best-fit direction and position for the muon track. Initial fits are performed using an SPE likelihood that uses the time of the leading edge of the first photon arriving in each DOM. These reconstructions yield robust results used for the first level of background rejection. All events that are reconstructed as up-going are kept, while events in the down-going region must pass an energy cut that tightens with decreasing zenith angle. Events pass this L1 filter at an average rate of about 22 Hz and are buffered before transmission via a communications satellite using the South Pole Archival and Data Exchange (SPADE) system.

The processing done in the North includes a broader base of reconstructions compared to what is done at the South Pole. Rather than just the simple SPE fit, the multiple photoelectron (MPE) fit uses the number of observed photons to describe the expected arrival time of the first photon. This first photon is scattered less than an average photon when many arrive at the same DOM. The MPE likelihood description uses more available information than SPE and improves the tracking resolution as energy increases, and this reconstruction is used for the final analysis. The offline processing also provides parameters useful for background rejection, reconstructs the muon energy, and estimates the angular resolution on an event-by-event basis. Reducing the filtered events to the final sample of this analysis requires cutting on the following parameters:

1. *Reduced log-likelihood.* The log-likelihood from the muon track fit divided by the number of degrees of freedom, given by the number of DOMs with hits minus five, the number of free parameters used to describe the muon. This parameter performed poorly on low-energy signal events. It was found that low-energy efficiency could be increased by instead dividing the likelihood by number of DOMs with photon hits minus 2.5. Both the standard and modified parameters were used, requiring events to pass one selection or the other. This kept the efficiency higher for a broader energy range.
2. *Angular uncertainty, σ.* An estimate of the uncertainty in the muon track direction. The directional likelihood space around the best track solution is sampled and fit to a paraboloid. The contour of the paraboloid traces an error ellipse indicating how well the muon direction is localized (Neunhoffer 2006). The rms of the major and minor axes of the error ellipse is used to define a circular error. This parameter is effective both for removing misreconstructed events and as an event-by-event angular uncertainty estimator.
3. *Muon energy proxy.* The average photon density along the muon track, used as a proxy for the muon energy. It is calculated accounting for the distance to DOMs, their angular acceptance, and average scattering and absorption properties of photons in the ice. The energy loss of a muon moving through the detector scales with the muon energy above about 1 TeV when stochastic energy losses due to bremsstrahlung, pair production, and photonuclear interactions dominate over ionization losses. The energy resolution obtained is of the order of 0.3 in the $\log_{10}$ of the muon energy (at closest approach to the average hit location) for energies between about 10 TeV and 100 PeV. Since the interaction vertex is often an unknown distance from the detector, the muon in the detection volume has already lost an unknown amount of energy. Figure 2 shows the distribution of this energy parameter versus the true neutrino energy for a simulated spectrum $d\Phi/dE \propto E^{-2}$. Despite the uncertainty on the neutrino energy, for a statistical sample of events this energy estimator is a powerful analysis tool because of the wide range over which energies are measured.
4. *Zenith-weighted likelihood ratio.* The likelihood ratio between an unbiased muon fit and a fit with an event weight according to the known down-going muon zenith distribution as a Bayesian prior. Applied to up-going tracks, a high likelihood ratio establishes strong evidence that the event is

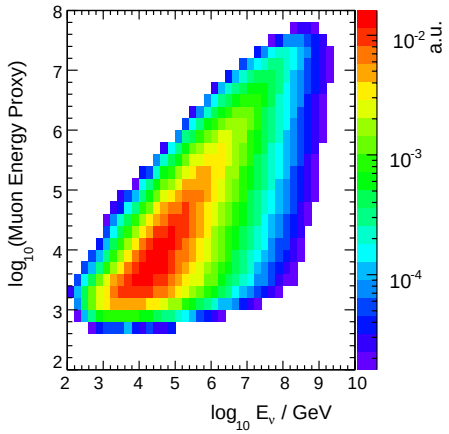

Figure 2. Distribution of the muon energy proxy (energy loss observed in the detector) vs. the true neutrino energy for a flux $d\Phi/dE \propto E^{-2}$.

actually up-going and not a misreconstructed down-going event.

5. *NDir.* The number of DOMs with direct photons, defined as arriving within −15 ns to +75 ns of the expectation from an unscattered photon emitted from the reconstructed muon track at the Cerenkov angle. Scattering of photons in the ice causes a loss of directional information and will delay them with respect to the unscattered expectation.
6. *LDir.* The maximum length between direct photons, projected along the best muon track solution.
7. *Zenith directions of split events.* The zenith angles resulting from splitting of an event into two parts and reconstructing each part separately. This is done in two ways: temporally, by using the mean photon arrival time as the split criterion, and geometrically, by using the plane both perpendicular to the track and containing the average hit location as the split criterion. This technique is effective against coincident muon bundles misreconstructed as single up-going tracks if both sub-events are required to be up-going.

In the up-going region, all parameters are used. The zenith-weighted likelihood ratio and event splitting are specifically designed to remove down-going atmospheric muon backgrounds that have been misreconstructed as up-going while the other parameters focus on overall track quality.

In the down-going region, without a veto or Earth filter, muons from CR showers overwhelm neutrino-induced muons, except possibly at high energies if the neutrino source spectra are harder than the CR spectrum. The aim of the analysis in this region is therefore to select high-energy, well-reconstructed events. We use the first three parameters in the list above as cut variables, requiring a higher track quality than in the up-going range. Energy cuts were introduced in the down-going region to reduce the number of events to a suitable size, cutting to achieve a constant number of events per solid angle (which also simplifies the background estimation in the analysis). This technique keeps the high-energy events which are most important for discovery. Cuts were optimized for the best sensitivity using a simulated signal of muon neutrinos with spectrum $d\Phi/dE \propto E^{-2}$. We checked that the same cuts resulted in a nearly optimal sensitivity for a softer spectrum $d\Phi/dE \propto E^{-3}$ in the up-going region where low-energy sensitivity is possible and for a harder spectrum $d\Phi/dE \propto E^{-1.5}$ in the down-going region.

Of the 36,900 events passing all selection criteria, 14,121 are up-going events from the northern sky, mostly muons induced by atmospheric neutrinos. Simulations of CR air showers with CORSIKA (Heck et al. 1998) show a 2.4% ± 0.8% contamination due to misreconstructed down-going atmospheric muons. The other 22,779 are down-going events from the southern sky, mostly high-energy atmospheric muons. An equatorial sky map of these events is given in Figure 3.

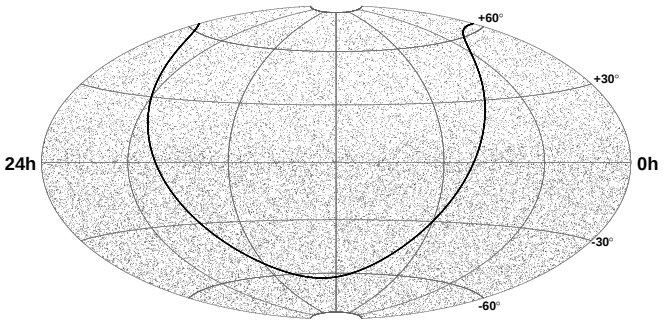

Figure 3. Equatorial skymap (J2000) of the 36,900 events in the final sample. The galactic plane is shown as the solid black curve. The northern sky (positive declinations) is dominated by up-going atmospheric neutrino-induced muons, and the southern sky (negative declinations) is dominated by muons produced in cosmic ray showers in the atmosphere above the South Pole.

3.2. Data and Simulation Comparison

Simulation of neutrinos is used for determining event selection and calculating upper limits. The simulation of neutrinos is based on ANIS (Gazizov & Kowalski 2005). Deep inelastic neutrino–nucleon cross sections use CTEQ5 parton distribution functions (Lai et al. 2000). Neutrino simulation can be weighted for different fluxes, accounting for the probability of each event to occur. In this way, the same simulation sample can be used to represent atmospheric neutrino models such as Bartol (Barr et al. 2004) and Honda (Honda et al. 2007) neutrino fluxes from pion and kaon decays (conventional flux). Neutrinos from charmed meson decays (prompt flux) have been simulated according to a variety of models (Martin et al. 2003; Enberg et al. 2008; Bugaev et al. 1989). Seasonal variations in atmospheric neutrino rates are expected to be a maximum of ±4% for neutrinos originating near the polar regions. Near the equator, atmospheric variations are much smaller and the variation in the number of events is expected to be less than ±0.5% (Ackermann & Bernardini 2005).

Atmospheric muon background is simulated mostly to guide and verify the event selection. Muons from CR air showers were simulated with CORSIKA (Heck et al. 1998) with the SIBYLL hadronic interaction model (Ahn et al. 2009). An October polar atmosphere, an average case over the year, is used for the CORSIKA simulation, ignoring the seasonal variations of ±10% in event rates (Tilav et al. 2010). Muon propagation through the Earth and ice is done using Muon Monte Carlo (Chirkin & Rhode 2004). Using measurements of the scattering and absorption lengths in ice (Ackermann et al. 2006), a detailed simulation propagates the photon signal to each DOM (Lundberg et al. 2007). The simulation of the DOMs includes their angular acceptance and electronics. Experimental and simulated data are processed and filtered in the same way.

In Figure 4, we show the cosine of zenith and in Figure 5 the muon energy proxy, reduced log-likelihood, and angular uncertainty estimator distributions of all events at trigger level, L1 filter level, and after final analysis cuts for data and Monte Carlo (MC). In these figures, the simulation uses a slightly modified version of the *poly-gonato* model of the galactic CR flux and composition (Hoerandel 2003). Above the galactic model cutoff at $Z \times 4 \times 10^{15}$ eV, a flux of pure iron is used with an E^{-3} spectrum. This is done because currently CORSIKA cannot propagate elements in the *poly-gonato* model that are heavier than iron. Moreover, the *poly-gonato* model only accounts for galactic CRs and does not fully account for the average measured flux above 10^{17} eV, even when all nuclei are considered (see Figure 11 in Hoerandel 2003). These corrections then reproduce the measured CR spectrum at these energies. There is a 23% difference in normalization of data and CR muon events at trigger level. This normalization offset largely disappears after quality cuts are made. Generally good agreement is achieved at later cut levels.

Figure 4 shows some disagreement between data and simulation for zenith angles around 80°. Muons created in CR showers in the atmosphere near this zenith angle must travel about 15 km to reach the bottom of IceCube. Only very high energy muons can travel such distances. For the simulation to produce the

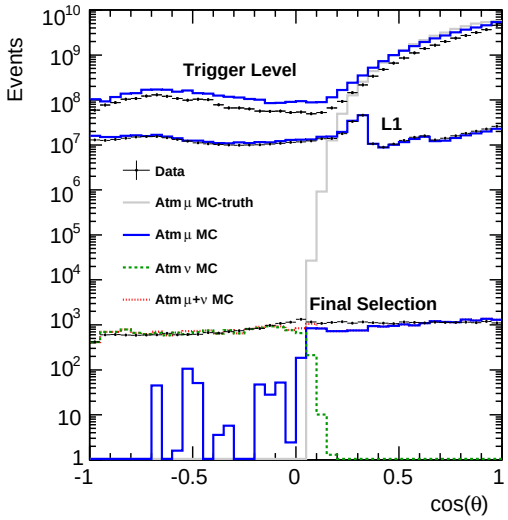

Figure 4. Distribution of reconstructed cosine zenith at trigger level, L1, and final cut level for data and simulation of atmospheric muons (Hoerandel 2003) and neutrinos (Barr et al. 2004; Bugaev et al. 1989). The true cosine zenith distribution of the muons at trigger level is also shown.

(A color version of this figure is available in the online journal.)

correct zenith distribution for these nearly horizontal events, CR composition can be important since protons can produce higher energy muons than iron nuclei with the same energy.

In addition to the slightly modified version of the *poly-gonato* model, discussed above, a simpler pure proton and iron two-component model with a much higher contribution of protons is used for comparison (Glasstetter & Hoerandel 1999). The final zenith distribution with each of these models is shown in Figure 6. The atmospheric muon simulation is not only affected by the primary composition uncertainties at high energy; it is also affected by the hadronic model, affecting the production rate of muons at the level of 15% in the region of interest for IceCube, greater than about 1 TeV, as discussed in the SIBYLL model paper (Ahn et al. 2009) and in the comparison between different hadronic models used in CORSIKA presented in Berghaus et al. (2008).

For the up-going region, several models of atmospheric neutrino fluxes, both conventional fluxes from pion and kaon decay and prompt fluxes from charmed meson decay, are shown in Figure 6. To represent the low and high predictions, conventional and prompt models are used in pairs: Honda (Honda et al. 2007) for the conventional flux paired with Sarcevic (Enberg et al. 2008) for the prompt flux represent the low prediction, and Bartol (Barr et al. 2004) for the conventional

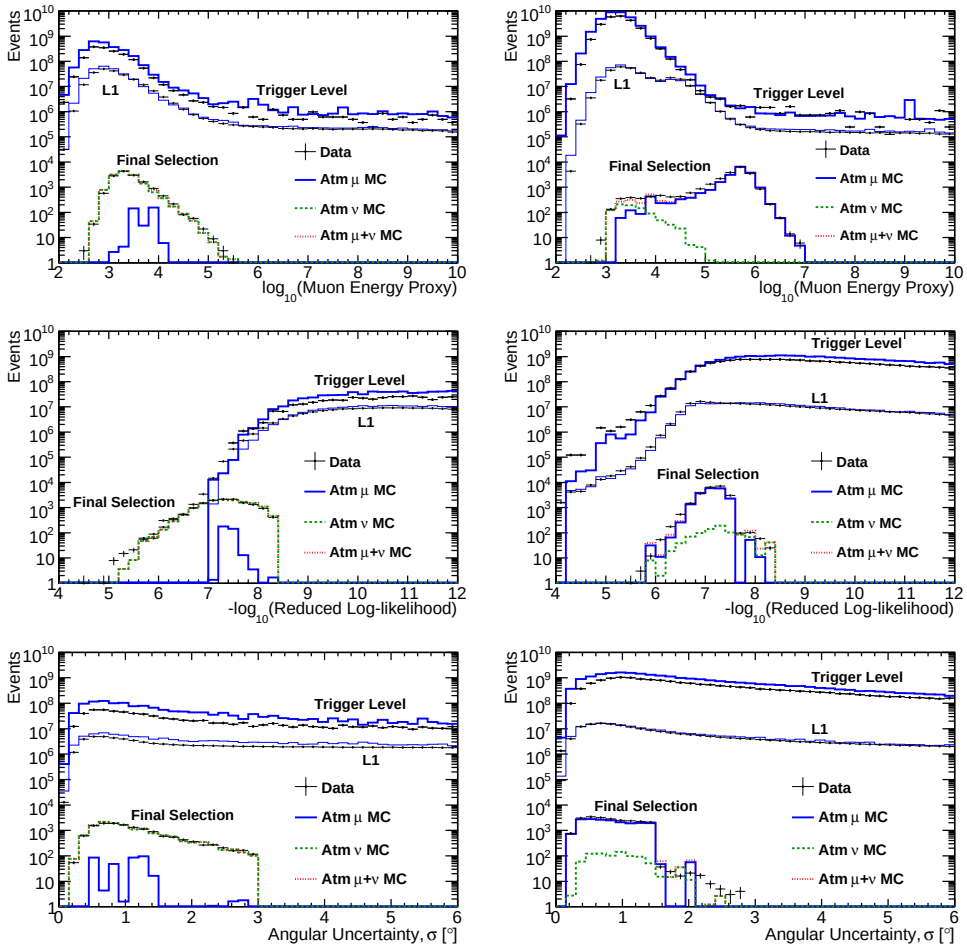

Figure 5. Distributions of muon energy proxy (top row), reduced log-likelihood (middle row), and angular uncertainty estimator (bottom row) for the up-going sample (left column) and the down-going sample (right column). Each is shown at trigger level, L1, and final cut level for data and simulation of atmospheric muons and neutrinos. In the up-going sample (left column), all atmospheric muons are misreconstructed, and at final level their remaining estimated contribution is about 2.4% ± 0.8%.

(A color version of this figure is available in the online journal.)

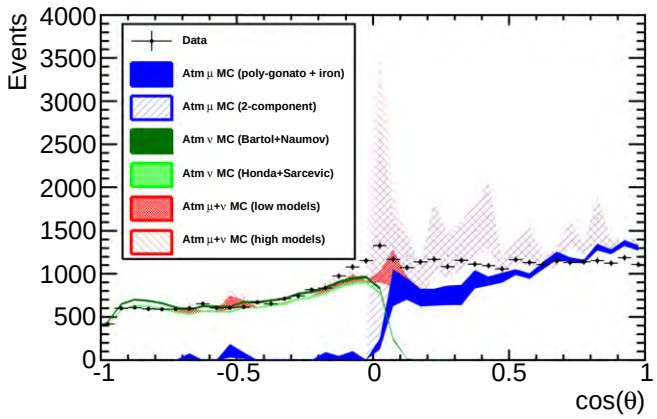

Figure 6. Distribution of reconstructed cosine zenith for the final event sample compared to the models discussed in the text. Honda and Sarcevic are summed with *poly-gonato* to represent the set of low predictions, and Bartol and Naumov are summed with the two-component model for the high predictions. Only statistical errors are shown. The two-component model has limited statistics, causing the peaks and valleys. Systematic uncertainties of neutrino production in CR showers are estimated to be about 40% at 1 TeV (Barr et al. 2006) and 15% in the muon rate greater than about 1 TeV (Ahn et al. 2009; Berghaus et al. 2008).

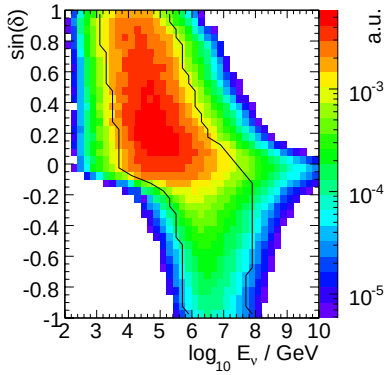

Figure 7. Energy distribution for a flux $d\Phi/dE \propto E^{-2}$ of neutrinos as a function of declination for the final event selection. The black contours indicate the 90% central containment interval for each declination.

flux paired with Naumov (Bugaev et al. 1989) for the prompt flux represent the high prediction. Additional uncertainty in the predicted atmospheric neutrino rate is estimated to be about 40% at 1 TeV (Barr et al. 2006). We conclude that our data agree with background simulation at the final level, within the range of uncertainties allowable by existing CR composition and atmospheric neutrino models.

4. DETECTOR PERFORMANCE

The performance of the detector and the analysis is characterized using the simulation described in Section 3.2. For a spectrum of neutrinos $d\Phi/dE \propto E^{-2}$, the median angular difference between the neutrino and the reconstructed direction of the muon in the northern (southern) sky is 0.°8 (0.°6). Along with more severe quality selection in the southern sky, the different energy distributions in each hemisphere, shown in Figure 7, cause the difference in these two values. This is because the reconstruction performs better at higher energy due to the larger amount of light and longer muon tracks. The cumulative point-spread function (PSF) is shown in Figure 8 for two energy ranges and compared with simulation of the complete IceCube detector using the same quality selection, as well as the median PSF versus energy for the two hemispheres.

The neutrino effective area $A_\nu^{\rm eff}$ is a useful parameter to determine event rates and the performance of a detector for different analyses and fluxes. The expected event rate for a given differential flux $d\Phi/dE$ is

$$N_{\rm events}(\delta_\nu) = \int dE_\nu A_\nu^{\rm eff}(E_\nu, \delta_\nu) \frac{d\Phi_\nu(E_\nu, \delta_\nu)}{dE_\nu}, \qquad (1)$$

and is calculable using simulation. The $A_\nu^{\rm eff}$ represents the size of an equivalent detector if it were 100% efficient. Figure 9 shows the $A_\nu^{\rm eff}$ for fluxes of $\nu_\mu + \bar{\nu}_\mu$ and $\nu_\tau + \bar{\nu}_\tau$, for events at final selection level. Neutrinos arriving from the highest declinations must travel through the largest column depth and can be absorbed: this accounts for the turnover at high energies for nearly vertical up-going muon neutrinos. Tau neutrinos have the advantage that the tau secondary can decay back into a tau neutrino before losing much energy.

Although tau (and electron) neutrino secondaries usually produce nearly spherical showers rather than tracks, tau leptons will decay to muons with a 17.7% branching ratio (Amsler et al. 2008). At very high energy (above about 1 PeV), a tau will travel far enough before decaying that the direction can be reconstructed well, contributing to any extraterrestrial signal in the muon channel. For the upper limits quoted in Section 8, we must make an assumption on the flavor ratios at Earth, after oscillations. It is common to assume $\Phi_{\nu_e}:\Phi_{\nu_\mu}:\Phi_{\nu_\tau} = 1:1:1$. This is physically motivated by neutrino production from pion decay and the subsequent muon decay, yielding $\Phi_{\nu_e}:\Phi_{\nu_\mu}:\Phi_{\nu_\tau} = 1:2:0$.

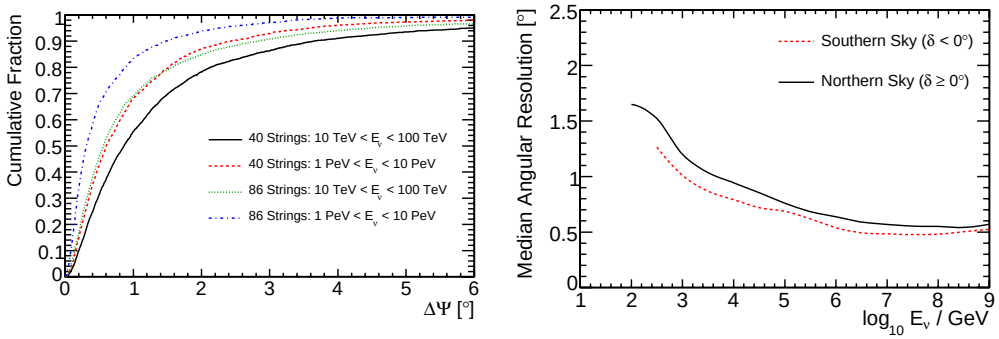

Figure 8. Cumulative point-spread function (angle between neutrino and reconstructed muon track) for simulated neutrino signal events following a spectrum $d\Phi/dE \propto E^{-2}$ at the final cut level in the up-going region (left). Also shown is the same distribution for the final IceCube configuration. The median of the PSF vs. energy is shown separately for the northern and southern skies (right). The improvement in the southern sky is because of the more restrictive quality cuts.

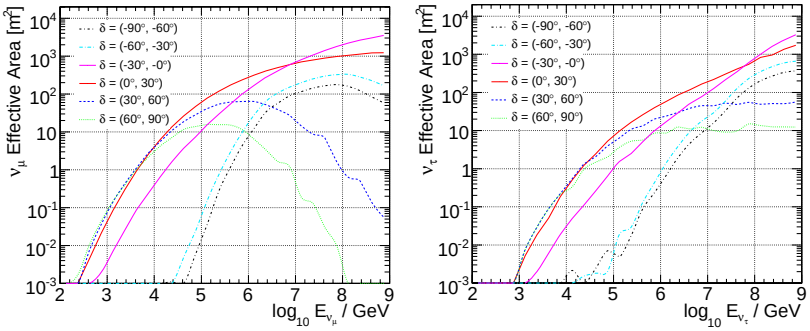

Figure 9. Solid-angle-averaged effective areas at final cut level for astrophysical neutrino fluxes in six declination bands for $\nu_\mu + \bar{\nu}_\mu$ (left) and $\nu_\tau + \bar{\nu}_\tau$ (right), assuming an equal flux of neutrinos and antineutrinos.

(A color version of this figure is available in the online journal.)

After standard oscillations over astrophysical baselines, this gives an equal flux of each flavor at Earth (Athar et al. 2000). Under certain astrophysical scenarios, the contribution from muon decay may be suppressed, leading to an observed flux ratio of $\Phi_{\nu_e}:\Phi_{\nu_\mu}:\Phi_{\nu_\tau} = 1:1.8:1.8$ (Kashti & Waxman 2005), or the contribution of tau neutrinos could be enhanced by the decay of charmed mesons at very high energy (Enberg et al. 2009). For a spectrum $d\Phi/dE \propto E^{-2}$ and equal muon and tau neutrino fluxes, the fraction of tau neutrino-induced events is about 17% for vertically down-going, 10% for horizontal, and 13% for vertically up-going. Because the contribution from tau neutrinos is relatively small, assuming only a flux of muon neutrinos can be used for convenience and to compare to other published limits. We have tabulated limits on both Φ_{ν_μ} and the sum $\Phi_{\nu_\mu} + \Phi_{\nu_\tau}$, assuming an equal flux of each, while in the figures we have specified that we only consider a flux of muon neutrinos. Limits are always reported for the flux at the surface of the Earth.

5. SEARCH METHOD

An unbinned maximum likelihood ratio method is used to look for a localized, statistically significant excess of events above the background. We also use energy information to help separate possible signal from the known backgrounds.

The method follows that of Braun et al. (2008). The data are modeled as a two-component mixture of signal and background. A maximum likelihood fit to the data is used to determine the relative contribution of each component. Given N events in the data set, the probability density of the ith event is

$$\frac{n_s}{N}\mathcal{S}_i + \left(1 - \frac{n_s}{N}\right)\mathcal{B}_i, \tag{2}$$

where $\mathcal{S}_i$ and $\mathcal{B}_i$ are the signal and background probability density functions (PDFs), respectively. The parameter n_s is the unknown contribution of signal events.

For an event with reconstructed direction $\vec{x}_i = (\alpha_i, \delta_i)$, where α_i is the right ascension (R.A.) and δ_i is the declination, we model the probability of originating from the source at $\vec{x}_s$ as a circular two-dimensional Gaussian,

$$\mathcal{N}(\vec{x}_i|\vec{x}_s, \sigma_i) = \frac{1}{2\pi\sigma_i^2}\exp\left(-\frac{|\vec{x}_i - \vec{x}_s|}{2\sigma_i^2}\right), \tag{3}$$

where σ_i is the angular uncertainty reconstructed for each event individually (Neunhoffer 2006) and $|\vec{x}_i - \vec{x}_s|$ is the space angle difference between the source and reconstructed event. While the average angular uncertainty decreases with increasing energy, the individual σ_i values are estimated from the reconstruction likelihood shape itself, and therefore the PSF incorporates this dependence without explicitly being a function of energy. The PSFs for different ranges of σ_i are in Figure 10, showing the correlation between the estimated angular uncertainty and actual track reconstruction error.

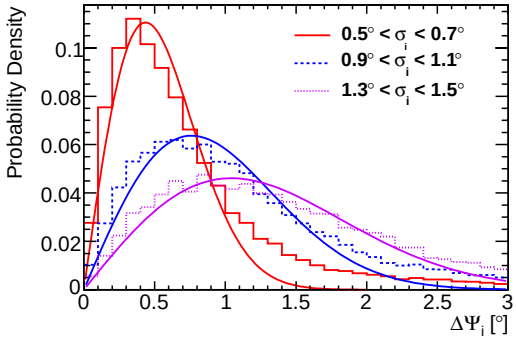

Figure 10. Angular deviation between neutrino and reconstructed muon direction $\Delta\Psi$ for ranges in σ_i, the reconstructed angular uncertainty estimator. Fits of these distributions to two-dimensional Gaussians projected into $\Delta\Psi$ are also shown. The value of σ_i is correlated to the track reconstruction error. A small fraction of events are not well represented by the Gaussian distribution, but these are the least well-reconstructed events and contribute the least to signal detection.

(A color version of this figure is available in the online journal.)

The energy PDF $\mathcal{E}(E_i|\gamma, \delta_i)$ describes the probability of obtaining a reconstructed muon energy E_i for an event produced by a source of a given neutrino energy spectrum $E^{-\gamma}$ at declination δ_i. We describe the energy distribution using 22 declination bands. Twenty bands, spaced evenly by solid angle, cover the down-going range where the energy distributions are changing the most due to the energy cuts in the event selection, while two are needed to sufficiently describe the up-going events, with the separation at $\delta = 15°$. We fit the source spectrum with a power law $E^{-\gamma}$; γ is a free parameter. The probability of obtaining a reconstructed muon energy E_i for an event produced by a source with spectral index γ, for spectral indices $1.0 < \gamma < 4.0$, is determined using simulation. Two examples of these energy PDFs are shown in Figure 11.

The full signal PDF is given by the product of the spatial and energy PDFs:

$$\mathcal{S}_i = \mathcal{N}(\vec{x}_i|\vec{x}_s, \sigma_i) \cdot \mathcal{E}(E_i|\gamma, \delta_i). \tag{4}$$

The background PDF $\mathcal{B}_i$ contains the same terms, describing the angular and energy distributions of background events:

$$\mathcal{B}_i = \mathcal{N}_{\rm Atm}(\vec{x}_i) \cdot \mathcal{E}(E_i|{\rm Atm}, \delta_i), \tag{5}$$

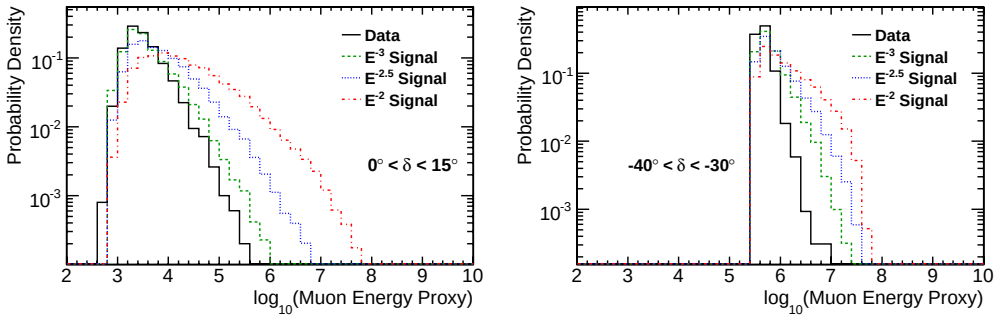

Figure 11. Probability densities for the muon energy proxy for data as well as simulated power-law neutrino spectra. Two declination bands are shown: $0^\circ < \delta < 15^\circ$ (left) and $-40^\circ < \delta < -30^\circ$ (right), representing two of the declination-dependent energy PDFs used in the likelihood analysis. There is an energy cut applied for negative declinations.

(A color version of this figure is available in the online journal.)

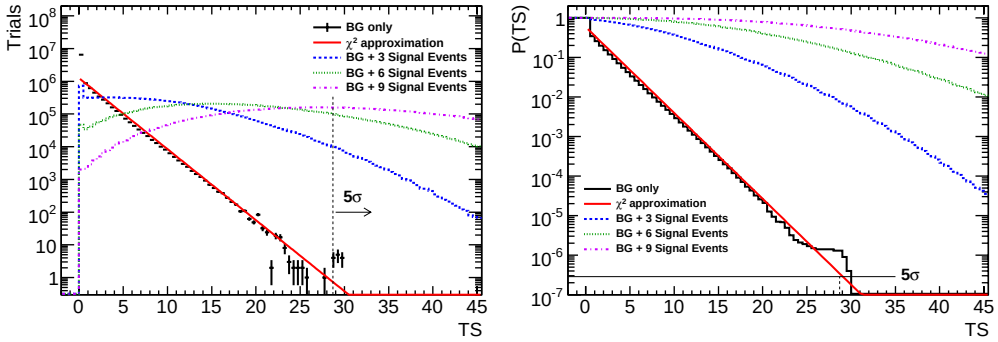

Figure 12. Distributions of the test statistic TS for a fixed point source at $\delta = 25^\circ$ for 10 million scrambled data sets (left) and the p-value, or the probability to obtain TS or higher (right). A χ^2 distribution with 2 degrees of freedom times one-half (because we only search for excesses) can be used as an approximation. Also shown are the distributions when simulated signal events are injected following a spectrum $d\Phi/dE \propto E^{-2}$. About nine events are needed for a discovery in 50% of trials at this declination since the median TS in this case is 29.1.

(A color version of this figure is available in the online journal.)

where $\mathcal{N}_{\rm Atm}(\vec{x}_i)$ is the spatial PDF of atmospheric background and $\mathcal{E}(E_i|{\rm Atm}, \delta_i)$ is the probability of obtaining E_i from atmospheric backgrounds (neutrinos and muons) at the declination of the event. These PDFs are constructed using data and, for the energy term, in the same 22 declinations bands as the signal PDF. All non-uniformities in atmospheric background event rates caused by the detector acceptance or seasonal variation average out in the time-integrated analysis. Therefore, $\mathcal{N}_{\rm Atm}(\vec{x}_i)$ has a flat expectation in R.A. and is only dependent on declination. Because the data are used in this way for background estimation, the analysis is restricted from -85° to 85° declination, so that any point-source signal will still be a small contribution to the total number of events in the same declination region.

The likelihood of the data is the product of all event probability densities:

$$\mathcal{L}(n_s, \gamma) = \prod_{i=1}^{N} \left[\frac{n_s}{N} \mathcal{S}_i + \left(1 - \frac{n_s}{N}\right) \mathcal{B}_i \right]. \quad (6)$$

The likelihood is then maximized with respect to n_s and γ, giving the best-fit values $\hat{n}_s$ and $\hat{\gamma}$. The null hypothesis is given by $n_s = 0$ (γ has no meaning when no signal is present). The fit has been restricted to the physical signal region $n_s \geqslant 0$. The likelihood ratio test statistic is

$$\mathrm{TS} = \begin{cases} -2 \log \dfrac{\mathcal{L}(n_s = 0)}{\mathcal{L}(\hat{n}_s, \hat{\gamma}_s)} & n_s \geqslant 0, \\ 0 & n_s < 0. \end{cases} \quad (7)$$

The significance of the analysis is determined by comparing the TS from the real data with the distribution of TS from the null hypothesis (events scrambled in R.A.). We define the p-value as the fraction of randomized data sets with equal or higher test statistic values than the real data. Since we do not allow negative values of n_s, all underfluctuations result in TS = 0, the lowest possible value. This yields a p-value of 100%, which happens in approximately half of the searches. We evaluate the median sensitivity and upper limits at a 90% confidence level (CL) using the method of Feldman & Cousins (1998) and calculate the discovery potential as the flux required for 50% of trials with simulated signal to yield a p-value less than 2.87×10^{-7} (i.e., 5σ significance if expressed as the one-sided tail of a Gaussian distribution). The distributions of TS and the corresponding p-value for 10 million trials are shown in Figure 12 for a fixed point source at $\delta = 25^\circ$. Distributions with simulated signal events injected following a spectrum $d\Phi/dE \propto E^{-2}$ are included, as well as a χ^2 distribution with 2 degrees of freedom, which is used to estimate the 5σ significance threshold for calculating the discovery potential since simulating enough scrambled data sets requires a large amount of processing time.

Although sensitivities and limits for sources with $d\Phi/dE \propto E^{-2}$ have become a useful benchmark for comparing performance, a wide range of other spectral indices are possible along with cutoffs over a wide range of energy. To understand the ability of the method to detect sources with cutoff spectra, typically observed in gamma rays to be in the range 1–10 TeV for galactic sources, Figure 13 shows the discovery potentials for a wide range of exponential cutoffs, demonstrating the ability of the method to detect sources with cutoff spectra. Typically, cutoffs observed in gamma rays are in the range 1–10 TeV for galactic

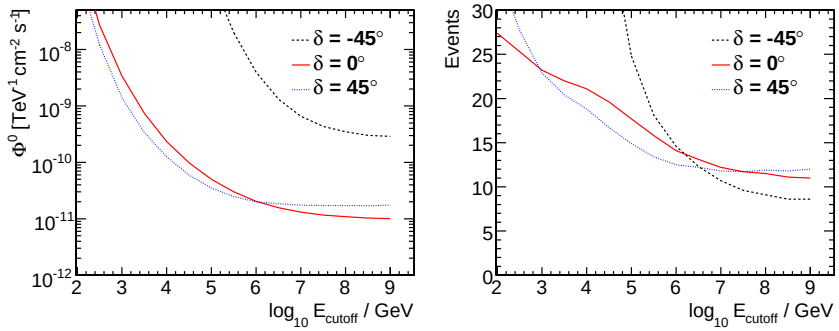

Figure 13. Discovery potential is shown as a function of the cutoff energy for a flux parameterized as $d\Phi/dE = \Phi^0 \cdot (E/\mathrm{TeV})^{-2}\exp(-E/E_{\mathrm{cutoff}})$. The discovery potential is given as the flux normalization Φ^0 (left) and the number of events at the final level (right). Curves are shown at three representative declinations. The likelihood fit is still performed using a pure power law.

(A color version of this figure is available in the online journal.)

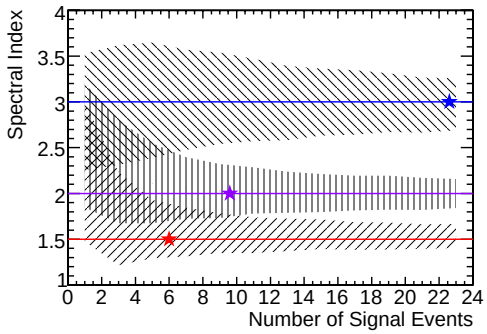

Figure 14. Reconstructed spectral index (1σ shaded area) vs. the number of signal events injected for three source spectra: $E^{-1.5}$, E^{-2}, and E^{-3}. The sources are pure power laws at a declination of 6°. The stars mark the average number of events required for a 5σ discovery for each spectrum. Systematic errors are not included.

(A color version of this figure is available in the online journal.)

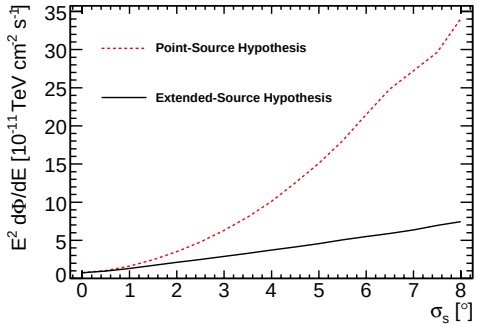

Figure 15. Discovery potential flux vs. the σ_s of an extended source (distributed as a two-dimensional Gaussian) with a spectrum $d\Phi/dE \propto E^{-2}$ at a declination of 25°. The case of a point-source hypothesis is compared against the correct extended-source hypothesis matching what was used to simulate the signal.

(A color version of this figure is available in the online journal.)

sources. The likelihood fit is still performed using a pure power law.

The likelihood analysis is not only more sensitive than binned methods, but it can also help extract astrophysical information. Figure 14 shows our ability to reconstruct the spectral index for power-law neutrino sources at a declination of 6°. The effective area is high for a broad range of energies here, and the spectral resolution is best. For each spectrum shown, the statistical uncertainty (1σ CL) in the spectral index will be about ± 0.3 when enough events are present to claim a discovery. Spectral resolution worsens to ± 0.4 at both $\delta = -45°$ and $\delta = 45°$ when enough events are present for a discovery in each case.

Stacking multiple sources in neutrino astronomy has been an effective way to enhance discovery potential and further constrain astrophysical models (Achterberg et al. 2006b; Abbasi et al. 2009c). We can consider the accumulated signal from a collection of sources using a method similar to Abbasi et al. (2006). Only a modification to the signal likelihood is necessary in order to stack sources, breaking the signal hypothesis into the sum over M sources:

$$\mathcal{S}_i \Rightarrow \mathcal{S}_i^{\mathrm{tot}} = \frac{\sum_{j=1}^{M} W^j R^j(\gamma) \mathcal{S}_i^j}{\sum_{j=1}^{M} W^j R^j(\gamma)}, \tag{8}$$

where W^j is the relative theoretical weight, $R^j(\gamma)$ is the relative detector acceptance for a source with spectral index γ (assumed to be the same for all stacked sources), and $\mathcal{S}_i^j$ is the signal probability density for the ith event, all for the jth source. As before, the total signal events n_s and collective spectral index γ are fit parameters. The W^j coefficients depend on our prior theoretical assumptions about the expected neutrino luminosity. They are higher for sources that are, on theoretical grounds, expected to be brighter. Tables for $R^j(\gamma)$, given as the mean number of events from a source with $d\Phi/dE \propto E^{-\gamma}$, are calculated using simulation. The flexibility built into the method by the relative detector acceptance and theoretical weights allows us to use source catalogs covering the whole sky and with large variations in source strengths, as well as to directly test model predictions.

We would also like to consider sources that are spatially extended (with respect to the PSF). For an example of how important this can be, the significance observed by the Milagro experiment in the location of the Fermi source J0634.0+1745 (associated with the Geminga pulsar) rises from 3.5σ to 6.3σ by fitting for an extended source (Abdo et al. 2009). The only modification to the method required is to convolve the source distribution with the PSF. Since we model our PSF as a circular two-dimensional Gaussian distribution, it is easy to also model a source as a circular two-dimensional Gaussian of width σ_s. The convolution results in a broader two-dimensional Gaussian of width $\sqrt{\sigma_i^2 + \sigma_s^2}$ and the likelihood uses this distribution for the signal spatial term. The discovery potential flux for a range of source extensions is shown in Figure 15 and compared to the (incorrect) hypothesis of a point source. For a source with true extent $\sigma_s = 2°$, the point-source hypothesis requires nearly

a factor of two times more flux for discovery compared to the correct extended-source hypothesis.

6. DESCRIPTION OF THE FIVE SEARCHES

We have performed five searches:

1. a scan for the most significant point source in the entire sky;
2. a search over an a priori defined list of 39 interesting astrophysical objects;
3. a stacking search for 16 Milagro TeV gamma-ray sources, some seen only in coincidence with the Fermi-LAT, and one unconfirmed hot spot (17 total sources);
4. a stacking search for 127 local starburst galaxies (Becker et al. 2009);
5. a stacking search for five nearby clusters of galaxies (CGs), testing four different models for the CR spatial distribution (Murase et al. 2008).

The analyses and event selection procedure were determined before unblinding the R.A. of the data. We require a 5σ significance for discovery. Final *p*-values are calculated for each search individually.

6.1. All-sky Scan

The first search is a scan for the single most significant point source of neutrinos over the declination range -85° to $+85^\circ$. The maximum likelihood ratio is defined continuously over the sky, and we sample it on a grid of $0.^\circ1$ in R.A. and $0.^\circ1$ in decl. The size of the grid is not important as long as it is small compared to the angular resolution of the detector. Using a finer grid increases the computation time with no added benefit. A grid size that is comparable to or larger than the angular resolution could miss the location of the peaks in the significance map, yielding sub-optimal performance.

6.2. A Priori Source List

In order to avoid the large number of effective trials associated with scanning the entire sky, we also perform a search for the most significant of 39 a priori selected source candidates, given in Table 3. These sources have been selected on the basis of observations in gamma rays or astrophysical modeling that predicts neutrino emission. We also added the most significant location observed in the 22-string IceCube configuration (a post-trial *p*-value of 1.3%; Abbasi et al. 2009b).

6.3. Milagro TeV Source Stacking

The Milagro Collaboration has reported 16 sources of TeV gamma rays (Abdo et al. 2007), several only after correlating with GeV gamma rays from the Fermi Gamma-ray Space Telescope source list (Abdo et al. 2009). These sources are promising candidates for detection by neutrino telescopes. Particularly interesting are sources in the complex Cygnus region (Beacom & Kistler 2007) and six SNR associations (Halzen et al. 2008; Gonzalez-Garcia et al. 2009), including MGRO J1852+01, a hot spot that falls below the significance threshold of the Milagro Collaboration to be claimed as a source. If confirmed as a source, MGRO J1852+01 could contribute a large fraction (about 42%) of the total neutrino flux from the SNR sources (Halzen et al. 2008). For the 40-string configuration of IceCube, the model of Halzen et al. (2008) predicts 3.0 neutrino events in 375.5 days, following a spectrum $d\Phi/dE \propto E^{-2.1}$ with an exponential cutoff at about 600 TeV.

We performed a stacking search for 17 sources observed in TeV gamma rays by Milagro (adding MGRO J1852+01 to the 16 sources which were found significant by the Milagro Collaboration) using an equal weight for each source in the likelihood. Assuming that neutrino and gamma-ray fluxes correlate and using these as weights in the likelihood did not appreciably improve the sensitivity in this case. Spatial extensions were used in the search for three of the sources where measurements were given (also used in the source simulation for limit calculations). The largest source was MGRO J2031+41, reported to have a diameter of $3.^\circ0 \pm 0.^\circ9$ (Abdo et al. 2007).

6.4. Starburst Galaxy Stacking

Starburst galaxies have a dense interstellar medium and high star formation rates, particularly of high-mass stars. This leads to both high supernova rates and heating of ambient dust. The model of Becker et al. (2009) associates the far-infrared (FIR) emission with this hot dust and the radio emission with synchrotron losses of CR electrons, presumably accelerated along with hadronic CRs in the elevated number of SNRs. The observed strong correlation between the FIR and radio emission points to the high star formation rate as the single underlying cause, and should also correlate with the neutrino flux. The increased production of CRs and high density of target material are ideal conditions for neutrino production. The starburst galaxies M82 and NGC 253 have been observed in gamma rays at GeV–TeV energies (Abdo et al. 2010; Acciari et al. 2009; Aharonian et al. 2005) and are the only observed steady extragalactic TeV gamma-ray sources not associated with AGNs.

We performed a stacking search for 127 starburst galaxies, weighting the sources by their observed FIR flux at 60 μm, as compiled in Table A.1 in Becker et al. (2009).

6.5. Galaxy Cluster Stacking

CGs are another potential source of high-energy protons and, through interactions with intracluster material (ICM), neutrinos. CGs are the largest gravitationally bound objects in the universe and continue to grow through merging and accretion of dark matter and baryonic gas, generating shock fronts on megaparsec scales. The possibility for CGs to be sources of ultra-high-energy CRs above 3×10^{18} eV is described in, e.g., Norman et al. (1995) and Kang et al. (1997). Murase et al. (2008) discuss the possibility of CGs being a significant contribution to the CR spectrum between the second knee at about 3×10^{17} eV and the ankle at about 3×10^{18} eV. They give predictions for neutrinos from five nearby ($z < 0.03$) CGs: Virgo, Centaurus, Perseus, Coma, and Ophiuchus. Information on location, distance, and size of CGs (virial radii) was taken from Reiprich & Boehringer (2002). These nearby CGs appear to us as spatially extended objects with virial radii subtending $1.^\circ3$–$6.^\circ9$, so an extended spatial distribution of neutrinos is possible. Whereas the distribution of the ICM is well known from X-ray observations (Pfrommer & Ensslin 2004), the distribution of CRs is highly uncertain. The distribution of neutrinos is given by the product of the CR and ICM distributions. Four CR models have been considered for neutrino production, discussed in Murase et al. (2008) and references therein (e.g., Colafrancesco & Blasi 1998; Berezinsky et al. 1997):

1. *Model A.* CRs are uniformly distributed within the cluster shock radius, taken to be 0.56 of the virial radius for the dynamical parameters considered.

Table 2
Galaxy Cluster Parameters

Source	R.A. (°)	Decl. (°)	Model	σ_s (°)	A (TeV^{-1} cm^{-2} s^{-1})	γ_1	γ_2	$E_{\rm break}$ (TeV)
Virgo	186.63	12.72	Model A	2.0	1.42×10^{-12}	−2.14	−4.03	2.16×10^{6}
			Model B	4.0	1.18×10^{-12}	−2.14	−4.03	2.16×10^{6}
			Isobaric	3.0	7.57×10^{-13}	−2.14	−4.03	2.16×10^{6}
			Central AGN	0.0	6.47×10^{-12}	−2.42	−4.24	2.13×10^{6}
Centaurus	192.20	−41.31	Model A	0.25	2.78×10^{-13}	−2.14	−4.03	2.15×10^{6}
			Model B	0.5	2.20×10^{-13}	−2.14	−4.03	2.15×10^{6}
			Isobaric	0.25	1.09×10^{-13}	−2.15	−4.07	2.33×10^{6}
			Central AGN	0.0	5.10×10^{-13}	−2.45	−4.28	2.39×10^{6}
Perseus	49.95	41.52	Model A	0.0	5.83×10^{-14}	−2.15	−4.07	2.32×10^{6}
			Model B	0.5	4.60×10^{-14}	−2.15	−4.07	2.32×10^{6}
			Isobaric	0.0	6.17×10^{-13}	−2.15	−4.07	2.32×10^{6}
			Central AGN	0.0	5.97×10^{-13}	−2.40	−4.20	1.88×10^{6}
Coma	194.95	27.94	Model A	0.25	2.14×10^{-14}	−2.14	−4.03	2.12×10^{6}
			Model B	0.25	1.34×10^{-14}	−2.14	−4.03	2.12×10^{6}
			Isobaric	0.25	1.83×10^{-13}	−2.15	−4.07	2.30×10^{6}
			Central AGN	0.0	2.13×10^{-13}	−2.41	−4.20	1.89×10^{6}
Ophiuchus	258.11	−23.36	Model A	0.0	4.87×10^{-14}	−2.15	−4.07	2.29×10^{6}
			Model B	0.5	1.50×10^{-14}	−2.15	−4.07	2.29×10^{6}
			Isobaric	0.0	5.50×10^{-13}	−2.15	−4.11	2.49×10^{6}
			Central AGN	0.0	2.55×10^{-13}	−2.43	−4.24	2.12×10^{6}

Notes. σ_s is the optimized sigma of a two-dimensional Gaussian distribution used in the likelihood. Numerical calculations of the differential fluxes (K. Murase 2009, private communication) for each model described in Murase et al. (2008) are fit well to broken power laws, parameterized in Equation (9).

2. *Model B.* CRs are uniformly distributed within the virial radius, yielding the most conservative neutrino flux distributed over the largest area.
3. *Isobaric.* CRs follow the distribution of thermal gas.
4. *Central AGN.* In a two-step acceleration scenario, CRs are accelerated in the central AGN up to a maximum energy before diffusing throughout the cluster and possibly undergoing further acceleration. For the purposes of IceCube searches, this model can be treated as a point source. This model is discussed in detail by Kotera et al. (2009).

Signal neutrinos were simulated according to each of the four models. We modeled the source extensions in the likelihood as two-dimensional Gaussian distributions with the width for each source and each model determined by optimizing for the best discovery potential. Although the modeling of the source extension as a Gaussian in the likelihood is not ideal, it is straightforward and computationally fast. The exact shape of the sources is not important for small signals; we may be able to analyze the shape with more detail depending on the intensity of any signal.

We performed a stacking search for five nearby CGs mentioned above following the model predictions of Murase et al. (2008) as weights in the likelihood. The size of the clusters in the likelihood fit was allowed to vary discretely between the optimal widths for each CR distribution model. The optimal width and ν_μ differential flux for each source and each model are given in Table 2. The differential fluxes are parameterized as broken power laws:

$$\frac{d\Phi}{dE}(\mathrm{TeV}^{-1}\,\mathrm{cm}^{-2}\,\mathrm{s}^{-1}) = \begin{cases} A \cdot (E/\mathrm{TeV})^{-\gamma_1} & E \leqslant E_{\rm break}, \\ B \cdot (E/\mathrm{TeV})^{-\gamma_2} & E > E_{\rm break}. \end{cases} \quad (9)$$

The parameter $B = A \cdot E_{\rm break}^{\gamma_2-\gamma_1}$ after enforcing continuity at the break energy.

7. SYSTEMATIC ERRORS

The analyses described in Section 6 give reliable statistical results (p-values) due to the ability to generate background-only data sets by scrambling the data in R.A. By using the data to estimate background, the systematic errors come only from signal and detector simulation used to calculate flux upper limits, sensitivities, and discovery potentials.

The main systematic uncertainties on the flux limits come from photon propagation in ice, absolute DOM sensitivity, and uncertainties in the Earth density profile as well as muon energy loss. All numbers are for a spectrum $d\Phi/dE \propto E^{-2}$ of muon neutrinos. We evaluate the systematic uncertainty due to photon propagation by performing dedicated signal simulations with scattering and absorption coefficients varied within their uncertainties of ±10% (Ackermann et al. 2006). The maximum difference was between the case where both scattering and absorption were increased by 10% and the case where both were decreased by 10%. The deviation in the observed number of events between these two cases was 11%. The range of uncertainty in the DOM sensitivity is taken as ±8%, based on the measured uncertainty in the PMT sensitivity (Abbasi et al. 2010a). Similarly, another dedicated simulation where we varied the DOM sensitivity inside the uncertainty leads to a maximum systematic uncertainty on the number of events of 9%. These uncertainties on the flux varied by only about 2% between the northern and southern sky, so only averages over the whole sky are reported. Finally, uncertainties in muon energy losses, the neutrino–nucleon cross section, and the rock density near the detector introduce an 8% systematic uncertainty for vertically up-going events (Achterberg et al. 2007). These events are the most affected, and this uncertainty is applied to all zeniths to be conservative. A sum in quadrature of the systematic uncertainties on the flux gives a total of 16% systematic uncertainty in the signal simulation. These

Table 3
Results for the A Priori Source Candidate List

Object	R.A. (°)	Decl. (°)	$\Phi^{90}_{\nu_\mu}$	$\Phi^{90}_{\nu_\mu+\nu_\tau}$	p-value	n_s	γ	N_{1°	B_{1°
Cyg OB2	308.08	41.51	6.04	10.54	1.00	0.0	...	2	1.8
MGRO J2019+37	305.22	36.83	7.50	13.3	0.44	1.0	2.8	2	1.9
MGRO J1908+06	286.98	6.27	3.73	6.82	0.43	1.5	3.9	4	3.1
Cas A	350.85	58.81	9.04	15.92	1.00	0.0	...	1	1.8
IC443	94.18	22.53	3.80	6.62	1.00	0.0	...	1	2.0
Geminga	98.48	17.77	3.91	6.66	0.48	0.7	2.1	1	2.3
Crab Nebula	83.63	22.01	3.70	6.58	1.00	0.0	...	1	2.0
1ES 1959+650	300.00	65.15	10.74	19.18	1.00	0.0	...	0	2.0
1ES 2344+514	356.77	51.70	7.24	12.96	1.00	0.0	...	0	1.8
3C66A	35.67	43.04	10.89	19.70	0.24	3.4	3.9	3	1.9
H 1426+428	217.14	42.67	6.14	10.94	1.00	0.0	...	3	1.8
BL Lac	330.68	42.28	10.80	18.70	0.25	2.6	3.9	3	1.8
Mrk 501	253.47	39.76	8.11	14.14	0.41	1.3	3.9	3	2.0
Mrk 421	166.11	38.21	11.71	20.14	0.15	2.6	1.9	2	2.0
W Comae	185.38	28.23	4.46	8.06	1.00	0.0	...	0	1.9
1ES 0229+200	38.20	20.29	6.89	12.06	0.19	4.0	2.8	4	2.1
M87	187.71	12.39	3.42	5.98	1.00	0.0	...	2	2.5
S5 0716+71	110.47	71.34	13.28	23.56	1.00	0.0	...	0	1.6
M82	148.97	69.68	19.14	32.84	0.40	2.0	3.9	4	1.8
3C 123.0	69.27	29.67	5.59	10.66	0.44	1.3	2.7	1	1.9
3C 454.3	343.49	16.15	3.42	5.92	1.00	0.0	...	1	2.3
4C 38.41	248.81	38.13	6.77	11.86	0.48	0.9	3.9	2	2.0
PKS 0235+164	39.66	16.62	6.77	11.62	0.15	5.3	3.0	5	2.3
PKS 0528+134	82.73	13.53	3.63	6.72	1.00	0.0	...	2	2.4
PKS 1502+106	226.10	10.49	3.26	5.78	1.00	0.0	...	0	2.5
3C 273	187.28	2.05	3.61	6.54	1.00	0.0	...	3	3.4
NGC 1275	49.95	41.51	6.04	10.54	1.00	0.0	...	2	1.8
Cyg A	299.87	40.73	7.84	13.44	0.46	1.0	3.5	3	1.9
IC-22 maximum	153.38	11.38	3.26	5.86	1.00	0.0	...	1	2.5
Sgr A*	266.42	−29.01	80.56	139.26	0.41	1.1	2.7	4	3.3
PKS 0537−441	84.71	−44.09	113.90	201.82	1.00	0.0	...	3	3.5
Cen A	201.37	−43.02	109.51	191.56	1.00	0.0	...	4	3.5
PKS 1454−354	224.36	−35.65	92.56	156.74	1.00	0.0	...	4	3.5
PKS 2155−304	329.72	−30.23	105.41	182.90	0.28	1.7	3.9	3	3.4
PKS 1622−297	246.53	−29.86	152.28	263.86	0.048	3.0	2.6	4	3.3
QSO 1730-130	263.26	−13.08	24.83	43.30	1.00	0.0	...	4	3.5
PKS 1406−076	212.24	−7.87	16.04	28.72	0.42	1.3	2.3	4	3.3
QSO 2022-077	306.42	−7.64	12.18	21.78	1.00	0.0	...	2	3.3
3C279	194.05	−5.79	11.94	21.36	0.33	3.6	3.0	7	3.5

Notes. $\Phi^{90}_{\nu_\mu}$ and $\Phi^{90}_{\nu_\mu+\nu_\tau}$ are the upper limits of the Feldman–Cousins 90% confidence intervals for a $d\Phi/dE \propto E^{-2}$ flux normalization of ν_μ and $\nu_\mu + \nu_\tau$, respectively, in units of 10^{-12} TeV^{-1} cm^{-2} s^{-1} (i.e., $d\Phi/dE \leqslant \Phi^{90} \cdot (E/\mathrm{TeV})^{-2}$). n_s is the best-fit number of signal events; the (pre-trial) p-value is also calculated and the spectral index γ is given when $n_s > 0$. N_{1° is the actual number of events observed in a bin of radius 1°. The background event density at the source declination is indicated by the mean number of background events B_{1° expected in a bin of radius 1°.

systematic uncertainties are incorporated into the upper limit and sensitivity calculations using the method of Conrad et al. (2003) with a modification by Hill (2003).

8. RESULTS

The results of the all-sky scan are shown in the map of the pre-trial p-values in Figure 16. The most significant deviation from background is located at 113.°75 R.A., 15.°15 decl. The best-fit parameters are $n_s = 11.0$ signal events above background, with spectral index $\gamma = 2.1$. Since the best-fit spectral index is substantially less than the expectation from background, much of the significance comes from the higher energies of the associated events. The pre-trial estimated p-value of the maximum log-likelihood ratio at this location is 5.2×10^{-6}. In trials using data sets scrambled in R.A., 1817 out of 10,000 have an equal or higher significance somewhere in the sky, resulting in the post-trial p-value of 18%. Upper limits for a flux $d\Phi/dE \propto E^{-2}$ of $\nu_\mu + \bar{\nu}_\mu$ are presented in Figure 17. In all cases, an equal flux of neutrinos and antineutrinos is assumed.

The results of the point-source search in the direction of 39 source candidates selected a priori are given in Table 3 and also shown in Figure 18 with the IceCube median sensitivity. Since the fit was restricted to physical signal values $n_s \geqslant 0$, approximately half of the results have $n_s = 0$ exactly, corresponding to p-values equal to 100% and upper limits equal to the median upper limit (i.e., the sensitivity). The most significant source on the list was PKS 1622−297 with a pre-trial estimated p-value of 5%. The post-trial p-value of 62% was again determined as the fraction of scrambled data sets with at least one source with an equal or higher significance. The mean number of events at the final cut level required for the discovery of a point source is also shown in Figure 19, along with the average background in a circular bin with 1° radius. Included

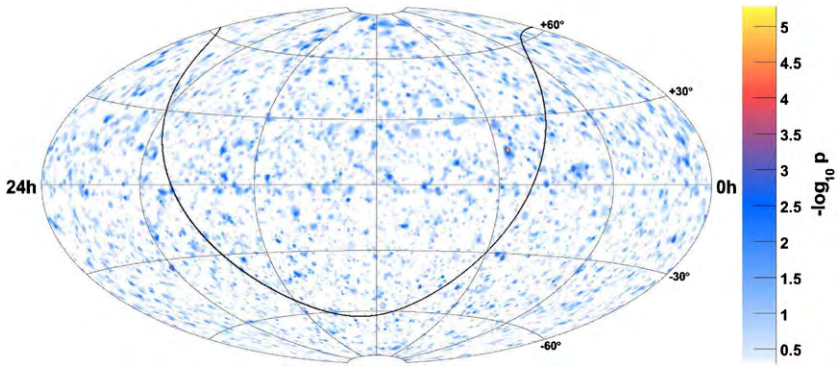

Figure 16. Equatorial skymap (J2000) of pre-trial significances (p-value) of the all-sky point-source scan. The galactic plane is shown as the solid black curve.

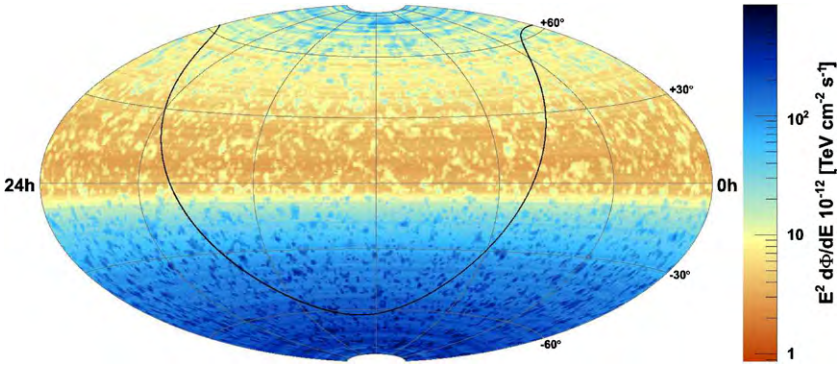

Figure 17. Equatorial skymap (J2000) of upper limits of Feldman–Cousins 90% confidence intervals for a flux $\Phi/dE \propto E^{-2}$ of $\nu_\mu + \bar{\nu}_\mu$. The galactic plane is shown as the solid black curve.

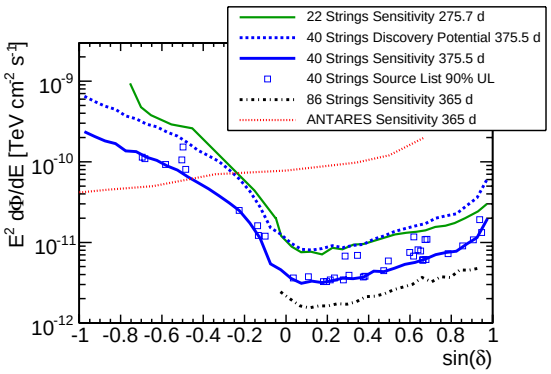

Figure 18. Median sensitivity to a point-source flux $d\Phi/dE \propto E^{-2}$ of $\nu_\mu + \bar{\nu}_\mu$ as a function of declination, shown for the 22-string IceCube southern and northern sky analyses (Abbasi et al. 2009a, 2009b), this 40-string analysis, and preliminary estimated sensitivities for one year for the ANTARES experiment, primarily sensitive in the GeV–TeV energy range (Coyle 2010), and the final IceCube configuration (using the event selection based on this work for the up-going region). For the a priori source list, upper limits of Feldman–Cousins 90% confidence intervals for a flux $d\Phi/dE \propto E^{-2}$ of $\nu_\mu + \bar{\nu}_\mu$ are shown. In addition, we show the discovery potential for this work.

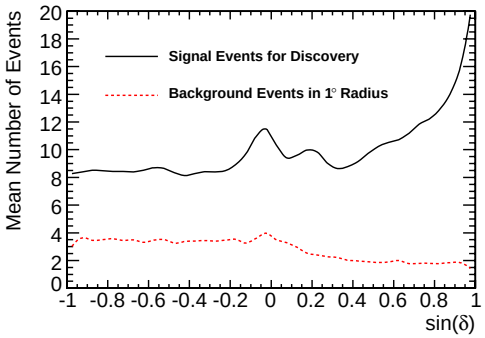

Figure 19. Mean number of $d\Phi/dE \propto E^{-2}$ signal events at the final cut level required for a discovery at 5σ in 50% of trials and the mean number of background events in a circular bin with a radius of 1° vs. sine of the declination.

in Figure 18 is a preliminary comparison to the ANTARES experiment (Coyle 2010). ANTARES is primarily sensitive to GeV–TeV energy neutrinos in the southern sky, so the coverage in energy is quite complementary to this IceCube analysis.

The Milagro TeV source stacking search resulted in a final p-value of 32% with best-fit $n_s = 7.6$ (total number of signal events above background) and spectral index $\gamma = 2.6$. The starburst galaxy stacking search resulted in an underfluctuation with best-fit $n_s = 0$ and a final p-value of 100%, since we do not allow negative values of n_s. Finally, the CGs stacking search yielded a final p-value of 78% with $n_s = 1.8$. These results, along with sensitivities and upper limits, are summarized in Table 4.

9. IMPLICATIONS FOR MODELS OF ASTROPHYSICAL NEUTRINO EMISSION

The IceCube Neutrino Observatory aims to further our understanding of astrophysical phenomena, constraining models even in the absence of a detection. Figure 20 shows our sensitivity to some specific predictions. The model of Morlino et al. (2009) is for SNR RX J1713.7-3946. This analysis is largely insensitive to spectra which cut off below 100 TeV in the southern sky. Applying this emission model at the location of the Crab

Table 4
Results for the Stacked Source Searches

Catalog	*N* Sources	Model	*p*-value	ν_μ Sensitivity	ν_μ Upper Limit	$\nu_\mu + \nu_\tau$ Sensitivity	$\nu_\mu + \nu_\tau$ Upper Limit
Milagro sources	17	E^{-2}, uniform	0.32	$\Phi^{90} = 9.0$	$\Phi^{90} = 12.3$	$\Phi^{90} = 15.8$	$\Phi^{90} = 24.5$
	6	6 SNR assoc.[a]	[b]			SF = 2.9	SF = 7.2
Starburst galaxies	127	E^{-2}, $\propto$ FIR flux	1.00	$\Phi^{90} = 33.1$	$\Phi^{90} = 33.1$	$\Phi^{90} = 58.6$	$\Phi^{90} = 58.6$
Clusters of galaxies	5	Model A[c]	0.78			SF = 8.4	SF = 7.8
		Model B[c]				SF = 14.4	SF = 12.0
		Isobaric[c]				SF = 13.2	SF = 13.2
		Central AGN[c]				SF = 6.0	SF = 6.0

Notes. Median sensitivities and upper limits at 90% CL for ν_μ and $\nu_\mu + \nu_\tau$ fluxes are given in two ways: as Φ^{90} for a spectrum $d\Phi/dE \propto E^{-2}$, i.e., the total flux from all sources $d\Phi/dE \leqslant \Phi^{90}\ 10^{-12}\ \mathrm{TeV}^{-1}\ \mathrm{cm}^{-2}\ \mathrm{s}^{-1}(E/\mathrm{TeV})^{-2}$, or as a scaling factor (SF) relative to the models given in the footnotes. For example, if the Central AGN model flux normalization were 6.0 times higher, we would rule it out at 90% CL. All models predict equal fluxes of tau and muon neutrinos.
[a] Halzen et al. (2008).
[b] We did not calculate an a priori *p*-value for just the six SNR associations discussed in Halzen et al. (2008), since they are included in the search over all Milagro sources. However, some of these sources were the most significant on the list. Analyzed as a single subgroup, an a posteriori *p*-value of 0.02 was found with best-fit parameters $n_s = 15.2$ and $\gamma = 2.9$. The true trial factor is incalculable since this was done after unblinding, but these remain sources of interest for future searches.
[c] Murase et al. (2008), see Table 2.

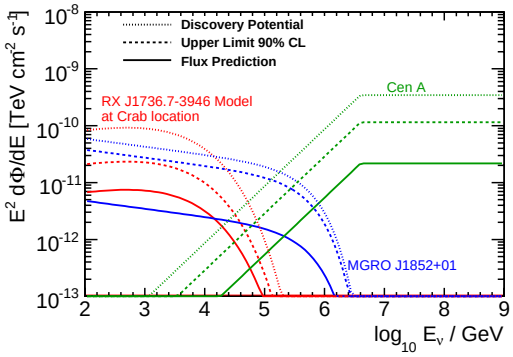

Figure 20. Differential flux of three theoretical models shown with the IceCube 40-string upper limit (90% CL) and discovery potential in each case. Shown are the $\nu_\mu + \bar{\nu}_\mu$ predictions of Morlino et al. (2009) for SNR RX J1713.7-3946 but moved to the location of the Crab Nebula, Halzen et al. (2008) for MGRO J1852+01, and Koers & Tinyakov (2008) for Cen A under the most optimistic condition, where the protons have a spectral index $\alpha_p = 3$.
(A color version of this figure is available in the online journal.)

Nebula ($\delta = 22.^\circ01$), we obtain an upper limit that rules out a flux 3.2 times higher than the prediction.

The Milagro hot spot MGRO J1852+01 is the brightest source of six SNR associations considered in Halzen et al. (2008). The stacking results were already shown in Table 4. Our upper limit for just this one brightest source is a factor of 7.9 away from excluding this model at 90% CL. The best fit for MGRO J1852+01 is to 7.0 events with $\gamma = 2.9$, which increases the upper limit compared to the average background-only case.

The nearest AGN, Centaurus A (Cen A), has been discussed as a potential source of ultra-high-energy CRs in the context of results from the Pierre Auger Observatory (PAO). The point-source likelihood fit at the location of Cen A resulted in zero signal events in this analysis, setting an upper limit that is 5.3 times higher than the ν_μ prediction by Koers & Tinyakov (2008) for the most optimistic case where the protons have a spectral index $\alpha_p = 3$.

Starburst galaxies were already presented as sources of interest in Section 6.4. Recent detections (Abdo et al. 2010; Acciari et al. 2009; Aharonian et al. 2005) of very high-energy photons from the nearest luminous starburst galaxies M82 and NGC 253, each characterized by star-forming regions with high supernova rates in the core, support the belief that the observed enhanced gamma-ray emission is due to CR interactions. Under the assumption that the GeV–TeV photons originate from the decay of neutral pions produced when protons that are shock-accelerated by SNRs in the starburst core inelastically scatter against target hydrogen atoms with densities of the order of $10^2\ \mathrm{cm}^{-3}$ (de Cea del Pozo et al. 2009; Persic et al. 2008), an order-of-magnitude calculation of the resulting flux of muon neutrinos based on Kelner et al. (2006) can be made. The muon neutrino upper limit from M82 is about 400 times higher than the rough prediction. For NGC 253 in the southern sky, the muon neutrino upper limit is about 6000 times higher than the prediction.

10. CONCLUSIONS

A search for sources of high-energy neutrinos has been performed using data taken during 2008–2009 with the 40-string configuration of the IceCube Neutrino Observatory. Five searches were performed: (1) a scan of the entire sky for point sources, (2) a predefined list of 39 interesting source candidates, (3) stacking 16 sources of TeV gamma rays observed by Milagro and Fermi, along with an unconfirmed hot spot (17 total sources), (4) stacking 127 starburst galaxies, and (5) stacking five nearby CGs, testing four different models for the CR distribution. The most significant result of the five searches came from the all-sky scan with a *p*-value of 18%. The cumulative binomial probability of obtaining at least one result of this significance or higher in five searches is 63%. This result is consistent with the null hypothesis of background only.

The sensitivity of this search using 375.5 days of 40-string data already improves upon previous point-source searches in the TeV–PeV energy range by at least a factor of two, depending on declination. The searches were performed using a data set of up-going atmospheric neutrinos (northern sky) and higher energy down-going muons (southern sky) in a unified manner. IceCube construction is now complete, with 86 strings in operation. The full IceCube detector should improve existing limits by at least another factor of two with one year of operation. Additional improvement is foreseeable

in the down-going region by developing sophisticated veto techniques and at lower energies by using the new dense subarray, DeepCore, to its fullest potential.

We thank K. Murase for helpful discussions regarding clusters of galaxies.

We acknowledge the support from the following agencies: U.S. National Science Foundation–Office of Polar Programs, U.S. National Science Foundation–Physics Division, University of Wisconsin Alumni Research Foundation, the Grid Laboratory Of Wisconsin (GLOW) grid infrastructure at the University of Wisconsin-Madison, the Open Science Grid (OSG) grid infrastructure; U.S. Department of Energy, and National Energy Research Scientific Computing Center, the Louisiana Optical Network Initiative (LONI) grid computing resources; National Science and Engineering Research Council of Canada; Swedish Research Council, Swedish Polar Research Secretariat, Swedish National Infrastructure for Computing (SNIC), and Knut and Alice Wallenberg Foundation, Sweden; German Ministry for Education and Research (BMBF), Deutsche Forschungsgemeinschaft (DFG), Research Department of Plasmas with Complex Interactions (Bochum), Germany; Fund for Scientific Research (FNRS-FWO), FWO Odysseus Programme, Flanders Institute to encourage scientific and technological research in industry (IWT), Belgian Federal Science Policy Office (Belspo); University of Oxford, UK; Marsden Fund, New Zealand; Japan Society for Promotion of Science (JSPS); the Swiss National Science Foundation (SNSF), Switzerland; A. Groß acknowledges support by the EU Marie Curie OIF Program; J. P. Rodrigues acknowledges support by the Capes Foundation, Ministry of Education of Brazil.

REFERENCES

Abbasi, R. U., et al. 2006, ApJ, 636, 680
Abbasi, R., et al. 2009a, Phys. Rev. Lett., 103, 221102
Abbasi, R., et al. 2009b, ApJ, 701, L47
Abbasi, R., et al. 2009c, Phys. Rev., D79, 062001
Abbasi, R., et al. 2009d, Nucl. Instrum. Methods, A601, 294
Abbasi, R., et al. 2010a, Nucl. Instrum. Methods, A618, 139
Abbasi, R., et al. 2010b, Phys. Rev., D83, 012001
Abdo, A. A., et al. 2007, ApJ, 664, L91
Abdo, A. A., et al. 2009, ApJ, 700, L127
Abdo, A. A., et al. 2010, ApJ, 709, L152
Acciari, V. A., et al. 2009, Nature, 462, 770
Achterberg, A., et al. 2006a, Astropart. Phys., 26, 155
Achterberg, A., et al. 2006b, Astropart. Phys., 26, 282
Achterberg, A., et al. 2007, Phys. Rev., D75, 102001
Ackermann, M., & Bernardini, E. 2005, in Proc. 29th ICRC, Pune, arXiv: astro-ph/0509330
Ackermann, M., et al. 2006, J. Geophys. Res., 111, D13203
Aharonian, F., et al. 2005, A&A, 442, 177
Ahn, E.-J., Engel, R., Gaisser, T. K., Lipari, P., & Stanev, T. 2009, Phys. Rev., D80, 094003
Ahrens, J., et al. 2004, Nucl. Instrum. Methods, A524, 169
Ambrosio, M., et al. 2001, ApJ, 546, 1038
Amsler, C., et al. 2008, Phys. Lett., B667, 1
Anchordoqui, L. A., & Montaruli, T. 2010, Ann. Rev. Nucl. Part. Sci., 60, 129
Athar, H., Jezabek, M., & Yasuda, O. 2000, Phys. Rev., D62, 103007
Barr, G. D., Gaisser, T. K., Lipari, P., Robbins, S., & Stanev, T. 2004, Phys. Rev., D70, 023006
Barr, G. D., Gaisser, T. K., Robbins, S., & Stanev, T. 2006, Phys. Rev., D74, 094009
Beacom, J. F., & Kistler, M. D. 2007, Phys. Rev., D75, 083001
Becker, J. K. 2008, Phys. Rep., 458, 173
Becker, J. K., Biermann, P. L., Dreyer, J., & Kneiske, T. M. 2009, arXiv:0901.1775
Bednarek, W., Burgio, G. F., & Montaruli, T. 2005, New Astron. Rev., 49, 1
Berezinsky, V. S., Blasi, P., & Ptuskin, V. S. 1997, ApJ, 487, 529
Berghaus, P., Birdsall, R., Desiati, P., Montaruli, T., & Ranft, J. 2008, J. Phys. Conf. Ser., 136, 042019
Boettcher, M., Reimer, A., & Marscher, A. 2009, ApJ, 703, 1168
Braun, J., Dumm, J., De Palma, F., Finley, C., Karle, A., & Montaruli, T. 2008, Astropart. Phys., 29, 299
Bugaev, E., Naumov, V., Sinegovsky, S., & Zaslavskaya, E. 1989, Nuovo Cim., C12, 41
Caprioli, D., Amato, E., & Blasi, P. 2010, Astropart. Phys., 33, 160
Chiarusi, T., & Spurio, M. 2010, Eur. Phys. J., C65, 649
Chirkin, D., & Rhode, W. 2004, arXiv:hep-ph/0407075
Colafrancesco, S., & Blasi, P. 1998, Astropart. Phys., 9, 227
Conrad, J., Botner, O., Hallgren, A., & Perez de los Heros, C. 2003, Phys. Rev., D67, 012002
Coyle, P. 2010, in Proc. 31st ICRC, Lodz
de Cea del Pozo, E., Torres, D. F., & Marrero, A. Y. R. 2009, ApJ, 698, 1054
Enberg, R., Reno, M. H., & Sarcevic, I. 2008, Phys. Rev., D78, 043005
Enberg, R., Reno, M. H., & Sarcevic, I. 2009, Phys. Rev., D79, 053006
Feldman, G. J., & Cousins, R. D. 1998, Phys. Rev., D57, 3873
Fermi, E. 1949, Phys. Rev., 75, 1169
Gaisser, T. K., Halzen, F., & Stanev, T. 1995, Phys. Rep., 258, 173
Gazizov, A., & Kowalski, M. P. 2005, Comput. Phys. Commun., 172, 203
Glasstetter, R., & Hoerandel, J. 1999, Nucl. Phys., 75, 238
Gonzalez-Garcia, M. C., Halzen, F., & Mohapatra, S. 2009, Astropart. Phys., 31, 437
Halzen, F., & Hooper, D. 2002, Rep. Prog. Phys., 65, 1025
Halzen, F., Kappes, A., & O'Murchadha, A. 2008, Phys. Rev., D78, 063004
Halzen, F., Kappes, A., & O'Murchadha, A. 2009, Phys. Rev., D80, 083009
Heck, D., et al. 1998, FZKA-6019
Hill, G. C. 2003, Phys. Rev., D67, 118101
Hoerandel, J. R. 2003, Astropart. Phys., 19, 193
Honda, M., Kajita, T., Kasahara, K., Midorikawa, S., & Sanuki, T. 2007, Phys. Rev., D75, 043006
Kang, H., Rachen, J. P., & Biermann, P. L. 1997, MNRAS, 286, 257
Kashti, T., & Waxman, E. 2005, Phys. Rev. Lett., 95, 181101
Kelner, S. R., Aharonian, F. A., & Bugayov, V. V. 2006, Phys. Rev. D 74, 034018
Koers, H. B. J., & Tinyakov, P. 2008, Phys. Rev., D78, 083009
Kotera, K., Allard, D., Murase, K., Aoi, J., Dubois, Y., Pierog, T., & Nagataki, S. 2009, ApJ, 707, 370
Lai, H. L., Huston, J., Kuhlmann, S., Morfin, J., Olness, F., Owens, J. F., Pumplin, J., & Tung, W. K. 2000, Eur. Phys. J., C12, 375
Learned, J. G., & Mannheim, K. 2000, Ann. Rev. Nucl. Part. Sci., 50, 679
Lipari, P. 2006, Nucl. Instrum. Methods, A567, 405
Lundberg, J., et al. 2007, Nucl. Instrum. Methods, A581, 619
Markov, M. A., & Zheleznykh, I. M. 1961, Nucl. Phys., 27, 385
Martin, A. D., Ryskin, M. G., & Stasto, A. M. 2003, Acta Phys. Polon., B34, 3273
Morlino, G., Blasi, P., & Amato, E. 2009, Astropart. Phys., 31, 376
Murase, K., Inoue, S., & Nagataki, S. 2008, ApJ, 689, L105
Neunhoffer, T. 2006, Astropart. Phys., 25, 220
Norman, C. A., Melrose, D. B., & Achterberg, A. 1995, ApJ, 454, 60
Persic, M., Rephaeli, Y., & Arieli, Y. 2008, A&A, 486, 143
Pfrommer, C., & Ensslin, T. A. 2004, A&A, 426, 777
Reiprich, T. H., & Boehringer, H. 2002, ApJ, 567, 716
Thrane, E., et al. 2009, ApJ, 704, 503
Tilav, S., et al. 2010, in Proc. 30st ICRC, Lodz, arXiv:1001.0776

Measurement of the atmospheric neutrino energy spectrum from 100 GeV to 400 TeV with IceCube

R. Abbasi,[28] Y. Abdou,[22] T. Abu-Zayyad,[33] J. Adams,[16] J. A. Aguilar,[28] M. Ahlers,[32] K. Andeen,[28] J. Auffenberg,[39] X. Bai,[31] M. Baker,[28] S. W. Barwick,[24] R. Bay,[7] J. L. Bazo Alba,[40] K. Beattie,[8] J. J. Beatty,[18,19] S. Bechet,[13] J. K. Becker,[10] K.-H. Becker,[39] M. L. Benabderrahmane,[40] S. BenZvi,[28] J. Berdermann,[40] P. Berghaus,[28] D. Berley,[17] E. Bernardini,[40] D. Bertrand,[13] D. Z. Besson,[26] M. Bissok,[1] E. Blaufuss,[17] J. Blumenthal,[1] D. J. Boersma,[1] C. Bohm,[34] D. Bose,[14] S. Böser,[11] O. Botner,[37] J. Braun,[28] S. Buitink,[8] M. Carson,[22] D. Chirkin,[28] B. Christy,[17] J. Clem,[31] F. Clevermann,[20] S. Cohen,[25] C. Colnard,[23] D. F. Cowen,[36,35] M. V. D'Agostino,[7] M. Danninger,[34] J. C. Davis,[18] C. De Clercq,[14] L. Demirörs,[25] O. Depaepe,[14] F. Descamps,[22] P. Desiati,[28] G. de Vries-Uiterweerd,[22] T. DeYoung,[36] J. C. Díaz-Vélez,[28] M. Dierckxsens,[13] J. Dreyer,[10] J. P. Dumm,[28] M. R. Duvoort,[38] R. Ehrlich,[17] J. Eisch,[28] R. W. Ellsworth,[17] O. Engdegård,[37] S. Euler,[1] P. A. Evenson,[31] O. Fadiran,[4] A. R. Fazely,[6] A. Fedynitch,[10] T. Feusels,[22] K. Filimonov,[7] C. Finley,[34] M. M. Foerster,[36] B. D. Fox,[36] A. Franckowiak,[11] R. Franke,[40] T. K. Gaisser,[31] J. Gallagher,[27] M. Geisler,[1] L. Gerhardt,[8,7] L. Gladstone,[28] T. Glüsenkamp,[1] A. Goldschmidt,[8] J. A. Goodman,[17] D. Grant,[21] T. Griesel,[29] A. Groß,[16,23] S. Grullon,[28] M. Gurtner,[39] C. Ha,[36] A. Hallgren,[37] F. Halzen,[28] K. Han,[16] K. Hanson,[13,28] K. Helbing,[39] P. Herquet,[30] S. Hickford,[16] G. C. Hill,[28] K. D. Hoffman,[17] A. Homeier,[11] K. Hoshina,[28] D. Hubert,[14] W. Huelsnitz,[17,*] J.-P. Hülß,[1] P. O. Hulth,[34] K. Hultqvist,[34] S. Hussain,[31] A. Ishihara,[15] J. Jacobsen,[28] G. S. Japaridze,[4] H. Johansson,[34] J. M. Joseph,[8] K.-H. Kampert,[39] A. Kappes,[9] T. Karg,[39] A. Karle,[28] J. L. Kelley,[28] N. Kemming,[9] P. Kenny,[26] J. Kiryluk,[8,7] F. Kislat,[40] S. R. Klein,[8,7] J.-H. Köhne,[20] G. Kohnen,[30] H. Kolanoski,[9] L. Köpke,[29] D. J. Koskinen,[36] M. Kowalski,[11] T. Kowarik,[29] M. Krasberg,[28] T. Krings,[1] G. Kroll,[29] K. Kuehn,[18] T. Kuwabara,[31] M. Labare,[14] S. Lafebre,[36] K. Laihem,[1] H. Landsman,[28] M. J. Larson,[36] R. Lauer,[40] R. Lehmann,[9] J. Lünemann,[29] J. Madsen,[33] P. Majumdar,[40] A. Marotta,[13] R. Maruyama,[28] K. Mase,[15] H. S. Matis,[8] M. Matusik,[39] K. Meagher,[17] M. Merck,[28] P. Mészáros,[35,36] T. Meures,[1] E. Middell,[40] N. Milke,[20] J. Miller,[37] T. Montaruli,[28,†] R. Morse,[28] S. M. Movit,[35] R. Nahnhauer,[40] J. W. Nam,[24] U. Naumann,[39] P. Nießen,[31] D. R. Nygren,[8] S. Odrowski,[23] A. Olivas,[17] M. Olivo,[37,10] A. O'Murchadha,[28] M. Ono,[15] S. Panknin,[11] L. Paul,[1] C. Pérez de los Heros,[37] J. Petrovic,[13] A. Piegsa,[29] D. Pieloth,[20] R. Porrata,[7] J. Posselt,[39] P. B. Price,[7] M. Prikockis,[36] G. T. Przybylski,[8] K. Rawlins,[3] P. Redl,[17] E. Resconi,[23] W. Rhode,[20] M. Ribordy,[25] A. Rizzo,[14] J. P. Rodrigues,[28] P. Roth,[17] F. Rothmaier,[29] C. Rott,[18] T. Ruhe,[20] D. Rutledge,[36] B. Ruzybayev,[31] D. Ryckbosch,[22] H.-G. Sander,[29] M. Santander,[28] S. Sarkar,[32] K. Schatto,[29] S. Schlenstedt,[40] T. Schmidt,[17] A. Schukraft,[1] A. Schultes,[39] O. Schulz,[23] M. Schunck,[1] D. Seckel,[31] B. Semburg,[39] S. H. Seo,[34] Y. Sestayo,[23] S. Seunarine,[12] A. Silvestri,[24] K. Singh,[14] A. Slipak,[36] G. M. Spiczak,[33] C. Spiering,[40] M. Stamatikos,[18,‡] T. Stanev,[31] G. Stephens,[36] T. Stezelberger,[8] R. G. Stokstad,[8] S. Stoyanov,[31] E. A. Strahler,[14] T. Straszheim,[17] G. W. Sullivan,[17] Q. Swillens,[13] H. Taavola,[37] I. Taboada,[5] A. Tamburro,[33] O. Tarasova,[40] A. Tepe,[5] S. Ter-Antonyan,[6] S. Tilav,[31] P. A. Toale,[36] S. Toscano,[28] D. Tosi,[40] D. Turčan,[17] N. van Eijndhoven,[14] J. Vandenbroucke,[7] A. Van Overloop,[22] J. van Santen,[28] M. Voge,[23] B. Voigt,[40] C. Walck,[34] T. Waldenmaier,[9] M. Wallraff,[1] M. Walter,[40] Ch. Weaver,[28] C. Wendt,[28] S. Westerhoff,[28] N. Whitehorn,[28] K. Wiebe,[29] C. H. Wiebusch,[1] G. Wikström,[34] D. R. Williams,[2] R. Wischnewski,[40] H. Wissing,[17] M. Wolf,[23] K. Woschnagg,[7] C. Xu,[31] X. W. Xu,[6] G. Yodh,[24] S. Yoshida,[15] and P. Zarzhitsky[2]

(IceCube Collaboration)

[1]*III. Physikalisches Institut, RWTH Aachen University, D-52056 Aachen, Germany*
[2]*Department of Physics and Astronomy, University of Alabama, Tuscaloosa, Alabama 35487, USA*
[3]*Department of Physics and Astronomy, University of Alaska Anchorage, 3211 Providence Drive, Anchorage, Alaska 99508, USA*
[4]*CTSPS, Clark-Atlanta University, Atlanta, Georgia 30314, USA*
[5]*School of Physics and Center for Relativistic Astrophysics, Georgia Institute of Technology, Atlanta, Georgia 30332, USA*
[6]*Department of Physics, Southern University, Baton Rouge, Louisiana 70813, USA*
[7]*Department of Physics, University of California, Berkeley, California 94720, USA*
[8]*Lawrence Berkeley National Laboratory, Berkeley, California 94720, USA*
[9]*Institut für Physik, Humboldt-Universität zu Berlin, D-12489 Berlin, Germany*
[10]*Fakultät für Physik und Astronomie, Ruhr-Universität Bochum, D-44780 Bochum, Germany*
[11]*Physikalisches Institut, Universität Bonn, Nussallee 12, D-53115 Bonn, Germany*
[12]*Department of Physics, University of the West Indies, Cave Hill Campus, Bridgetown BB11000, Barbados*
[13]*Université Libre de Bruxelles, Science Faculty CP230, B-1050 Brussels, Belgium*
[14]*Vrije Universiteit Brussel, Dienst ELEM, B-1050 Brussels, Belgium*

[15]*Department of Physics, Chiba University, Chiba 263-8522, Japan*
[16]*Department of Physics and Astronomy, University of Canterbury, Private Bag 4800, Christchurch, New Zealand*
[17]*Department of Physics, University of Maryland, College Park, Maryland 20742, USA*
[18]*Department of Physics and Center for Cosmology and AstroParticle Physics, Ohio State University, Columbus, Ohio 43210, USA*
[19]*Department of Astronomy, Ohio State University, Columbus, Ohio 43210, USA*
[20]*Department of Physics, TU Dortmund University, D-44221 Dortmund, Germany*
[21]*Department of Physics, University of Alberta, Edmonton, Alberta, Canada T6G 2G7*
[22]*Department of Subatomic and Radiation Physics, University of Gent, B-9000 Gent, Belgium*
[23]*Max-Planck-Institut für Kernphysik, D-69177 Heidelberg, Germany*
[24]*Department of Physics and Astronomy, University of California, Irvine, California 92697, USA*
[25]*Laboratory for High Energy Physics, École Polytechnique Fédérale, CH-1015 Lausanne, Switzerland*
[26]*Department of Physics and Astronomy, University of Kansas, Lawrence, Kansas 66045, USA*
[27]*Department of Astronomy, University of Wisconsin, Madison, Wisconsin 53706, USA*
[28]*Department of Physics, University of Wisconsin, Madison, Wisconsin 53706, USA*
[29]*Institute of Physics, University of Mainz, Staudinger Weg 7, D-55099 Mainz, Germany*
[30]*Université de Mons, 7000 Mons, Belgium*
[31]*Bartol Research Institute and Department of Physics and Astronomy, University of Delaware, Newark, Delaware 19716, USA*
[32]*Department of Physics, University of Oxford, 1 Keble Road, Oxford OX1 3NP, United Kingdom*
[33]*Department of Physics, University of Wisconsin, River Falls, Wisconsin 54022, USA*
[34]*Oskar Klein Centre and Department of Physics, Stockholm University, SE-10691 Stockholm, Sweden*
[35]*Department of Astronomy and Astrophysics, Pennsylvania State University, University Park, Pennsylvania 16802, USA*
[36]*Department of Physics, Pennsylvania State University, University Park, Pennsylvania 16802, USA*
[37]*Department of Physics and Astronomy, Uppsala University, Box 516, S-75120 Uppsala, Sweden*
[38]*Department of Physics and Astronomy, Utrecht University/SRON, NL-3584 CC Utrecht, The Netherlands*
[39]*Department of Physics, University of Wuppertal, D-42119 Wuppertal, Germany*
[40]*DESY, D-15735 Zeuthen, Germany*

(Received 20 October 2010; published 5 January 2011)

A measurement of the atmospheric muon neutrino energy spectrum from 100 GeV to 400 TeV was performed using a data sample of about 18 000 up-going atmospheric muon neutrino events in IceCube. Boosted decision trees were used for event selection to reject misreconstructed atmospheric muons and obtain a sample of up-going muon neutrino events. Background contamination in the final event sample is less than 1%. This is the first measurement of atmospheric neutrinos up to 400 TeV, and is fundamental to understanding the impact of this neutrino background on astrophysical neutrino observations with IceCube. The measured spectrum is consistent with predictions for the atmospheric $\nu_\mu + \bar{\nu}_\mu$ flux.

DOI: 10.1103/PhysRevD.83.012001 PACS numbers: 95.55.Vj, 14.60.Lm, 29.40.Ka, 95.85.Ry

I. INTRODUCTION

The IceCube neutrino telescope [1], currently under construction in the glacial ice at the South Pole, is capable of detecting high energy neutrinos of all three flavors. In particular, charged current (CC) interactions between ν_μ or $\bar{\nu}_\mu$ and nucleons in the ice produce muons. IceCube detects the Cherenkov radiation produced as these muons propagate and undergo radiative losses. By reconstructing the muon's track and energy loss, the direction and energy of the incident neutrino can be inferred.

Atmospheric neutrinos are produced in the decay chains of particles created by the interaction of cosmic rays with the Earth's atmosphere [2–4]. IceCube has an unprecedented high-statistics, high energy reach for these atmospheric neutrinos. Hence, IceCube can be used to test predictions for the flux of atmospheric neutrinos at high energies, including the uncertain contribution from charm production above about 100 TeV. The atmospheric neutrino flux can also be used to verify that the IceCube detector is performing as expected [5]. Understanding the energy and zenith dependence of the atmospheric neutrino flux in IceCube is important since this is an irreducible background for searches for a diffuse flux, or for point sources, of astrophysical neutrinos.

This analysis used data taken from April 2008 to May 2009, while IceCube was operating in a 40-string configuration. The signal events were up-going atmospheric ν_μ and $\bar{\nu}_\mu$ interactions. The background was down-going atmospheric muons that were misreconstructed as up-going. An as-yet-unmeasured but anticipated diffuse flux of astrophysical neutrinos was ignored. Predictions for this flux are negligible compared to predictions for the atmospheric neutrino flux, over most of the energy range for this

*Corresponding author: whuelsnitz@icecube.umd.edu
†Also at Sezione INFN, Dipartimento di Fisica, I-70126, Bari, Italy
‡Also at NASA Goddard Space Flight Center, Greenbelt, Maryland 20771, USA

analysis, and it can readily be accommodated within the reported uncertainties.

Boosted decision trees (BDTs) were used to obtain an event sample with negligible background contamination. An unfolding of the atmospheric neutrino energy spectrum, over the neutrino energy range 100 GeV to 400 TeV, was performed. Systematic uncertainties in the unfolded spectrum were estimated and highlight the efforts that are underway to reduce systematic uncertainties in neutrino measurements with IceCube.

We will briefly review the production and distribution of atmospheric neutrinos in Sec. II. In Sec. III, we will discuss the IceCube detector, and the detection of muon neutrino events in IceCube. Event reconstruction and event selection specific to this analysis will be discussed in Sec. IV. The unfolding analysis and systematic uncertainties will be discussed in Sec. V. In Sec. VI, we will discuss the implications of the unfolded result.

II. ATMOSPHERIC NEUTRINOS

Cosmic rays are high energy particles, mostly protons and helium nuclei, but also heavier ionized nuclei, that are believed to be accelerated in various astrophysical phenomena [6,7]. Possible cosmic ray production sites include active galactic nuclei, gamma ray bursts, and supernova explosions. Detecting astrophysical neutrinos, produced in conjunction with cosmic rays at point sources such as these, is one of the primary goals of IceCube. The energy spectrum of cosmic rays is rather steep, $dN/dE \propto E^{-2.7}$, and steepens to $dN/dE \propto E^{-3}$ above the "knee," or about 10^6 GeV [7]. A possible second knee is a steepening to about $E^{-3.2}$ above 5×10^8 GeV [8]. A further kink in the spectrum has been observed at $\sim 3 \times 10^9$ GeV, where the spectrum flattens to $dN/dE \propto E^{-2.7}$ again. The event sample for this analysis is primarily the result of interactions of cosmic rays with energies below the first knee.

Hadronic interactions between cosmic rays and particles in the Earth's atmosphere produce large numbers of mesons, primarily pions and kaons. Hundreds or even thousands of these mesons can be produced in the shower that follows the interaction of a single high energy cosmic ray. Neutrinos are produced in the leptonic or semileptonic decays of charged pions or kaons, as well as in the subsequent decay of the muons. Neutrinos from muon decay are important up to a few GeV. Pions and kaons that decay in-flight are the primary source of atmospheric muon neutrinos from a few GeV up to about 100 TeV. With rest-frame lifetimes on the order of 10^{-8} s, these mesons often lose some of their energy in collisions prior to decaying, leading to lower energy neutrinos among the decay products. Hence, the spectral slope of this "conventional" atmospheric neutrino flux [2,3] asymptotically becomes one power steeper than that of the primary cosmic ray spectrum. Theoretical uncertainties in predictions for the conventional flux are dominated by uncertainties in the normalization and spectral distribution of the cosmic ray flux. Additional uncertainties include the ratio of pions to kaons produced by cosmic ray interactions, which affects the zenith angle distribution, particularly near the horizon.

At sufficiently high energies, another production mechanism is possible. The "prompt" atmospheric neutrino flux [9–11] is made up of neutrinos produced in the semileptonic decays of charmed mesons and baryons. These particles decay almost immediately (rest-frame lifetimes on the order of 10^{-12} s), before losing energy in collisions. Hence, the spectrum for the prompt flux more closely follows the cosmic ray spectrum and is about one power harder than the conventional flux at high energy. The prompt flux has not yet been measured, but is expected to be important above about 100 TeV [9,12]. Just like the conventional flux, predictions for the prompt flux are impacted by uncertainties in the normalization and spectral distribution of the cosmic ray flux. Additional sources of uncertainty for the prompt flux include charm production cross sections [13] and fragmentation functions, which have not been measured at these energies in accelerator experiments. Figure 1 shows the predicted flux of conventional and prompt atmospheric muon neutrinos [3,9].

Although high energy cosmic rays arrive almost isotropically, with deviations less than 0.1% [14], the zenith angle dependence of high energy atmospheric neutrino production is complicated by the direction of the shower through the atmosphere. The energy spectrum of nearly

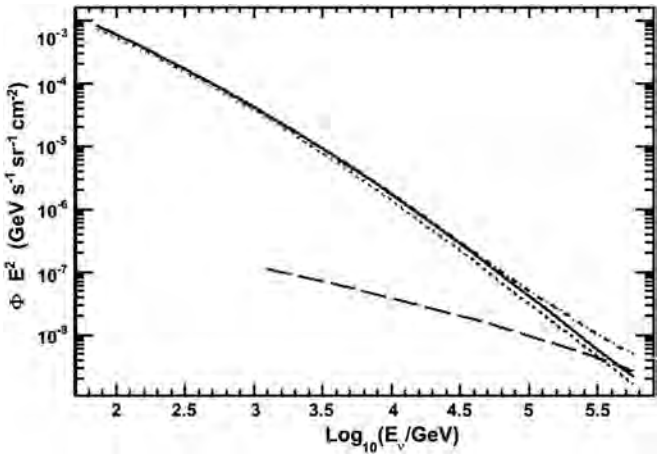

FIG. 1. The predicted flux of atmospheric muon neutrinos. The solid line is the conventional $\nu_\mu + \bar{\nu}_\mu$ flux [3], averaged over the zenith range 90° to 180°. The long-dashed line is the prompt $\nu_\mu + \bar{\nu}_\mu$ flux [9], also averaged over the zenith range 90° to 180°. The dot-dashed curve is the sum of the conventional and prompt models. The flux predictions from [3] were extended to higher energies as discussed in Sec. III C. For reasons discussed in Sec. V B, the zenith region from 90° to 97° was not used in the analysis. The zenith-averaged conventional flux, for the range 97° to 180°, is shown in the figure as the short-dashed line. The prediction for the zenith-averaged prompt flux is not affected by this change in angular region.

horizontal conventional atmospheric neutrinos is flatter than that of almost vertical neutrinos because pions and kaons in inclined showers spend more time in the tenuous atmosphere where they are more likely to decay before losing energy in collisions. Additionally, attenuation of the neutrino flux by the Earth is a function of energy and zenith angle. Above about 10 TeV, attenuation of the neutrino flux in the Earth is important, and it affects the zenith and energy dependence of the flux at the detector.

III. NEUTRINO DETECTION WITH ICECUBE

A. The IceCube detector

IceCube [1,15] is able to detect neutrinos over a wide energy range, from about 100 GeV to more than 10^9 GeV. The design is a balance between energy resolution, angular resolution, energy range, and cost, and was driven by the goal of detecting astrophysical neutrino point sources, which are believed to be correlated with cosmic ray production sites. A large detector is required as a result of the extremely small cross sections for neutrino interactions, as well as the low fluxes expected for astrophysical neutrinos.

When completed in 2011, IceCube will comprise 86 strings, with 5160 photomultiplier tubes (PMT). Each string includes 60 digital optical modules (DOM). A DOM is a single PMT and associated electronics in a glass pressure sphere. The instrumented part of the array extends from 1450 m to 2450 m below the surface of the ice. Horizontally, 78 of the strings are 125 m apart and spread out in a triangular grid over a square kilometer, so that the entire instrumented volume will be 1 km^3 of ice. Vertical DOM spacing is a uniform 17 m for these 78 strings. A subset of the detector, known as ''DeepCore,'' consists of eight specialized and closely spaced strings of sensors located around the center IceCube string.

Figure 2 shows the IceCube observatory and its component arrays. This analysis used data from 359 days of live time while operating in a 40-string configuration, from April 2008 to May 2009. Figure 3 shows an overhead view of the layout of the 40-string configuration, which was roughly twice as long in one horizontal direction as in the other.

At the heart of each DOM is a 10 in. (25 cm) Hamamatsu PMT [16] (see Fig. 4). A single Cherenkov photon arriving at a DOM and producing a photoelectron is defined as a hit. DOM main board electronics [17] apply a threshold trigger to the PMT analog output. This threshold is equivalent to 0.25 of the signal generated by a photoelectron, after amplification by the PMT. When this threshold is exceeded, local coincidence checks between this DOM and nearest neighbor or next-to-nearest neighbor DOMs on a string are performed to reduce false triggers that result from dark noise. If a nearest or next-to-nearest neighbor DOM also has a detection above threshold within a ± 1000 ns window, the PMT total charge waveforms are digitized, time stamped, and sent to the surface. The digitized waveform from a DOM can contain several pulses, and each pulse can be the result of multiple photoelectrons. The simple majority trigger for building an event is eight hit DOMs within a 5000 ns trigger window.

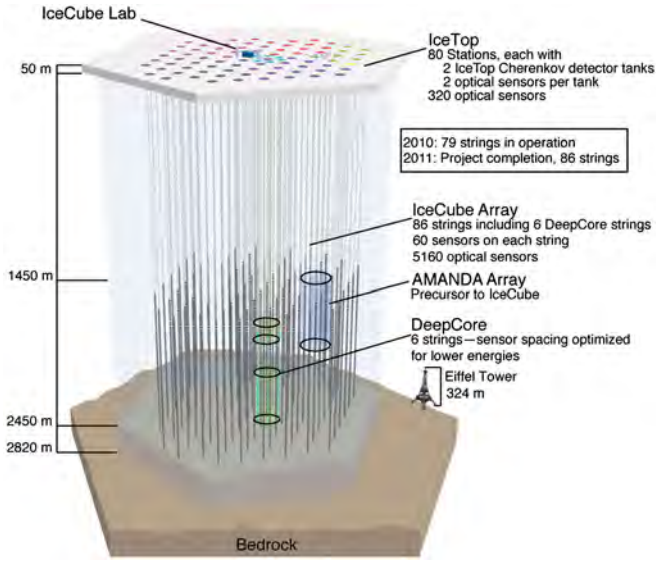

FIG. 2 (color online). IceCube Neutrino Observatory and its component arrays.

The data rate from the data acquisition system at the South Pole far exceeds the amount of data that can be transmitted via satellite. Hence, a significant reduction in the trigger-level data must be accomplished with software-based filtering at the South Pole. A cluster of processors performs a variety of fast reconstructions on the data, and applies multiple software-based filters to the results. These filters either reject events that are uninteresting background events, or extract particular classes of events. Events are sent to a buffer if they pass one or more of the filters. The

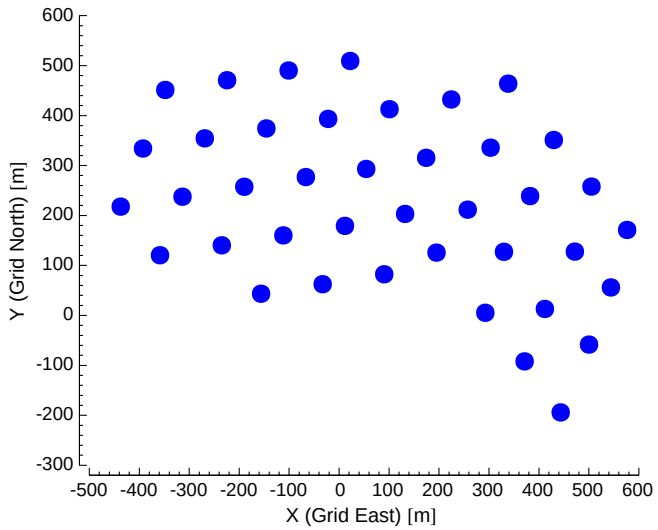

FIG. 3 (color online). Overhead view of IceCube 40 string configuration.

transfer of data from this buffer over a communications satellite is handled by the South Pole Archival and Data Exchange (SPADE) system.

The deep glacial ice at the South Pole is optically transparent, making it an ideal medium for a large-volume Cherenkov detector. The ice sheet is just over 2800 m thick and was created over a period of roughly 165 000 years [18]. It serves multiple roles: a stable platform for the DOMs, the target medium for neutrino interactions, the propagation and detection medium for Cherenkov photons produced by charged particles, and an overburden for attenuation of down-going atmospheric muons. Upward moving particles will have had to result from particles that penetrated the Earth and can readily be identified as resulting from neutrino interactions.

Optical properties of the ice are discussed in [19–21]. Scattering and absorption of photons in the ice is caused by bubbles, dust particles, and crystal defects. Below about 1400 m, the ice is essentially free of bubbles, and scattering is dominated by dust. Micron-sized dust grains were carried as wind-borne aerosols during the periods of ice formation, and deposited in the ice. Variations with depth are due to the periodic build up of dust that resulted from the prevailing atmospheric conditions when the layers of ice were being formed.

The depth and wavelength dependence of scattering and absorption as measured in the ice around the AMANDA detector is discussed in Ref. [19]. Now surrounded by IceCube and no longer operating, AMANDA was the predecessor and prototype for IceCube. Ice properties were extrapolated to lower depths using ice core measurements taken at Vostok Station and Dome Fuji in Antarctica, and then scaled to the location of IceCube using an age vs depth relationship [18]. Studies are ongoing that use LEDs on flasher boards within each DOM to directly measure ice properties in the deepest ice instrumented by IceCube.

B. Muon neutrino detection

Muon neutrinos undergoing CC interactions in the ice produce muons. The muons on average carry about 75% of the initial neutrino energy [22]. Simulation studies indicate that muon angular resolution is typically between 0.5° and 1°, depending on the angle of incidence and the muon energy. The energy loss per meter, for a muon propagating through the ice, is related to its energy [6]:

$$-\left\langle \frac{dE}{dX} \right\rangle = \alpha(E) + \beta(E)E, \tag{1}$$

where E is the muon energy, $\alpha \approx 0.24$ GeV/m is the ionization energy loss per unit propagation length, and $\beta \approx 3.3 \times 10^{-4}$ m^{-1} is the radiative energy loss through bremsstrahlung, pair production, and photonuclear scattering. (α and β are both weak functions of energy.) For muon energies less than about a TeV, energy loss is dominated by ionization, and the light produced is nearly independent of energy. However, for higher energy muons, there are many stochastic interactions along the muon's path and there is a linear relationship between the energy loss per meter and the muon energy. Most of the Cherenkov light emitted along the muon's path comes from the secondary particles produced in radiative losses. An estimation of dE/dX, based on the amount of detected light, the event geometry, and the ice properties, was used in the energy spectrum unfolding discussed in Sec. V. The energy of individual events was not estimated. Rather, the distribution of neutrino energies was directly inferred from the distribution of reconstructed muon dE/dX values.

The detection rate for high energy ν_μ ($\bar{\nu}_\mu$) is aided by the fact that the CC interaction cross section, as well as the range of the resultant muon, are proportional to the neutrino energy. High energy muons have a significant path length and can reach the detector even if produced outside of the detector, hence increasing the effective volume. Muons in earth or ice can have a track length from several tens of meters, up to several kilometers, depending on the muon energy and the detection threshold. The average track length, before the muon energy falls below a detection threshold E_μ^{th}, is given by:

$$x_\mu = \frac{1}{\beta} \ln\left[\frac{\alpha + \beta E_\mu}{\alpha + \beta E_\mu^{\text{th}}}\right], \tag{2}$$

where E_μ is the initial muon energy.

C. Simulation

Simulation of atmospheric muons and neutrinos was used for determining event selection and background rejection cuts. Simulation was also used for the response matrix (discussed in Sec. V) and the predicted dE/dX distribution for the unfolding analysis. Several specialized simulated data sets were used for systematics studies and toy Monte Carlo (MC) studies.

Muons from air showers were simulated with CORSIKA [23]. The primary cosmic ray energy spectrum known as the Hörandel polygonato model [8] was used. In this model, the spectrum of each component is a combination of two power laws, with the turnover between the two power laws being a function of the nuclear charge Z of the primary cosmic ray. CORSIKA propagates cosmic ray primaries (up to Fe) to their point of interaction with a nucleus in the atmosphere. Hadronic interactions in the atmosphere were modeled using the interaction model SIBYLL [24]. Secondary particles were then tracked until they interacted or decayed. Coincident muons in the detector, originating from separate cosmic ray events, were accounted for by combining simulated events and reweighting them to account for the probability of coincident events occurring.

Muon propagation and energy loss within and around the detector was simulated with the program MMC (Muon Monte Carlo) [25]. MMC accounts for ionization,

bremsstrahlung, photonuclear interactions, and pair production. In addition to muon tracks and energies, secondary particles from the stochastic energy losses are included in the output of MMC. The production and propagation of Cherenkov light from the muons and secondary particles was simulated using the program PHOTONICS [26], which accounts for the depth-dependent scattering and absorption properties of the ice. Direct tracking of Cherenkov photons through the layered glacial ice was too computationally intensive for simulation production. PHOTONICS was run beforehand to create lookup tables which were then used during the detector simulation. The tables included light yield and photon propagation time distributions at a given location in the ice from a given source type and location. Simulation of the detector response to electromagnetic and hadronic showers (so-called cascade events) also used pretabulated light yield tables and photon propagation time information generated by PHOTONICS. An energy-dependent scaling factor was applied for hadronic cascades, to account for the fact that hadronic cascades produce less Cherenkov light than their electromagnetic counterparts [27].

Neutrino propagation from point of origin in the atmosphere to interaction in or near the detector was simulated with ANIS [28]. ANIS generates neutrinos of any flavor according to a specified flux, propagates them through the Earth, and in a final step simulates neutrino interactions within a specified volume. All simulated neutrinos were forced to interact, but their probability of interacting was included in the event weight assigned by ANIS. ANIS accounts for CC and neutral current (NC) neutrino-nucleon interactions, as well as neutrino regeneration following NC interactions. Also accounted for is the offset between neutrino propagation direction and the direction of the outgoing muon following a CC interaction. Cross sections for ν_μ and $\bar{\nu}_\mu$ CC and NC interactions were based on the CTEQ5 parton distributions [29] from the Coordinated Theoretical-Experimental project on QCD. The density profile in the Earth was modeled using the preliminary reference Earth model [30].

Simulated neutrino events were generated with an E^{-2} spectral index, and then weighted according to their contribution to the atmospheric neutrino flux. The flux predictions of Honda *et al.* [3] were used for conventional atmospheric muon neutrinos, and those of Enberg *et al.* [9] for prompt atmospheric muon neutrinos. The predictions for muon neutrinos from pions and kaons were extended to higher energies by fitting a physics-motivated analytical equation based on energy and zenith angle (Ref. [12] and Ch. 7 of Ref. [7]) in an overlapping region with the detailed calculations of Honda *et al.* [3].

Since simulated events were generated with a harder spectrum than atmospheric neutrinos, the effective live time for high energy events was boosted. Additionally, since all events were forced to interact in or near the detector, the effective live time for low energy events was boosted. The effective live time of the neutrino simulation used to train the unfolding algorithm is shown in Fig. 5.

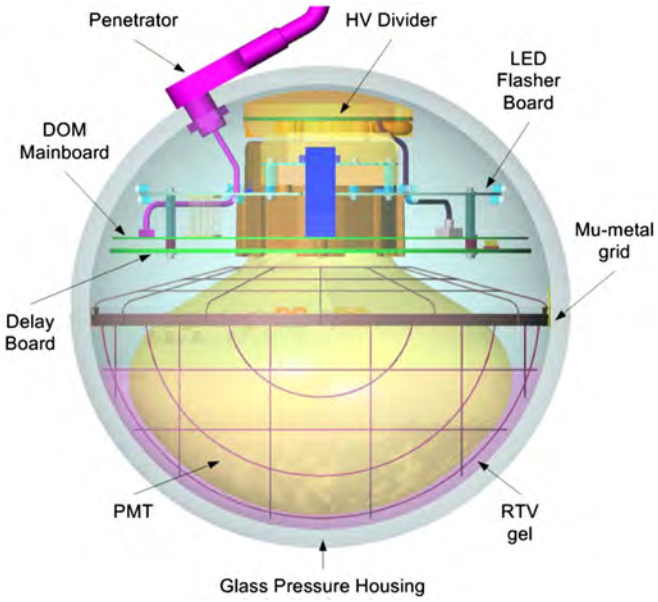

FIG. 4 (color online). Digital Optical Module.

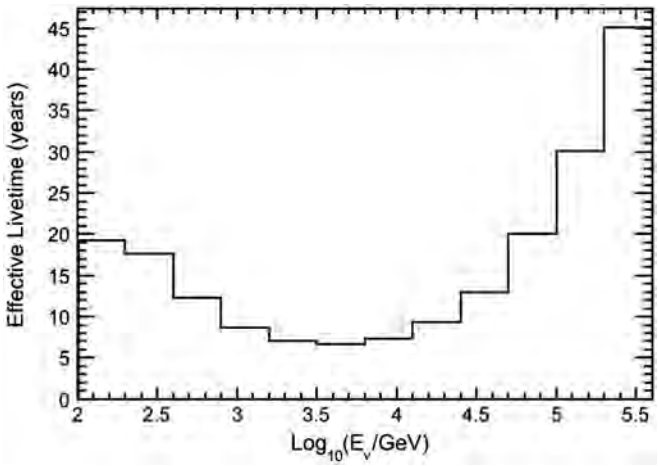

FIG. 5. Effective live time of the simulation used to train the unfolding algorithm, as a function of neutrino energy.

IV. EVENT RECONSTRUCTION AND BACKGROUND REJECTION

A variety of algorithms is used in IceCube for event reconstruction, classification, and background rejection, depending on the energy range, the anticipated signal and backgrounds for a particular analysis, as well as the neutrino flavor. The background for this analysis was down-going atmospheric muons that were misreconstructed as up-going. Despite the depth of IceCube, the ratio of down-going atmospheric muons to muons produced in or near the

detector by neutrino interactions is roughly 1×10^6 to one [1]. Below is a brief summary of the muon track reconstruction algorithms and event selection methods that were used in this analysis.

A. Event reconstruction

The LINEFIT reconstruction is a fast, first-guess algorithm based on the assumption that the Cherenkov photons from a muon propagate on a wave front perpendicular to the track. This assumption leads to a fitting algorithm that is extremely fast, and often estimates the muon track direction within ten degrees. LINEFIT, and likelihood-based reconstructions (discussed next) seeded with the LINEFIT track, were used as part of the software filtering at the South Pole. Additionally, the wave front velocity estimated byLINEFIT is correlated with how well the track hypothesis fits the distribution of recorded light and was used as an event selection cut prior to one of the two BDTs.

Maximum likelihood reconstruction algorithms account for the geometric dependence of photon arrival times, as well as the stochastic variability in arrival times due to scattering in the ice. The likelihood function to be maximized is the function [31]

$$\mathcal{L} = \prod_j p(\mathbf{a}, t_{\mathrm{hit},j}), \tag{3}$$

where $\mathbf{a}$ is the set of parameters characterizing the hypothesized track, i.e., three coordinates for the vertex location, two angles for the direction, and possibly energy, and $p(\mathbf{a}, t_{\mathrm{hit}})$ is the probability distribution function [32] for photon hit times, given the track hypothesis. The product is over all photon hits in the event. In practice, the maximum of the likelihood function is found by minimizing the negative of the log of the likelihood, so the product becomes a sum. To further simplify implementation, a transformation is made and time residual, t_{res}, is used in place of hit time, t_{hit}, where

$$t_{\mathrm{res}} \equiv t_{\mathrm{hit}} - t_{\mathrm{geo}}. \tag{4}$$

The geometric travel time, t_{geo}, is based on a straight photon path with no scattering.

Single photoelectron (SPE) fits are likelihood reconstructions that use only the arrival time of the first photoelectron in all hit DOMs. Typically, 16 or 32 iterations of the SPE fit are performed, with the seed track randomly altered for each iteration. This helps ensure that a local minimum is not chosen as the final track. The multiple photoelectron (MPE) fit is similar to the SPE fit; however, it uses the total number of observed photons to describe the arrival time of the first photon. When many photons arrive at the same DOM, the first photon is scattered less than an average photon. Since more information is used, the directional accuracy of the fit is often improved slightly, as compared to the SPE fit. Moreover, using track quality parameters based on the MPE fit rather than on the SPE fit provided better event discrimination and improved the signal efficiency of the BDTs by about 10%.

In addition to track location and direction, the likelihood reconstructions return several variables that are used to estimate fit quality. These variables include the log-likelihood (LogL) and the reduced log-likelihood (RLogL). RLogL = LogL/n_{dof}, where n_{dof} is the number of degrees of freedom in the minimization, i.e., the number of hit DOMs minus the number of parameters to be fit. RLogL is then (ideally) independent of the number of hit DOMs. A similarly scaled parameter called partial log-likelihood, PLogL, equal to LogL/(number of hit $DOMs - 2.5$), has also been found to provide additional discriminatory power. Figure 6 shows the distribution of the PLogL variable from the MPE fit that was used by the BDTs.

Figure 7 shows the distribution of the difference between LINEFIT zenith angle and MPE fit zenith angle, for signal simulation and for data. This angular difference was used as an input to the BDTs.

PHOTOREC is a reconstruction algorithm that accounts for spatially variable ice properties [33]. It does this by incorporating light propagation tables created by Photonics [26]. The output of PHOTOREC used in this analysis was the estimation of dE/dX, the average muon energy loss per unit propagation length (GeV/m) that would produce the detected amount of light. The reconstructed dE/dX is proportional to the number of photons detected and hence to the number of photons emitted along the muon's track. To correctly scale the proportionality, changes in the photon intensity due to the distance between the track and the hit DOMs and the amount of scattering and absorption between light generation and detection points are accounted for. The reconstruction algorithm incorporates the detailed ice model, but assumes that stochastic energy losses are uniform along the track. As mentioned in Sec. III B, the amount of light emitted along the track of

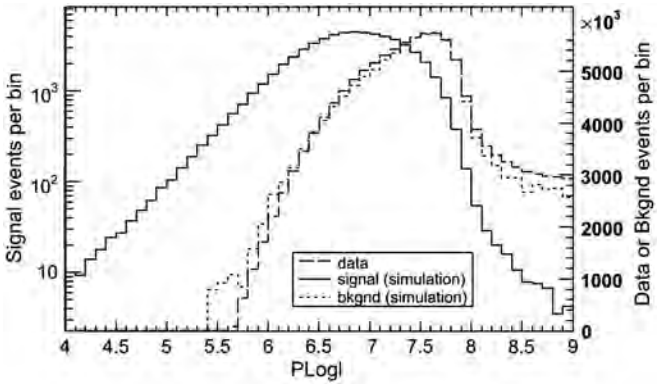

FIG. 6. Distribution of the PLogL variable (from the MPE fit), for neutrino simulation, muon background simulation, and for data. A cut at a value of 8 based on the PLogL from a 32-iteration SPE fit has already been applied to reduce the amount of data requiring higher level processing. PLogL was then recalculated based on the result of the MPE fit.

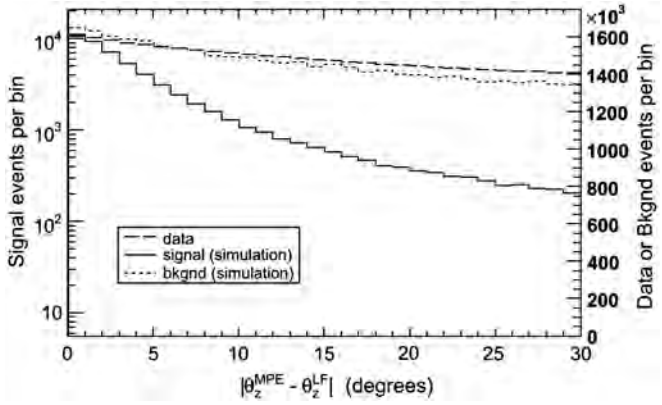

FIG. 7. Distribution of the difference between LINEFIT zenith angle and MPE fit zenith angle, for neutrino simulation, muon background simulation, and for data.

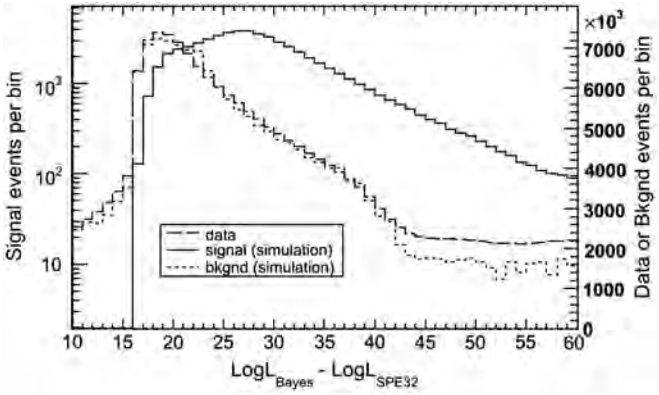

FIG. 8. Distribution of the Bayesian likelihood ratio, for neutrino simulation, muon background simulation, and for data.

a high energy muon (greater than about a TeV) is linearly correlated with the muon's energy, and it is possible to estimate the muon's energy (near the center of the detected track), using dE/dX, with an accuracy of 0.3 on a log scale. However, for low energy muons, the amount of light emitted along the track is nearly independent of energy, as discussed in Sec. III B. Additionally, the PHOTOREC algorithm does not account for the fraction of detected photons that may be from the hadronic shower at the interaction point (if that occurs inside the detector), nor does it account for the length of the muon track inside the detector. Hence, the correlation between dE/dX and muon energy degrades below a TeV.

The paraboloid algorithm [34] analyzes the value of the likelihood function around a seed track. After transforming the coordinate space to one centered on the direction of the seed track, it fits a constant likelihood ellipse to the likelihood space around the direction of the track. The important result is the paraboloid sigma, calculated from the major and minor axes of the constant likelihood ellipse. Paraboloid sigma provides an estimate of the pointing error of the track.

In a Bayesian reconstruction, the standard likelihood function is multiplied by a bias function which depends only on the event hypothesis and not on the actual event data. The bias is used as a way to include prior knowledge of the characteristics of the data, that misreconstructed down-going tracks dominate the signal by about 3 orders of magnitude at this stage. The Bayesian likelihood ratio is the useful result from this reconstruction, $\mathrm{LogL}_{\mathrm{Bayes}} - \mathrm{LogL}_{\mathrm{SPE32}}$, where SPE32 refers to a 32-iteration SPE fit. Figure 8 shows the distribution of the Bayesian likelihood ratio, for simulation and for data.

In a reconstruction algorithm known as the umbrella fit, the minimizer is constrained to track directions with space angles more than 90° from a seed track. The likelihood ratio $\mathrm{LogL}_{\mathrm{Umbr}} - \mathrm{LogL}_{\mathrm{SPE32}}$ is used as an event selection parameter. Good tracks have a higher SPE likelihood than a fit constrained to have a directional component in the opposite direction. This reconstruction provides discriminating power for certain events that are stuck in a local minimum in the likelihood space, such as down-going or near-horizontal events that reconstruct as directly up-going.

Split track reconstructions begin by creating four subevents from the initial event. Two subevents are created by separating all hit DOMs into the group hit before the average time, and the group hit after the average time. Two additional subevents are based on geometry. All hit DOMs are projected perpendicularly along the track. Then, the DOMs are split into two groups based on whether they fall before or after the location of the center of gravity of the pulses. LINEFIT and SPE reconstructions are performed on each of these four subsets. These fits provide discrimination for poorly reconstructed tracks, as well as for tracks that reconstruct as up-going due to the superposition of hits from two separate down-going muons. A loose cut on zenith angles from the split track reconstructions was used as an event selection cut prior to one of the two BDTs. Additionally, the zenith angles were used as input variables for the BDTs. Figure 9 compares the zenith angles from the SPE fits for the two subevents found by the geometric split.

In addition to zenith angles and likelihood ratios, several other measured or reconstructed variables were used for event discrimination. For example, the likelihood that a track is properly reconstructed is correlated with the number of hit strings (NString), the more hit strings the better.

Photons originating from farther away from the DOM are more likely to have been scattered, and their associated distributions of arrival time probabilities are more spread out. A larger number of direct hits, that is, hits that propagate directly to the DOM with little or no scattering, has been found to be correlated with better track reconstruction. The number of direct hits (NDir) is defined as the number of DOMs that have a hit with a residual time difference of $-15\ \mathrm{ns} < t_{\mathrm{res}} < 75\ \mathrm{ns}$. The ratio of direct hits to the total number of detected pulses (NDir/NPulses) in an event was also used as a cut parameter.

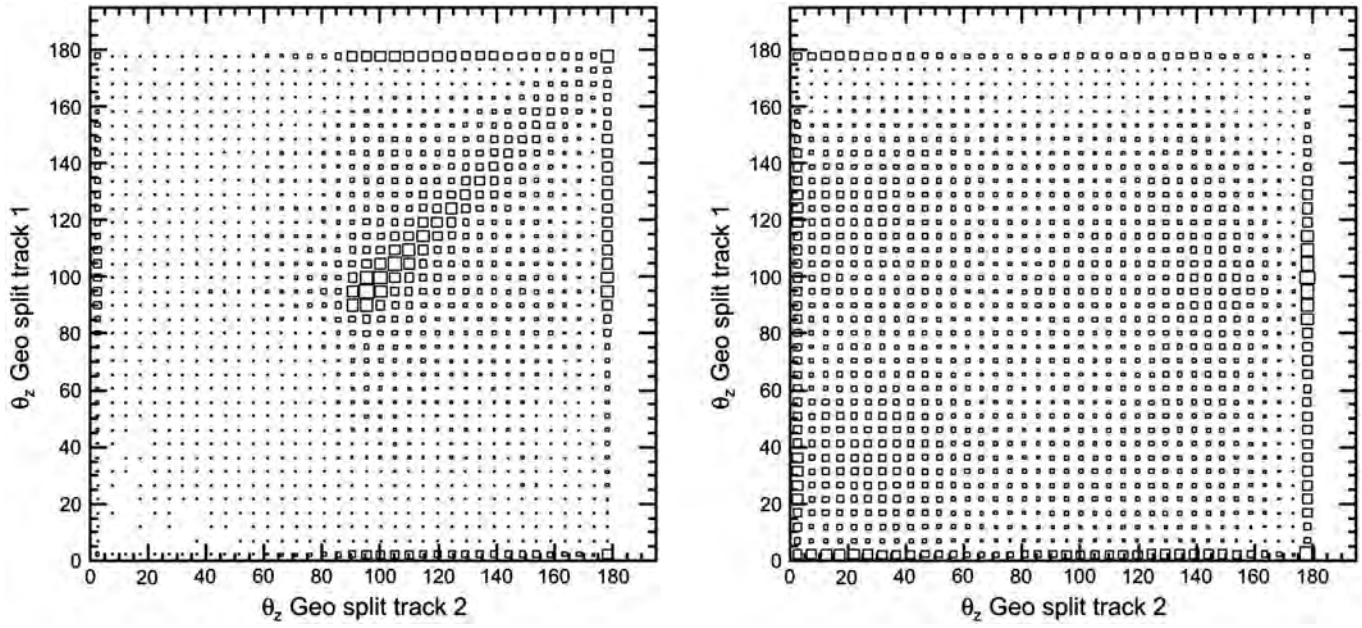

FIG. 9. Zenith angles from the SPE fits for the two subevents created by the geometric split. Neutrino simulation (left) and data (right). Box size is proportional to the event density.

The length of the event, LDir, is determined by projecting hit DOMs onto the reconstructed track and calculating the distance between the two endpoints of the projection. Larger values indicate a more reliable reconstruction of track direction. LDir is calculated using direct hits only.

Smoothness is a measure of how well the observed hit pattern is explained by the hypothesis of constant light emission along the reconstructed muon track. High quality tracks have hits equally spaced along the track. This parameter, called SmoothAll, is calculated using all hits.

B. Filtering and event selection

At trigger level, misreconstructed atmospheric muon events in the zenith region 90° to 180° outnumbered atmospheric neutrinos by a factor of about 10^5. These misreconstructed tracks were either individual muon tracks or coincident atmospheric muons that mimicked a single up-going event.

Although a variety of filters was deployed at the South Pole for the 2008–2009 physics run, events used for this analysis were only required to pass the muon filter. The muon filter was the primary filter for rejecting down-going atmospheric muons and retaining generic ν_μ events from near or below the horizon. Simple and fast reconstructions were performed in real time at the South Pole. These initial reconstructions were less accurate than ones performed later, during offline data processing. However, they could be accomplished within the time and CPU constraints at the South Pole while keeping up with the trigger rate. Zenith angles from LINEFIT and single-iteration SPE likelihood fits, as well as the number of hit DOMs (NChannel) and the average number of pulses per DOM, were used as selection variables in the muon filter. After muon filter event selection was applied, background was reduced to a factor of about 10^4 times the neutrino event rate.

Higher-level reconstructions included improved likelihood reconstructions for better angular resolution and background rejection, as well as reconstruction of additional parameters, such as energy estimation. Fits to additional track hypotheses were also performed. Some higher-level reconstructions incorporated the detailed ice model. Prior to higher-level off-line data processing, events that were uninteresting or unusable, and that clearly were not going to pass final event selection, were removed by applying loose cuts based on the results of an SPE fit: zenith angle $>80°$, RLogL < 12, and PLogL < 8. This reduced the amount of background to roughly a factor of 10^3 relative to signal.

Final event selection was accomplished with BDTs that used multiple reconstructed and observed parameters as input.

C. Boosted decision tree event selection

The Toolkit for Multivariate Data Analysis (TMVA) with ROOT [35] was used to implement BDT event classification. BDTs outperform straight cuts because the decision trees are able to split the phase space into a large number of hypercubes, each of which is identified as either signallike or backgroundlike [35]. Additionally, BDTs often outperform other multivariate techniques because either there are not enough training events available for the other classifiers, or the optimal configuration (e.g., how many hidden layers for a neural network, which variables to use, etc.) is not known and is difficult to determine [35]. Testing with

several different multivariate algorithms within TMVA indicated that the best results for separating signal from background in this case could be achieved with BDTs.

The nodes of a decision tree form what looks like an inverted tree. At each node, the algorithm chose the particular cut variable and cut value that provided the best discrimination between signal and background for the events in that node. Events were then split into additional nodes that made up the next layer of the tree, and the process was repeated until a minimum number of events in a node was reached. Variables were used multiple times in a tree, with different cut values each time. The final nodes were classified as signal or background, depending on the classification of the majority of training events that ended up in each node.

Boosting was used to overcome problems associated with statistical fluctuations in the simulation used to train the BDTs. 200 trees were derived from the same training ensemble by reweighting events. After one tree was created, events that were misclassified in that tree had their weights increased, and the next tree was created. This next tree then chose different variables and cut values at each node as a result of the altered weights. The final classifier used a weighted average of the individual decisions of all 200 trees.

Two BDTs were used: one having better efficiency at lower energies, the other having better efficiency at middle and higher energies. Events were accepted if their classification score from either BDT exceeded an optimized threshold. The function of the BDTs was to distinguish between poorly reconstructed background events, and signal events that included some that were well reconstructed and some that were poorly reconstructed. By applying preselection cuts prior to training the BDTs, some of the poorly reconstructed events were removed from the signal event samples, and the overall performance of each BDT was improved. For the low energy BDT (BDT 1), the preselection cut was based on LINEFIT velocity (LINEFIT velocity $>0.2c$). For the other BDT (BDT 2), the preselection cut was based on zenith angles from the split track fits (all four zenith angles $>80°$). The same cuts were applied to the actual data as were applied to the simulated background and signal event samples used for BDT training and testing.

Muon neutrino simulation with an E^{-1} spectrum was used for signal events in the BDT training. Although the true signal spectrum is much steeper than this, testing indicated this spectrum for training produced a BDT that performed better for higher energy events, with no compromise in performance for low energy events. Cosmic ray muon simulation from CORSIKA was used for background events. Following training, the BDTs were tested using independent signal and background event simulation. Neutrino simulation weighted to an atmospheric spectrum, as well as single, double, and triple-coincident muon events, weighted to the cosmic ray muon spectrum, were used for testing the BDTs.

Table I lists the specific variables used in the BDTs. The NString variable was only used by BDT 1. One additional difference between the two BDTs was the source of the split track fits. For BDT 1, which was optimized for lower energies, the LINEFIT reconstructions for each of the four split tracks (two split geometrically and two split in time) were used. For BDT 2, if 16-iteration SPE fits were successful for the split tracks, then those results were used; otherwise the LINEFIT results were used. SPE fit results were not available for events in which there were too few hit DOMs in one or more of the splits to perform a likelihood fit.

Figure 10 shows the output of each BDT, for the data and for simulation weighted to the same live time (359 days). The cut value of 0.73 was chosen to achieve greater than 99% purity. Testing the BDTs with simulated signal and background data sets indicated that the background contamination was less than 0.25%. However, the effective live time of the background simulation available for testing was not representative of a year of data. The lack of sufficient background simulation near the chosen cut values can be seen in Fig. 10. Because we did not have a reliable estimate of background contamination, comparisons between data and neutrino simulation were used to further verify that background rejection was performing as expected. In particular, the data passing rate as a function of BDT cut values was compared to the predicted rate from atmospheric muon and neutrino simulation. At looser BDT cut values, where sufficient simulated background events passed the BDT cuts to provide a statistically significant estimate, the background from simulation underestimated the apparent background in the data by about a factor of 3. Hence, the amount of background contamination in the final data set was conservatively estimated to be less than 1%. The additional cut at a zenith angle of 97°, discussed

TABLE I. Reconstruction variables used in the BDTs. θ_Z refers to the zenith angle. See Sec. IVA for explanations.

BDT Variables
Paraboloid Sigma for the MPE fit
RLogL from the MPE fit
PLogL from the MPE fit
NDir
LDir
SmoothAll
NDir/NPulses
$\mathrm{LogL}_{\mathrm{Bayes}} - \mathrm{LogL}_{\mathrm{SPE32}}$
NString
$\lvert\theta_Z^{\mathrm{MPE}} - \theta_Z^{\mathrm{LineFit}}\rvert$
$\mathrm{LogL}_{\mathrm{Umbr}} - \mathrm{LogL}_{\mathrm{SPE32}}$
θ_Z from each of the split tracks

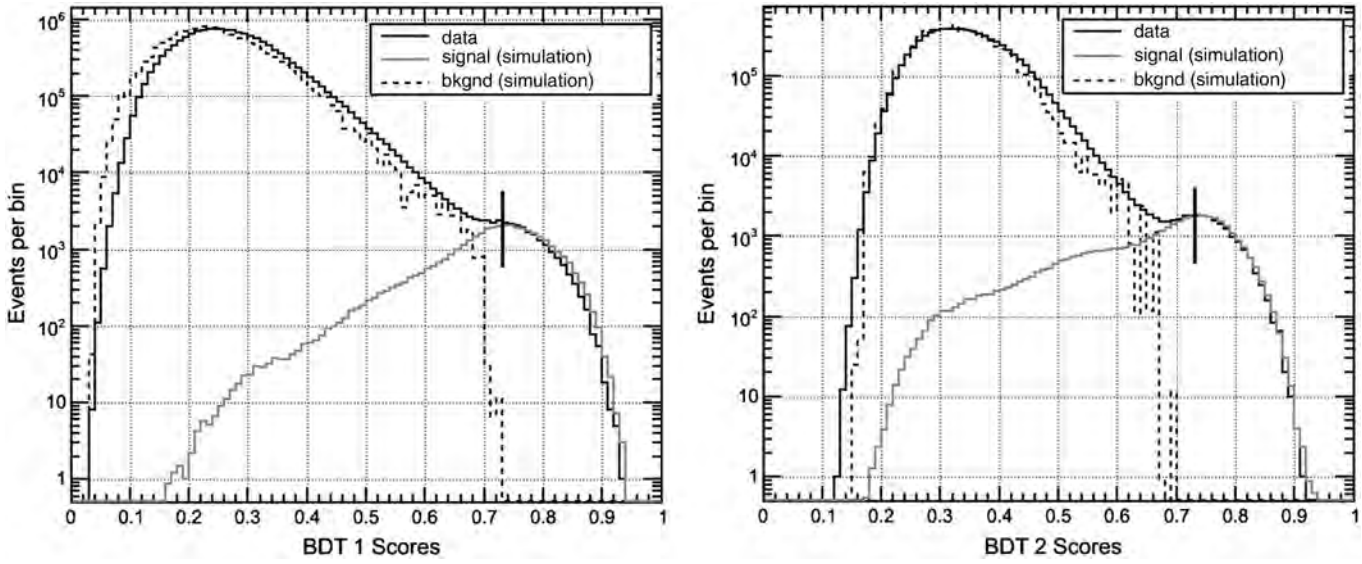

FIG. 10. Output of the BDTs for data, as well as neutrino and muon background simulation weighted to the same live time (359 days). The vertical solid lines mark the chosen cut value of 0.73 for each BDT.

shortly, further reduced the potential for background contamination.

The effective area, A_{eff}, is the area occupied by a hypothetical detector with the same collecting power as IceCube, but with 100% efficiency. A_{eff} satisfies the equation

$$N_{\text{events}} = \int dt \int d\Omega \int dE \cdot \Phi(E, \theta) \cdot A_{\text{eff}}(E, \theta), \quad (5)$$

where N_{events} is the number of events passing final selection cuts and $\Phi(E, \theta)$ is the true flux of atmospheric neutrinos with units of $\text{GeV}^{-1}\,\text{s}^{-1}\,\text{sr}^{-1}\,\text{cm}^{-2}$. In practice, the effective area is numerically calculated based on the number of neutrino events generated in simulation, the number passing final event selection cuts, and the event weights assigned in simulation to account for the probability of reaching and interacting in the detector. Figure 11 shows the effective area as a function of energy, for different zenith ranges, at the final cut level. Figure 12 shows the effective areas as a function of energy for BDT 1 and BDT 2 separately.

After eliminating data runs with some strings not operating, testing in progress, or various faults, there remained a total of 359 days of live time from April 2008 to May 2009. After final event selection cuts, the number of up-going neutrino events was 20 496, with zenith angles between 90° and 180°. An apparent excess of horizontal

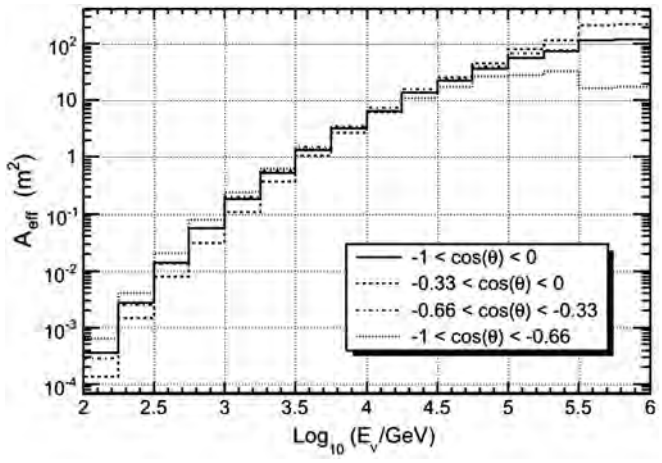

FIG. 11. Effective area for up-going muon neutrinos as a function of neutrino energy, for various zenith regions.

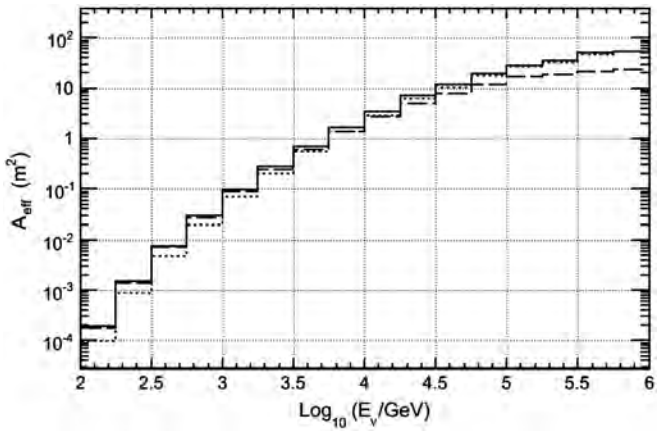

FIG. 12. Effective areas as a function of energy for each BDT. BDT 1 (long-dashed line) performs better than BDT 2 at low energies, while BDT 2 (short-dashed line) performs better than BDT 1 at higher energies. Events are required to pass only one of the BDTs, and the net effective area is the solid line. In contrast to Fig. 11, this plot reflects the zenith-averaged effective area for the region 97° to 180°. This corresponds to the zenith region used for the analysis.

events in the data, or deficit in simulation, from 90° to 97°, will be discussed in more detail in Sec. V B. Since the origin of this mismatch could not be verified, an additional zenith angle cut was applied at 97°. This resulted in a data sample of 17 682 atmospheric muon neutrino events from 97° to 180°.

V. SPECTRUM UNFOLDING

A. Methodology

The distribution of the energy-related observable, dE/dX, can be expressed as

$$b(dE/dX) = A(E_\nu, dE/dX)\Phi(E_\nu), \tag{6}$$

where Φ is a vector representing the true atmospheric neutrino flux as a function of energy, at the point of origin in the atmosphere, the vector b is the distribution of dE/dX for events in the final sample, and A is the response matrix that accounts for the effects of propagation through the Earth, interaction in or near the detector, detector response, and event selection. An analytical solution for A is not known, so it is created from simulation.

The desired result from the energy spectrum unfolding is the true neutrino flux, Φ. Ideally, this could be determined by inverting the response matrix:

$$\Phi(E_\nu) = A^{-1}(E_\nu, dE/dX)b(dE/dX). \tag{7}$$

However, direct solution is complicated by the fact that events are lost because the detector has limited efficiency. (Many neutrinos either do not interact near the detector or the events do not pass event selection cuts.) Additionally, the detector response is affected by limited energy resolution and there is significant smearing of events between bins (large off-diagonal elements in the response matrix). Moreover, statistical fluctuations in the data can lead to unphysical variations in the unfolded spectrum.

The singular value decomposition unfolding algorithm [36] was used to solve Eq. (7) and regularize the solution. The singular value decomposition method involves factoring a noninvertible matrix into the product of two orthogonal matrices and a diagonal matrix, that can then be manipulated as necessary. This algorithm has been implemented in the ROOUNFOLD package [37] for use in the ROOT [38] data analysis framework. The inputs to the unfolding algorithm are the response matrix, the predicted histogram for the observed distribution, and a histogram for the expected true flux.

The expected true flux, Φ_{MC}, is a 12 bin histogram binned in $\log_{10}(E_\nu/\mathrm{GeV})$ from 2 to 5.6, where E_ν is the neutrino energy in GeV. The predicted observables histogram, b_{MC}, is a 12 bin histogram of the expected dE/dX distribution of events passing final cuts, binned in $\log_{10}((dE/dX)/(\mathrm{GeV/m}))$ from -2.1 to 1.5. Figure 13 shows the distributions, comparing data to simulation, for the observable dE/dX. The response matrix, A, is a 12 by 12 histogram binned in $\log_{10}((dE/dX)/(\mathrm{GeV/m}))$ vs $\log_{10}(E_\nu/\mathrm{GeV})$, and filled with all events in b_{MC}.

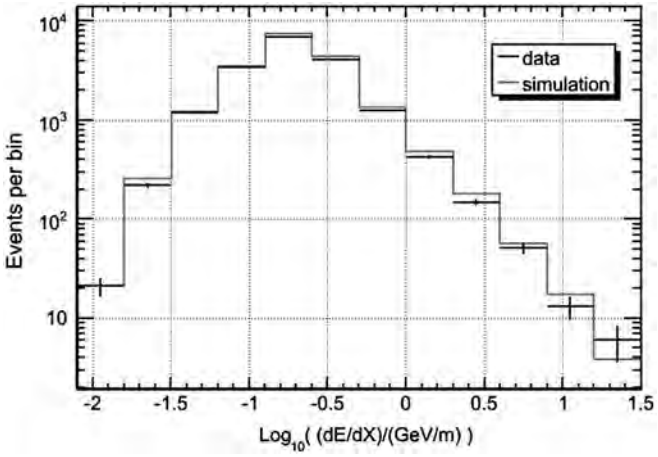

FIG. 13. Distributions of the dE/dX observable, for data and for simulation. The additional cut at zenith angle of 97° has been applied. Error bars for data are statistical only.

The response matrix maps the distribution of reconstructed muon dE/dX values to the distribution of neutrino energies. The correlation between muon energy in the detector and the reconstructed dE/dX is not exact, and neither is the correlation between muon energy in the detector and the incident neutrino energy. The neutrino flux in or near the detector is affected by propagation through the Earth, during which CC interactions attenuate the neutrino flux and NC interactions alter the neutrino energy distribution. The muon energy is only a fraction of the neutrino energy, and only a fraction of the muon energy is observed. Below about a TeV, where ionization rather than stochastic energy losses dominate, the energy loss rate is nearly independent of energy. Additionally, the stochastic, radiative losses are not uniform along the muon's track, as assumed in the reconstruction algorithm. If the muon is created in the detector, Cherenkov photons generated by the hadronic shower at the location of the CC interaction can be detected. If the muon is created outside of the detector, it loses some of its energy before reaching the detector.

Figure 14 shows the correlation between neutrino energy and reconstructed muon dE/dX. An estimate of neutrino energy resolution, as a function of $\mathrm{Log}_{10}(E_\nu/\mathrm{GeV})$, is shown in Fig. 15. To estimate this resolution, a Gaussian fit was performed to the distribution of $\mathrm{Log}_{10}((dE/dX)/(\mathrm{GeV/m}))$ in each of 12 $\mathrm{Log}_{10}(E_\nu/\mathrm{GeV})$ bins, and the standard deviations from these fits are shown in the figure. At higher energies, the correlation between neutrino energy and reconstructed muon dE/dX is hindered by the fact that the muon tracks are not contained within the detector and the muon can originate from a significant distance outside of the detector. At lower energies, the resolution is aided by the fact that the events are more fully contained within the detector and

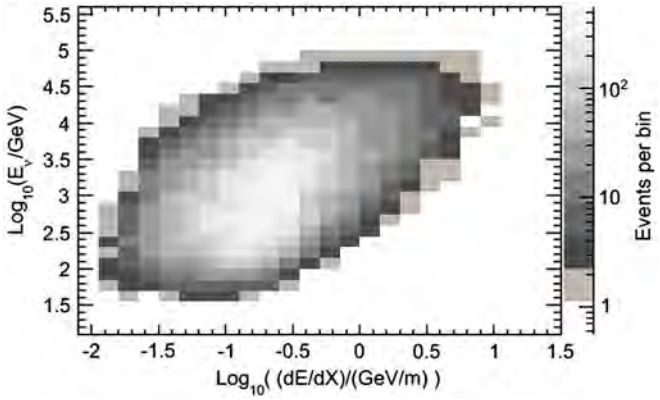

FIG. 14 (color online). Correlation between neutrino energy and the reconstructed muon dE/dX observable, from simulation weighted to the atmospheric neutrino spectrum of [3,9].

the amount of detected light depends on the track length within the detector.

In addition to numerically inverting the response matrix, the unfolding algorithm applies smoothing (regularization) to the solution to ensure that statistical fluctuations in the data do not propagate as unphysical fluctuations in the unfolded spectrum. The curvature in the solution, how sharply it can fluctuate from bin to bin, is regulated. A regularization parameter enforces a smooth cutoff of higher frequency terms in the solution. A lower cutoff biases the solution toward the shape of the expected spectrum, whereas a higher cutoff allows the solution to be influenced to a greater extent by fluctuations in the data.

The optimal choice of the regularization parameter depends on the number of bins and the sample size. Two methods for determining the appropriate amount of regularization were used, as discussed in Ref. [36]. The primary method used a result directly from the unfolding algorithm, where the coefficients of a particular decomposition of the rescaled measurement histogram were examined. At lower indices these coefficients fall exponentially, and the critical term that determines the setting of the regularization parameter is at the end of the exponential fall, after which the coefficients are not significant.

As suggested in Ref. [36], this result was checked using a series of toy simulations that were made systematically and statistically different from the expected true distribution. The atmospheric neutrino flux models from Refs. [3,9] were used as a baseline. Variations in the spectral slope (up to ± 0.1) and normalization about this baseline were implemented. For each underlying assumed true flux, many randomly fluctuated data sets were generated and each simulated data set was unfolded several times, using different choices for the regularization term. The χ^2 of each unfolded result relative to the true assumed spectrum was calculated and the distributions examined. The regularization term giving the best average χ^2 was the same as that found by the direct method using the decomposition coefficients.

Figure 16 shows the performance of the unfolding algorithm to a toy spectrum. In this example, a toy data set was created by arbitrarily modifying the event weights in simulation. The spectral slope of the conventional atmospheric neutrino flux (Ref. [3]) was made steeper by an index correction of -0.05, and the overall normalization was reduced to 80%. Additionally, the prompt flux was not included in the toy spectrum, creating a change in the shape of the energy spectrum at higher energies, where the shape of the actual flux is most uncertain. As can be seen from Fig. 16, some bias is introduced by the regularization process at the highest energies where the event count is low and the shape of the true spectrum is different from the assumed spectrum.

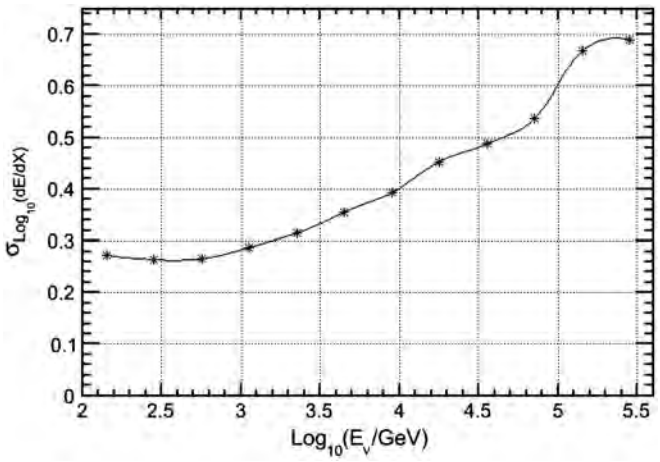

FIG. 15. Estimated neutrino energy resolution, from simulation.

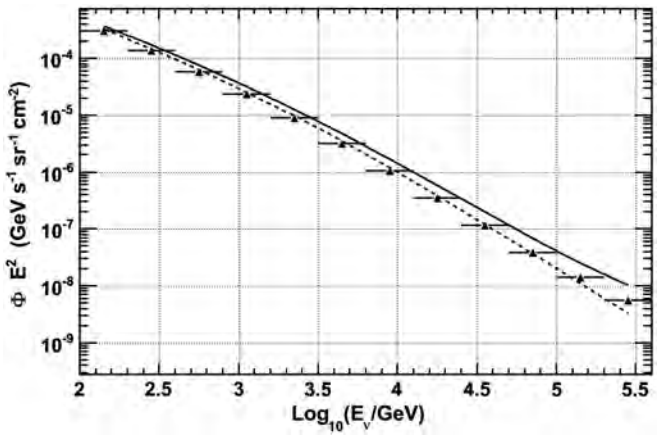

FIG. 16. Unfolding of known, toy spectrum. The solid line is the assumed spectrum used for regularization, the sum of the conventional and prompt atmospheric neutrino flux models from Refs. [3,9]. The dashed line is the arbitrary, toy spectrum used for generating the toy data. The unfolded result is shown without error bars.

B. Results and systematic uncertainties

The results of the atmospheric neutrino energy spectrum unfolding can be seen in Fig. 17. Event selection cuts that isolated tracklike events, caused by the muons created in ν_μ CC interactions, eliminated localized events from the electromagnetic showers induced by ν_e CC interactions and the hadronic showers induced by NC interactions. Additionally, production of ν_τ ($\bar{\nu}_\tau$) by cosmic rays is negligible. IceCube is not able to distinguish between neutrino and antineutrino events. Hence, the unfolded spectrum is the sum of ν_μ and $\bar{\nu}_\mu$, averaged over the zenith region 97°–180°.

The major uncertainties in the unfolded spectrum are from four categories. These are uncertainties in DOM sensitivity and ice properties, zenith-dependent data/simulation inconsistencies, statistical uncertainties and the impact of the regularization process, and miscellaneous normalization errors such as neutrino cross section and muon energy loss uncertainties. The bin-by-bin values for estimates of each of these error sources were added in quadrature to obtain the final uncertainty estimate for each bin of the unfolded flux.

Systematic uncertainties in ice properties and DOM sensitivities lead to systematic errors in the distribution of reconstructed dE/dX values, as well as the energy dependence of the detector's effective area. To estimate the impact of these uncertainties, two specialized neutrino simulation data sets were created. In one data set, the number of photons striking each DOM was boosted by 10%. In the other data set, the number of photons was reduced by 10%. From this, it was found that a $\pm 10\%$ change in the photon flux leads to a $\pm 15\%$ change in event rate and a ± 0.09 change in the ''apparent'' spectral index of the neutrino flux. These factors were found from a three-parameter fit that determined the changes in normalization, spectral index, and zenith angle tilt, of standard atmospheric neutrino simulation, to reproduce the best fits to the dE/dX distributions of the simulated event samples from these specialized data sets.

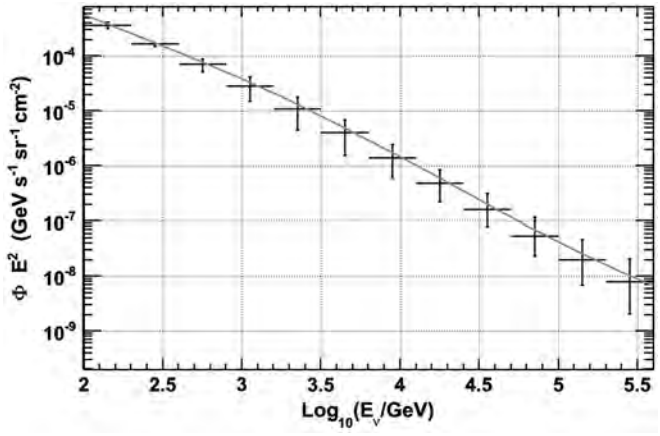

FIG. 17. Results of the atmospheric neutrino energy spectrum unfolding. The unfolded spectrum is shown in black; vertical lines are the estimated uncertainties. The gray line is the spectrum that provided the expected shape for the regularization, and includes the conventional atmospheric neutrino flux according to Honda *et al.* [3] and the prompt flux according to Enberg *et al.* [9]. This is the zenith-averaged $\nu_\mu + \bar{\nu}_\mu$ flux for the region 97°–180°.

The uncertainty in the DOM sensitivity is taken as $\pm 8\%$, based on the measured uncertainty in the PMT sensitivity [16]. The $\pm 10\%$ change in photon flux in the specialized simulation is effectively the same as a $\pm 10\%$ change in PMT sensitivity, so the normalization and spectral index correction factors just mentioned were scaled to the $\pm 8\%$ uncertainty for PMT sensitivity. To apply these values to ice property uncertainties, the change in the average number of photons striking a DOM that would result from a change in the ice properties had to be estimated.

First, we assumed a mean propagation length $L_p = 30$ m with $\pm 10\%$ uncertainty [19]. The propagation length for diffusive photon transport from a point source is defined as

$$L_p = \sqrt{\frac{L_e L_a}{3}}, \tag{8}$$

where L_e is the effective scattering length and L_a is the absorption length. Then, we estimated the fractional change in the number of photons at a distance d from the muon's track as

$$\frac{N' - N}{N} \sim e^{\pm .1d/(1\pm .1)L_p} - 1, \tag{9}$$

where $N \sim (1/d)e^{-d/L_p}$ is the number of photons at distance d for the nominal propagation length, and $N' \sim (1/d)e^{-d/(1\pm .1)L_p}$ is the number of photons at distance d for the perturbed propagation length (nominal $\pm 10\%$). The average distance between the track and the hit DOMs, per event, was estimated from simulation to be about 35 m. The net result of this approximation was that the uncertainty in the average photon flux reaching the DOMs was estimated to be $\pm 12\%$ on average, as a result of ice property uncertainties. The normalization and spectral index correction factors from the specialized simulated data sets were scaled to this $\pm 12\%$ uncertainty in the photon flux.

It should be pointed out that this method of estimating the impact of ice property uncertainties is affected by two approximations. First, the accuracy of the diffuse flux equation is limited at ranges less than several propagation lengths. Second, changes in ice properties would also change the distribution of photon arrival times at the hit DOMs, an effect which is not accounted for in the specialized simulation data sets. Comparisons were made between these simulated data sets and simulation generated using PHOTONICS tables derived from a modified ice model. In this modified ice model, scattering and absorption in the

cleaner layers of the ice were arbitrarily reduced. This comparison, as well as preliminary results from ongoing work to improve the simulation of photon propagation in the ice and derive a more accurate estimate of uncertainties related to ice properties, indicated that the method used here likely overestimates the impact of ice property uncertainties on the normalization and apparent spectral index, particularly in the higher energy bins.

Adding the uncertainties in detector response due to ice properties and DOM sensitivity in quadrature leads to an estimated $\pm 22\%$ uncertainty in the normalization, correlated with an uncertainty of ± 0.13 in the apparent spectral index. These detector uncertainties lead to uncertainties in the apparent neutrino flux. For a given detector response, i.e., a measurement of the dE/dX distribution, the true normalization and spectral index of the neutrino flux cannot be constrained better than allowed by these uncertainties. Figure 18 shows the resulting range of uncertainty in the measurement of the atmospheric neutrino energy spectrum.

As mentioned in Sec. IV C, there was a statistically significant excess of events in data, or a deficit in simulation, between 90°–97°, i.e., near the horizon. Figure 19 shows the cos(zenith) distributions for data and for simulation, with simulation normalized to the data. A similar excess was also observed in the AMANDA detector [39]. A number of checks and tests were performed, including evaluation of track quality parameters, the depth-dependence of the excess, the strength of the BDT scores, and visual examination of a subset of events in a software-based event viewer. The horizontal excess in data does not decrease with depth, nor with tightened BDT cuts. If the BDT cut is loosened, misreconstructed muons show up predominantly near the top of the detector, as expected. These checks are consistent with the possibility that the excess events are due to muons from atmospheric neutrino interactions. However, it is also possible that they are due to an excess of misreconstructed atmospheric muons.

It is likely that the lower event rate in simulation, close to the horizon, is due to uncertainties in the simulation of Cherenkov photon propagation in the ice or of inaccuracies in the simulation of cosmic ray events, such as insufficient live time, limitations with the cosmic ray model or its implementation in CORSIKA, or uncertainties in muon propagation and energy loss. Hence, it cannot be excluded that the horizontal excess is due to residual and unsimulated atmospheric muons and coincident events. It could also be related to uncertainties in the atmospheric neutrino flux due to atmospheric variability, discussed shortly. Since we were not able to verify the precise origin of the mismatch near the horizon, events in the zenith region 90° to 97° were not used.

To estimate the impact of any remaining zenith-dependent systematic uncertainties in the zenith range 97°–180°, separate unfoldings were performed for the zenith range 97°–124° and the zenith range 124°–180°. The results of this test are shown in Fig. 20, together with the predicted zenith-averaged flux corresponding to each angular range. The differences between result and prediction are not consistent between the two regions. For the more vertical events (gray in Fig. 20), the flux is lower than predicted for middle and higher energies. For the more horizontal events (black in Fig. 20), the flux is slightly lower than predicted at low and at high energies. The relative differences between result and prediction for the two zenith regions was taken as an estimate of the impact of anisotropic uncertainties.

Seasonal and regional variations in the atmospheric temperature profile are expected to lead to variations in the atmospheric neutrino flux [40] and could be causing the

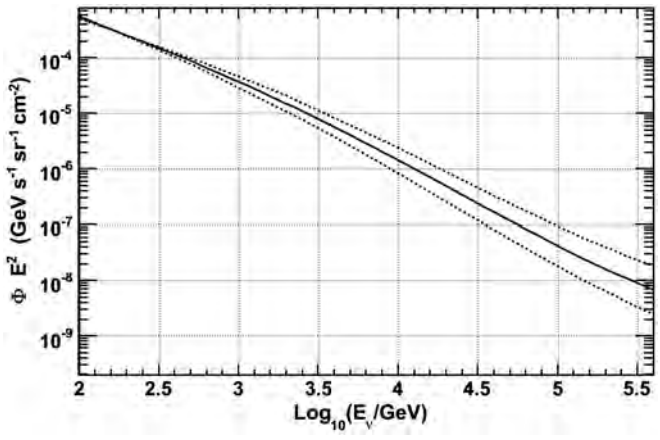

FIG. 18. Possible variability in the true neutrino flux consistent with DOM sensitivity and ice property uncertainties. The solid line is the predicted atmospheric neutrino flux ([3,9]). The dashed lines are the maximum and minimum of the possible range of variability consistent with DOM sensitivity and ice model uncertainties. As mentioned in the text, work is ongoing to reduce this range of uncertainty.

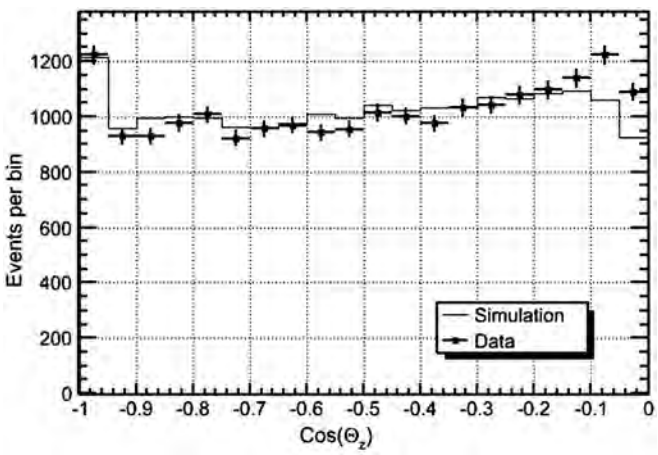

FIG. 19. Cosine(θ_Z) distributions for data and for simulation, using zenith angle from the MPE fit. Simulation has been normalized to the data. Error bars for data are statistical only.

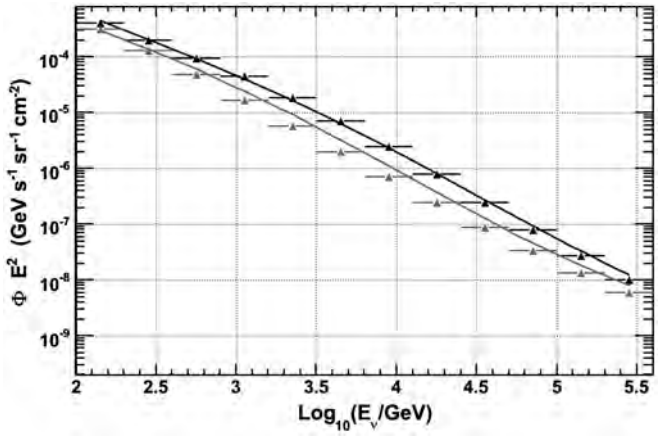

FIG. 20. Comparison of unfolded energy spectra for different zenith ranges. Separate unfoldings were performed for the zenith range 97°–124° (black) and the zenith range 124°–180° (gray). The unfolded results for each region (horizontal lines) and the predicted spectrum corresponding to each region (curves) are shown. Uncertainties for these results are not shown.

direction-dependent differences between data and simulation. Colder temperatures correspond to a greater air density and a shallower atmosphere. Greater atmospheric density leads to more collisions of pions and kaons prior to their decay. Hence, the production of high energy neutrinos is reduced. The converse occurs for warmer temperatures. The kinematics of collision and decay, and slant angle through the atmosphere, conspire to lead to variations in the energy and zenith angle dependence of atmospheric neutrino production for different atmospheric conditions. The normalization uncertainty on the Honda *et al.* conventional atmospheric neutrino flux model includes an estimated 3% uncertainty due to uncertainties in the atmospheric density profile [3,41]. However, the flux calculation uses a climatological average atmosphere (the US Standard Atmosphere 1976). The estimate of the error in the flux calculation is based on the error in the climatological average atmospheric density profile. It does not account for changes in the energy and zenith distribution of atmospheric neutrinos that result from regional and seasonal atmospheric variability.

The impact of statistical uncertainty in the data, as well as bias due to the regularization process, and the possibility that the assumed spectrum used to compute the amount of regularization may be different from the true spectrum were estimated using toy simulations. First, a six-parameter forward folding fit to the data was performed. In the forward folding fit, the general form of the flux was assumed to be consistent with the shape of the theoretical predictions [3,9], but corrections to the normalization, spectral index, and zenith angle tilt of the conventional and prompt atmospheric neutrino flux models were propagated through simulation. The fit variables that produced the best fit between the simulated detector response and the data were used to reweight simulated events in the toy experiments to mimic the data. The results of the forward folding fit indicated a possible systematic suppression of the neutrino event rate at higher energies, and this suppression was included in the toy simulations.

One thousand trials were performed, with events in each bin of the toy dE/dX distributions fluctuated according to a Poisson distribution. Statistical uncertainties in the neutrino simulation were also included. The difference between the unfolded energy spectrum and the known, ''true'' spectrum that the toy experiments were based on was computed for each trial. The 68th percentile of the errors in each bin from the 1000 trials was assigned as the uncertainty. The result of this analysis of statistical and regularization uncertainties is shown in Fig. 21, where the errors in each bin are given as the percent of the true flux. A potential systematic bias between the shape of the true flux and the shape of the assumed flux used to train the unfolding algorithm accounts for roughly half of the uncertainty indicated in Fig. 21 for the two highest energy bins.

A 3% uncertainty in the charged current, deep-inelastic neutrino-nucleon scattering cross section is estimated to lead to a 3% uncertainty in atmospheric neutrino event rates, and uncertainties in muon energy loss are estimated to lead to a 1% uncertainty [42]. Reconstruction and cut biases are estimated to introduce a 2% uncertainty in event rate. Adding these, and the 1% background contamination, in quadrature gives a 4% uncertainty in the event rate, assumed to be independent of energy.

A summary of uncertainties in the unfolded result can be seen in Fig. 22, as well as Table II. At the lower end of the unfolded energy range, uncertainties are dominated by zenith-dependent inconsistencies. At the middle of the range, uncertainties are dominated by the DOM sensitivity and ice property uncertainties, as well as the zenith-dependent uncertainties. Uncertainties in DOM sensitivity and ice properties dominate at higher energies.

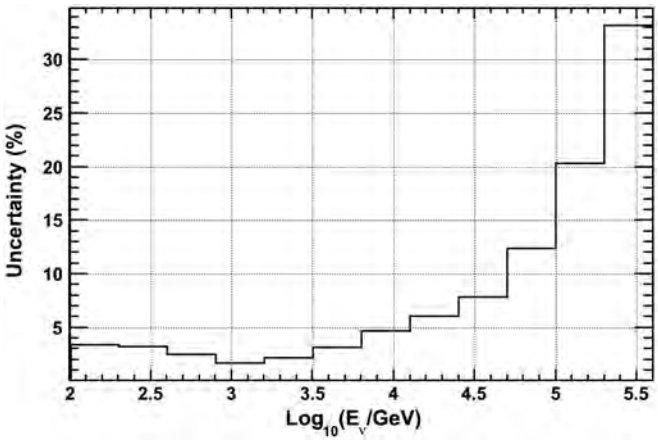

FIG. 21. Statistical and regularization-induced uncertainties in the unfolded result. The errors in each bin are given as the percent of the true flux.

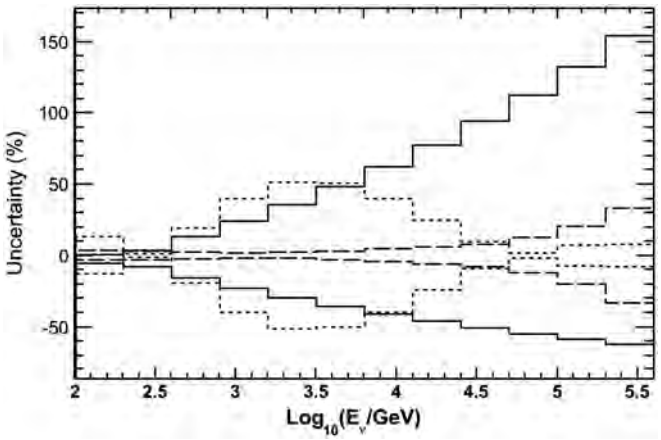

FIG. 22. Sources of uncertainty in the unfolded energy spectrum. The solid lines are the systematic uncertainties due to DOM sensitivity and ice property uncertainties; the short-dashed lines are the uncertainties implied by zenith-dependent inconsistencies in data/simulation comparisons; and the long-dashed lines are the statistical and regularization uncertainties from toy MC studies. Not shown is the uniform 4% uncertainty due to miscellaneous normalization errors assumed to be independent of energy.

VI. CONCLUSIONS AND OUTLOOK

A zenith-averaged unfolding of the atmospheric muon neutrino flux (ν_μ plus $\bar{\nu}_\mu$), from 100 GeV to 400 TeV, was performed. This is the first atmospheric neutrino measurement to such high energies, and the spectrum is consistent with predictions for the atmospheric muon neutrino flux. However, systematic uncertainties will need to be reduced before specific flux models [2,3,9–11] can be constrained. In particular, we are as yet unable to confirm the contribution of a prompt flux. Figure 23 compares the results of this analysis (IC40 unfolding) to previous measurements of the atmospheric neutrino energy spectrum. As discussed in Sec. V B, the estimates of uncertainties in the IceCube result are dominated by DOM sensitivity and ice property uncertainties, as well as the zenith-dependent mismatch between data and simulation. These uncertainty estimates are expected to be reduced as our simulation is improved.

TABLE II. Zenith-averaged, unfolded atmospheric muon neutrino energy spectrum.

$\log_{10}(E_\nu/\mathrm{GeV})$	$dN/dE_\nu \cdot E_\nu^2$ (GeV s^{-1} sr^{-1} cm^{-2})	% Uncertainty
2.0–2.3	3.6×10^{-4}	+29, −28
2.3–2.6	1.6×10^{-4}	+21, −22
2.6–2.9	7.0×10^{-5}	+31, −32
2.9–3.2	2.8×10^{-5}	+50, −50
3.2–3.5	1.1×10^{-5}	+65, −62
3.5–3.8	4.0×10^{-6}	+71, −63
3.8–4.1	1.4×10^{-6}	+74, −58
4.1–4.4	4.7×10^{-7}	+82, −53
4.4–4.7	1.6×10^{-7}	+95, −53
4.7–5.0	5.4×10^{-8}	+113, −57
5.0–5.3	2.0×10^{-8}	+135, −64
5.3–5.6	7.9×10^{-9}	+158, −72

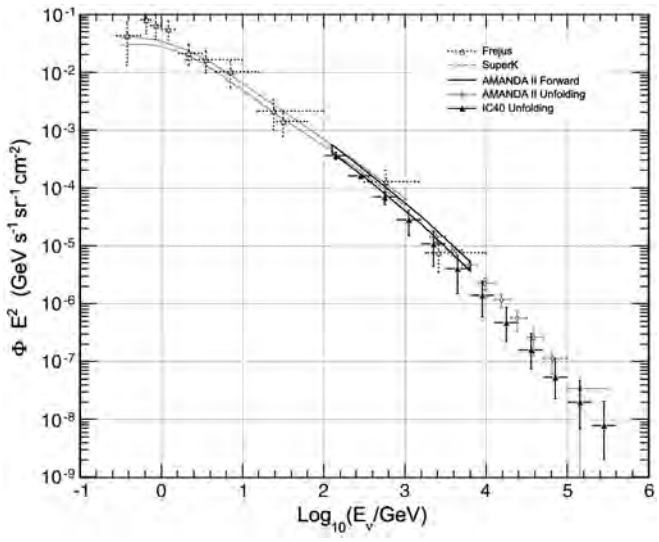

FIG. 23. Comparison with previous measurements of the atmospheric neutrino energy spectrum; the Fréjus result [43], upper and lower bands from SuperK [44], an AMANDA forward folding analysis [45], and an AMANDA unfolding analysis [39]. All measurements include the sum of neutrinos and antineutrinos. The AMANDA unfolding analysis was a measurement of the zenith-averaged flux from 100° to 180°. The present analysis (IC40 unfolding), which extends the measurement up to 400 TeV, is a measurement of the zenith-averaged flux from 97° to 180°. Vertical error bars include systematic as well as statistical uncertainty.

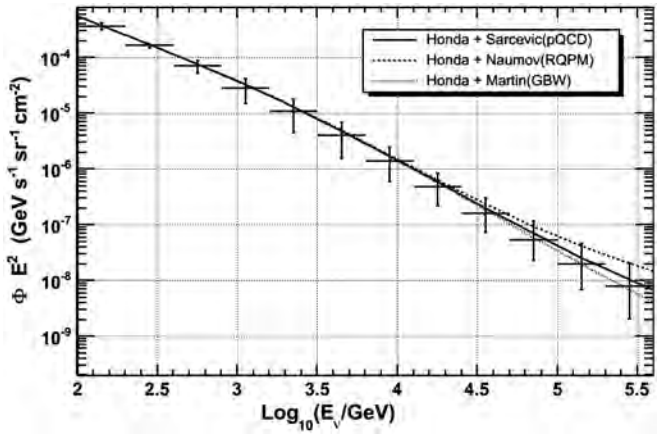

FIG. 24. Comparison of various prompt flux models to the unfolded result. The models shown are the sum of the Honda flux [3], plus one of Sarcevic [9], Naumov [11], or Martin [10]. Vertical error bars include systematic as well as statistical uncertainty.

A comparison between the unfolded spectrum and various prompt flux models [9–11] is shown in Fig. 24.

Several improvements are anticipated in atmospheric neutrino measurements with IceCube. Correlations between variations in atmospheric temperature profiles, and the energy and zenith angle dependence of the atmospheric neutrino flux, are being investigated using *in situ* atmospheric temperature measurements. Pulsed LED sources installed on each DOM are being used to extend the ice description to the deepest ice in the detector with *in situ* measurements like those done in AMANDA for the ice down to 2100 m. Studies with cosmic ray muons are being used to reduce the uncertainty in DOM sensitivity. Work is also ongoing to identify and correct potential problems in simulation that could be contributing to data/simulation mismatch. Perhaps most significantly, this includes improving the simulation of light propagation within the detector, which is anticipated to improve the data to simulation agreement for several measured and reconstructed variables. These improvements will be discussed in a future paper. Once simulation of light propagation in the ice has been improved, it should be possible to use a more sophisticated and realistic method for estimating the impact of ice model uncertainties. As data collection continues, and improvements to simulation are implemented, it will be possible to extend the measurement of the atmospheric neutrino energy spectrum with IceCube to PeV energies, as well as to significantly reduce the uncertainties.

ACKNOWLEDGMENTS

We acknowledge support from the following agencies: U.S. National Science Foundation, Office of Polar Programs, U.S. National Science Foundation, Physics Division, University of Wisconsin Alumni Research Foundation, the Grid Laboratory Of Wisconsin (GLOW) grid infrastructure at the University of Wisconsin—Madison, the Open Science Grid (OSG) grid infrastructure; U.S. Department of Energy, and National Energy Research Scientific Computing Center, the Louisiana Optical Network Initiative (LONI) grid computing resources; National Science and Engineering Research Council of Canada; Swedish Research Council, Swedish Polar Research Secretariat, Swedish National Infrastructure for Computing (SNIC), and Knut and Alice Wallenberg Foundation, Sweden; German Ministry for Education and Research (BMBF), Deutsche Forschungsgemeinschaft (DFG), Research Department of Plasmas with Complex Interactions (Bochum), Germany; Fund for Scientific Research (FNRS-FWO), FWO Odysseus programme, Flanders Institute to encourage scientific and technological research in industry (IWT), Belgian Federal Science Policy Office (Belspo); University of Oxford, United Kingdom; Marsden Fund, New Zealand; Japan Society for Promotion of Science (JSPS); the Swiss National Science Foundation (SNSF), Switzerland. A. Groß acknowledges support by the EU Marie Curie OIF Program. J. P. Rodrigues acknowledges support by the Capes Foundation, Ministry of Education of Brazil.

[1] A. Karle (IceCube Collaboration), in "Proceedings of the 31st International Cosmic Ray Conference, Lodz, Poland, 2009," arXiv:1003.5715; See also http://icecube.wisc.edu.
[2] G. D. Barr, T. K. Gaisser, P. Lipari, S. Robbins, and T. Stanev, Phys. Rev. D **70**, 023006 (2004).
[3] M. Honda, T. Kajita, K. Kasahara, S. Midorikawa, and T. Sanuki, Phys. Rev. D **75**, 043006 (2007).
[4] T. K. Gaisser and M. Honda, Annu. Rev. Nucl. Part. Sci. **52**, 153 (2002).
[5] F. Halzen and S. R. Klein, Rev. Sci. Instrum. **81**, 081101 (2010).
[6] C. Amsler *et al.* (Particle Data Group), Phys. Lett. B **667**, 1 (2008).
[7] T. K. Gaisser, *Cosmic Rays and Particle Physics* (Cambridge University, Cambridge, England, 1991).
[8] J. R. Hörandel, Astropart. Phys. **21**, 241 (2004).
[9] R. Enberg, M. H. Reno, and I. Sarcevic, Phys. Rev. D **78**, 043005 (2008).
[10] A. D. Martin, M. G. Ryskin, and A. M. Stasto, Acta Phys. Pol. B **34**, 3273 (2003).
[11] G. Fiorentini, A. Naumov, and F. L. Villante, Phys. Lett. B **510**, 173 (2001).
[12] T. K. Gaisser, Nucl. Phys. B, Proc. Suppl. **118**, 109 (2003).
[13] C. G. S. Costa, Astropart. Phys. **16**, 193 (2001).
[14] R. Abbasi *et al.* (IceCube Collaboration), Astrophys. J. Lett. **718**, L194 (2010).
[15] A. Achterberg, *et al.* (IceCube Collaboration), Astropart. Phys. **26**, 155 (2006).
[16] R. Abbasi *et al.* (IceCube Collaboration), Nucl. Instrum. Methods Phys. Res., Sect. A **618**, 139 (2010).
[17] R. Abbasi *et al.* (IceCube Collaboration), Nucl. Instrum. Methods Phys. Res., Sect. A **601**, 294 (2009).
[18] P. B. Price, K. Woschnagg, and D. Chirkin, Geophys. Res. Lett. **27**, 2129 (2000).
[19] M. Ackermann *et al.* (AMANDA Collaboration), J. Geophys. Res. **111**, D13203 (2006).
[20] P. B. Price and L. Bergstrom, Appl. Opt. **36**, 4181 (1997).
[21] P. Askebjer *et al.*, Appl. Opt. **36**, 4168 (1997).
[22] J. F. Beacom, P. Crotty, and E. W. Kolb, Phys. Rev. D **66**, 021302 (2002).
[23] D. Heck *et al.*, *CORSIKA: A Monte Carlo Code to Simulate Extensive Air Showers*, Forschungszentrum Karlsruhe Report No. FZKA 6019, 1998.

[24] E. J. Ahn, R. Engel, T. K. Gaisser, P. Lipari, and T. Stanev, Phys. Rev. D **80**, 094003 (2009).
[25] D. Chirkin and W. Rhode, arXiv:hep-ph/0407075.; Muon Monte Carlo (MMC) can be downloaded at http://icecube.wisc.edu/~dima/work/MUONPR/.
[26] J. Lundberg *et al.*, Nucl. Instrum. Methods Phys. Res., Sect. A **581**, 619 (2007).
[27] M. V. D'Agostino, Ph.D. thesis, University of California, Berkeley, 2009, arXiv:0910.2555.
[28] M. Kowalski and A. Gazizov, arXiv:astro-ph/0312202.
[29] H. L. Lai *et al.*, Eur. Phys. J. C **12**, 375 (2000).
[30] A. Dziewonski in *The Encyclopedia of Solid Earth Geophysics*, edited by D. E. James (Van Nostrand Reinhold, New York, 1989), p. 331.
[31] J. Ahrens *et al.* (IceCube Collaboration), Nucl. Instrum. Methods Phys. Res., Sect. A **524**, 169 (2004).
[32] N. van Eijndhoven, O. Fadiran, and G. Japaridze, Astropart. Phys. **28**, 456 (2007).
[33] S. Grullon, D. Boersma, and G. Hill, IceCube Internal Report No. 200807001.
[34] T. Neunhoffer, Astropart. Phys. **25**, 220 (2006).
[35] H. Voss, A. Höcker, J. Stelzer, and F. Tegenfeldt, Proc. Sci. ACAT (2007) 040; A. Hoecker *et al.*, Proc. Sci. ACAT (**2007**) 040.
[36] A. Hoecker and V. Kartvelishvili, Nucl. Instrum. Methods Phys. Res., Sect. A **372**, 469 (1996).
[37] ROOUNFOLD: ROOT Unfolding Framework, http://hepunx.rl.ac.uk/~adye/software/unfold/RooUnfold.html.
[38] CERN, ROOT, 1994, http://root.cern.ch.
[39] R. Abbasi *et al.* (IceCube Collaboration), Astropart. Phys. **34**, 48 (2010).
[40] A. Achterberg *et al.* (IceCube Collaboration), arXiv:astro-ph/0509330.
[41] T. Sanuki, M. Honda, T. Kajita, K. Kasahara, and S. Midorikawa, Phys. Rev. D **75**, 043005 (2007).
[42] A. Achterberg *et al.* (IceCube Collaboration), Phys. Rev. D **75**, 102001 (2007).
[43] K. Daum *et al.*, Z. Phys. C **66**, 417 (1995).
[44] C. Gonzalez-Garcia, M. Maltoni, and J. Rojo, J. High Energy Phys. 10 (2006) 075.
[45] R. Abbasi *et al.* (IceCube Collaboration), Phys. Rev. D **79**, 102005 (2009).

Search for a diffuse flux of astrophysical muon neutrinos with the IceCube 40-string detector

R. Abbasi,[28] Y. Abdou,[22] T. Abu-Zayyad,[33] J. Adams,[16] J. A. Aguilar,[28] M. Ahlers,[32] D. Altmann,[1] K. Andeen,[28] J. Auffenberg,[38] X. Bai,[31] M. Baker,[28] S. W. Barwick,[24] R. Bay,[7] J. L. Bazo Alba,[39] K. Beattie,[8] J. J. Beatty,[18,19] S. Bechet,[13] J. K. Becker,[10] K.-H. Becker,[38] M. L. Benabderrahmane,[39] S. BenZvi,[28] J. Berdermann,[39] P. Berghaus,[31] D. Berley,[17] E. Bernardini,[39] D. Bertrand,[13] D. Z. Besson,[26] D. Bindig,[38] M. Bissok,[1] E. Blaufuss,[17] J. Blumenthal,[1] D. J. Boersma,[1] C. Bohm,[34] D. Bose,[14] S. Böser,[11] O. Botner,[37] A. M. Brown,[16] S. Buitink,[8] K. S. Caballero-Mora,[36] M. Carson,[22] D. Chirkin,[28] B. Christy,[17] J. Clem,[31] F. Clevermann,[20] S. Cohen,[25] C. Colnard,[23] D. F. Cowen,[36,35] M. V. D'Agostino,[7] M. Danninger,[34] J. Daughhetee,[5] J. C. Davis,[18] C. De Clercq,[14] L. Demirörs,[25] T. Denger,[11] O. Depaepe,[14] F. Descamps,[22] P. Desiati,[28] G. de Vries-Uiterweerd,[22] T. DeYoung,[36] J. C. Díaz-Vélez,[28] M. Dierckxsens,[13] J. Dreyer,[10] J. P. Dumm,[28] R. Ehrlich,[17] J. Eisch,[28] R. W. Ellsworth,[17] O. Engdegård,[37] S. Euler,[1] P. A. Evenson,[31] O. Fadiran,[4] A. R. Fazely,[6] A. Fedynitch,[10] J. Feintzeig,[28] T. Feusels,[22] K. Filimonov,[7] C. Finley,[34] T. Fischer-Wasels,[38] M. M. Foerster,[36] B. D. Fox,[36] A. Franckowiak,[11] R. Franke,[39] T. K. Gaisser,[31] J. Gallagher,[27] L. Gerhardt,[8,7] L. Gladstone,[28] T. Glüsenkamp,[1] A. Goldschmidt,[8] J. A. Goodman,[17] D. Gora,[39] D. Grant,[21] T. Griesel,[29] A. Groß,[16,23] S. Grullon,[28,*] M. Gurtner,[38] C. Ha,[36] A. Hajismail,[22] A. Hallgren,[37] F. Halzen,[28] K. Han,[39] K. Hanson,[13,28] D. Heinen,[1] K. Helbing,[38] P. Herquet,[30] S. Hickford,[16] G. C. Hill,[28] K. D. Hoffman,[17] A. Homeier,[11] K. Hoshina,[28] D. Hubert,[14] W. Huelsnitz,[17] J.-P. Hülß,[1] P. O. Hulth,[34] K. Hultqvist,[34] S. Hussain,[31] A. Ishihara,[15] J. Jacobsen,[28] G. S. Japaridze,[4] H. Johansson,[34] J. M. Joseph,[8] K.-H. Kampert,[38] A. Kappes,[9] T. Karg,[38] A. Karle,[28] P. Kenny,[26] J. Kiryluk,[8,7] F. Kislat,[39] S. R. Klein,[8,7] J.-H. Köhne,[20] G. Kohnen,[30] H. Kolanoski,[9] L. Köpke,[29] S. Kopper,[38] D. J. Koskinen,[36] M. Kowalski,[11] T. Kowarik,[29] M. Krasberg,[28] T. Krings,[1] G. Kroll,[29] N. Kurahashi,[28] T. Kuwabara,[31] M. Labare,[14] S. Lafebre,[36] K. Laihem,[1] H. Landsman,[28] M. J. Larson,[36] R. Lauer,[39] J. Lünemann,[29] J. Madsen,[33] P. Majumdar,[39] A. Marotta,[13] R. Maruyama,[28] K. Mase,[15] H. S. Matis,[8] K. Meagher,[17] M. Merck,[28] P. Mészáros,[35,36] T. Meures,[13] E. Middell,[39] N. Milke,[20] J. Miller,[37] T. Montaruli,[28,†] R. Morse,[28] S. M. Movit,[35] R. Nahnhauer,[39] J. W. Nam,[24] U. Naumann,[38] P. Nießen,[31] D. R. Nygren,[8] S. Odrowski,[23] A. Olivas,[17] M. Olivo,[10] A. O'Murchadha,[28] M. Ono,[15] S. Panknin,[11] L. Paul,[1] C. Pérez de los Heros,[37] J. Petrovic,[13] A. Piegsa,[29] D. Pieloth,[20] R. Porrata,[7] J. Posselt,[38] P. B. Price,[7] G. T. Przybylski,[8] K. Rawlins,[3] P. Redl,[17] E. Resconi,[23] W. Rhode,[20] M. Ribordy,[25] A. Rizzo,[14] J. P. Rodrigues,[28] P. Roth,[17] F. Rothmaier,[29] C. Rott,[18] T. Ruhe,[20] D. Rutledge,[36] B. Ruzybayev,[31] D. Ryckbosch,[22] H.-G. Sander,[29] M. Santander,[28] S. Sarkar,[32] K. Schatto,[29] T. Schmidt,[17] A. Schönwald,[39] A. Schukraft,[1] A. Schultes,[38] O. Schulz,[23] M. Schunck,[1] D. Seckel,[31] B. Semburg,[38] S. H. Seo,[34] Y. Sestayo,[23] S. Seunarine,[12] A. Silvestri,[24] A. Slipak,[36] G. M. Spiczak,[33] C. Spiering,[39] M. Stamatikos,[18,‡] T. Stanev,[31] G. Stephens,[36] T. Stezelberger,[8] R. G. Stokstad,[8] A. Stössl,[39] S. Stoyanov,[31] E. A. Strahler,[14] T. Straszheim,[17] M. Stür,[11] G. W. Sullivan,[17] Q. Swillens,[13] H. Taavola,[37] I. Taboada,[5] A. Tamburro,[33] A. Tepe,[5] S. Ter-Antonyan,[6] S. Tilav,[31] P. A. Toale,[2] S. Toscano,[28] D. Tosi,[39] D. Turčan,[17] N. van Eijndhoven,[14] J. Vandenbroucke,[7] A. Van Overloop,[22] J. van Santen,[28] M. Vehring,[1] M. Voge,[11] C. Walck,[34] T. Waldenmaier,[9] M. Wallraff,[1] M. Walter,[39] Ch. Weaver,[28] C. Wendt,[28] S. Westerhoff,[28] N. Whitehorn,[28] K. Wiebe,[29] C. H. Wiebusch,[1] D. R. Williams,[2] R. Wischnewski,[39] H. Wissing,[17] M. Wolf,[23] T. R. Wood,[21] K. Woschnagg,[7] C. Xu,[31] X. W. Xu,[6] G. Yodh,[24] S. Yoshida,[15] P. Zarzhitsky,[2] and M. Zoll[34]

(IceCube Collaboration)

[1]*III. Physikalisches Institut, RWTH Aachen University, D-52056 Aachen, Germany*
[2]*Department of Physics and Astronomy, University of Alabama, Tuscaloosa, Alabama 35487, USA*
[3]*Department of Physics and Astronomy, University of Alaska Anchorage, 3211 Providence Drive, Anchorage, Alaska 99508, USA*
[4]*CTSPS, Clark-Atlanta University, Atlanta, Georgia 30314, USA*
[5]*School of Physics and Center for Relativistic Astrophysics, Georgia Institute of Technology, Atlanta, Georgia 30332, USA*
[6]*Department of Physics, Southern University, Baton Rouge, Louisiana 70813, USA*
[7]*Department of Physics, University of California, Berkeley, California 94720, USA*
[8]*Lawrence Berkeley National Laboratory, Berkeley, California 94720, USA*
[9]*Institut für Physik, Humboldt-Universität zu Berlin, D-12489 Berlin, Germany*
[10]*Fakultät für Physik & Astronomie, Ruhr-Universität Bochum, D-44780 Bochum, Germany*
[11]*Physikalisches Institut, Universität Bonn, Nussallee 12, D-53115 Bonn, Germany*
[12]*Department of Physics, University of the West Indies, Cave Hill Campus, Bridgetown BB11000, Barbados*
[13]*Université Libre de Bruxelles, Science Faculty CP230, B-1050 Brussels, Belgium*
[14]*Vrije Universiteit Brussel, Dienst ELEM, B-1050 Brussels, Belgium*
[15]*Department of Physics, Chiba University, Chiba 263-8522, Japan*

[16]*Department of Physics and Astronomy, University of Canterbury, Private Bag 4800, Christchurch, New Zealand*
[17]*Department of Physics, University of Maryland, College Park, Maryland 20742, USA*
[18]*Department of Physics and Center for Cosmology and Astro-Particle Physics, Ohio State University, Columbus, Ohio 43210, USA*
[19]*Department of Astronomy, Ohio State University, Columbus, Ohio 43210, USA*
[20]*Department of Physics, TU Dortmund University, D-44221 Dortmund, Germany*
[21]*Department of Physics, University of Alberta, Edmonton, Alberta, Canada T6G 2G7*
[22]*Department of Physics and Astronomy, University of Gent, B-9000 Gent, Belgium*
[23]*Max-Planck-Institut für Kernphysik, D-69177 Heidelberg, Germany*
[24]*Department of Physics and Astronomy, University of California, Irvine, California 92697, USA*
[25]*Laboratory for High Energy Physics, École Polytechnique Fédérale, CH-1015 Lausanne, Switzerland*
[26]*Department of Physics and Astronomy, University of Kansas, Lawrence, Kansas 66045, USA*
[27]*Department of Astronomy, University of Wisconsin, Madison, Wisconsin 53706, USA*
[28]*Department of Physics, University of Wisconsin, Madison, Wisconsin 53706, USA*
[29]*Institute of Physics, University of Mainz, Staudinger Weg 7, D-55099 Mainz, Germany*
[30]*Université de Mons, 7000 Mons, Belgium*
[31]*Bartol Research Institute and Department of Physics and Astronomy, University of Delaware, Newark, Delaware 19716, USA*
[32]*Department of Physics, University of Oxford, 1 Keble Road, Oxford OX1 3NP, United Kingdom*
[33]*Department of Physics, University of Wisconsin, River Falls, Wisconsin 54022, USA*
[34]*Oskar Klein Centre and Department of Physics, Stockholm University, SE-10691 Stockholm, Sweden*
[35]*Department of Astronomy and Astrophysics, Pennsylvania State University, University Park, Pennsylvania 16802, USA*
[36]*Department of Physics, Pennsylvania State University, University Park, Pennsylvania 16802, USA*
[37]*Department of Physics and Astronomy, Uppsala University, Box 516, S-75120 Uppsala, Sweden*
[38]*Department of Physics, University of Wuppertal, D-42119 Wuppertal, Germany*
[39]*DESY, D-15735 Zeuthen, Germany*

(Received 28 April 2011; published 3 October 2011)

The IceCube Neutrino Observatory is a 1 km^3 detector currently taking data at the South Pole. One of the main strategies used to look for astrophysical neutrinos with IceCube is the search for a diffuse flux of high-energy neutrinos from unresolved sources. A hard energy spectrum of neutrinos from isotropically distributed astrophysical sources could manifest itself as a detectable signal that may be differentiated from the atmospheric neutrino background by spectral measurement. This analysis uses data from the IceCube detector collected in its half completed configuration which operated between April 2008 and May 2009 to search for a diffuse flux of astrophysical muon neutrinos. A total of 12 877 upward-going candidate neutrino events have been selected for this analysis. No evidence for a diffuse flux of astrophysical muon neutrinos was found in the data set leading to a 90% C.L. upper limit on the normalization of an E^{-2} astrophysical ν_μ flux of 8.9×10^{-9} GeV cm^{-2} s^{-1} sr^{-1}. The analysis is sensitive in the energy range between 35 TeV and 7 PeV. The 12 877 candidate neutrino events are consistent with atmospheric muon neutrinos measured from 332 GeV to 84 TeV and no evidence for a prompt component to the atmospheric neutrino spectrum is found.

DOI: 10.1103/PhysRevD.84.082001 PACS numbers: 95.85.Ry, 14.60.Lm, 95.30.Cq, 95.55.Vj

I. INTRODUCTION

There are many objects in our Universe that involve extremely high-energy processes such as matter accreting into black holes at the centers of active galaxies and violent explosions such as supernovae and gamma-ray bursts. Understanding the physics of these astrophysical objects requires the observation of nonthermal high-energy radiation in the form of charged cosmic rays (protons and nuclei), gamma rays, and neutrinos. Despite progress in cosmic-ray and gamma-ray astrophysics, the nature of high-energy astrophysical sources is still far from understood. Neutrinos may elucidate the fundamental connection between the sources of high-energy cosmic rays and gamma rays.

Cosmic rays have been well studied by both space and ground based instruments. As astrophysical messengers, their main disadvantage is that they are charged particles and thus are deflected by magnetic fields, subsequently losing their directional information. High-energy gamma rays have been detected from many galactic and extragalactic objects, but their effectiveness as cosmic messengers over long distance scales is limited by absorption on extragalactic background light. Neutrinos could provide a fundamental connection between cosmic rays and gamma rays.

Even if individual astrophysical neutrino sources are too weak to be detected, a superposition of all the sources may

*Corresponding author: Sean Grullon.
grullon@icecube.wisc.edu
†Also at Sezione INFN, Bari, I-70124, Italy.
‡Also at NASA Goddard Space Flight Center, Greenbelt, MD 20771, USA.

give rise to a detectable extraterrestrial flux. In this paper, we present results from a search for a diffuse flux of astrophysical muon neutrinos performed with the IceCube detector using data collected in its half completed configuration between April 2008 and May 2009. We first summarize astrophysical and atmospheric neutrino models in Sec. II and describe the IceCube detector in Sec. III. We outline in Sec. IV how our final neutrino sample was obtained. The analysis methodology is discussed in detail in Sec. V and we present our final results in Sec. VI.

II. ASTROPHYSICAL AND ATMOSPHERIC NEUTRINO FLUXES

The benchmark diffuse astrophysical ν_μ search presented in this paper assumes an astrophysical flux, Φ, with a spectrum $\Phi \propto E^{-2}$ resulting from shock acceleration. In addition to the E^{-2} spectral shape, astrophysical models of varying normalization and spectral shapes were tested as well. The Waxman-Bahcall upper bound [1] was derived for optically thin sources assuming a $\Phi \propto E^{-2}$ primary cosmic-ray spectrum. Becker, Biermann, and Rhode [2] calculated the diffuse astrophysical neutrino flux from active galactic nuclei using observations from Fanaroff and Riley Class II (FR-II) radio galaxies. These sources were used to normalize the flux of neutrinos by assuming a relationship between the disk luminosity, the luminosity in the observed radio band, and the calculated neutrino flux. Mannheim [3] and Stecker [4] derived models for optically thick active galactic nuclei sources assuming the sub-TeV diffuse gamma-ray flux observed by the Compton Gamma Ray Observatory [5] is produced by the decay of neutral pions. BL Lacertae objects that emit TeV gamma rays can be interpreted to be optically thin to photon-neutron interactions. The model calculated by Mücke *et al.* [6] assumes that charged cosmic rays are produced in these sources through the decay of escaping neutrons. An average spectrum of neutrinos from the precursor and prompt phases of gamma-ray bursts is calculated in Ref. [7] by correlating the gamma-ray emission to the observed flux of ultrahigh-energy cosmic rays.

The primary backgrounds in the search for diffuse astrophysical ν_μ are the atmospheric muons and neutrinos arising from cosmic-ray-induced extensive air showers. The substantial downward-going atmospheric muon background persists over a wide energy range from primary cosmic-ray energies of around a GeV to the highest measured extensive air showers of 100 EeV [8]. These events were removed by using the Earth as a filter in order to select upward-going neutrinos traversing through the Earth. Two classes of atmospheric neutrinos were considered: neutrinos arising from the decay of pions and kaons (the conventional atmospheric neutrino flux) and neutrinos arising from the decay of charm-containing mesons (the prompt atmospheric neutrino flux). Detailed three-dimensional calculations of the energy spectrum and angular distribution of the conventional atmospheric neutrino flux are summarized in Refs. [9,10]. The conventional atmospheric neutrino spectrum approximately follows an $E^{-3.7}$ spectrum in the TeV energy range. The prompt component of the atmospheric neutrino flux is yet to be measured, but full calculations of the prompt flux are given in Refs. [11–13]. The prompt component of the atmospheric neutrino flux is predicted to follow the primary cosmic-ray energy spectrum which is approximately $E^{-2.7}$. Since a hypothetical diffuse astrophysical neutrino flux would have a harder energy spectrum than atmospheric neutrino backgrounds, evidence for a diffuse flux would appear as a hardening of an energy-related observable distribution.

III. THE ICECUBE DETECTOR

IceCube consists of three detectors operating together. The main in-ice array is composed of 4800 digital optical modules (DOMs) arranged in 80 strings which are deployed vertically with 60 DOMs per string. The detector is deployed deep in the Antarctic ice between a depth of 1450 and 2450 m. The vertical spacing between each DOM is 17 m and the horizontal spacing between each string of DOMs is 125 m giving a total instrumented volume of 1 km^3. The design is optimized for the energy range of 100 GeV to 100 PeV [14]. The DeepCore extension is deployed within the main in-ice array and consists of six specialized strings which lower the energy reach to 10 GeV. IceCube was deployed in stages with the first string deployed during the 2005–2006 Austral summer. This analysis is based on 1 yr of data taken with the 40-string configuration (Fig. 1) which was deployed during

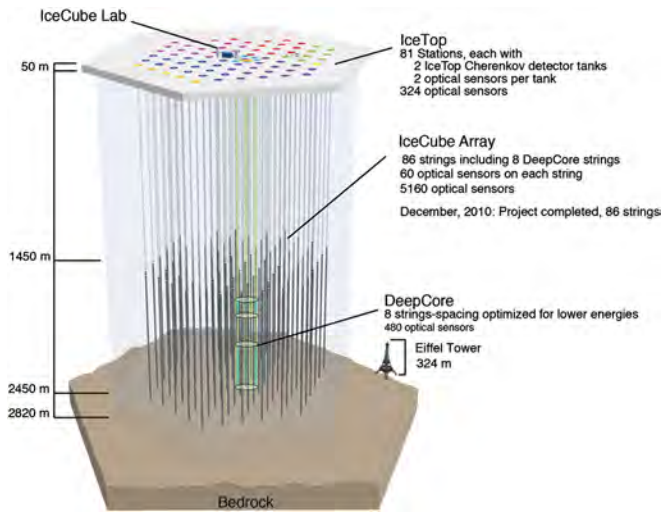

FIG. 1 (color online). Three-dimensional view of the IceCube detector layout. This work was based on the 40-string configuration which was half of the completed detector. The 40-string configuration was operational from April 2008 to May 2009.

the 2007–2008 Austral summer and was operational from April 2008 to May 2009.

Each DOM consists of a 13 in. (33.02 cm) pressurized sphere, a 10 in. (25 cm) Hamamatsu photomultiplier tube [15] (model R7081-02), a mu-metal magnetic shield, and associated electronics responsible for the operation and control of the photomultiplier tube as well as amplification, filtering, and calibration [14]. The DOMs are triggered by Cherenkov photons produced by charged particles in the Antarctic ice. In particular, ν_μ-induced charged-current interactions produce muons that can traverse the entire IceCube array. Analog waveforms captured by the photmultiplier tubes are digitized *in situ* by the DOM main board. The capture process is initiated by a signal derived from a discriminator connected to a high-gain signal path if the threshold (0.25 photoelectrons) is surpassed [16]. For the data set considered in this work, the triggered event was sent to a buffer for further filtering if it satisfied a simple majority trigger of eight triggered DOMs within a 5 μs time window.

Below a depth of 1450 m, the Antarctic ice is free of air bubbles and exhibits exceptional optical clarity with absorption lengths ranging from 100 to 200 m and effective scattering lengths ranging from 20 to 70 m [17,18]. The scattering and absorption lengths vary due to the concentration of dust in the glacial ice, which varies quite strongly with depth [19] due to varying atmospheric conditions and volcanic activity during the glacial history of Antarctica. The depth and wavelength dependence of the scattering and absorption have been measured with a variety of *in situ* light sources [17]. The ice properties have recently been measured over the full depth range [18] of the IceCube detector using the *in situ* LEDs present in every DOM main board resulting in what is called the South Pole Ice (SPICE) model.

IV. SIMULATION AND DATA FILTERING

A. Simulation

This work required an accurate Monte Carlo simulation of the down-going atmospheric muon background, the atmospheric neutrino flux, and the subsequent detector response. The simulation was used to determine event selection criteria in order to remove the misreconstructed atmospheric muon background and in the profile construction method (Sec. V) to compare the predicted neutrino-energy-correlated observable distribution with the data to search for evidence of astrophysical neutrinos.

The generation of extensive air showers initiated by high-energy cosmic-ray particles and the propagation of the subsequent muons through the atmosphere was handled by the CORSIKA (COsmic Ray SImulations for KAscade) [20] event generator. Hadronic interactions of the cosmic-ray primaries in the atmosphere were modeled using the SIBYLL [21] interaction model. The composition of the primary cosmic-ray spectrum was taken from the Hörandel poly-gonato [22] model which modeled the primary cosmic-ray spectrum as a combination of two power laws for each primary particle type.

The generation of neutrinos of all flavors was handled by the ANIS (All Neutrino Interaction Simulation) code [23]. ANIS uses the parton structure functions from CTEQ-5 [24]. Neutrinos were generated on a random position on the Earth's surface and then propagated through the Earth. The structure of the Earth is modeled by the PREM, or Preliminary Reference Earth Model [25]. In order to reduce computation time, neutrinos that reach the detector were forced to interact with the nearby Antarctic ice or bedrock to produce secondary particles that automatically trigger the detector. Each event was assigned a weight that represents the probability that this particular neutrino interaction occurred. Neutrinos were typically generated with a baseline energy spectrum of either E^{-1} or E^{-2}. The event weights that were calculated can be used to reweight the baseline generated spectra to any astrophysical or atmospheric neutrino model.

A daughter muon from a muon neutrino charged-current interaction or an atmospheric muon passing from the atmosphere into Earth rock was propagated using the Muon Monte Carlo (MMC) [26] code. MMC incorporates the various continuous and stochastic energy loss mechanisms of ionization, bremsstrahlung, photonuclear interactions, and pair production. The Cherenkov light produced by the muon and the various secondaries was then propagated from the muon track through the detector volume to the DOMs by using one of two methods: numerical tabulation and direct tracking.

The first method was provided by the PHOTONICS [27] software package which incorporates numerically tabulated photon distribution results of various simulation runs with different light sources. PHOTONICS tables are computationally efficient and have the added benefit of allowing the full ice description to be used in the reconstruction of muon events. The second method used direct photon tracking provided by the Photon Propagation Code (PPC) [18] which allows for a more complete description of photon propagation in the Antarctic ice since every photon is individually tracked and propagated. This work used PPC for the simulation of neutrinos and PHOTONICS for the simulation of the background atmospheric muons. This choice was made since the computational efficiency of PHOTONICS is well suited to the generation of a large amount of atmospheric muon background simulation which subsequently helps to reduce the uncertainty of the estimated misreconstructed atmospheric muon background. The numerical accuracy of PPC is appropriate for the generation of neutrino simulation which includes the atmospheric neutrino background. Benchmark neutrino simulation sets generated with PPC and PHOTONICS revealed that the largest discrepancy was a 30% difference in the neutrino event rate near a prominent dust layer

2050 m deep in the South Pole ice, whereas the overall neutrino event rate disagreement was 9%.

B. Event selection

The event selection strategy in this analysis used the Earth as a filter to remove all muons from cosmic-ray-induced extensive air showers and retain as many neutrino-induced muon events as possible. The reconstructed energy spectrum of the neutrino sample that remained (roughly from the TeV to PeV energy range) was then analyzed using the method outlined in Sec. V for evidence of astrophysical neutrinos. The IceCube 40-string data set used in this analysis yielded a total live time of 375.5 days.

The primary trigger for this analysis was a multiplicity condition which required eight DOMs to exceed their discriminator threshold within a 5 μs time window. In addition, a local coincidence condition was enforced that requires the vertical neighbors of the triggered DOMs to trigger within 1 μs of each other. The rate for this primary trigger was $\sim$1 kHz. Since the trigger rate was dominated by atmospheric muons, the data was processed in several stages in order to remove the atmospheric muon background and retain only neutrino events at the final analysis level. First, the triggered event rate at the South Pole was reduced to 22 Hz by using an online software filter. The arrival directions of the muon tracks in the IceCube detector were determined with a maximum likelihood reconstruction procedure. The muon track geometry is uniquely described by an arrival direction and a vertex position along the track which result in 5 degrees of freedom for the reconstruction. The likelihood function [28] parametrizes the probability of observing the Cherenkov photon arrival times given the muon track geometry. Preliminary reconstructions were performed using a single photoelectron likelihood which utilizes the arrival time of the first Cherenkov photon arriving in each DOM. All events reconstructed as upward-going through the Earth ($\theta > 90°$) were kept in the initial first stage of filtering. Events reconstructed as down-going must pass an energy cut that tightens for more vertical events. This ensures that truly up-going high-energy events, initially reconstructed as down-going, may be correctly reconstructed and kept in the final up-going event sample.

The second filtering stage involved more CPU intensive reconstructions performed offline outside of the South Pole. Among these reconstructions is the multiple photoelectron (MPE) fit which utilizes the likelihood description of the arrival time of the first Cherenkov photon given N expected photons. The first photon is less scattered than the average single photon and hence the likelihood description of the detected photoelectron is modified when this information is taken into account The MPE likelihood is a more sophisticated likelihood description than the single photoelectron likelihood reconstruction. It gives improved direction resolution at higher energies. Estimates of the muon energy (see the next section), the angular resolution, and quality parameters used for background rejection are calculated during the offline processing stage. About 5% of the cosmic-ray-induced muons in the atmosphere that trigger the IceCube detector are misreconstructed as going up through the Earth and need to be separated from neutrino-induced muons at the final analysis level. This is accomplished using quality criteria which are based on parameters derived from the reconstructed muon track. Table I summarizes the analysis cuts applied to the level 1 filtered data and simulation. Table II summarizes the number of data and simulation events that satisfied each successive analysis cut defined in Table I. The quality parameters used to obtain the final analysis sample are

(i) *Reconstructed zenith angle* (θ): The zenith angle of the reconstructed muon track is used as a cut parameter to select muon events with reconstructed directions that traverse through the Earth.

(ii) *Reduced log-likelihood*: The log-likelihood value of the reconstructed track was divided by the number of degrees of freedom of the fit. The number of degrees of freedom is given by the number of triggered DOMs ($N_{\rm ch}$) minus five, which is the number of free parameters in the reconstruction. Since $N_{\rm ch}$ loosely correlates with the muon energy, the reduced log-likelihood should be approximately energy independent. A smaller value indicates that the Cherenkov photons arrived at the individual DOMs more consistent with the likelihood description of photon arrival times. It is an efficient observable for separating high-energy atmospheric neutrinos from misreconstructed atmospheric muons. This variable was found not to be energy independent for lower-energy atmospheric neutrinos, however, and was subsequently found to be not efficient at background rejection at lower energies. This was resolved empirically by redefining the effective degrees of freedom to $N_{\rm ch} - 2.5$ for low values of $N_{\rm ch}$.

TABLE I. Summary of the analysis level selection criteria applied to the IceCube data, neutrino simulation, and the atmospheric muon background simulation to obtain the final event sample for the analysis.

Observable and selection criteria
$\theta > 90°$
$\frac{\log(L)}{(N_{\rm ch}-5)} < 8$ OR $\frac{\log(L)}{(N_{\rm ch}-2.5)} < 7.1$
$\sigma < 3°$
$\log(L_{\rm Bayes}/L) > 25$ for $\cos(\theta) < -0.2$
$\log(L_{\rm Bayes}/L) > (75\cos(\theta) + 40)$ for $\cos(\theta) > -0.2$
$\log(\frac{L_{\rm Bayes1}+L_{\rm Bayes2}}{L}) > 35$
$\theta_{\rm SplitTime} > 80°$
$\theta_{\rm SplitGeo} > 80°$
NDir > 5
LDir > 240
$\lvert$SDir$\rvert < 0.52$

TABLE II. Number of events at each purity level for data and simulation for atmospheric muons, conventional atmospheric ν_μ, and E^{-2} astrophysical ν_μ with a normalization of $N_a = 10^{-7}$ GeV cm^{-2} s^{-1} sr^{-1} for the full 40-string data set of 375.5 days. The background atmospheric μ was simulated with a total live time of 11 days. A weighting scheme was used to increase the live time at high energies resulting in 240 days of background live time above a primary cosmic-ray energy of 100 TeV. The quality parameter used for the purity cut is shown and the specific values of the cuts are defined in Table I.

Purity criterion	Data	Total atmospheric μ	Coincident μ	Atmospheric ν_μ	$E^{-2}\nu_\mu$
Triggered	3.3×10^{10}	2.98×10^{10}	1.72×10^{10}	1×10^{6}	1.03×10^{4}
L1 Filter	8.0×10^{8}	7.5×10^{8}	3.9×10^{8}	1.14×10^{5}	1956
$\theta > 90°$	2.4×10^{8}	3.0×10^{8}	1.79×10^{8}	91 246	1353
$\log(L)$	8.46×10^{6}	4.58×10^{6}	1.12×10^{6}	43 183	934
σ	1.43×10^{6}	1.05×10^{6}	4.1×10^{5}	37 174	677
$\log(L_{\mathrm{Bayes}}/L)$	2.88×10^{5}	2.73×10^{5}	2.36×10^{5}	27 411	659
$\log(\frac{L_{\mathrm{Bayes1}}+L_{\mathrm{Bayes2}}}{L})$	44 309	24 032	17 648	18 400	622
$\theta_{\mathrm{SplitTime}}$	22 154	3004	2253	15 771	556
$\theta_{\mathrm{SplitGeo}}$	17 648	1126	751	15 020	532
NDir	15 771	751	370	14 645	524
LDir	13 518	374	325	14 269	499
SDir	12 877	4	0	13 466	475

(iii) *Error estimate from the MPE reconstruction* (σ): The directional error ellipse for the MPE log-likelihood reconstruction was estimated following [29]. It provides an event by event 1σ uncertainty of the arrival direction in the likelihood function used in the reconstruction of muon tracks.

(iv) *Minimum zenith angle of a two-muon reconstruction* ($\theta_{\mathrm{SplitGeo}}$, $\theta_{\mathrm{SplitTime}}$): A substantial fraction of the atmospheric muon background results from two or more muons triggering the IceCube detector during the trigger window. In order to reduce this background, two muons were reconstructed for each event after splitting the triggered DOMs in two groups. The separation is accomplished one of two ways. The first uses a geometric approach by constructing a plane perpendicular to the MPE-reconstructed track while containing the average Cherenkov photon arrival positions. The second method is performed temporally by using the mean Cherenkov photon arrival time. Each group of DOMs is used to reconstruct a single muon hypothesis resulting in two reconstructed muon tracks. Requiring the zenith angle from both reconstructed tracks to traverse through the Earth reduces the coincident atmospheric muon background.

(v) *Log-likelihood ratio between a zenith-weighted Bayesian reconstruction and a standard reconstruction*: The Bayesian likelihood ratio compares the hypothesis of an up-going muon track with the alternative hypothesis of a down-going muon track consistent with the known zenith-dependent flux of atmospheric muons. The Bayesian likelihood reconstruction is performed by minimizing the product of the standard likelihood and a Bayesian prior. The Bayesian prior is based on the known zenith dependence of the down-going muon flux. Since the prior goes to zero near the horizon, the reconstruction always results in a down-going muon. Low values of the negative log-likelihood ratio support the alternative hypothesis of a down-going muon, whereas higher values indicate an up-going muon track. Further details are found in Ref. [28]. The likelihood ratio is zenith-dependent and our selection criterion based on this quality parameter varies with the zenith angle of the MPE-reconstructed track.

(vi) *Log-likelihood ratio between a zenith-weighted two-muon Bayesian reconstruction and a standard reconstruction*: The two-muon Bayesian likelihood ratio compares the hypothesis of a single up-going muon track with the alternative hypothesis of two down-going muon tracks consistent with the known zenith-dependent flux of atmospheric muons. Two down-going muons were reconstructed separately using the DOM splitting strategies discussed above. Each muon is reconstructed with a Bayesian prior defined with a zenith-dependent weight of the atmospheric muon flux. This observable is constructed to reject misreconstructed coincident atmospheric muons. As in the single muon case, low values support the alternative hypothesis of two down-going atmospheric muons whereas higher values indicate an up-going muon track.

(vii) *Number of DOMs with direct photoelectrons (NDir)*: The number of Cherenkov photons arriving between -15 and $+75$ ns of their expected unscattered photon arrival times from a reconstructed track is known as the number of direct photons, or NDir [28]. More direct photons would indicate a better reconstructed track.

(viii) *Direct length of the reconstructed track (LDir)*: The number of direct photons, NDir, are projected back onto the reconstructed track. The direct

length, LDir [28], is the maximum separation distance between these projected photons.

(ix) *Smoothness of the reconstructed track (SDir)*: The direct photons (NDir) are again projected back onto the reconstructed track. The smoothness, SDir, is a measurement of how uniformly distributed these projected photons are along the reconstructed track. The smoothness parameter is defined between −1 and 1. Positive values of smoothness indicate that the projected photons cluster at the beginning of the track, whereas negative values of smoothness indicate there are more at the end of the track. A smoothness that is close to 0 indicates a uniform distribution of projected Cherenkov photons. Further details of the smoothness parameter can be found in Ref. [28].

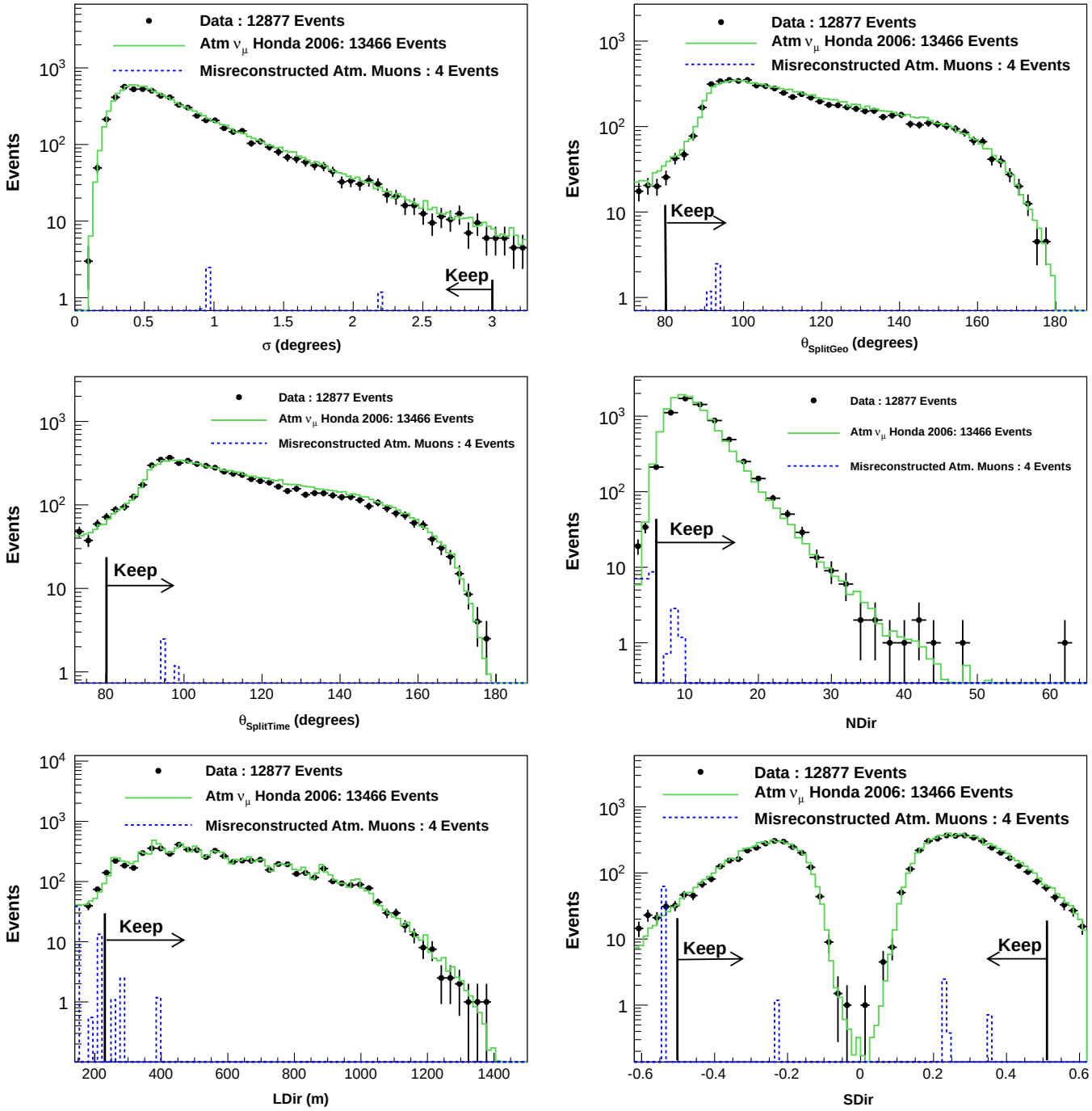

FIG. 2 (color online). Track quality observables for data (black), atmospheric neutrino simulation (green), and misreconstructed atmospheric muon simulation (blue) after all analysis cuts have been applied.

After all analysis level cuts have been applied, we were left with 12 877 candidate neutrino events below the horizon for the IceCube 40-string data set [30]. These cuts were designed, in particular, to maximize the retention efficiency of the simulated E^{-2} astrophysical neutrino flux, which is 35.1% with respect to up-going events passing the level 1 filter. The final analysis level (after all analysis cuts have been applied) distributions for the track quality observables summarized above are shown in Figs. 2 and 3 for data and Monte Carlo simulation. The zenith distribution at the final analysis level is shown in Fig. 4. The background atmospheric muon contamination was estimated to be 4 events in the final sample with a relative error of 60%. The background contamination was estimated from simulated down-going atmospheric muons that survived the analysis cuts. To estimate the background contamination, one would ideally have as much simulated background live time as the data. In practice, the simulated background live time was significantly less than the live time of the data with 11 simulated days over all energies. A weighting

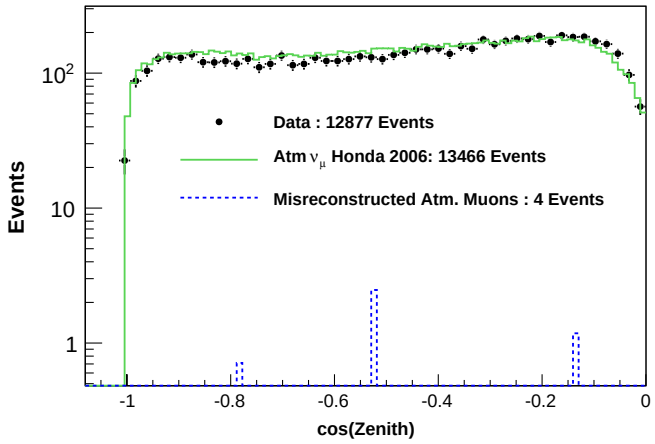

FIG. 4 (color online). The zenith angle distribution at final analysis level for 375.5 days of IceCube 40-string data (black) and atmospheric neutrino Monte Carlo (green).

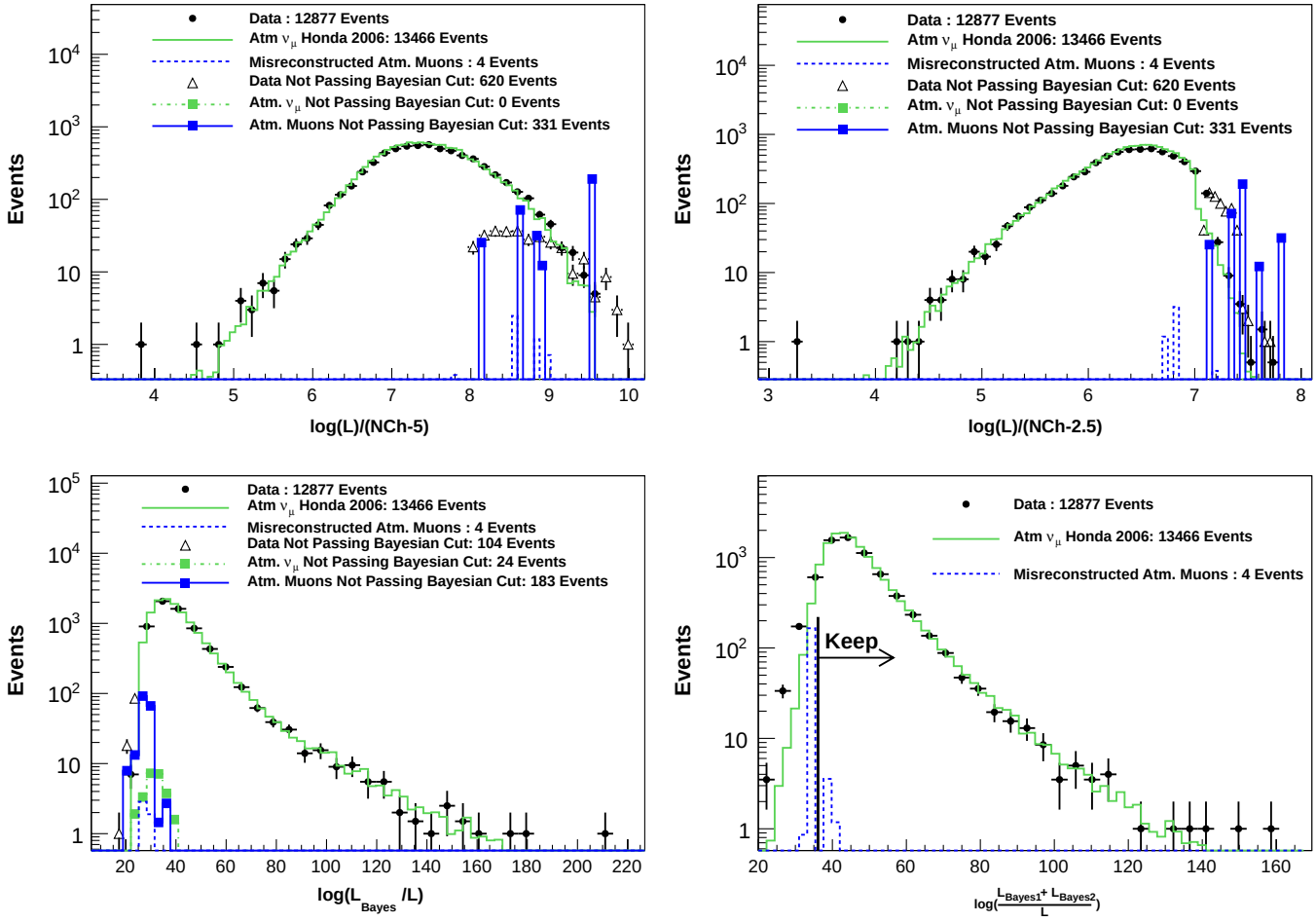

FIG. 3 (color online). Reduced log-likelihood and Bayesian likelihood ratio quality observables for data (black), atmospheric neutrino simulation (green), and atmospheric muon simulation (blue) after all analysis cuts have been applied. Events that do not pass the final two-dimensional quality criteria for the reduced log-likelihood and the Bayesian likelihood ratio are also shown.

scheme was used to increase the number of generated events at high energies resulting in 240 days of equivalent background live time above a primary cosmic-ray energy of 100 TeV. The simulated atmospheric muons over all energy decades were then extrapolated to 1 yr of live time.

The efficiency of neutrino detection for a particular analysis, which includes the efficiency of the analysis level cuts and physical effects like the absorption due to the Earth, can be characterized by the effective area which is defined as the area $A_{\rm eff}(E, \theta, \phi)$ of a detector that would have a 100% neutrino detection efficiency. The total number of detected events is

$$N_{\rm events} = \int dE_\nu d\Omega dt \Phi_\nu(E_\nu, \theta, \phi) A_{\rm eff}(E, \theta, \phi). \quad (1)$$

Figure 5 shows the effective area for $\nu_\mu + \bar{\nu}_\mu$ as a function of energy for this analysis averaged over different zenith angle ranges.

The final sample of candidate neutrino events is analyzed for the presence of astrophysical neutrinos. The astrophysical models considered predict a flavor ratio at the source of $\nu_\mu:\nu_e:\nu_\tau = 2:1:0$, which subsequently oscillate to a flavor ratio of $\nu_\mu:\nu_e:\nu_\tau = 1:1:1$ at Earth. Tau neutrinos that propagate through the Earth undergo a regeneration effect with a branching ratio $\tau \rightarrow \mu\nu_\mu\nu_\tau$ of 17% and this ν_μ contribution was taken into account by incorporating a separate ν_τ Monte Carlo simulation. The final astrophysical Φ_μ results were derived assuming a flavor ratio of $\nu_\mu:\nu_e:\nu_\tau = 1:1:1$ at Earth. As discussed in Sec. II, evidence for a diffuse astrophysical ν_μ flux would manifest in the IceCube detector as a hardening at the high-energy tail of the reconstructed energy observable distribution above the expectation from the atmospheric ν_μ spectrum. The energy-correlated observable used in the analysis is the muon energy loss per unit length and is described in the next section.

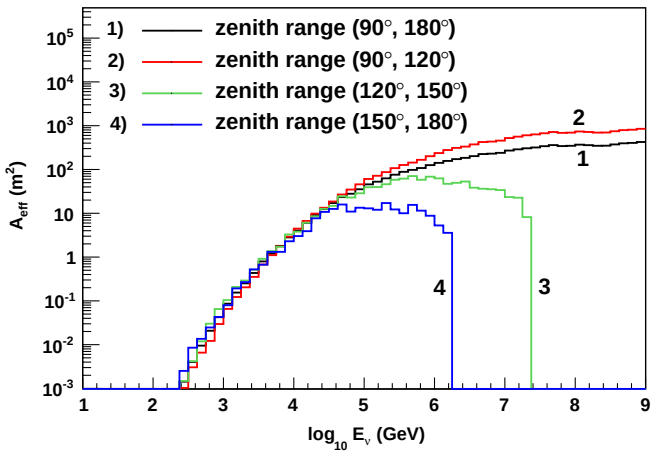

FIG. 5 (color online). Effective area for $\nu_\mu + \bar{\nu}_\mu$ as a function of the true neutrino energy in intervals of the true zenith angle of the neutrino. The angle-averaged area is represented by the solid black line.

C. Energy reconstruction

It was natural in this analysis to use the average muon energy loss per meter ($dE_{\rm reco}/dX$) as the energy-correlated observable since IceCube measures the muon energy loss (and not the muon energy directly) in the form of the Cherenkov photons emitted by the various stochastic muon energy loss mechanisms. In order to estimate $dE_{\rm reco}/dX$ from the observed collection of Cherenkov photoelectrons (denoted by $\{n\}$) and the expected Cherenkov photoelectron profile (denoted by μ and is explicitly a function of dE/dX), a log-likelihood based reconstruction method is used. There is an observed $\{n\}$ and expected μ for every DOM in the detector. With an observed photoelectron collection $\{n\}$ given an expected photoelectron distribution $\mu(dE/dX)$ binned into N bins of photoelectrons in a single DOM, a Poisson likelihood function yields

$$\log L\left(\frac{dE_{\rm reco}}{dX} \,\middle|\, \{n\}\right) = \sum_{i=1}^{N} n_i \log\mu_i - \mu_i, \quad (2)$$

where n_i and μ_i are the observed and expected number of photoelectrons in the ith bin, respectively. The Cherenkov photoelectrons are binned according to their respective arrival times at the DOM. To obtain the total likelihood function for the detector, the log-likelihood values of the individual DOMs were summed together:

$$\log L_{\rm total} = \sum_{j=1}^{N_{\rm DOMs}} \log L_j. \quad (3)$$

The direction and geometry of the muon were fixed to the results of the MPE reconstruction. The muon light profile $\mu(dE/dX)$ was parametrized in terms of the stochastic cascade energy which was varied until the likelihood function was maximized. The estimation of $dE_{\rm reco}/dX$ is contingent on modeling μ, which depends both on the light yield of the muon and the optical properties of the South Pole ice. Incorporating the muon light yield to the likelihood fit proved a challenge due to the stochastic energy loss processes of pair production, photonuclear interactions, and bremsstrahlung radiation which dominate over continuous energy losses above $\gtrsim 1$ TeV. The relationship is approximately linear in the stochastic energy regime, however, with $dE/dX = a + bE$ with $a = 0.259\,58$ GeV/mwe and $b = 3.5709 \times 10^{-4}$ mwe^{-1} in ice [31]. The continuous and stochastic energy losses were parametrized by the coefficients a and b, respectively, and both are written in terms of meters of water equivalent (mwe). The reconstruction algorithm therefore modeled the stochastic energy loss of a muon as uniform along the track.

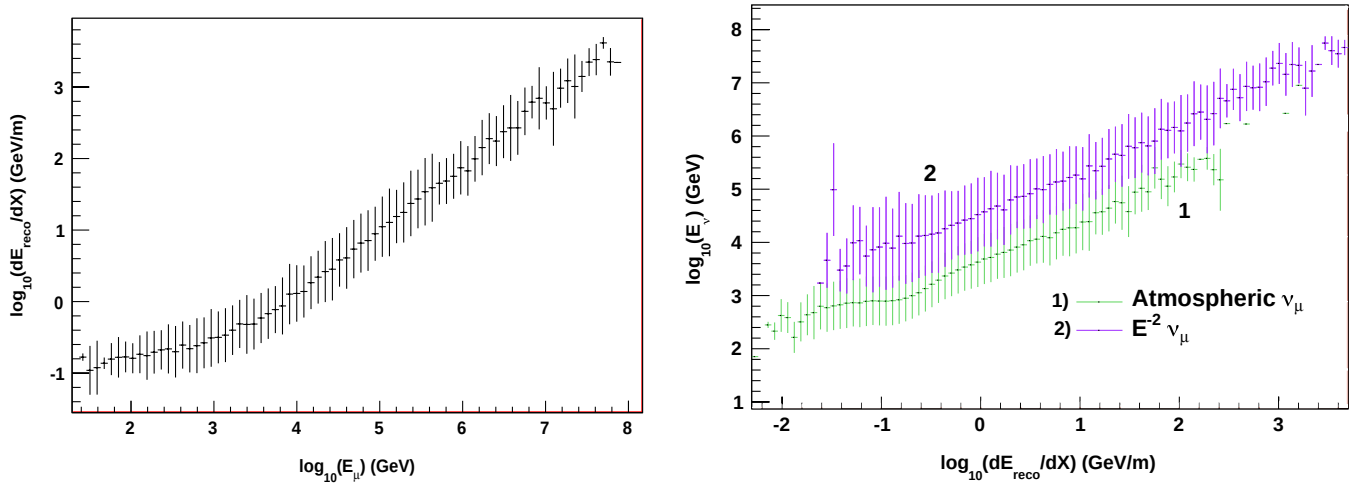

FIG. 6 (color online). The left plot shows a profile of the average reconstructed muon energy loss dE_{reco}/dX vs the true energy of the muon at closest approach. The error bars indicate the root mean square of the reconstructed dE/dX for a given slice in the parent muon energy. The right plot shows a profile of the energy of the primary neutrino for different bands in reconstructed dE/dX. The error bars indicate the root mean square of the parent neutrino energy. Shown are spectra for atmospheric neutrinos and a hypothetical E^{-2} astrophysical ν_μ flux.

The uniform energy loss model allows one to differentiate Eq. (2) with respect to a muon energy scale factor. This leads to an analytic solution for dE_{reco}/dX in terms of the ratio of the total observed charge across all DOMs to the total predicted charge. The dE/dX reconstruction algorithm incorporated the optical properties of the South Pole ice into the reconstruction. The dE/dX reconstruction algorithm did not account for Cherenkov light from the hadronic shower initiated by the charged-current neutrino interaction and only reconstructed the energy loss due to the muon track itself. This was not a limitation here, since the majority of events in our final sample ($\sim 73\%$) are through-going tracks where the neutrino interaction occurred outside the instrumented volume of the detector.

The performance of the dE/dX reconstruction was characterized using simulated high-energy muons and neutrinos that satisfy the analysis level selection criteria applied to the data. Since IceCube measures the energy loss of the muon in the form of Cherenkov light from stochastic showers, we first characterized the intrinsic resolution of the dE/dX reconstruction by using a sample of simulated high-energy muons. The correlation of dE_{reco}/dX with the muon energy closest to the center of the IceCube array is given in the left-hand plot of Fig. 6. The relationship is

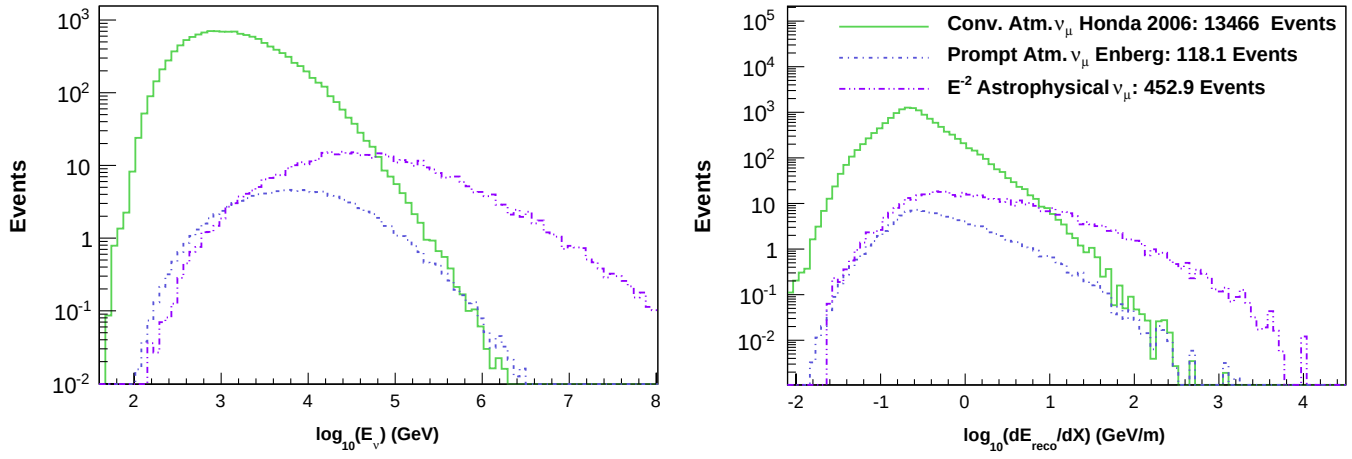

FIG. 7 (color online). Simulated neutrino energy distribution (left plot) and the simulated reconstructed muon energy loss distribution (right plot) of the final event sample for the Honda *et al.* conventional atmospheric ν_μ (green) flux model, the Enberg *et al.* prompt atmospheric ν_μ (light blue) flux model, and an astrophysical E^{-2} (purple) flux with a normalization of $N_a = 10^{-7}$ GeV cm^{-2} s^{-1} sr^{-1}.

linear over a large energy range. The correlation changes for energies below 1 TeV since the energy loss is no longer stochastic and the Cherenkov light output is nearly independent of energy. The spread in $dE_{\rm reco}/dX$ does not vary strongly as a function of the muon energy. The muon energy resolution over all energy decades in the stochastic energy regime above a TeV of the dE/dX reconstruction is 0.27 in $\log(E)$. The energy resolution was estimated from the 1σ width of a Gaussian fit to the reconstructed dE/dX distribution over all energies. The right-hand plot of Fig. 6 shows a profile of the simulated neutrino energy for conventional atmospheric neutrinos and astrophysical neutrinos vs $dE_{\rm reco}/dX$. Muons of a given energy would result in a measured $dE_{\rm reco}/dX$ distribution with a mean and root mean square spread as indicated by the left-hand plot of Fig. 6 independent of the primary energy spectrum. An estimate of the parent neutrino energy from a given measured $dE_{\rm reco}/dX$, however, depends on the assumed primary energy spectrum.

The simulated $dE_{\rm reco}/dX$ response of the IceCube 40-string detector at final analysis level to the Honda *et al.* conventional atmospheric neutrino flux [10], the Enberg *et al.* prompt atmospheric neutrino flux [11], and a hypothetical astrophysical E^{-2} flux is shown in Fig. 7. It clearly shows how the different parent spectra map into distinguishable reconstructed muon energy spectra.

V. ANALYSIS METHOD

To test the compatibility of the observed $dE_{\rm reco}/dX$ distribution in the data set with the hypotheses of muons arising from conventional atmospheric ν_μ, prompt atmospheric ν_μ, and astrophysical ν_μ while incorporating various sources of systematic uncertainty, we incorporated the frequentist approach suggested by Feldman [32]. The *profile likelihood construction* procedure extends the original frequentist method of Feldman and Cousins [33] in order to incorporate sources of systematic uncertainties parametrized as nuisance parameters in the analysis.

A. Profile likelihood construction

The profile likelihood construction method results in fully frequentist confidence intervals for the physics parameters of interest (denoted by θ_r) while using values of the nuisance parameters (denoted by θ_s) that fit the data the best. Specifically, we first constructed a Poisson likelihood function and binned our $dE_{\rm reco}/dX$ observable distribution into N bins:

$$L(\{n_i\}|\{\mu_i(\theta_r,\theta_s)\}) = \prod_{i=1}^{N} \frac{e^{-\mu_i}}{n_i!}\,\mu_i^{n_i}, \tag{4}$$

where n_i and μ_i denote the observed and expected event counts in the ith $dE_{\rm reco}/dX$ bin, respectively. We then iterated over the physics parameter space and calculated the profile likelihood [34] ratio test statistic R_p at each point θ_r. Defining $\mathcal{L} = -2\log(L)$,

$$\begin{aligned} R_p(\theta_r) &= \mathcal{L}(\theta_r,\hat{\hat{\theta}}_s) - \mathcal{L}(\hat{\theta}_r,\hat{\theta}_s) \\ &= -2\log\left(\frac{L(\{n_i\}|\{\mu_i(\theta_r,\hat{\hat{\theta}}_s)\})}{L(\{n_i\}|\{\mu_i(\hat{\theta}_r,\hat{\theta}_s)\})}\right) \\ &= 2\sum_{i=1}^{N}\left(\mu_i - \hat{\mu}_i + n_i\log\frac{\mu_i}{\hat{\mu}_i}\right), \end{aligned} \tag{5}$$

where $\hat{\mu}_i = \mu_i(\hat{\theta}_r,\hat{\theta}_s)$ and $\mu_i = \mu_i(\theta_r,\hat{\hat{\theta}}_s)$. $\hat{\theta}_r$ and $\hat{\theta}_s$ denote the values of the physics and nuisance parameters that globally minimize the profile likelihood $\mathcal{L}(\hat{\theta}_r,\hat{\theta}_s)$ and therefore describe the data the best. The value of the nuisance parameter $\hat{\hat{\theta}}_s$ conditionally minimizes the profile likelihood $\mathcal{L}(\theta_r,\hat{\hat{\theta}}_s)$ at the physics parameter point θ_r. The profile likelihood test statistic was marginalized over nuisance parameters in the likelihood ratio such that confidence intervals were constructed solely for the physics parameters of interest.

Confidence intervals were constructed at confidence level α by comparing the profile likelihood test statistic to a critical value $R_{p,\rm crit}$ at each point θ_r. The critical profile likelihood value determines if a hypothesis is accepted or rejected at a certain confidence level. Following the prescription outlined in Refs. [32,33], we defined $R_{p,\rm crit}(\theta_r)$ by examining the spread of the profile likelihood test statistic $R_p(\theta_r)$ caused by statistical fluctuations. This was facilitated by generating a number of Monte Carlo experiments to obtain the distribution of $R_p(\theta_r)$ at each physics point θ_r while fixing the values of the nuisance parameters to $\hat{\hat{\theta}}_s$. Confidence intervals were constructed at confidence level α by finding the critical value of the profile likelihood, $R_{p,\rm crit}(\theta_r)$, such that the fraction α of experiments at θ_r satisfied $R_p(\theta_r) < R_{p,\rm crit}(\theta_r)$. The acceptance region is the parameter space $\{\theta_r\}$ such that $R_{p,\rm data}(\theta_r) < R_{p,\rm crit}(\theta_r)$ at a chosen confidence level α. By utilizing the profile likelihood distribution to determine the confidence level, we have used the likelihood ratio as an ordering principle in order to sort the possible experimental outcomes by increasing statistical significance.

B. Systematic uncertainties

Systematic errors were incorporated into the analysis as nuisance parameters in the likelihood. The profile likelihood construction method discussed in the last section was used to define confidence regions for the physics parameters of interest while incorporating the various sources of systematic uncertainty outlined in this section. This work considered sources of systematic errors that affect the shape and overall normalization of the observed

dE_{reco}/dX distribution. The sources of systematic uncertainty are summarized in Table III.

One of the largest sources of systematic uncertainty is the overall normalization of the atmospheric neutrino flux. The model used in this analysis for the conventional component of the atmospheric neutrino flux was derived by Honda *et al.* [10], where the uncertainty in the absolute normalization was estimated to be $\pm 25\%$. The prompt component of the atmospheric neutrino flux has yet to be experimentally measured and there exists a large range in the overall normalization as calculated in various model predictions. The baseline model used in this analysis for the prompt component of the atmospheric neutrino flux is the calculation from Enberg *et al.* [11] where the authors quoted a standard perturbative QCD model prediction with an asymmetric error range in the overall flux normalization of -44% to $+25\%$.

The spectral shape of the atmospheric neutrino flux is affected by the uncertainty in the spectral slope of the primary cosmic-ray spectrum. The uncertainty in the primary cosmic-ray spectrum was estimated by considering the uncertainty in the spectral slopes of cosmic-ray protons (which comprise 79% of the flux) and of helium nuclei (15% of the flux). The remaining 6% predominately consists of elements heavier than helium. Gaisser *et al.* [35] estimated the spectral slope uncertainty for protons to be ± 0.01 and for helium nuclei to be ± 0.07. Scaling the individual spectral index uncertainties by the fraction of the total flux for the respective component gave an uncertainty in the primary cosmic-ray spectral slope of ± 0.03. This range is valid for a primary cosmic-ray energy up to about 1 PeV. Above this energy appears a region between 1 and 10 PeV known as the knee where the primary cosmic-ray spectrum steepens [36]. The cosmic-ray composition around the knee is still an active area of research. The nominal prediction of the model calculated in Ref. [10] was calculated up to a neutrino energy of only 10 TeV. We extrapolated the Honda *et al.* model beyond this energy by assuming the model followed its approximate $E^{-3.7}$ shape above 10 TeV. We note that such an extrapolation does not reflect the steepening in the spectrum expected above 1 PeV/nucleon as a consequence of the knee.

There are two main sources of systematic uncertainties which affect the response of the IceCube detector to Cherenkov light. The first is the uncertainty in the absolute sensitivity of the digital optical module. The DOM sensitivity was assumed to be dominated by the uncertainty in the absolute efficiency of the photomultiplier tube which was measured to be $\pm 8\%$ [15]. The DOM sensitivity is further reduced by a shadowing effect from the main cable and the magnetic shield in the DOM, which reduces the sensitivity by 7%. The second dominant source of systematic uncertainty affecting the detector response is the uncertainty in the measured properties of the glacial ice at the South Pole. The measured uncertainty in the scattering and absorption coefficients of the South Pole ice was measured to be $\pm 10\%$ [18] at a flasher LED wavelength of 405 nm.

Other relatively minor sources of systematic error were quantified with dedicated simulation studies. The uncertainty in the charged-current, deep-inelastic neutrino-nucleon cross section was calculated in [37] to be $\pm 3\%$ using the parton distribution function error tables from [24] and the error calculation prescription in Ref. [38]. The 3% uncertainty in the cross section corresponds to a 3% uncertainty in the overall neutrino event rate. The uncertainty in the muon energy loss cross sections was estimated from [26] to be 1% which has a negligible effect on the overall event rate since a decrease or increase in the stochastic cross sections is accompanied by a corresponding increase or decrease in the muon range. The uncertainty in the density of the bedrock under the polar ice was measured to be 10% [39]. This provided a negligible difference in the atmospheric neutrino event rates of $<0.1\%$, since the increase in the neutrino interaction probability is offset by a corresponding decrease in the range of the muon. The background contamination in the final event sample was estimated to be less than 1%, and was therefore a negligible source of systematic uncertainty in the analysis.

TABLE III. Systematic uncertainties in the atmospheric neutrino flux and the detector response that affect the shape and overall normalization of the dE_{reco}/dX observable. The effect on the rate of triggered atmospheric ν_μ is shown in the third column.

Systematic uncertainty	Magnitude	Atmospheric ν_μ rate
Conventional atmospheric $\nu_\mu + \bar{\nu}_\mu$ flux	$\pm 25\%$	$\pm 25\%$
Prompt atmospheric $\nu_\mu + \bar{\nu}_\mu$ flux	-44%, $+25\%$	-44%, $+25\%$ [a]
Cosmic-ray spectral slope	± 0.03	Negligible
DOM sensitivity	$\pm 8\%$	$\pm 15\%$
Scattering and absorption coefficients	$\pm 10\%$	-13.5%, $+14.2\%$
Neutrino-nucleon cross section	$\pm 3\%$	$\pm 3\%$
Muon energy loss	$\pm 1\%$	Negligible
Bedrock density	$\pm 10\%$	Negligible

[a]The asymmetric error range in the overall flux normalization of the prompt atmospheric neutrino flux only affects the overall rate of prompt atmospheric neutrinos.

C. Final analysis parameters

The systematic errors summarized in Table III were incorporated into the profile likelihood as nuisance parameters. During minimization, each nuisance parameter was allowed to vary freely within the allowed range around its nominal value. The nominal values of the nuisance parameters correspond to the predictions of the Honda *et al.* model for the conventional atmospheric flux and baseline values as given by simulation for the other nuisance parameters. Each point in the likelihood space gave a specific prediction for the dE_{reco}/dX observable, and the profile construction method was used to define confidence regions for the physics parameters of interest.

The likelihood methodology could be used for two main analyses. The primary analysis is the search for a diffuse astrophysical ν_μ signal while simultaneously fitting for a potential prompt component of the atmospheric ν_μ flux. In the absence of any signal, the profile likelihood construction could be used to measure the conventional atmospheric neutrino flux.

The generic astrophysical diffuse ν_μ flux was parametrized as an E^{-2} spectrum and the normalization is the main physics parameter of interest:

$$\Phi_a = N_a E^{-2}, \tag{6}$$

where N_a has units of $\mathrm{GeV\,cm^{-2}\,s^{-1}\,sr^{-1}}$. Astrophysical models that do not predict an E^{-2} spectral shape were also considered in this work. The second physics parameter of interest denotes the absolute normalization of the prompt atmospheric neutrino flux:

$$\Phi_p = (1 + \alpha_p)\left(\frac{E}{E_{\mathrm{median},p}}\right)^{\Delta\gamma}\Phi_{\mathrm{Enberg}}, \tag{7}$$

where $1 + \alpha_p$ describes the deviation in the absolute normalization of the prompt atmospheric neutrino flux from the reference prompt atmospheric neutrino model which was taken to be the calculation from Enberg *et al*. The uncertainty in the primary cosmic-ray slope, $\Delta\gamma$, changes the shape of the predicted atmospheric neutrino flux and was a nuisance parameter in the analysis. It was allowed to float in the ± 0.03 range quoted in Table III. The shape dependent term was modeled by introducing an energy dependent weight $(E/E_{\mathrm{median},p})^{\Delta\gamma}$ where $E_{\mathrm{median},p}$ is the median neutrino energy at final purity level. The median energy is 7 TeV for the nominal prediction by Enberg *et al*.

The conventional component of the atmospheric neutrino flux was treated as a nuisance parameter in the main analysis and was parametrized in the same fashion as the prompt flux:

$$\Phi_c = (1 + \alpha_c)\left(\frac{E}{E_{\mathrm{median},c}}\right)^{\Delta\gamma}\Phi_{\mathrm{Honda}}, \tag{8}$$

where $1 + \alpha_c$ describes the deviation in the absolute normalization of the conventional atmospheric neutrino flux from the reference model by Honda *et al.*, $\Delta\gamma$ is again the uncertainty in the primary cosmic-ray slope, and $E_{\mathrm{median},c}$ is the median conventional atmospheric neutrino energy at final purity level. A shape dependent term was again modeled by an energy dependent weight $(E/E_{\mathrm{median},c})^{\Delta\gamma}$ where $E_{\mathrm{median},c}$ is 1.2 TeV for the nominal prediction by Honda *et al.*

The detector efficiency, denoted by ϵ, affects the overall event rate in the IceCube detector. The magnitude of this systematic error combines in quadrature the systematic uncertainties in the absolute DOM sensitivity, the neutrino interaction cross section, the muon energy loss cross sections, and the bedrock density giving an allowed range of $\pm 8.3\%$. The detector efficiency nuisance parameter was implemented by assuming that the absolute DOM sensitivity is independent of energy. Although the uncertainty in the absolute DOM sensitivity affects the event rate for lower-energy neutrino events more than higher-energy events, this energy dependence was neglected since the primary astrophysical diffuse search is dominated by the high-energy tail of the dE_{reco}/dX distribution.

The scattering and absorption coefficients $b(\lambda = 405\ \mathrm{nm})$ and $a(\lambda = 405\ \mathrm{nm})$ (both measured at a LED wavelength of 405 nm [18,40]) were implemented as discrete nuisance parameters in the likelihood function. This was facilitated by generating Monte Carlo neutrino simulation sets with the scattering and absorption coefficients increased by 10%, decreased by 10%, the scattering increased and absorption decreased by 10%, and the scattering decreased and absorption increased by 10%.

To summarize, the profile likelihood used in the main analysis incorporated two physics parameters and five nuisance parameters. In the absence of any signal, the conventional atmospheric neutrino flux measurement promotes the deviation in the conventional atmospheric flux $1 + \alpha_c$ and the uncertainty in the primary cosmic-ray spectral slope $\Delta\gamma$ to physics parameters, giving a likelihood with two main physics parameters and three nuisance parameters. The physics and nuisance parameters for the two analyses are summarized in Table IV.

TABLE IV. Physics parameters and nuisance parameters used for the astrophysical diffuse ν_μ search and the measurement of the atmospheric neutrino spectrum.

Analysis	Physics parameters	Nuisance parameters
Astrophysical ν_μ	N_a, $1 + \alpha_p$	$1 + \alpha_c$, $\Delta\gamma$, ϵ, $b(405)$, $a(405)$
Atmospheric ν_μ	$1 + \alpha_c$, $\Delta\gamma$	ϵ, $b(405)$, $a(405)$

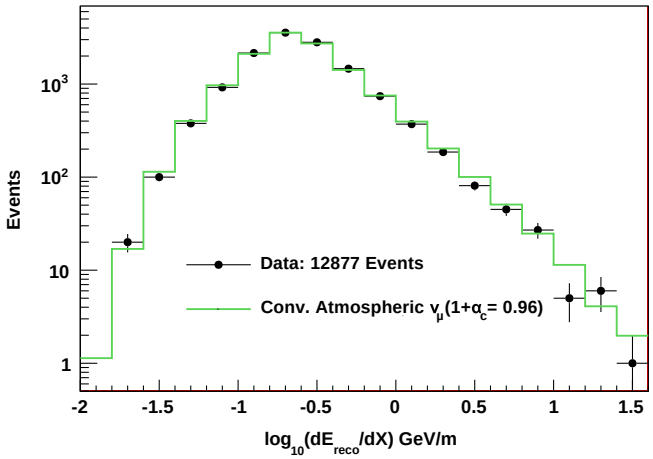

FIG. 8 (color online). The fitted muon energy loss distribution of the final event sample is shown. The best fit to the data (black, shown with 1σ error bars) consists only of conventional atmospheric ν_μ, and no evidence is found for a prompt atmospheric ν_μ flux or an astrophysical E^{-2} ν_μ flux.

D. Sensitivity and discovery potential

A blindness procedure was followed in order to prevent any inadvertent tuning of the purity cuts that would bias the analysis. To establish a context for the unblinded results, we quantified the limit setting potential of the analysis (the analysis sensitivity) and the ability to discover an astrophysical neutrino flux (the discovery potential). Specifically, the sensitivity is defined as the median 90% upper limit obtained over an ensemble of simulated experiments with no true signal. The discovery potential is defined to be the strength a hypothetical astrophysical ν_μ flux required to obtain a 5σ discovery in 90% of simulated experiments in the ensemble. The sensitivity of this analysis to a diffuse flux of astrophysical ν_μ with an E^{-2} spectrum is 1.22×10^{-8} GeV cm^{-2} s^{-1} sr^{-1} and the E^{-2} discovery potential is 6.1×10^{-8} GeV cm^{-2} s^{-1} sr^{-1}.

VI. RESULTS

After we performed the profile likelihood construction analysis on the $dE_{\rm reco}/dX$ distribution, no evidence was found for an astrophysical neutrino flux or a prompt component of the atmospheric neutrino flux. The fitted $dE_{\rm reco}/dX$ distribution is shown in Fig. 8 and the best fit values of the analysis parameters to the data are summarized in Table V. No evidence for a signal was seen, so upper limits were set for astrophysical neutrino flux models.

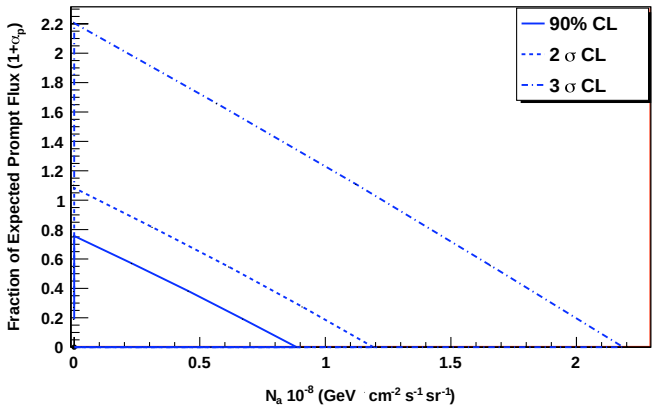

FIG. 9 (color online). Allowed regions for astrophysical muon neutrinos with an E^{-2} spectrum and prompt atmospheric neutrinos at 90%, 2σ, and 3σ confidence level. The lines indicate the boundary of the allowed region at the stated confidence level. The best fit point is indicated by the black dot at the origin.

A. Upper limits on astrophysical neutrino fluxes

The allowed regions for the normalization of the astrophysical flux N_a corresponding to an $E^{-2}\nu_\mu$ flux and the normalization for prompt atmospheric neutrinos are shown in Fig. 9. The upper limit for the astrophysical normalization N_a at 90% confidence level was obtained from Fig. 9 by finding the point on the 90% C.L. boundary along the null hypothesis of no prompt atmospheric neutrinos. The 90% upper limit on a hypothetical astrophysical $\Phi_{\nu_\mu} = N_a E^{-2}$ flux at Earth with systematic uncertainties included is $N_a^{90\%} = 8.9 \times 10^{-9}$ GeV cm^{-2} s^{-1} sr^{-1}. The analysis is sensitive in the energy range between 35 TeV and 7 PeV. The energy range was determined from MC simulation studies of the analysis sensitivity, which was calculated

TABLE V. Likelihood fit results and associated errors reported by the fit. Errors are quoted as 1σ unless otherwise noted. The allowed range of the nuisance parameters are also given as 1σ Gaussian constraints.

Parameter	Best fit	Error	Constrained range
N_a	0	8.9×10^{-9} $\frac{\rm GeV}{\rm cm^2\ s\ sr}$ (90% U.L.)	
$1 + \alpha_p$	0	0.73 (90% U.L.)	
$1 + \alpha_c$	0.96	± 0.16	± 0.25
$\Delta\gamma$	-0.032	± 0.014	± 0.03
ϵ	+2%	$\pm 8.3\%$	$\pm 8.3\%$
$b_e(\lambda = 405$ nm)	Nominal	$\pm 10\%$	$\pm 10\%$
$a(\lambda = 405$ nm)	Nominal	$\pm 10\%$	$\pm 10\%$

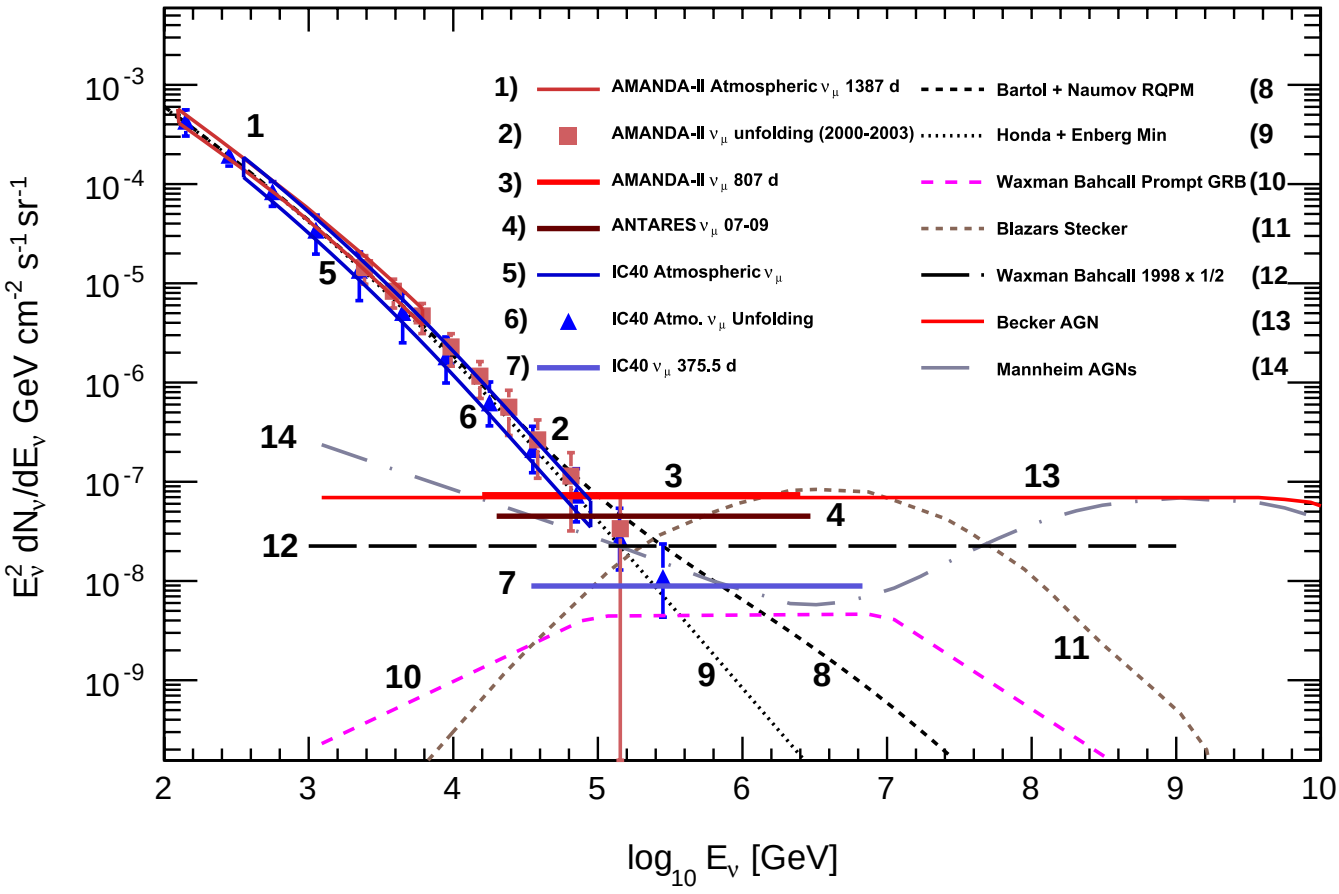

FIG. 10 (color online). Upper limits on an astrophysical ν_μ flux with an E^{-2} spectrum are shown along with theoretical model predictions of diffuse astrophysical muon neutrinos from different sources. The astrophysical $E^{-2}\nu_\mu$ upper limits shown are from AMANDA-II [49], ANTARES [50], and the current work utilizing the IceCube 40-string configuration (IC40 ν_μ375.5 d). The atmospheric ν_μ measurements shown are from AMANDA-II [47,51], the IceCube 40-string (IC40) unfolding measurement [45], and the current work (IC40 Atmospheric ν_μ).

to be 1.22×10^{-8} GeV cm^{-2} s^{-1} sr^{-1}. The energy range was determined by introducing an energy threshold and ceiling such that the analysis sensitivity changed by 5%. The 90% upper limit derived in this work on a hypothetical astrophysical ν_μ flux is compared to other ν_μ limits and flux models in Fig. 10.

Astrophysical neutrino models that do not predict an E^{-2} spectrum from various source classes were tested in the analysis. Of the models considered, this analysis was sensitive to the blazar model derived by Stecker [41], the active galactic nucleus (AGN) neutrino model derived by Mannheim [3], and the radio galaxy neutrino model from Becker, Biermann, and Rhode [2]. These models were rejected at the 5σ confidence level. The analysis also rules out the Waxman-Bahcall upper bound [1] at a 3σ confidence level. The upper limits on astrophysical ν_μ for the different models are summarized in Table VI. The upper limits for the models are expressed in terms of the model

TABLE VI. Upper limits for astrophysical ν_μ for different astrophysical models. The upper limits are expressed in terms of the model rejection factor [42], which is the percentage of the reference model rejected at the stated confidence level such that $\Phi_{\text{C.L}} = \text{MRF} \times \Phi_{\text{ref}}$.

Model	90% C.L.	3σ C.L.	5σ C.L	90% Energy range (TeV–PeV)
$E^{-2}(\frac{\text{GeV}}{\text{cm}^2\ \text{s}\ \text{sr}})$	0.89×10^{-8}	2.2×10^{-8}	4.0×10^{-8}	35–7
Waxman-Bahcall upper bound	0.4	0.97	1.78	35–7
Stecker blazar	0.1	0.32	0.42	120–15
BBR FSRQ	0.12	0.34	0.46	35–7
Mannheim AGN	0.05	0.21	0.4	9–1

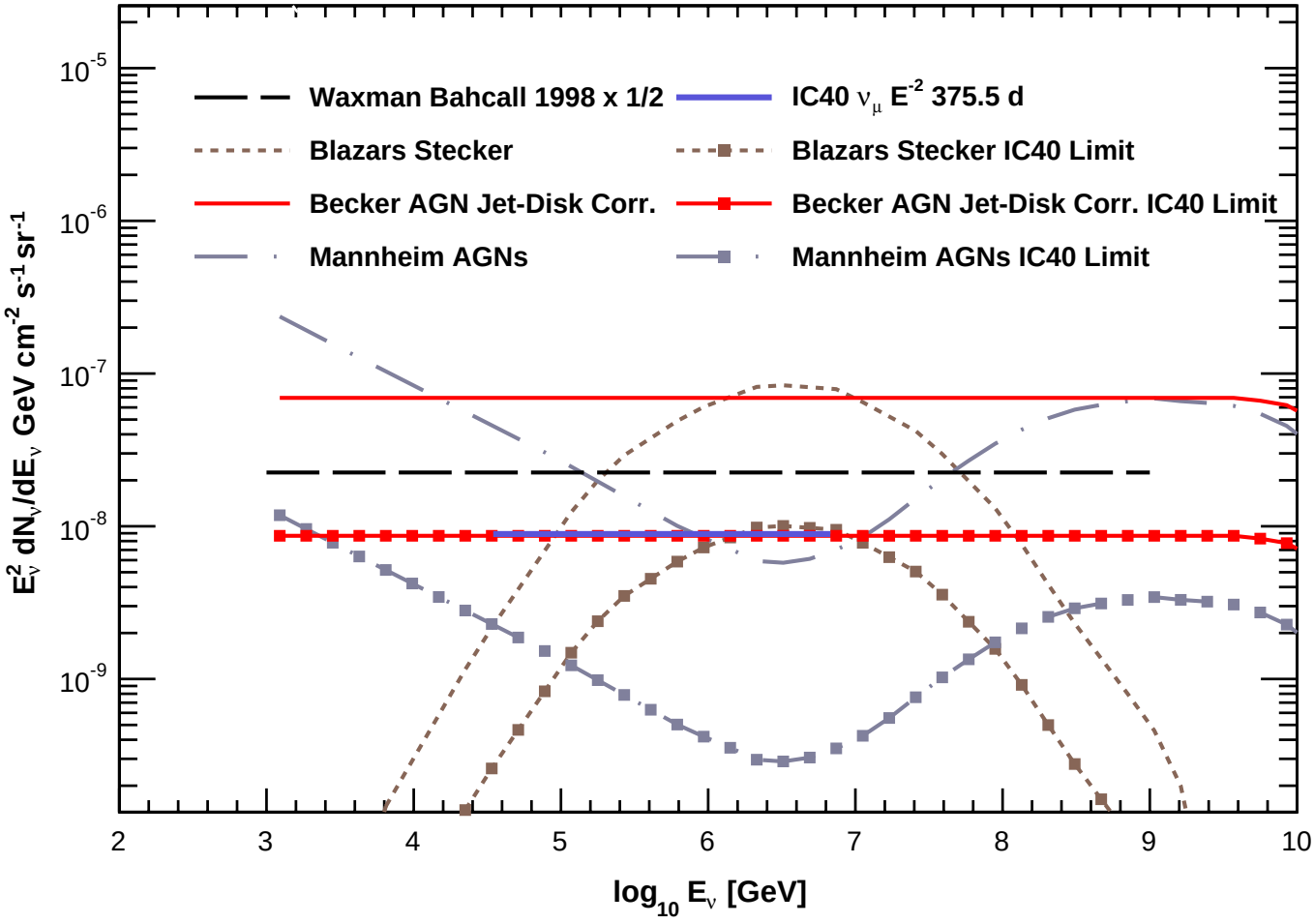

FIG. 11 (color online). Upper limits derived by this work utilizing the IceCube 40-string configuration (IC40) are shown for an E^{-2} astrophysical ν_μ flux and theoretical model predictions that do not predict an E^{-2} spectrum.

rejection factor [42], which in the context of this analysis is the percentage of the reference model rejected at the stated confidence level, such that $\Phi_{\mathrm{C.L}} = \mathrm{MRF} \times \Phi_{\mathrm{ref}}$. The 90% upper limits on these flux models are shown in Fig. 11. We note that the radio galaxy neutrino model from Becker, Biermann, and Rhode rejected at a 5σ confidence level was derived with a primary proton cosmic-ray energy spectrum of E^{-2} and an optical thickness $\tau = 0.2$. The authors summarized in Ref. [2] a range of neutrino flux models with different spectral shapes of the primary proton cosmic-ray spectrum and varying optical thickness which are below the sensitivity of these results.

B. Upper limits on prompt atmospheric neutrino flux models

This analysis showed no evidence for a prompt component to the atmospheric neutrino flux. Hypotheses other than the reference model from Enberg *et al.* are shown in the left-hand side in Fig. 12 and were tested in this analysis. The results of the prompt model tests are summarized in Table VII and on the right-hand side of Fig. 12. In the same fashion as the astrophysical model tests described above, the upper limits on prompt atmospheric neutrinos were expressed in terms of the model rejection factor. The standard calculation from Enberg *et al.* which is used as the reference flux in this analysis was rejected at 90% confidence level valid from an energy range between 9 and 613 TeV.

Under the assumptions of the present analysis, we reject the RQPM [12] (recombination quark parton model) at a 3σ confidence level, which strongly disfavors the authors' nonperturbative quantum chromodynamics (pQCD) approach to calculating the prompt flux. The maximum and minimum calculations from Enberg *et al.* represent an allowed theoretical uncertainty band due to the authors' choices of the parton distribution function (PDF), the charm quark mass, and the factorization scale which affect the pQCD calculation of the prompt atmospheric neutrino flux. The reference model used the MRST 2001 [43] for the PDF, a factorization scale $\mu_F = 2m_c$ where m_c is the charm quark mass, and a charm quark mass of 1.3 GeV.

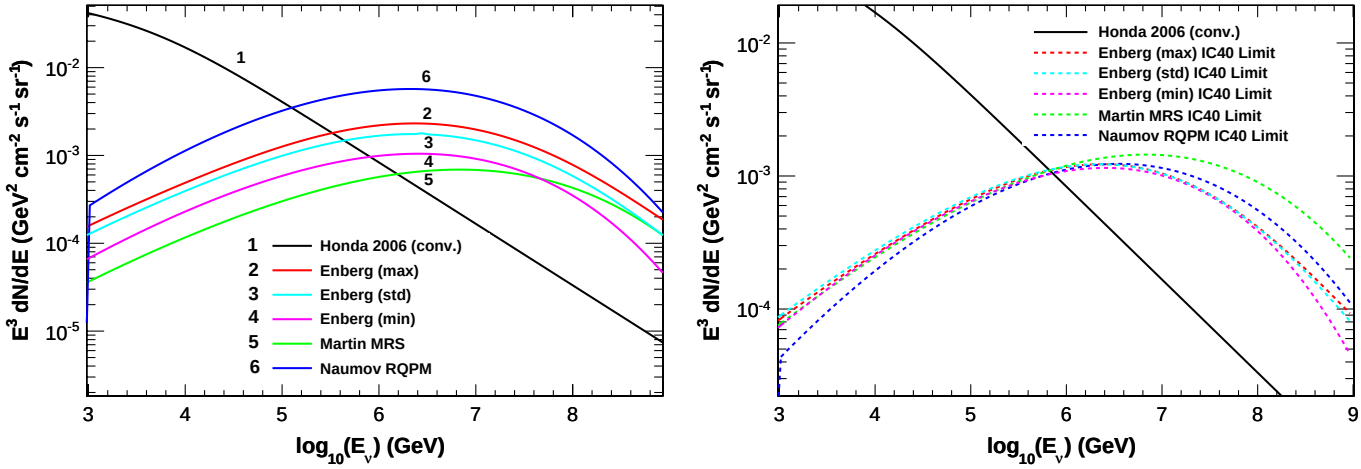

FIG. 12 (color online). The left plot shows the predicted prompt atmospheric neutrino fluxes averaged over zenith angle and multiplied by E^3 to enhance features. The Honda 2006 model is shown for comparison. The right plot shows the 90% confidence level upper limit on the prompt models.

The theoretical uncertainty represented by the minimum and maximum calculations was obtained by varying the quark mass between 1.3 and 1.5 GeV, varying the factorization scale between $\mu_F = m_c$ and $\mu_F = 2m_c$, and varying the PDFs by using MRST 2001 or CTEQ 6 [44]. We ruled out the maximum calculation at 95% C.L. and the standard prediction at 90% C.L. These limits favor the CTEQ 6 parameterization of the PDF, a lower quark mass, and a low factorization scale.

C. Measurement of the atmospheric neutrino spectrum

There was no evidence for astrophysical neutrinos or prompt atmospheric neutrinos in the final event sample, and therefore the final neutrino distribution was interpreted as a flux of conventional atmospheric muon neutrinos. The profile construction method was used to measure the atmospheric neutrino flux in order to determine the normalization and any change in shape from the reference atmospheric neutrino flux model considered. The best fit result of the atmospheric neutrino flux is of the form

$$\Phi_{\mathrm{BestFit}} = (0.96 \pm 0.16)\left(\frac{E}{1.17\ \mathrm{TeV}}\right)^{-0.032\pm0.014}\Phi_{\mathrm{Honda}}, \tag{9}$$

where the normalization of the atmospheric neutrino flux was found to be 4% ± 16% lower than the nominal prediction from Honda *et al.* and the spectral index was found to be steeper by $\Delta\gamma = -0.032 \pm 0.014$. The allowed regions of $(1 + \alpha_c)$ and $\Delta\gamma$ are shown with the band of allowed atmospheric neutrino spectra in Fig. 13. The displayed band of allowed atmospheric neutrino spectra in black in the right plot was constructed from the envelope of the set of curves allowed by the 90% boundary in the left plot. We note that our best fit for the spectral index rejected the nominal spectral index prediction from Honda *et al.* at a 95% confidence level, neglecting the theoretical uncertainty. The overall flux normalization is consistent with the nominal model prediction at 90% confidence level. The energy range of the atmospheric neutrino flux measurement is valid from 332 GeV to 84 TeV. This energy range was derived from the median atmospheric neutrino energy

TABLE VII. Upper limits on prompt atmospheric neutrinos for different models. The upper limits are expressed in terms of the model rejection factor [42], which is the percentage of the reference model rejected at the stated confidence level such that $\Phi_{\mathrm{C.L.}} = \mathrm{MRF} \times \Phi_{\mathrm{ref}}$.

Model	90%	95%	3σ	90% Energy range (TeV)
Enberg (minimum)	1.25	1.8	3.6	9–615
Enberg (standard)	0.73	1.1	2.2	9–613
Enberg (maximum)	0.53	0.85	1.89	9–610
Naumov RQPM	0.2	0.41	0.87	9–620
Martin MRS	2.1	4.0	8.9	9–613

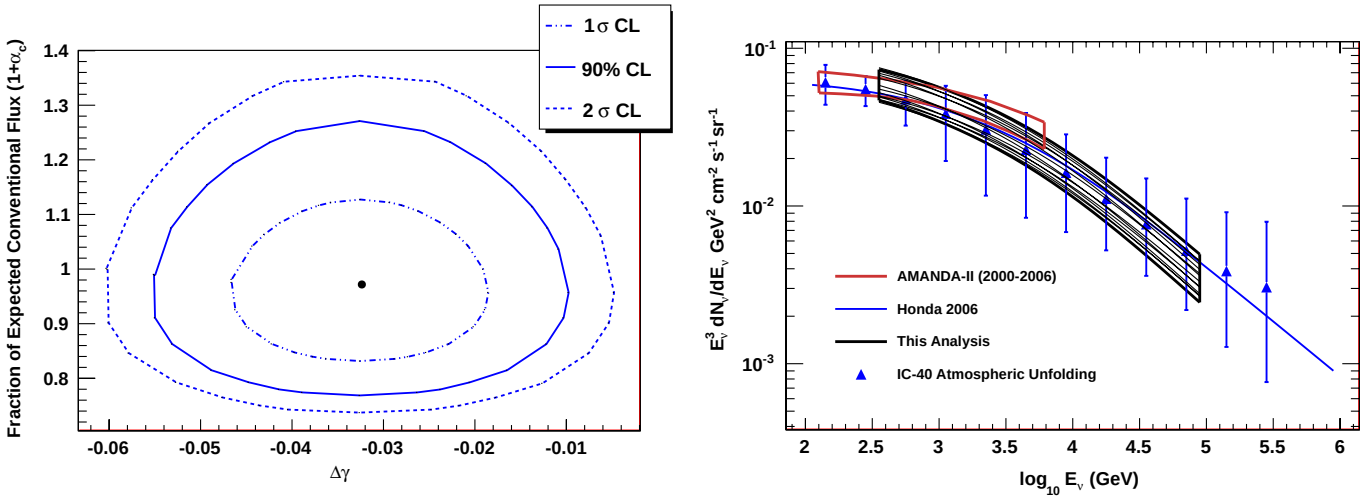

FIG. 13 (color online). The left plot shows allowed regions for the normalization $(1 + \alpha_c)$ and the change in spectral index $(\Delta\gamma)$ of the conventional atmospheric neutrino flux relative to Honda *et al.* [10]. The right plot compares the angle-averaged $\nu_\mu + \bar{\nu}_\mu$ measurement of the atmospheric neutrino flux of this work to the model prediction from Honda *et al.* The fluxes are multiplied by E^3 to enhance features. The displayed set of black curves is the band of allowed atmospheric neutrino spectra constructed from the 90% boundary of the left plot in this work as described in the text. Also shown (blue triangles) is the IceCube 40-string unfolding analysis [45], and the AMANDA-II (empty brown band) result [47].

as predicted by simulation for the lowest and highest dE_{reco}/dX values from the data.

Also shown in the right plot of Fig. 13 is the atmospheric neutrino unfolding analysis discussed in Ref. [45] where no prior assumption was made regarding the shape of the atmospheric neutrino spectrum, while this work parametrized the atmospheric neutrino flux as a power law. Such a bias in the prior assumption of the atmospheric neutrino flux resulted in tighter error bars than in the unfolding analysis.

VII. CONCLUSIONS AND OUTLOOK

To summarize, we have set the field's most stringent limit on astrophysical muon neutrinos from unresolved sources. The 90% upper limit on an astrophysical flux with an E^{-2} spectrum is 8.9×10^{-9} GeV cm^{-2} s^{-1} sr^{-1}, valid from the energy range of 35 TeV to 7 PeV. Several optimistic astrophysical neutrino production models have been rejected at a 5σ confidence level. We have set limits on the prompt component of the atmospheric neutrino flux, with a preference for perturbative QCD models in the energy range between 9 and 613 TeV. Finally, we have also measured the atmospheric muon neutrino flux from 332 GeV to 84 TeV and found a fit to the overall normalization of the atmospheric neutrino flux that is 4% lower than the calculation from Honda *et al.* [10]. The preferred spectrum is somewhat steeper than the assumed extrapolation of the Honda spectrum, perhaps reflecting the steepening of the spectrum associated with the knee, as discussed in Ref. [46]. Overall, our result here is consistent with other measurements made of the atmospheric neutrino flux with the IceCube detector. The 90% error band on the measured flux overlaps with the 90% error band of the result from IceCube's predecessor, the AMANDA-II experiment [47].

The 90% upper limits on the astrophysical ν_μ models and the prompt component of the atmospheric neutrino flux are dependent on the assumptions made on the conventional atmospheric neutrino flux. We extrapolated the model from Honda *et al.* above the maximum calculated energy of 10 TeV by assuming the conventional spectrum continued to follow its approximate $E^{-3.7}$ spectral shape. This extrapolation is dependent on the location and primary cosmic-ray composition of the knee which are currently not well known. The spectrum of all nuclei steepens in an energy region around 3 PeV total energy per nucleus. With standard assumptions about the composition, and assuming that the underlying physics depends on magnetic rigidity, the spectrum of protons must become steeper around 1 PeV or lower. This has the consequence that the spectrum of neutrinos from decay of pions and kaons must steepen at around 100 TeV [46], which is just in the crossover region for the prompt component. What is needed is a detailed calculation of atmospheric neutrinos based on a realistic treatment of the primary cosmic-ray spectrum and composition through the knee region that extends beyond the current limits of 10 TeV. Because of the steepening, the limits on prompt neutrinos in Fig. 12 will be relaxed to some extent. For future work, it is critically important also to obtain more precise measurements of the primary composition and spectra in the knee region. The KASCADE experiment [48] already suggests that the proton component

is suppressed in the knee region. IceCube itself, with its surface component IceTop, has the potential to measure the spectrum and composition in the knee region and beyond.

The stringent 90% upper limit on a diffuse astrophysical flux of muon neutrinos reported by this work implies that the IceCube detector in its 40 string configuration (as used in this analysis) is not yet sensitive enough to discover astrophysical neutrinos from unresolved sources. The full 86-string array has been completed during the 2010–2011 summer construction season at the South Pole. A 5σ discovery of an astrophysical $E^{-2}\nu_\mu$ flux at the 90% limit derived by this work will take three years of the full IceCube array.

This time scale for discovery can be made shorter by an improved understanding of the various sources of systematic uncertainty and considering new analysis techniques. With a proper measurement of the prompt component of the atmospheric neutrino flux, the time scale for discovery becomes more tractable. In this analysis we have not yet made use of the difference in angular behavior of prompt neutrinos (which are isotropic) and conventional atmospheric neutrinos (which have a higher intensity near the horizon). Analyses dedicated to the study of leptons from the decay of charmed mesons would also yield a better understanding of the physics of air showers and atmospheric neutrinos. Strategies other than using atmospheric ν_μ to search for the prompt component involve a thorough investigation of the down-going muon flux and a measurement of the atmospheric neutrino spectrum from ν_e. The measurement of the atmospheric ν_e flux has an advantage that the transition energy from conventional ν_e to prompt ν_e occurs at an order of magnitude lower in energy than in ν_μ.

The event selection in this analysis used the Earth as a filter to remove the large down-going atmospheric muon background. An improved simulation of atmospheric muons would allow a diffuse astrophysical ν_μ search to incorporate the down-going region in the analysis and search for astrophysical neutrinos over the entire sky. We note that there is a slight tilt in the measured angular distribution of atmospheric neutrinos with respect to our extrapolation based on the angular dependence in [10], as illustrated in Fig. 4. This discrepancy did not affect our limit on astrophysical ν_μ or our reconstructed atmospheric neutrino spectrum. However, understanding the origin of the discrepancy is important for future work.

Although this analysis focuses on ν_μ, IceCube is sensitive to all flavors of neutrinos. As the detector grows, reconstruction methods mature, and the understanding of the various sources of systematic uncertainty improve, it would be possible to combine event topologies from different neutrino flavors in a multiflavor analysis. A simultaneous search for neutrinos of all flavors from unresolved astrophysical sources would be significantly more sensitive than an analysis focusing exclusively on a single neutrino flavor.

ACKNOWLEDGMENTS

We acknowledge the support from the following agencies: U.S. National Science Foundation—Office of Polar Programs, U.S. National Science Foundation—Physics Division, University of Wisconsin Alumni Research Foundation, the Grid Laboratory of Wisconsin (GLOW) grid infrastructure at the University of Wisconsin–Madison, the Open Science Grid (OSG) grid infrastructure; U.S. Department of Energy, and National Energy Research Scientific Computing Center, the Louisiana Optical Network Initiative (LONI) grid computing resources; National Science and Engineering Research Council of Canada; Swedish Research Council, Swedish Polar Research Secretariat, Swedish National Infrastructure for Computing (SNIC), and Knut and Alice Wallenberg Foundation, Sweden; German Ministry for Education and Research (BMBF), Deutsche Forschungsgemeinschaft (DFG), Research Department of Plasmas with Complex Interactions (Bochum), Germany; Fund for Scientific Research (FNRS-FWO), FWO Odysseus programme, Flanders Institute to encourage scientific and technological research in industry (IWT), Belgian Federal Science Policy Office (Belspo); University of Oxford, United Kingdom; Marsden Fund, New Zealand; Japan Society for Promotion of Science (JSPS); the Swiss National Science Foundation (SNSF), Switzerland; A. Groß acknowledges support by the EU Marie Curie OIF Program; J. P. Rodrigues acknowledges support by the Capes Foundation, Ministry of Education of Brazil.

[1] E. Waxman and J. Bahcall, Phys. Rev. D **59**, 023002 (1998).
[2] J. Becker, P. L. Biermann, and W. Rhode, Astropart. Phys. **23**, 355 (2005).
[3] K. Mannheim, Astropart. Phys. **3**, 295 (1995).
[4] F. W. Stecker, Phys. Rev. D **72**, 107301 (2005).
[5] S. Hunter *et al.*, Astrophys. J. **481**, 205 (1997).
[6] A. Mücke *et al.*, Astropart. Phys. **18**, 593 (2003).
[7] S. Razzaque and P. Meszaros, Phys. Rev. D **68**, 083001 (2003).
[8] T. K. Gaisser, *Particle Physics and Cosmic Rays* (Cambridge University Press, Cambridge, England, 1991).
[9] G. Barr *et al.*, Phys. Rev. D **70**, 023006 (2004).
[10] M. Honda *et al.*, Phys. Rev. D **75**, 043006 (2007).

[11] R. Enberg *et al.*, Phys. Rev. D **78**, 043005 (2008).
[12] E. Bugaev *et al.*, Il Nuovo Cimento **12C**, 41 (1989).
[13] A. Martin *et al.*, Acta Phys. Pol. B **34**, 3273 (2003).
[14] A. Achterberg *et al.*, Astropart. Phys. **26**, 155 (2006).
[15] R. Abbasi *et al.*, Nucl. Instrum. Methods Phys. Res., Sect. A **618**, 139 (2010).
[16] R. Abbasi *et al.*, Nucl. Instrum. Methods Phys. Res., Sect. A **601**, 294 (2009).
[17] M. Ackerman *et al.*, J. Geophys. Res. **D13203**, 111 (2006).
[18] R. Abbasi *et al.* (unpublished).
[19] P. B. Price *et al.*, Geophys. Res. Lett. **27**, 2129 (2000).
[20] D. Heck *et al.*, CORSIKA: A Monte Carlo Code to Simulate Extensive Air Showers, Tech. Rep. (FZKA, 1998).
[21] E. Ahn *et al.*, Phys. Rev. D **80**, 094003 (2009).
[22] J. Hoerandel, Astropart. Phys. **21**, 241 (2004).
[23] A. Gazizov and M. Kowalski, Comput. Phys. Commun. **172**, 203 (2005).
[24] H. Lai *et al.*, Eur. Phys. J. C **12**, 375 (2000).
[25] A. Dziewonski and D. Anderson, Phys. Earth Planet. Int. **25**, 297 (1981).
[26] D. Chirkin and W. Rhode, arXiv:hep-ph/0407075v2.
[27] J. Lundberg *et al.*, Nuclear Instrumentation and Methods A **581**, 619 (2007).
[28] J. Ahrens *et al.*, Nuclear Instrumentation and Methods A **524**, 169 (2004).
[29] T. Neunhoer, Astropart. Phys. **25**, 220 (2006).
[30] A table of the event sample used in this analysis is available at http://www.icecube.wisc.edu/science/data/.
[31] W. Rhode and D. Chirkin, in *Proceedings of the 27th International Cosmic Ray Conference* (Copernicus Gesellschaft, Hamburg Germany, 2001), Vol. 3, p. 1017.
[32] G. J. Feldman, in Workshop on Confidence Intervals, Fermilab (2000) [http://www.hepl.harvard.edu/~feldman/Journeys.pdf].
[33] G. Feldman and R. Cousins, Phys. Rev. D **57**, 3873 (1998).
[34] A. Stuart *et al.*, *Kendall's Advanced Theory of Statistics* (John Wiley and Sons, Hoboken, NJ, 1999), 6th ed., Vol. 2A.
[35] T. Gaisser *et al.*, in *Proceedings of the 27th International Cosmic Ray Conference* (Copernicus Gesellschaft, Hamburg Germany, 2001).
[36] T. Gaisser, J. Phys. Conf. Ser. **47**, 15 (2006).
[37] A. Achterberg *et al.*, Phys. Rev. D **75**, 102001 (2007).
[38] J. Pumplin *et al.*, J. High Energy Phys. 07 (2002) 012.
[39] W. Lowry, *Fundamentals of Geophysics* (Cambridge University Press, Cambridge, England, 1997).
[40] J. Kiryluk *et al.*, in *Proceedings of the 30th International Cosmic Ray Conference* (Merida, Mexico, 2007), p. 95.
[41] F. W. Stecker, Phys. Rev. D **72**, 107301 (2005).
[42] G. Hill and K. Rawlins, Astropart. Phys. **19**, 393 (2003).
[43] A. Martin *et al.*, Phys. Lett. B **531**, 216 (2002).
[44] J. Pumplin *et al.*, J. High Energy Phys. 07 (2002) 012.
[45] R. Abbasi *et al.*, Phys. Rev. D **83**, 012001 (2011).
[46] J. Illanan *et al.*, Astropart. Phys. **34**, 663 (2011).
[47] R. Abbasi *et al.*, Phys. Rev. D **79**, 102005 (2009).
[48] T. Antoni *et al.*, Astropart. Phys. **24**, 1 (2005).
[49] A. Achterberg *et al.*, Phys. Rev. D **76**, 042008 (2007).
[50] S. Biagi, Search for a Diffuse Flux of Muon Neutrinos with the Antares Telescope, Conference presentation at NEUTRINO 2010 Athens, Greece (2010).
[51] R. Abbasi *et al.*, Astropart. Phys. **34**, 48 (2010).

Limits on Neutrino Emission from Gamma-Ray Bursts with the 40 String IceCube Detector

R. Abbasi,[28] Y. Abdou,[22] T. Abu-Zayyad,[33] J. Adams,[16] J. A. Aguilar,[28] M. Ahlers,[32] K. Andeen,[28] J. Auffenberg,[38] X. Bai,[31] M. Baker,[28] S. W. Barwick,[24] R. Bay,[7] J. L. Bazo Alba,[39] K. Beattie,[8] J. J. Beatty,[18,19] S. Bechet,[13] J. K. Becker,[10] K.-H. Becker,[38] M. L. Benabderrahmane,[39] S. BenZvi,[28] J. Berdermann,[39] P. Berghaus,[28] D. Berley,[17] E. Bernardini,[39] D. Bertrand,[13] D. Z. Besson,[26] D. Bindig,[38] M. Bissok,[1] E. Blaufuss,[17] J. Blumenthal,[1] D. J. Boersma,[1] C. Bohm,[34] D. Bose,[14] S. Böser,[11] O. Botner,[37] J. Braun,[28] A. M. Brown,[16] S. Buitink,[8] M. Carson,[22] D. Chirkin,[28] B. Christy,[17] J. Clem,[31] F. Clevermann,[20] S. Cohen,[25] C. Colnard,[23] D. F. Cowen,[36,35] M. V. D'Agostino,[7] M. Danninger,[34] J. Daughhetee,[5] J. C. Davis,[18] C. De Clercq,[14] L. Demirörs,[25] O. Depaepe,[14] F. Descamps,[22] P. Desiati,[28] G. de Vries-Uiterweerd,[22] T. DeYoung,[36] J. C. Díaz-Vélez,[28] M. Dierckxsens,[13] J. Dreyer,[10] J. P. Dumm,[28] R. Ehrlich,[17] J. Eisch,[28] R. W. Ellsworth,[17] O. Engdegård,[37] S. Euler,[1] P. A. Evenson,[31] O. Fadiran,[4] A. R. Fazely,[6] A. Fedynitch,[10] T. Feusels,[22] K. Filimonov,[7] C. Finley,[34] T. Fischer-Wasels,[38] M. M. Foerster,[36] B. D. Fox,[36] A. Franckowiak,[11] R. Franke,[39] T. K. Gaisser,[31] J. Gallagher,[27] M. Geisler,[1] L. Gerhardt,[8,7] L. Gladstone,[28] T. Glüsenkamp,[1] A. Goldschmidt,[8] J. A. Goodman,[17] D. Grant,[21] T. Griesel,[29] A. Groß,[16,23] S. Grullon,[28] M. Gurtner,[38] C. Ha,[36] A. Hallgren,[37] F. Halzen,[28] K. Han,[16] K. Hanson,[13,28] D. Heinen,[1] K. Helbing,[38] P. Herquet,[30] S. Hickford,[16] G. C. Hill,[28] K. D. Hoffman,[17] A. Homeier,[11] K. Hoshina,[28] D. Hubert,[14] W. Huelsnitz,[17] J.-P. Hülß,[1] P. O. Hulth,[34] K. Hultqvist,[34] S. Hussain,[31] A. Ishihara,[15] J. Jacobsen,[28] G. S. Japaridze,[4] H. Johansson,[34] J. M. Joseph,[8] K.-H. Kampert,[38] A. Kappes,[9] T. Karg,[38] A. Karle,[28] J. L. Kelley,[28] N. Kemming,[9] P. Kenny,[26] J. Kiryluk,[8,7] F. Kislat,[39] S. R. Klein,[8,7] J.-H. Köhne,[20] G. Kohnen,[30] H. Kolanoski,[9] L. Köpke,[29] S. Kopper,[38] D. J. Koskinen,[36] M. Kowalski,[11] T. Kowarik,[29] M. Krasberg,[28] T. Krings,[1] G. Kroll,[29] K. Kuehn,[18] T. Kuwabara,[31] M. Labare,[14] S. Lafebre,[36] K. Laihem,[1] H. Landsman,[28] M. J. Larson,[36] R. Lauer,[39] R. Lehmann,[9] J. Lünemann,[29] J. Madsen,[33] P. Majumdar,[39] A. Marotta,[13] R. Maruyama,[28] K. Mase,[15] H. S. Matis,[8] K. Meagher,[17,*] M. Merck,[28] P. Mészáros,[35,36] T. Meures,[1] E. Middell,[39] N. Milke,[20] J. Miller,[37] T. Montaruli,[28,†] R. Morse,[28] S. M. Movit,[35] R. Nahnhauer,[39] J. W. Nam,[24] U. Naumann,[38] P. Nießen,[31] D. R. Nygren,[8] S. Odrowski,[23] A. Olivas,[17] M. Olivo,[37,10] A. O'Murchadha,[28] M. Ono,[15] S. Panknin,[11] L. Paul,[1] C. Pérez de los Heros,[37] J. Petrovic,[13] A. Piegsa,[29] D. Pieloth,[20] R. Porrata,[7] J. Posselt,[38] P. B. Price,[7] M. Prikockis,[36] G. T. Przybylski,[8] K. Rawlins,[3] P. Redl,[17] E. Resconi,[23] W. Rhode,[20] M. Ribordy,[25] A. Rizzo,[14] J. P. Rodrigues,[28] P. Roth,[17] F. Rothmaier,[29] C. Rott,[18] T. Ruhe,[20] D. Rutledge,[36] B. Ruzybayev,[31] D. Ryckbosch,[22] H.-G. Sander,[29] M. Santander,[28] S. Sarkar,[32] K. Schatto,[29] T. Schmidt,[17] A. Schoenwald,[39] A. Schukraft,[1] A. Schultes,[38] O. Schulz,[23] M. Schunck,[1] D. Seckel,[31] B. Semburg,[38] S. H. Seo,[34] Y. Sestayo,[23] S. Seunarine,[12] A. Silvestri,[24] A. Slipak,[36] G. M. Spiczak,[33] C. Spiering,[39] M. Stamatikos,[18,‡] T. Stanev,[31] G. Stephens,[36] T. Stezelberger,[8] R. G. Stokstad,[8] S. Stoyanov,[31] E. A. Strahler,[14] T. Straszheim,[17] G. W. Sullivan,[17] Q. Swillens,[13] H. Taavola,[37] I. Taboada,[5] A. Tamburro,[33] O. Tarasova,[39] A. Tepe,[5] S. Ter-Antonyan,[6] S. Tilav,[31] P. A. Toale,[36] S. Toscano,[28] D. Tosi,[39] D. Turčan,[17] N. van Eijndhoven,[14] J. Vandenbroucke,[7] A. Van Overloop,[22] J. van Santen,[28] M. Vehring,[1] M. Voge,[23] B. Voigt,[39] C. Walck,[34] T. Waldenmaier,[9] M. Wallraff,[1] M. Walter,[39] C. Weaver,[28] C. Wendt,[28] S. Westerhoff,[28] N. Whitehorn,[28,*] K. Wiebe,[29] C. H. Wiebusch,[1] D. R. Williams,[2] R. Wischnewski,[39] H. Wissing,[17] M. Wolf,[23] K. Woschnagg,[7] C. Xu,[31] X. W. Xu,[6] G. Yodh,[24] S. Yoshida,[15] and P. Zarzhitsky[2]

(IceCube Collaboration)

[1]*III. Physikalisches Institut, RWTH Aachen University, D-52056 Aachen, Germany*
[2]*Department of Physics and Astronomy, University of Alabama, Tuscaloosa, Alabama 35487, USA*
[3]*Department of Physics and Astronomy, University of Alaska Anchorage, 3211 Providence Drive, Anchorage, Alaska 99508, USA*
[4]*CTSPS, Clark-Atlanta University, Atlanta, Georgia 30314, USA*
[5]*School of Physics and Center for Relativistic Astrophysics, Georgia Institute of Technology, Atlanta, Georgia 30332, USA*
[6]*Department of Physics, Southern University, Baton Rouge, Louisiana 70813, USA*
[7]*Department of Physics, University of California, Berkeley, California 94720, USA*
[8]*Lawrence Berkeley National Laboratory, Berkeley, California 94720, USA*
[9]*Institut für Physik, Humboldt-Universität zu Berlin, D-12489 Berlin, Germany*
[10]*Fakultät für Physik und Astronomie, Ruhr-Universität Bochum, D-44780 Bochum, Germany*
[11]*Physikalisches Institut, Universität Bonn, Nussallee 12, D-53115 Bonn, Germany*
[12]*Department of Physics, University of the West Indies, Cave Hill Campus, Bridgetown BB11000, Barbados*
[13]*Université Libre de Bruxelles, Science Faculty CP230, B-1050 Brussels, Belgium*
[14]*Vrije Universiteit Brussel, Dienst ELEM, B-1050 Brussels, Belgium*
[15]*Department of Physics, Chiba University, Chiba 263-8522, Japan*

[16]Department of Physics and Astronomy, University of Canterbury, Private Bag 4800, Christchurch, New Zealand
[17]Department of Physics, University of Maryland, College Park, Maryland 20742, USA
[18]Department of Physics and Center for Cosmology and Astro-Particle Physics, Ohio State University, Columbus, Ohio 43210, USA
[19]Department of Astronomy, Ohio State University, Columbus, Ohio 43210, USA
[20]Department of Physics, TU Dortmund University, D-44221 Dortmund, Germany
[21]Department of Physics, University of Alberta, Edmonton, Alberta, Canada T6G 2G7
[22]Department of Subatomic and Radiation Physics, University of Gent, B-9000 Gent, Belgium
[23]Max-Planck-Institut für Kernphysik, D-69177 Heidelberg, Germany
[24]Department of Physics and Astronomy, University of California, Irvine, California 92697, USA
[25]Laboratory for High Energy Physics, École Polytechnique Fédérale, CH-1015 Lausanne, Switzerland
[26]Department of Physics and Astronomy, University of Kansas, Lawrence, Kansas 66045, USA
[27]Department of Astronomy, University of Wisconsin, Madison, Wisconsin 53706, USA
[28]Department of Physics, University of Wisconsin, Madison, Wisconsin 53706, USA
[29]Institute of Physics, University of Mainz, Staudinger Weg 7, D-55099 Mainz, Germany
[30]Université de Mons, 7000 Mons, Belgium
[31]Bartol Research Institute and Department of Physics and Astronomy, University of Delaware, Newark, Delaware 19716, USA
[32]Department of Physics, University of Oxford, 1 Keble Road, Oxford OX1 3NP, United Kingdom
[33]Department of Physics, University of Wisconsin, River Falls, Wisconsin 54022, USA
[34]Oskar Klein Centre and Department of Physics, Stockholm University, SE-10691 Stockholm, Sweden
[35]Department of Astronomy and Astrophysics, Pennsylvania State University, University Park, Pennsylvania 16802, USA
[36]Department of Physics, Pennsylvania State University, University Park, Pennsylvania 16802, USA
[37]Department of Physics and Astronomy, Uppsala University, Box 516, S-75120 Uppsala, Sweden
[38]Department of Physics, University of Wuppertal, D-42119 Wuppertal, Germany
[39]DESY, D-15735 Zeuthen, Germany

(Received 7 January 2011; published 7 April 2011)

IceCube has become the first neutrino telescope with a sensitivity below the TeV neutrino flux predicted from gamma-ray bursts if gamma-ray bursts are responsible for the observed cosmic-ray flux above 10^{18} eV. Two separate analyses using the half-complete IceCube detector, one a dedicated search for neutrinos from $p\gamma$ interactions in the prompt phase of the gamma-ray burst fireball and the other a generic search for any neutrino emission from these sources over a wide range of energies and emission times, produced no evidence for neutrino emission, excluding prevailing models at 90% confidence.

DOI: 10.1103/PhysRevLett.106.141101 PACS numbers: 98.70.Rz, 95.85.Ry, 98.70.Sa

Gamma-ray bursts (GRBs) have long been proposed [1] as one of the most plausible sources of the highest energy cosmic rays, as the observed flux can be entirely explained if the primary engine of the bursts accelerates protons and electrons with comparable efficiencies. The electrons would produce the observed gamma-ray emission by synchrotron emission and, possibly, inverse Compton scattering, while the protons escape to form the high-energy cosmic rays observed at Earth. Waxman and Bahcall observed [2] that, in this case, a potentially detectable flux of high-energy neutrinos is produced by $p\gamma$ interactions when protons and photons coexist in the primary fireball. The detailed flux predictions are dependent on the fireball parameters; here we use the model by Guetta *et al.* [3] to compute these parameters from observations by gamma-ray telescopes. Past searches with IceCube and other neutrino telescopes have met with negative results [4–6] but have never before had sensitivities at the level of the expected flux. We search in this work for neutrinos in coincidence with 117 GRBs with half of the IceCube detector complete and for the first time reach a sensitivity that would yield a positive result given expected fireball parameters, with a 4σ expected excess.

IceCube is a TeV-scale neutrino telescope currently under construction at the South Pole which detects neutrinos by measuring the Cherenkov light from secondary charged particles produced in neutrino-nucleon interactions. A total of 5160 digital optical modules [7] containing 10-inch photomultipliers and arranged in 86 strings frozen in the ice will make up the full detector; the results presented here were obtained by using the first 40 of these strings. Although capable of detecting multiple flavors of neutrinos from the entire sky, for point sources the detector is sensitive primarily to up-going muons produced in muon neutrino charged-current interactions. Searches in the muon channel benefit from good angular resolution ($\sim 0.7^\circ$ for $E_\nu \gtrsim 10$ TeV) and from the long range of high-energy muons (several kilometers at TeV energies), which substantially increases the effective volume of the detector. By using up-going tracks, Earth is used to shield against the much larger flux of down-going muons from cosmic-ray interactions in the atmosphere. Backgrounds from cosmic-ray-produced muons and atmospheric neutrinos can be further reduced by using the muon energy, as neutrinos from GRBs are expected to have higher energies than from either atmospheric source.

The origin of observed events in IceCube is determined by fitting a track to the hit pattern of the detected Cherenkov light by using a maximum likelihood method [8]. The location of the maximum is used as the source of the associated neutrino (collinear with the muon), and the statistical uncertainty in the fit provides an estimate of the uncertainty on the reconstructed direction [9].

Because of the stochastic nature of muon energy-loss processes and the rarity of events fully contained within the detector, it is not possible to measure the energy of either the muon or the primary neutrino directly. It is, however, possible to measure the mean energy-loss rate of muons in the detector, which is correlated at high energies with the muon energy and with the original neutrino energy [10]. The uncertainty of the muon energy using this method is on the order of 0.3–0.4 in $\log_{10}E$.

IceCube operated in a 40 string configuration from April 5, 2008 until May 20, 2009. During that time 129 GRBs were reported in the northern hemisphere via the GRB Coordinates Network (GCN) [11]. We assembled a catalog using data from GCN notices and circulars, where the position of the burst was taken from the notice with the lowest reported positional error. For bursts which were localized only by the Fermi Gamma-ray Burst Monitor (GBM), the position was instead taken from the GBM Burst Catalog [12]. The start and stop times of the prompt gamma-ray phase, $T_{\rm start}$ and $T_{\rm stop}$, respectively, were determined by taking the earliest and latest times any satellite reported detecting gamma rays. The fluence and spectral information were taken preferentially from Fermi GBM, Konus-Wind, Suzaku Wide-band All-sky Monitor, and then Swift.

Fermi GRBs for which no fluence was reported because the burst was too weak were removed. GRB080521, GRB081113, and GRB090515 occurred during detector downtime and were removed from the catalog. GRB090422 and GRB090423 occurred during a preliminary run with 59 strings in operation and will be analyzed later. The final catalog contained 117 bursts.

Neutrino spectra were calculated [3,4] by using data from the gamma-ray spectra of individual bursts or average parameters if no spectral measurements were available. Definitions of parameters and equations used to calculate neutrino fluence are identical to Appendix A of Ref. [4]. Spectra were calculated as power laws with two breaks: a low-energy break associated with the break in the photon spectrum and a high-energy break from synchrotron losses of muons and pions (Fig. 1).

From the length of gamma emission and energy spectrum, bursts are classified by GCN into two groups (long-soft and short-hard), which may have different underlying sources. If a burst was not explicitly identified as one class in a GCN notice, we used average values for a short-hard burst if 90% of the gamma emission was in less than 2 s [4] and a long-soft burst otherwise. Parameters for average

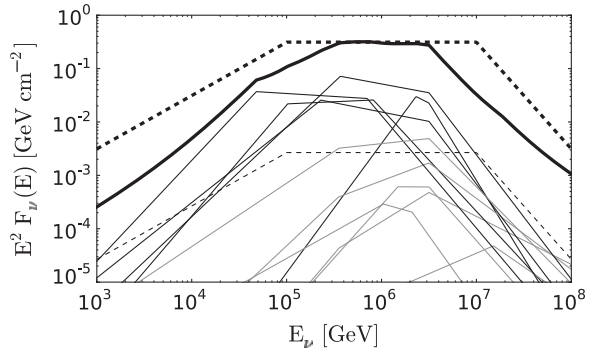

FIG. 1. The neutrino spectra, including oscillations, of the five brightest GRBs are shown along with eight randomly selected bursts (thin lines). A single burst with Waxman 2003 parameters [16], assuming a cosmic-ray energy density of 10^{44} erg Mpc^{-3} yr^{-1}, is shown by a thin dashed line. The sum of all 117 individual bursts is shown as a thick solid line along with the Waxman 2003 [16] prediction in a thick dashed line.

long-soft bursts are from Ref. [4]. For short-hard bursts, we used $L_\gamma^{\rm iso} = 10^{51}$ erg/s, $t_{\rm var} = 0.001$ s, and for redshift (z) the average of all Swift short burst measurements.

Two independent searches were conducted: one searching for neutrinos with the specific energy spectrum predicted by Guetta *et al.* [3] during the period of maximum gamma emission and the other searching generically for high-energy neutrinos within up to 24 h of the observed bursts.

The first of the two analyses, the model-dependent analysis, was designed specifically to find neutrinos produced in $p\gamma$ interactions during the prompt phase of the GRB. Events observed in the detector were reduced by a series of cuts designed to select neutrinolike events, resulting in a data sample of primarily atmospheric neutrinos, an irreducible background for this analysis. We then conducted an unbinned maximum likelihood search [4] in which each event passing these cuts was assigned likelihoods of being a signal event (from a GRB) and of being a background event. Both the signal and background likelihoods for each event i were the product of three independent probability density functions (PDFs) based on direction, arrival time, and muon energy.

The spatial signal PDF was a two-dimensional Gaussian:

$$P^S(\vec{x}_i) = \frac{1}{2\pi(\sigma_{\rm GRB}^2 + \sigma_i^2)} \exp\left(-\frac{|\vec{x}_{\rm GRB} - \vec{x}_i|^2}{2(\sigma_{\rm GRB}^2 + \sigma_i^2)}\right), \quad (1)$$

where $|\vec{x}_{\rm GRB} - \vec{x}_i|$ is the angle between the reconstructed neutrino direction and the best location of the gamma-ray burst provided by GCN and $\sigma_{\rm GRB}$ and σ_i are the localization uncertainty of the GRB and the muon reconstruction, respectively. The spatial background PDF was computed by using a smoothed histogram of all off-source data in detector coordinates, accounting for zenith and azimuth asymmetry in the detector.

The temporal signal PDFs were constant during the prompt phase of the gamma-ray burst (between T_{start} and T_{stop}), with Gaussian tails of width $T_{\text{stop}} - T_{\text{start}}$ (constrained to at minimum 2 s and at maximum 30). The background PDFs were constant in time.

The signal energy PDF was computed from the reconstructed muon energy loss (dE/dx) for neutrinos simulated with the average of the individual burst spectra (Fig. 1), while the background energy PDF was computed from the dE/dx distribution of off-source data.

From these likelihoods, we then computed the maximally likely number of signal events. The resulting likelihood ratio (the *test statistic*) was then compared to the distribution from scrambled background data sets to compute the significance of a result.

As well as looking for neutrinos with properties modeled from measured burst parameters, we conducted an additional search (the model-independent analysis) by using wider time search windows and looser event selection criteria, allowing observation of events with late or early arrival times or with unexpected energies due to unanticipated emission mechanisms.

Starting at the interval from -10 to $+10$ s from the GRB trigger time, we expanded a search time window in 1 s increments in both directions out to ± 1 day, looking for a significant excess of neutrinos at each iteration. High correlation between adjacent time windows reduces the trials correction to the significance of any excess to only a few hundred.

Event selection for the model-independent search was based entirely on rejecting misreconstructed down-going atmospheric cosmic-ray muons, which are the dominant background to this analysis, constituting more than 99.9% of the final 1.61×10^8 event sample. To avoid assuming a signal neutrino spectrum, no attempt was made to reject the small low-energy background from atmospheric neutrinos.

To ensure that no events were missed due to incorrect assumptions, this analysis was designed to maximize the number of signal neutrinos in the final analysis instead of the significance of an excess. Instead of being selected by hard cuts, events were weighted by their probabilities of being signal neutrinos [13]. Each probability was the product of the event's point-spread probability density function [Eq. (1)] and the probability that the event was a neutrino, determined by dividing smoothed histograms of detector data and neutrino simulation in several variables related to reconstruction accuracy. These were then summed in each time window to form the expectation of the on-source signal neutrino density, which was then compared to the expected background value obtained by scrambling the observed data in time.

Although the use of scrambled data for the background reduces many possible uncertainties, the use of simulation for the signal introduces some systematic errors. The dominant sources of uncertainties in the final limits from both analyses are photon propagation in the ice, the quantum efficiency of the photomultiplier tubes, and theoretical uncertainties in both the neutrino-nucleon cross section and cross sections for muon energy-loss processes at high energies. Depending on the analysis and time interval, the cumulative effect of these uncertainties amounts to 2%–13% and has been included in the final limits by using a Bayesian marginalization procedure [14].

No events were observed in the model-dependent search with a signal to background likelihood ratio greater than 1, with 2.99 signal events expected on a background of 0.097. The closest event to its associated GRB was 26° from GRB090301A. This sets a 90% upper limit of 82% of the expected flux in the region 37–2400 TeV where 90% of the events were expected, including a systematic uncertainty of ~2% (Fig. 2).

In the model-independent search, no candidate events were observed in the interval ± 2248 s with 4.2 expected from the Guetta *et al.* calculation. The variation of the upper limit (Fig. 3) with Δt reflects statistical fluctuations in the background, as well as the presence of individual events of varying quality. The three most significant of these occurred at -2249, -3594, and -6430 s, respectively, and were low-energy (~ 1 TeV) neutrinos consistent with the atmospheric neutrino background. In addition to a constant $^{+6}_{-2}$% uncertainty on the effective area (the ratio of fluence to the expected number of events), there is a systematic uncertainty in the limit on the number of expected events that increases with the size of the time window from 0%–10% (included in Fig. 3). This arises from the increased effect of systematic uncertainties in the event selection as the amount of background in the search window increases and the ability to distinguish GRB neutrinos from background events becomes correspondingly more important.

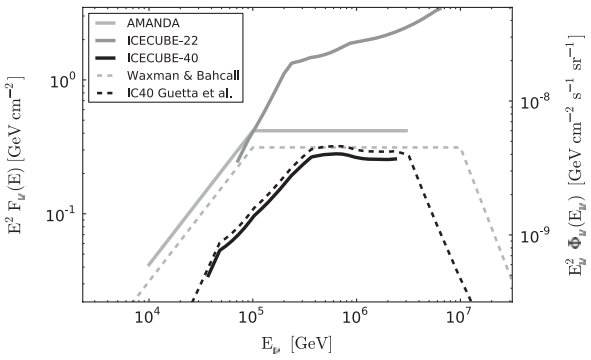

FIG. 2. 90% C.L. Neyman [17] upper limit (including systematics) set by model-dependent analysis in solid black with the expected Guetta *et al.* flux in dotted black. The 22 string IceCube limit [4] is in dark gray and AMANDA [5] in light gray. The Waxman 2003 flux [16] is shown for comparison in dotted light gray. Diffuse fluxes were obtained from fluences assuming a total of 667 uniformly distributed bursts per year. Fluences are aggregate for 117 bursts.

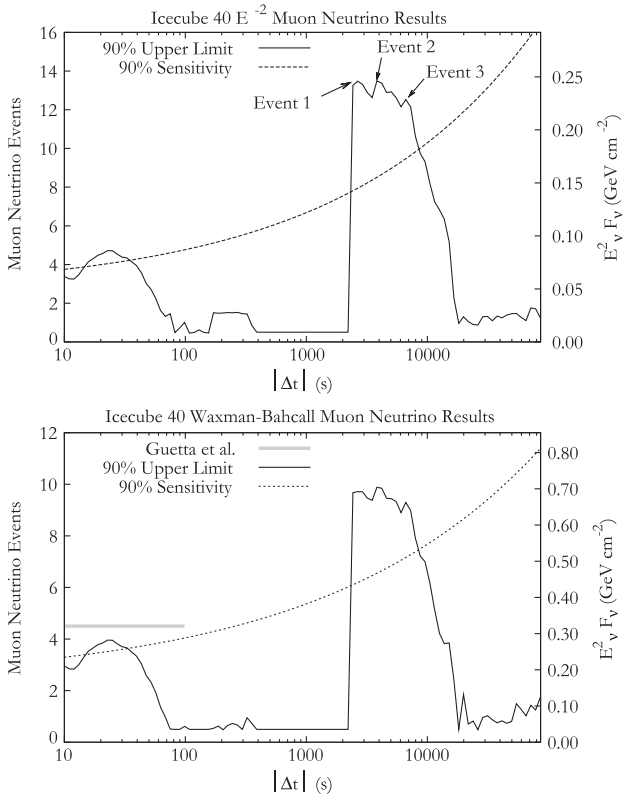

FIG. 3. 90% C.L. Feldman-Cousins [18] upper limit (fluence normalization at 642 TeV, the first peak of the expected spectrum) set by the model-independent analysis in each time window for an E^{-2} and for the Guetta *et al.* spectrum. Systematic errors on the number of events are included. There is an additional $^{+6}_{-2}\%$ uncertainty on the effective area and thus on the right-hand axis. The three sharp peaks between 2000 and 7000 s are caused by three low-energy neutrino events consistent with the atmospheric background.

While the specific neutrino-flux predictions of the fireball model provided by Waxman and Bahcall [2] and by Guetta *et al.* [3] are excluded (90% confidence) by this work, we have not yet ruled out the general picture of fireball phenomenology. The neutrino flux we compute for GRBs is determined by the flux of protons accelerated in the fireball and by the fraction of proton energy transferred to charged pions (f_π). The proton flux can be chosen either such that the energy in gammas and protons is equal or set to the flux of cosmic rays above 10^{18} eV, with similar results. f_π is determined largely by assuming protons are accelerated, in conjunction with the observed low optical thickness of the source. Because of uncertainties in the bulk boost factor and internal structure of the shocks, f_π may range from 10% to 30% [15], causing an uncertainty of about a factor of 2 on our calculation of the flux, which used $f_\pi \approx 0.2$. Future observations by IceCube will push our sensitivity below the level of this theoretical uncertainty on f_π and allow direct constraints on acceleration of protons to ultrahigh energies in gamma-ray bursts.

We acknowledge support from the following agencies: U.S. NSF—Office of Polar Programs, U.S. NSF—Physics Division, University of Wisconsin Alumni Research Foundation, the GLOW and OSG grids; U.S. DOE, NERSCC, the LONI grid; NSERC, Canada; Swedish Research Council, Swedish Polar Research Secretariat, SNIC, K. and A. Wallenberg Foundation, Sweden; German Ministry for Education and Research, Deutsche Forschungsgemeinschaft; FSR, FWO Odysseus, IWT, BELSPO, Belgium; Marsden Fund, New Zealand; JSPS, Japan; SNSF, Switzerland. A. Groß is supported by the EU Marie Curie OIF Program, J. P. R. by the Capes Foundation, Brazil, and N. W. by the NSF GRFP.

*To whom all correspondence should be addressed.
†Also at Università di Bari and Sezione INFN, Dipartimento di Fisica, I-70126, Bari, Italy.
‡Also at NASA Goddard Space Flight Center, Greenbelt, MD 20771, USA.

[1] E. Waxman, Phys. Rev. Lett. **75**, 386 (1995).
[2] E. Waxman and J. Bahcall, Phys. Rev. Lett. **78**, 2292 (1997).
[3] D. Guetta, D. Hooper, J. Alvarez-Mũniz, F. Halzen, and E. Reuveni, Astropart. Phys. **20**, 429 (2004).
[4] R. Abbasi *et al.* (IceCube Collaboration), Astrophys. J. **710**, 346 (2010).
[5] A. Achterberg *et al.* (IceCube Collaboration), Astrophys. J. **674**, 357 (2008).
[6] E. Thrane *et al.* (Super-Kamiokande Collaboration), Astrophys. J. **704**, 503 (2009).
[7] R. Abbasi *et al.* (IceCube Collaboration), Nucl. Instrum. Methods Phys. Res., Sect. A **601**, 294 (2009).
[8] J. Ahrens *et al.* (AMANDA Collaboration), Nucl. Instrum. Methods Phys. Res., Sect. A **524**, 169 (2004).
[9] T. Neunhöffer, Astropart. Phys. **25**, 220 (2006).
[10] S. Grullon, D. Boersma, G. Hill, K. Hoshina, and K. Mase, in *Proceedings of the 30th ICRC, Merida, Mexico* (Universidad Nacional Autonoma de Mexico, Mexico City, 2008).
[11] "GRB Coordinates Network," http://gcn.gsfc.nasa.gov/.
[12] "Fermi GBM Burst Catalog," http://heasarc.gsfc.nasa.gov/W3Browse/fermi/fermigbrst.html.
[13] M. F. Morales, D. A. Williams, and T. De Young, Astropart. Phys. **20**, 485 (2004).
[14] J. Conrad and F. Tegenfeldt, Nucl. Instrum. Methods Phys. Res., Sect. A **539**, 407 (2005).
[15] D. Guetta, M. Spada, and E. Waxman, Astrophys. J. **559**, 101 (2001).
[16] E. Waxman, Nucl. Phys. B, Proc. Suppl. **118**, 353 (2003).
[17] K. Nakamura (Particle Data Group), J. Phys. G **37**, 075021 (2010).
[18] G. J. Feldman and R. D. Cousins, Phys. Rev. D **57**, 3873 (1998).